Optical Metrology with Lasers and Position-Sensitive Detectors

Submitted by

Salman Iqbal
(01-FET/PhD/F03)

Supervised by

Prof. Dr. M. M. S. Gualini
Prof. Dr. Khalid Rashid

Faculty of Engineering & Technology
International Islamic University, Islamabad, Pakistan
(2007)

Final Approval

It is certified that we have read the thesis submitted by Mr. Salman Iqbal (01-FET/ PhD/F03) and it is our judgment that this thesis is of sufficient status to warrant the acceptance by International Islamic University, Islamabad for the degree of Doctor of Philosophy.

Prof. Dr. I. M. Qureshi
Internal Examiner

Prof. Dr. Aslam Baig
External Examiner

Prof. Dr. M. M. S. Gualini
Supervisor

Prof. Dr. Khalid Rashid
Supervisor

28/7/2007

International Islamic University, Faculty Block 2, H-10, Islamabad, Pakistan
Faculty of Engineering & Technology

Dedicated
to
My Late Parents

Mr & Mrs Muhammad Iqbal Qureshi

A Thesis submitted to the
Faculty of Engineering & Technology,
International Islamic University, Islamabad
as a partial fulfillment of the requirements
for the award of the degree of
Doctor of Philosophy

Declaration

I hereby declare that this thesis, neither as a whole nor as a part thereof, has been copied out from any source. It is further declared that I have carried out this research by myself and have completed this thesis on the basis of my personal efforts under the guidance and help of my supervisors. If any part of this is proved to be copied out or earlier submitted, I shall stand by the consequences. No portion of the work presented in this thesis has been submitted in support of any application for any other degree or qualification of this or any other university or institute of learning.

Salman Iqbal
01-FET/PhD/F03

Acknowledgements

My deepest thanks and praises are to the Almighty, the Most Kind and the Most Merciful, who enabled me to complete this work and who has showed us right path through His last prophet SAW. After this, I want to say that I am deeply indebted to my late parents whose untiring efforts and prayers are behind all my successes and who did used to dream that their son may become a qualified scientist one day.

I want to express my gratitude to my supervisors Dr. M. M. S. Gualini and Dr. Khalid Rashid for all their guidance throughout this research process. They have been a source of inspiration for me all the way. In terms of guidance, my gratitude is also for Dr. A. K. Asundi of Nanyang Technological University Singapore, where I did a major part of my research work. I am also grateful to Prof. Afaq Hussain, Dean and Head of Electrical Engineering Department, Prof. Sikandar Hayat Khiyal, Head of Computer Science Department, Mr. Gulzar Khwaja, Director (Academics), Mr. Karim Ahmad and Dr. Aslam Farooq from Institute of Industrial Control Systems and all the helping staff in International Islamic University and Institute of Industrial Control Systems. At the same time, I am thankful to Pakistan Higher Education Commission, Dr. Atta-ur-Rehman, Dr. Sohail Naqvi and scholarship scheme coordinators Mr. Muhammad Saeed, Mr. Muhammad Ashfaq and Mrs. Noshaba Awais for the financial support of merit PhD scholarship and foreign research scholarship.

In my family, I have no doubt that I am indebted to my brother Dr. Imran Iqbal and uncle Maj. Gen. (R) W. D. Arshad for all their help and support. Also, besides many others in the family, I am very much indebted to my wife for her untiring and never-failing support, and do thank for the patience shown by her and by my children during all these years.

Salman Iqbal
01-FET/PhD/F03

Thesis in Brief

Title:	Optical Metrology with Lasers and Position-Sensitive Detectors
Author:	Salman Iqbal (01-FET/PhD/F03)
Supervised By:	Prof. Dr. M. M. S. Gualini Prof. Dr. Khalid Rashid International Islamic University, Islamabad
Work Facilities:	IIUI Computer Lab, Islamabad IICS Optical Lab, Rawalpindi NTU Photonics Lab, Singapore Prima Industries, Torino, Italy
Tools Used:	WaveSense Wavefront Sensor Camera PEMI Moire Inteferometer SpotOn Positioning System Data Translation Image Capture Tool Pentium III Machines and Windows OS Optical Lab Kit Matlab
Date Started:	January 2004
Date Completed:	June 2007

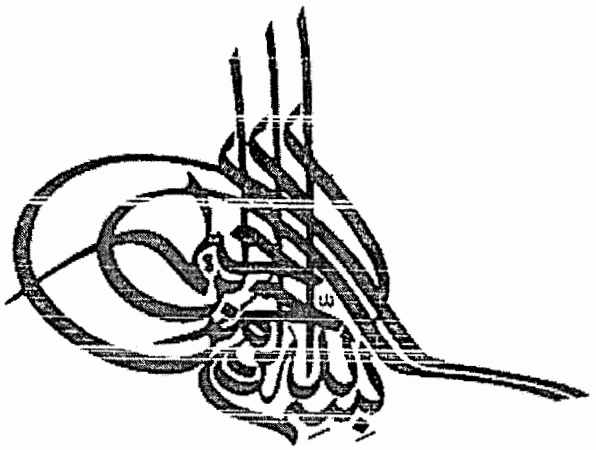

In the Name of Allah The Most Beneficent The Most Merciful

Abstract

This thesis presents ***optical metrology systems using laser & position-sensitive detectors***. In this area, a new diffraction strain measurement technique is developed, implemented, analyzed and characterized. ***Related research work on the optical metrology components*** is also included, dealing with position-sensitive detectors analysis and laser-beam applications.

The research in optical metrology systems using lasers and PSDs comprises development of a novel whole-field strain measurement technique and its implementation as Multipoint Diffraction Strain and Tilt Sensor using Moire Interferometer and Multichannel PSD. All the different variations of diffraction strain sensors as developed by different researchers up to date, measure single point strain on the sample only. At the same time, the whole-field strain measurement techniques like Moire Interferometry and ESPI have their own shortcomings like lengthy fringe processing and image subtraction algorithms. Besides this is the obvious degradation of their spatial resolution at lower strain values owing to the sparse fringes. On the other hand, the developed system has the unique feature of direct and near-real-time diffraction-based strain and tilt measurement at a large array of points on the sample surface. The system uses simultaneous position tracking of smaller beamlets diffracted differently from different regions of the component surface under test. Using this setup, whole-field strain and tilt distribution patterns over the component body can be obtained immediately, without the need for fringe processing. Furthermore, the system also has capability of measuring rotation and shear strain, making it a truly versatile whole-field strain sensing system. Simultaneous strain and tilt measurement at more than one thousand points is being reported in this research. Complete microcomputer-based implementation of this system is described. Detailed characterization and analysis of the developed system is presented along with some important development decisions. The system offers a promising combination of features like direct and fast calculation of whole-field strain with a fine spatial resolution and good sensitivity. These make this technique suitable for precision

applications in structures, mechanics and micro-mechanics, while offering a considerable saving in time and equipment cost.

Work on Optical Metrology components starts with a unique analysis of position-sensitive detectors used in noisy industrial environment, where several other light sources also coexist and thus produce unpredicted effects on PSD output. Many researchers of other photo-sensors have analyzed their performance in presence of these stray noises, while this problem has many times been outlined in context of PSDs too. Nonetheless, detailed performance analysis of PSDs with stray optical noises is very much needed. For this purpose, we first describe and model these stray noises with respect to the operation of PSDs and then analyze the response of the detectors in the presence of these spurious signals. The experimental results are compared with the results from the proposed mathematical model and it is observed that the measured performance is within a fraction of a percent of the calculated one. The analysis of systematic errors encountered during data collection is also presented. The study is expected to be very useful for the accurate & precise use of PSD-based sensors in the industrial units like production lines, workshops and others.

Following this, the work on laser beams analyzes their use in a novel material processing technique. Laser welding of galvanized steel sheets in lap configuration is the challenging problem being investigated for more than two decades, originating due to the difference in the melting points of steel and zinc. Earlier solutions are either insufficient for desired results or too cumbersome to be realized in practice. For this purpose, dual laser beams method is being discussed modeled and analyzed, involving a pre-cursor beam and a higher-power welding beam. The first beam cuts a slot, thus making an exit path for the zinc vapours, while the second beam performs the needed welding. The work also presents some experiments performed on the shop floor using this method, along with the metallurgical analysis from laboratory showing successful absence of Zinc in the weld area. Owing to its simpler approach and lesser time consumption, this technique is expected to be very attractive in terms of workshop implementation and welding throughput.

List of Terms, Abbreviations and Symbols

Terms

The use of terms and parameters is largely in view of their utilization within the experimental mechanics and metrology communities.

Accuracy	The stability of measurement in terms of standard deviation present in multiple readings of the same input.
Linearity	Maximum deviation of output from input for a specified range of measurements as a fraction of full-scale reading.
Position Resolution	The minimum displacement that can be resolved by a given position sensor.
Range	The maximum difference between two extreme values which can be dependably measured without significant distortion.
Sensitivity	The smallest change in input that produces a statistically significant change in response.
Spatial Resolution	Distance between two distinct adjacent micro-measurements made from a set of input data.
Position Uncertainty	Maximum error present in the position measurement due to the (optical) noises
Systemetic Error	The inherent bias of a measurement sensor or process.

Abbreviations

BiCMOS	Bipolar complementary metal oxide semiconductor
CCD	Charge-coupled device

CMOS	Complementary metal oxide semiconductor
CNC	Computerized numerical control
CO_2 Laser	Carbon dioxide laser
CW Laser	Continuous wave laser
DC	Duty cycle
ESPI	Electron speckle pattern interferometry
FSD	Full-scale deflection range
FSR	Full-scale reading
HAZ	Heat-affected zone
HeNe	Helium Neon
HPDL	High-power diode laser
LASER	Light amplification through stimulated emission of radiation
LE	Lateral effect
LEP	Lateral effect photodiode
MEMS	Micro-electro-mechanical structure
M^2	Beam quality factor
Nd:YAG Laser	Neodymium-yittrium-aluminum garnet laser
Nd:YVO_4 Laser	Neodymium-yittrium-vanadate laser
PSD	Position-sensitive detector
QD	Quadrant detector
SEM EDS	Scanning electron microscopy energy dispersive spectroscopy
SI	Systeme Internationale d'unites
S/N	Signal-to-noise ratio
TEM	Transverse mode of laser
1-D	One-dimensional
2-D	Two-dimensional
3-D	Three-dimensional

Symbols

α	Incidence angle on diffraction grating
β	Diffraction angle from diffraction grating
β_y	Vertical angle of diffracted beam
$d\alpha$	Change in incidence angle
$d\beta$	Change in diffraction angle
dP	Change in grating pitch
δP	Error in position calculation
$\Delta\phi$	Change in rotation angle
Δs	Fringe spacing
$\Delta\theta_x$	Tilt angle in xz-plane
$\Delta\theta_y$	Tilt angle in yz-plane
Δx	Shift in light spot in x-axis
Δy	Shift in light spot in y-axis
ε_x	Normal strain in x-axis
ε_y	Normal strain in y-axis
f	Focal length of focusing lens
f_v	Frequency of virtual grating
g_e	Acceleration of gravity
g	Gap width in material processing
I	Intensity of radiation
i	Current output of sensor
i_n	Current output from n-terminal
i'_n	Noise current output from n-terminal
K_f	Error factor for uncollimated beam
L	Length of sensor
λ	Wavelength of incident light
m	Diffraction order (+1/-1 used)
$m\varepsilon$	Milli-strains

$mrad$	Milli-radians
$\mu\varepsilon$	Micro-strains
μrad	Micro-radians
ν	Frequency of radiation
Ω	Beam solid angle
P	Pitch of diffraction grating
P_x	Position calculated in x-axis
P_y	Position calculated in y-axis
ϕ	Rotation angle of specimen
ρ	Density of material
t	Thickness of sample
u	Displacement field in x-axis
V	Velocity of material processing
Vol	Volume of material
v	Displacement field in y-axis
v_2	Velocity of moving material

List of International Publications

Journal Publications

1. S. Iqbal and A. Asundi, *Characterization of Multipoint Diffraction Strain Sensor (MISS)*, Key Engineering Materials Vol 326-328 (2006), pp 87-90.
2. S. Iqbal and A. Asundi, *Multipoint Diffraction Strain Sensor: Theory and Results*, Measurement Science and Technology 17 (2006), pp 2306-2312.
3. S. Iqbal and A. Asundi, *Characterization of Multipoint Strain and Tilt Sensor based on Moire Interferometer and Multi-channel Imaging Position-sensitive Detector,* Review of Scientific Instruments 77 (2006), 113110.
4. S. Iqbal, M. M. S. Gualini and K. Rashid, *Impact of Stray Illumination Noise on the Position Response of Position-Sensitive Devices*, Journal of Applied Sciences Vol 6-3 (2006), pp 682-687.
5. M. M. S. Gualini, S. Iqbal and F. Grassi, *Modified dual-beam method for welding galvanized steel sheets in lap configuration*, Journal of Laser Applications Vol 18-3 (2006), pp185-191.
6. S. Iqbal, M. M. S. Gualini, and F. Grassi, *Laser Welding of Zinc-Coated Steel with Tandem Beams: Analysis and Comparison*, Journal of Material Processing Technology 184 (2007) pp 12-18.

Conference Publications

1. S. Iqbal, S. Mhaisalkar and A. Asundi, *Multipoint Diffraction Strain Sensor: an add-on to Moiré Interferometer*, SPIE Optics & Photonics, San Diego, USA, 2006.
2. S. Iqbal and A. Asundi, *Simultaneous Micro Measurements of Strain and Tilt using Multichannel PSD,* Asia-Pacific Conference on Transducers & Micro-Nano Technology, Singapore, 2006

3. S. Iqbal, M. M. S. Gualini and K. Rashid, *Stray noises and illuminations disturbing the performance of position-sensitive devices*, SPIE Optics & Photonics, SanDiego, USA, 2005, Proceedings-5867, Paper-5.

Table of Contents

Chapter # 1

Introduction

1. Introduction

As many of the hi-tech industrial products of the world are moving towards miniaturization and larger integration, the importance of micro and nano technologies is growing exponentially. This is also coupled with the increasing requirements of industrial automation and quality control. These trends are giving rise to the need of measurement techniques, which can work on these smaller scales with accuracy, reliability and ease of integration. Optical measurement or metrology techniques, having these and other attractive features, have thus seen an unprecedented boom along with the above-mentioned trends.

1.1 Optical Metrology

Optical Metrology is the science, which deals with the measurement techniques utilizing optical methods. Of major interest in these has been the measurement of distances and angles, though a whole lot of other parameters can also be directly or indirectly measured [1]. Recent advances in optical devices, vision systems and computer technology have enabled the diverse development of new optical systems and techniques for measurement.

In optical metrology, different properties of light or electro-magnetic waves are utilized one way or the other including interference, diffraction, speckle and polarization. There are diverse techniques employed in optical metrology basing on these effects including normal interferometry, speckle interferometry, Moire interferometry, holography, spectroscopy, photoelasticity, profilometry and fiber optics technology. Optical metrology systems may utilize processes of simple detection, triangulation, signal processing and image processing. The target measurements with optical metrology include different parameters and physical properties including distance, angle, velocity, frequency, irradiance, vibration, temperature, flow and strain [2,3,4].

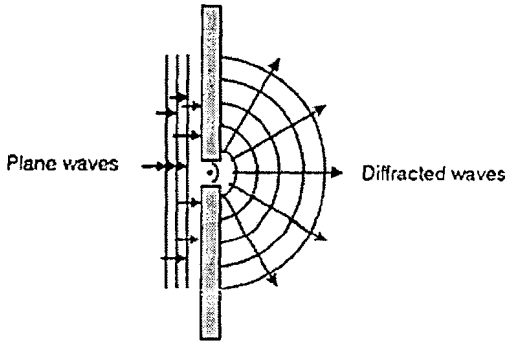

Figure 1.1. Phenomena of Diffraction [2]

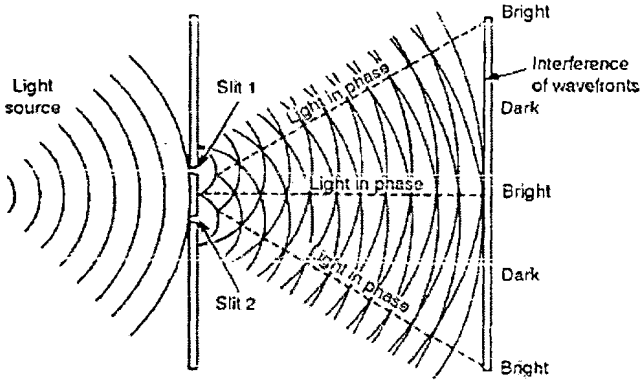

Figure 1.2. Phenomena of Interference [2]

1.2 Lasers

The advent of lasers in early 1960s has provided an invaluable tool for the development of advanced optical instrumentation. There are many properties of lasers, which have given rise to sophisticated techniques in optical metrology. Along with metrology applications, laser beams are usefully applied in telecommunication, medicine, environmental monitoring, defence and material processing [5].

1.2.1 Properties of Lasers

Some specific properties of laser light make it distinctly useful and suitable for different applications including metrology and material processing. One of these properties is directionality, which makes the laser beam travel for long distances with minimum

divergence. This is the reason for narrow beam formation of laser light and also makes its detection easy and predictable. Due to this property the output power of laser light gets concentrated in small areas and the brightness of laser light is very high compared to other sources. The focused power thus produced is very useful for laser-based material processing.

Another useful property of laser is monochromaticity so that a normal laser beam contains only a narrow range of wavelengths compared to normal light sources. With the special line-narrowing techniques, this property can be improved further for specific applications like spectroscopy. Another unique property of laser is coherence so that the electromagnetic waves in a laser beam are traveling in phase with one-another. Thus the coherence length or the distance over which the light remains in phase for lasers is very high compared to other conventional or scientific light sources. Similar effects are observed in terms of time over which the laser light remains coherent [6].

1.2.2 Lasers in Optical Metrology

The above-mentioned properties of lasers make them very attractive for a number of metrology applications, which are not practicable with other light sources. One of the major example for this is interferometry, which has become possible due to the properties of coherence and monochromaticity. With these properties, the interference of laser light beams produces fringes, which are visible and useful for the measurement applications. On the other hand, interference between the waves of the normal light cannot produce visible fringes. At the same time, incident beams on the diffraction elements like gratings produce distinctly rotating output beams due to the properties of directionality and monochromaticity. Such useful phenomena may not be possible with conventional light sources.

The laser-based metrology instruments include different types like alignment tools, trackers, telemeters, interferometers, speckle interferometers, holographic interferometers, velocimeters, profilometers, vibrometers, gyroscopes, shearographic instruments and different fiber-optics sensors [7].

1.2.3 Lasers in Material Processing

Due to high directionality of laser beams, the irradiance, fluence and brightness of these beams are very high. This makes them very useful for a number of material processing applications including engraving, cutting, welding, drilling, cladding and surface treatment. Some of the advantages of using lasers for such purposes are precision, surface finish, neatness and working with diverse geometries and material configurations [8,9].

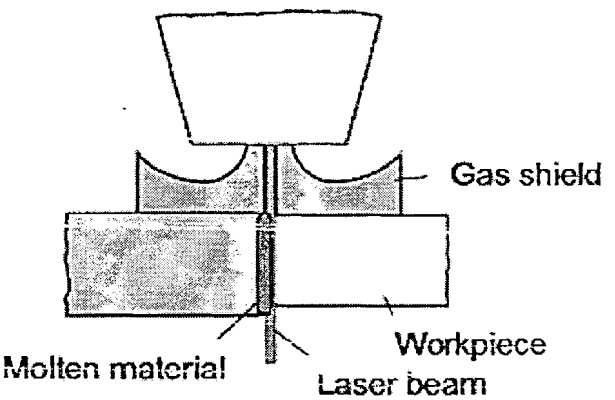

Figure 1.3. Laser welding as an area of laser material processing

1.3 Optical Displacement Measurement

Many of the applications in the industry, telecommunications and other fields require accurate measurement of displacement of objects through non-contact methods. The needed applications may include slow-moving tools or the components vibrating at moderately high frequencies and may involve measurement ranges varying from the sub-millimetric ranges for the precision instruments to tens of meters in the case of the remotely-controlled vehicles or robots. The requirements may also warrant position-measurement in the axial or lateral direction w.r.t. the optical axis of the measuring instruments [10,51].

Measurement of linear displacement may have different possible solutions. Due to its ruggedness and often contact-less characteristics, optical systems are very popular, particularly when fast changes in displacement need to be measured. Many of these methods allow measurement in sub-micrometer or even sub-nanometer range [10,67].

Among the important optical or electro-optical displacement measurement techniques first may be Optical Interferometry, which is mostly used in the applications requiring high resolution and accuracy in the measurement of small or very small linear displacements. Among others, it is used in precision tooling, calibration instruments and for measurement of different engineering parameters.

Some systems to measure displacement by optical means are based on a light source and a light sensor where displacement produces change in optical power detected by the sensor. This change may be due to the closer-farther movement of the reflecting body or due to the light obstruction caused by the movement of a body.

Position-sensitive-detectors (PSD) are semiconductor devices, which give electrical output based on the position of the light spot falling on the surface of these devices. These may be of different types as described in later sections [52,53].

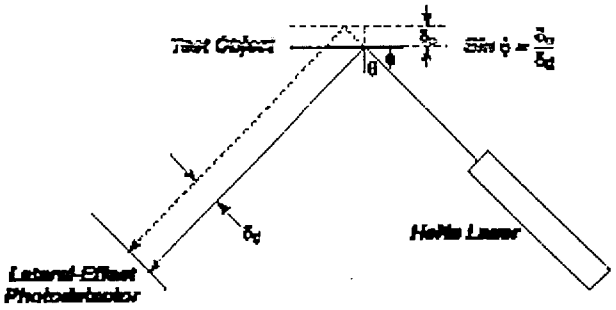

Figure 1.4. Linear displacement measurement with PSD and laser [58]

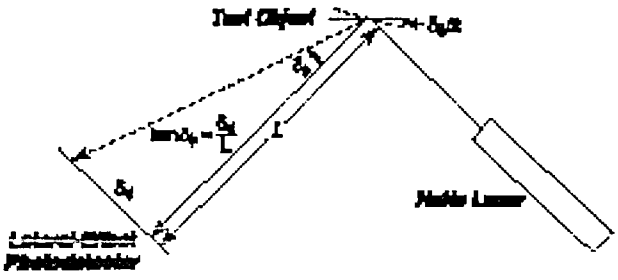

Figure 1.5. Angular displacement measurement with PSD and laser [58]

Linear displacement optical encoders are basically made of a light source and a light detector, optically connected through a 'ruler' of alternate constant-size transparent and opaque zones. With the movement of the 'ruler', the sensor sees a train of light pulses and can thus convert them to the information of the object movement.

Another displacement sensor system proposed is based on the determination of the coordinates of a self-luminous object through the measurement of the wave fronts emitted by the object and detected by a Shack-Hartman wave-front sensor [10].

1.4 Position-Sensitive Detectors - Discrete

Semiconductor position-sensitive detectors (PSDs) offer very good solutions for position measurement applications and since their inception in late fifties, these devices have become a major tool for lateral position measurement. These detectors are mostly semiconductor devices and can be of different types, which are suitable for different applications. For normal measurement or alignment applications discrete detectors are used such as quadrant detectors etc. For more detailed tracking or profiling applications imaging or array type detectors are utilized which also include CCD cameras used as PSD by processing the light spot image on it. In addition there can be non-semiconductor devices like Vidicon tubes, which also function as PSDs.

In discrete PSDs, two types of devices are commonly used for position-sensing applications as shown in figure. The segmented PSDs or four-quadrant detectors are used more for applications with smaller movement span or for alignment. On the other hand, the continuous PSDs or the lateral-effect photodiodes are used for wider displacement measurement with high linearity. In addition to these two types, some times devices are also made with other geometries like wedges etc [54].

The illumination angle is chosen such that the diffracted beam emerges normal to the grating or $\beta = 0$. Also during the experiment, the illumination angle remains unchanged or $d\alpha = 0$. Thus:

$$d\beta = -\frac{dP}{P}\sin\alpha = -\frac{du}{dx}\sin\alpha = -\varepsilon_x \sin\alpha . \tag{2-3}$$

Here ε_x is derivative of the displacement component along the grating principle direction (du/dx), i.e. the normal component of the strain in the x-direction. The change in diffracted angle $d\beta$ can be calculated using the spot shift on the sensor surface and focal length f as

$$\Delta x_I = f d\beta = -\varepsilon_x f \sin\alpha . \tag{2-4}$$

It may be considered that if the sample undergoes some out-of-plane horizontal tilt in x-z plane, this produces the shift in the individual light spots which is understandably in the same direction. For this case if strain is not present or $dP = 0$, and angle of incidence changes as much as the tilt of the sample or $d\alpha = \Delta\theta$, from the earlier differential of the diffraction equation it comes to

$$d\beta = -\Delta\theta\cos\alpha . \tag{2-5}$$

In Equation (2-5) the measured shift of the beam on the sensor is due to both to the tilt of the grating and to the resulting change in the diffraction angle. Thus,

$$d\beta = \Delta\theta - \Delta x_I / f . \tag{2-6}$$

The change in diffraction angle can be deduced when the specimen is subject to the strain, ε_x, and out-of plane tilt, $\Delta\theta$. Important point to consider here is that due to divergent nature of the non-collimated beams used, an extra factor K_f will be inserted. Hence the corresponding shift, Δx, of a typical spot on CCD plane can be related to the strain and tilt as

$$K_f \Delta x_1 / f = -\varepsilon_x \sin\alpha + \Delta\theta(1+\cos\alpha) \tag{2-7}$$

and

$$K_f \Delta x_2 / f = +\varepsilon_x \sin\alpha + \Delta\theta(1+\cos\alpha), \tag{2-8}$$

where f is focal length of each micro-lens, α is the angle of incidence and K_f is a multiplication factor which is 1 if the two beams are collimated and the subscripts 1 and 2 refer to the two incident beams. Solving these two equations give

$$\varepsilon_x = K_f \frac{\Delta x_2 - \Delta x_1}{2f\sin\alpha} \tag{2-9}$$

and

$$\Delta\theta = K_f \frac{\Delta x_2 + \Delta x_1}{2f(1+\cos\alpha)}. \tag{2-10}$$

The two incident beams, thus, enable to separately compute the strains and the rigid body tilts of the specimen. The y-axis strain can similarly be calculated.

2.5 System Construction

The basic Multipoint Diffraction Strain Sensor (MDSS) setup (Figure 2.3) is compact, simple and versatile. The current system uses a 1/2" CCD camera with a 44 x 33 micro-lens array. Each micro-lens has a diameter of 144 μm and a focal length of 8.190 mm. The specimen grating is a 1200 lines/mm reflective diffraction grating. The specimen can be tilted using a precision rotation stage. Also the specimen has a strain gauge attached to the back side. A 685 nm laser diode is coupled into two optical fibers and provides the two symmetric incident beams. The spot image is digitized and processed using custom-developed software written in MATLAB® according to Equations (2-9) and (2-10).

Lateral-effect devices have been in use since early 1960s. The first such device was presented in 1957 being a 2-axis device consisting of four point contact electrodes placed on a common resistive sheet. Its response was highly non-linear, which was corrected by later improvements in its geometry. The improved devices (duo-lateral) were later shown to be very much linear in their response and also having better precision in measurement [53,57].

Lateral effect detectors have several advantages over quadrant devices for normal metrology applications. Because there is no gap in the active areas, the size of the image is not subject to constraints on minimum diameter. Also, the position information is available as long as the light falls somewhere on the active area of the detector. And that the position is determined according to the optical centroid of the light spot, making it indifferent to the spot shape or intensity distribution. One disadvantage is that frequency response of such detectors tends to be lower because of the series resistance that the divided photo-currents encounter. Also, these devices exhibit lower signal-to-noise ratio.

These devices are also available in one or two-dimensional configurations and have mainly four different types. The duo-lateral type has electrodes on both front and rear surfaces and typically has minimum error and good resolution. Tetra-lateral type has four electrodes on the front surface of the device and is characterized by low leakage and fast response. Pin-cushion type is an improved form of the tetra-lateral with reduced signal non-linearity at the edges. Transparent duo-lateral detectors are essentially the same in principle as duo-lateral, but they are constructed on transparent substrate. Sometimes odd-shaped PSDs are also manufactured for specific applications like circular and spherical shapes for angular position measurement [11,20,58,59].

The lateral-effect photodiodes are used for wider displacement measurement with high linearity, good resolution and fast response. Besides normal displacement sensing as shown in figure, the application areas include optical metrology, industrial automation, training simulation and many others [2,12,51,54].

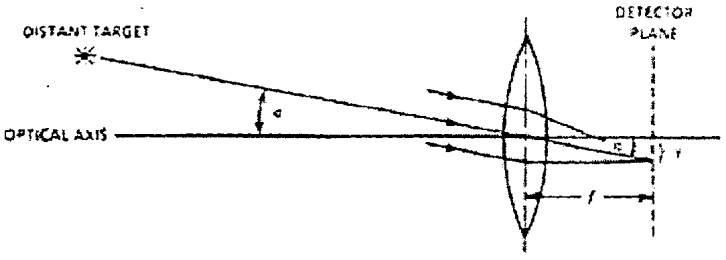

Figure 1.9. Principle of PSD-based incident light displacement sensor [2]

1.5 Position-Sensitive Detectors – Integrated

There are other devices which consist of an array of some sort of simpler light detectors and thus can sense the position of the light falling on the surface like an imager. They can provide information about the shape and distribution of the incident light spot. They are generally used with some signal processing algorithm and this way they can help discerning true incident light from the cluttered environment of false lights. Most familiar and useful example of this category includes photodiode arrays and CCD arrays.

1.5.1 PSD or PD Arrays

Arrays of photo-diodes can provide a simple indication of the location of the laser beam through the observation and determination of which diodes are illuminated. Two-dimensional arrays with hundreds of diodes in each axis are commercially available. These normally consist of one-dimensional or two-dimensional arrays of detector cells like charge-coupled detectors or photodiodes along with multiplexers, which enable sequential reading of these devices as given in figure [54].

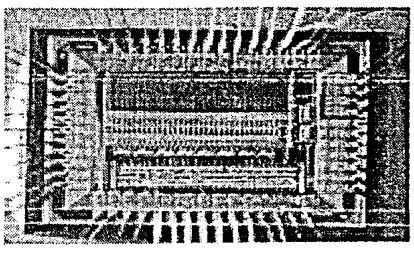

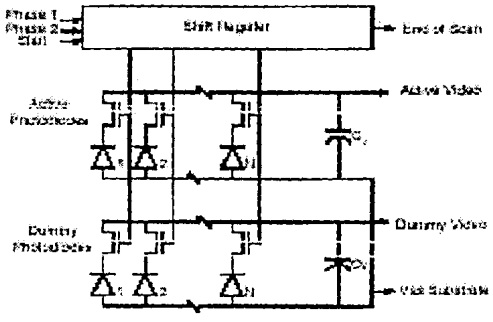

Figure 1.10. Integrated photodiode arrays with multiplexing [54]

There has been interest in producing photodetector array based sensors using CMOS or BiCMOS technology, where specific architectures are also developed for light spot centroid computation. Arrays have been made with individual current divisions as per lateral-effect devices or as per quadrant devices. There have also been experiments for the manufacturing of lateral-effect detectors using standard IC technologies like planar, CMOS or BiCMOS, which are useful for larger device integration.

A useful device among these is Digital PSD or the array of active digital pixels. This consists of 1-D or 2-D array of digital pixels along with circuits for triggering and readout. Computational circuitry for centroid determination may also be added. Each pixel may include a photodiode along with a comparator circuit for one-bit amplitude quantification. The device function is similar to CCD imagers in many ways, while the advantage is easier processing for binary pixel values instead of grey-scale [13,51].

1.5.2 CCD Imagers

CCD or Charge-Coupled Device is very popular technology for imaging and cameras. Construction of CCD is as an array of closely spaced MOS diodes. The light is recorded as an electric charge in each diode. Using a proper sequence of clock voltage pulses, the accumulated charges can be transferred in a controlled manner to the output of the device. The relatively complicated structure as shown in figure makes CCDs costlier and harder to manufacture. The CCD imagers give a digital output, which may be of different resolutions depending on the pixel size used in the array [14].

The imaging detectors like CCDs are sometimes used for light spot position sensing instead of PSDs, particularly in instrumentation applications requiring higher accuracy and noise rejection. Light spot detection algorithm is needed for its use as PSD. It is obvious that the mass production of low-cost CMOS imagers and the rapid development of digital signal processing ICs together will partially replace PSDs in some of the traditional applications [52,59].

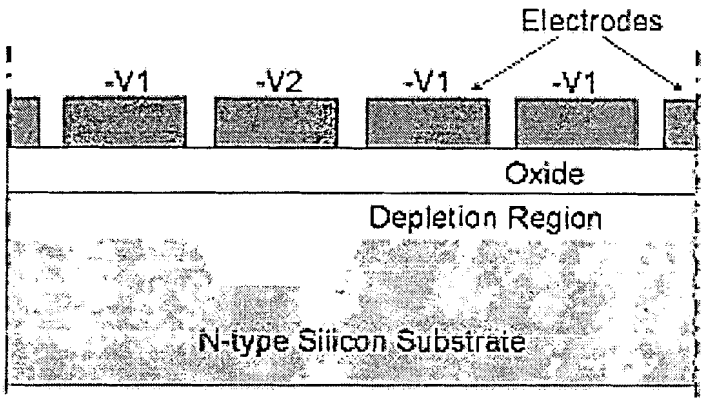

Figure 1.11. CCD Imager Technology

1.5.3 Discrete vs Imaging PSDs

Functionally speaking, PSD gives an output that is a function of the center of gravity of the total light distribution on the active area. The CCD on the other hand detects the peak value of the light quantity distribution over the active area for each individual pixel, and the values are put out sequentially [14].

There are many areas where there comes a choice between using imaging PSD vs discrete PSD basing on their different merits and demerits. As an example, PSDs are frequently used for the industrial coordinate measuring systems. Many such systems basing on CCD imagers have been reported where the advantage of using CCDs mainly is the possibility to perform processing operations on the images and thus to satisfy the performance requirements which are not possible with discrete PSDs. This means lower sensitivity to background-induced noise and better tolerance to lower light-to-background contrast. Simultaneously, there is also possibility of processing multiple light spots at the same time. These advantages come from the individual processing of the pixel signals. Most of these are also present for the digital photodiode arrays.

The major disadvantage is in terms of time, The need of image processing makes the operation very slow, and takes the per-point operating time to many seconds or even 10s of

seconds. On the other hand a suitable 4Q detector can be used with sufficiently high precision and bandwidth needed for normal industrial operations with well-marked target points [15,51].

1.6 Position-Sensitive Detectors - Tubes

Some non-semiconductor tube detectors are also used as PSDs. One important type is Image Dissector, which is a modified photomultiplier tube (PMT). The modifications make it possible to identify the areas of the photocathode that is generating the photocurrent. It consists of normal photomultiplier elements, such as the photocathode, dynodes and anode. The modifications that make a PMT an image dissector are the electron-beam-defining aperture, an electrostatic field that focuses the photoelectron beam from the photocathode, and a deflection scheme that makes it possible to steer the beam through the aperture.

Another tube PSD as shown in figure is Vidicon, which is a type of imaging detector used in television cameras. Vidicons in tracking or positioning systems are used in a manner very similar to the image dissector. That is, position information is gathered from the deflection current that was being applied when a signal was picked up.

Such tube type photodetectors have been extensively used in advanced areas like high energy physics already for some time. Also some of the precision aerospace tracking applications are also implemented using such tube detectors [2,54].

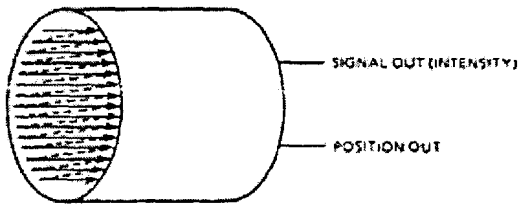

Figure 1.12. Image-dissector or Vidicon tube [2]

1.7 Metrology Applications of PSDs

PSDs are widely used in commercial and industrial applications. Lateral-effect detectors are mostly used in optical distance measurement based on the triangulation principle etc as shown in figure [54]. Such sensors are used in various kinds of position, height, thickness and vibration measurements needed in different industrial processes. Quadrant detectors are mostly used as centering indicators rather than as linear position sensors. Imaging PSDs are used where noise rejection or multiple beam tracking is required [16,58].

1.7.1 Engineering Measurements with PSDs

For the normal engineering and measurement applications simplest and cheapest way to measure the position through light spot is to use a PSD. In many straightforward applications this is exactly what is done. Examples are alignment systems where the position of a reference laser beam relative to the PSD is measured. Such systems are used for alignment of everything from bridges to optical systems. As PSDs can be made to operate at very low temperatures, this alignment method has also been applied to infrared optics.

The shortcoming of the normal PSD for many precision or complex applications is that it cannot differ between a direct beam and a noise or reflected beam. It will just output the resulting center of gravity from the two spots. Using a CCD or digital PSD in such applications gives the possibility to differ between direct hits and reflections by evaluating the signal strengths and other image processing techniques in the light spots. Of course this will add to the complexity of the system and slow it down [11].

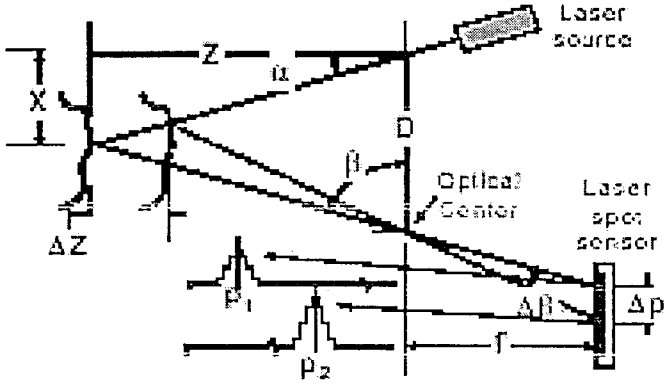

Figure 1.13. Laser-based optical triangulation system for profilometry [54]

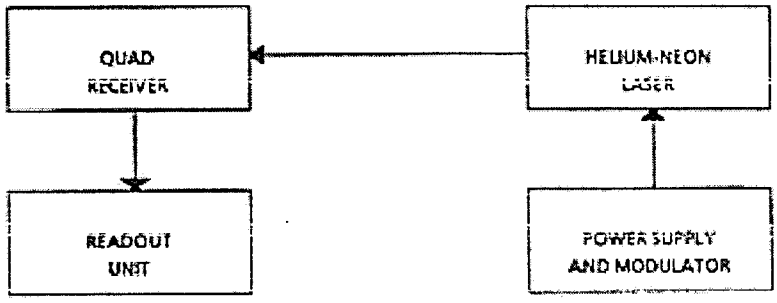

Figure 1.14. Components of a laser alignment system with quadrant PSD [2]

1.7.2 Strain Measurement with PSDs

Along with other measurement applications of optical systems, strain measurement is very important one, specifically in mechanics, material science and engineering. A number of optical techniques such as moire', speckle and holography have been developed and are routinely used in these areas. Among these optical techniques, diffraction methods provide strain information directly and possess several other advantages, such as the fact that the system is simple and easily integrated. Since the early use of diffraction grating strain gauge, this technique has advanced steadily and is now widely applied. An important application in such measurement systems is the one using PSDs to measure the shift in the diffracted beam and hence to get a measure of strain in the component as shown in figure. The detector can be interfaced with a micro-computer, for the ease of operation and data recording [26,27,28].

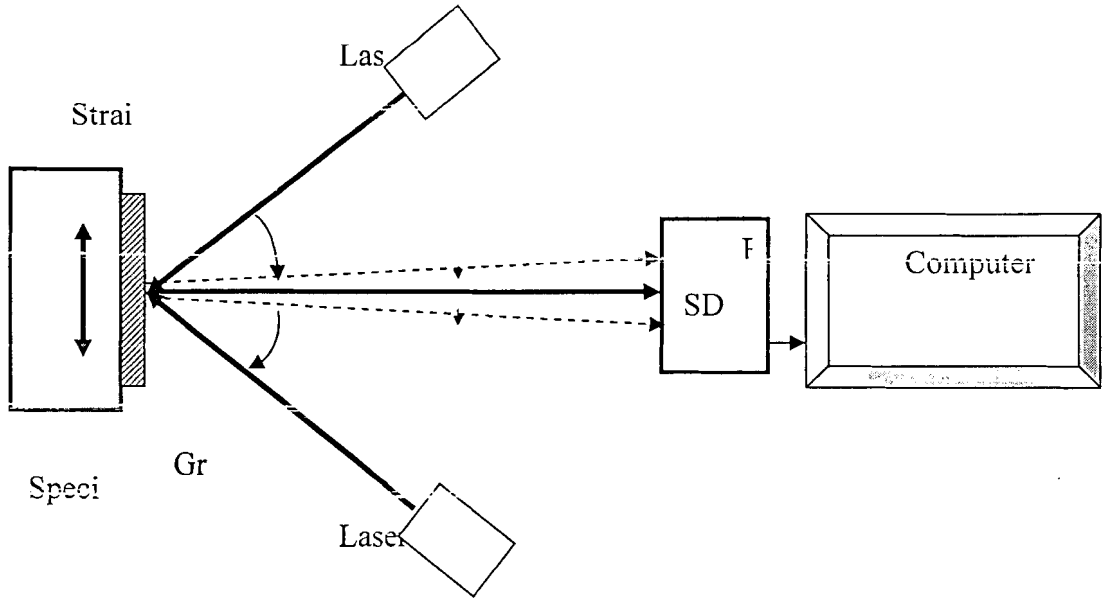

Figure 1.15. PSD-based diffraction strain sensor (extended in our research)

1.8 Target Research in Optical Metrology and its Components

The research in the field of PSDs and optical metrology in our study is organized to be valuable and somewhat comprehensive, and thus impart thorough understanding of the area to the researchers. The research is also constrained by the availability of the needed research resources and by the flow of the on-going projects in the laboratory. At device level, some work was done while working for the performance analysis of lateral-effect PSDs. Major part of work was done at system level, while targeting the strain measurement application using imaging PSDs. For this, a novel technique in this field was developed, tested and characterized. In addition to these, some work was also done on the application of laser beams, but material processing was target in this part of research, as required by the running projects in the laboratory.

1.8.1 Target Research in Optical Strain Metrology

PSD-based diffracted-beam strain measurement is a useful technique due to direct measurement, straightforward approach and easier integration. An important factor in its usefulness is the absence of fringe analysis requirement present in many approaches, which makes the system simpler, lighter and faster [26,27].

All the existing works on diffraction-based strain measurement deal with sensing strain at a single point like a strain gauge. Many applications in the industry warrant the measurement of strain distribution rather than sensing strain at a single point only. Current diffraction strain sensors, or the electrical strain gauges, cannot fulfill this need unless placed in an array. A possible research avenue can be of using many smaller diffracted beams, to fulfill this need of mapping strain at the body of a target component. To our knowledge, this is unprecedented in research literature.

For the proposed research on PSD-based strain metrology systems, earlier figure illustrates the principle of strain measurement using diffraction. Here the diffraction grating bonded to the surface of the specimen follows the deformation of the underlying specimen. The grating is illuminated by two superimposed laser beams and thus diffracted orders are produced by both the beams according to the diffraction equation. The incident beams are placed at the angle such that the first diffracted orders of both the beam emerge normal to the surface of the grating and are detected by the CCD camera.

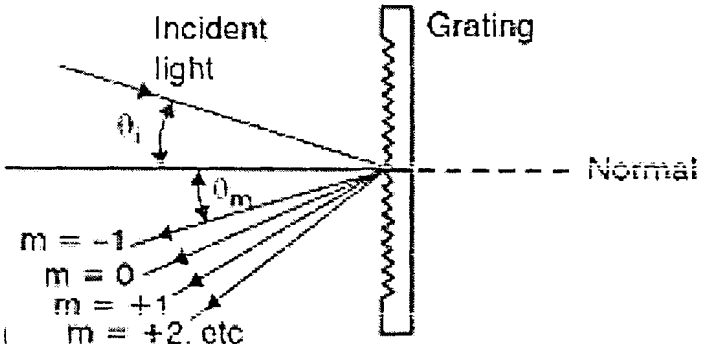

Figure 1.17. Operation of diffraction grating [2]

In the proposed research, a CCD camera or imaging PSD will be fitted with beam-division optics. In this camera, the diffracted beam is decomposed into many smaller beams, which should be incident on the CCD surface all in parallel. Now these beamlets should represent the diffraction from different areas of the sample surface. When the grating is deformed, tilted or rotated, the position of the diffracted beamlets shift accordingly. Processing these relative shifts of the light spots, amount of the strain or the tilt experienced by the sample can be calculated. The operational and mathematical [21] analysis of such sensor will be done under different conditions of laser beams and with different types of movements present in the specimen along with the strain.

Use of imaging PSDs for this purpose can be useful as light-position accuracy of about 1/10 pixel can easily be obtained if the incident light spot is having circular span of few pixels width [17].

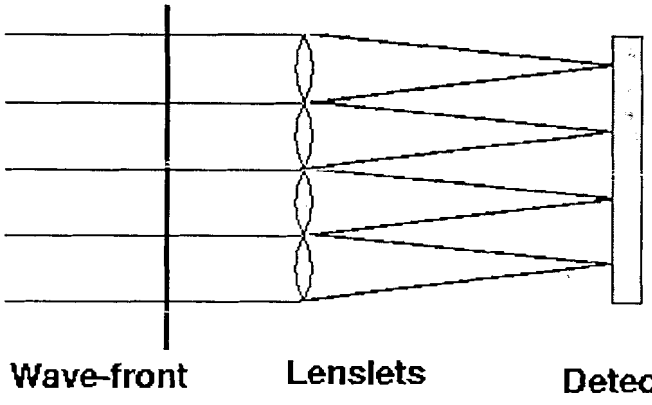

Figure 1.18. Imaging detector with beam-division optics

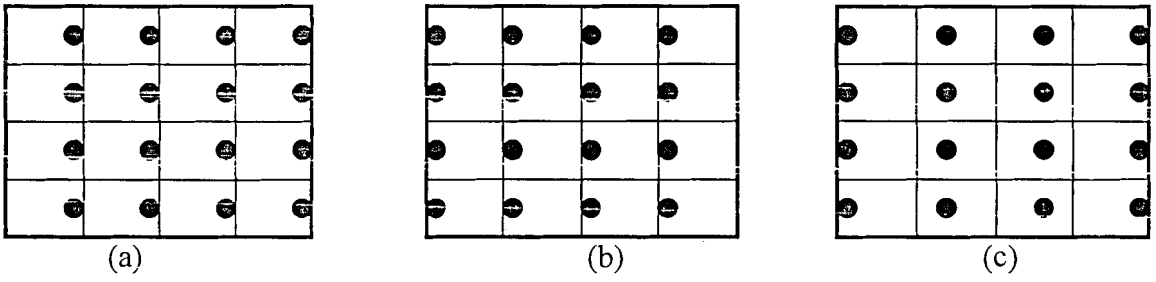

Figure 1.19. Position shifting of sampled diffracted beam microspots in the condition of (a) No strain (reference position), (b) Uniform strain and (c) Non-uniform strain

1.8.2 Target Research in PSDs

In the industrial environment, the role of PSDs is diverse, including alignment, displacement sensing and as a part of other analysis instrumentation. In such environment, the system laser source is co-existing with different kinds of light sources, laser and non-laser, along with their reflections and back-scatters from various surfaces. Some of the systems may involve scanning or rotating laser beams too. They may produce different effects while mixing with the real signal. Though the analysis of internal noises has been done [18,19], these external noise sources have been mentioned or described by some of the earlier authors [51,54]. Thus it is felt that a detailed operational analysis in such environment is very much needed.

For the proposed research on PSD performance in industrial environments, the needed theory will be developed first and the mathematical model will be built using that. Experimental setup will be used to find out actual lab results with such spurious beam environments. The setup will include main and noise laser sources of adjustable intensity. Other optical sources may also be used as the interference. PSD detector along with its requisite circuit will be used for the experimentation. The setup should be interfaced with the computer so that the data can be logged. The figure shows the proposed setup while the noise beam and the diverse illumination mix with the original laser beam on a PSD surface.

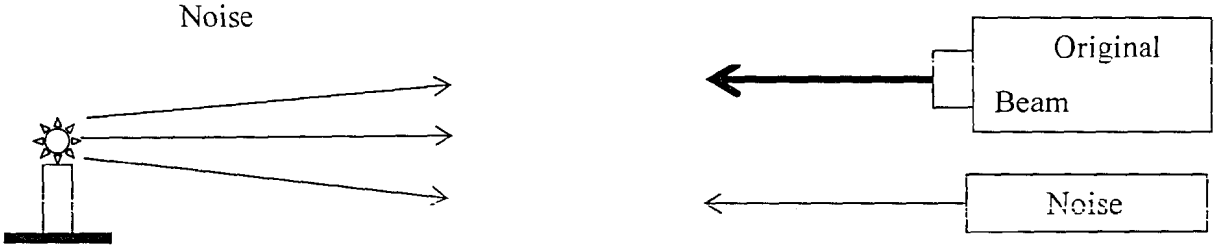

Figure 1.20. Different noise sources co-existing with original beam for optical metrology

1.8.3 Target Research in Laser Beams

As discussed, the laser beams have diverse applications in the areas of optical metrology and material processing etc. Owing to a running project in material processing, some research on laser beams and their effects will be carried out for the laser-based welding techniques.

Laser welding of zinc-coated steel sheets in lap configuration poses a challenging problem to the researchers. The solutions proposed in the last many years have not yet found an easy-to-apply realization to replace conventional resistance spot welding. The many advantages offered by laser welding still justify a quest for very efficient methods. The ideal solution should firstly solve the technological problem of the residual Zinc vapors trapped in the joint weld due to the lower boiling point of the Zinc (907°C) with respect to melting point

of steel Fe (1530°C). The solution should also be practical and economical enough to be installed on the production lines [76,77,78].

For this purpose, a novel dual beam solution for such configuration is proposed. In this new two beam method, the front beam of the tandem system shall cut a slot with a minimal kerf, while the second beam shall seam-weld, joining the two sides of the kerf, while the residual zinc evaporates through the slot ahead of it. For this purpose, two different laser beams one for cutting and other for welding can be used, while alternately both beams can be derived from the same source and split for these jobs.

Chapter # 2

Optical Metrology System-1:

Multipoint Diffraction Strain Sensor with Basic Setup

2. Optical Metrology System – 1: Multipoint Diffraction Strain Sensor with Basic Setup

A Multipoint Diffraction Strain and Tilt Sensor based on multichannel imaging PSD is developed and characterized with the novel feature of simultaneous strain measurement at multiple points. Unlike conventional interferometry based systems, this sensor uses principles of diffraction to directly measure strain at large number of points. In this sensor, a high-frequency diffraction grating is illuminated by two symmetric laser beams and the diffracted beams are sampled on a CCD camera via a micro-lens array into an array of dots. The shift of the individual dots is sensed and strains or rigid body tilt are calculated directly. This novel technique is expected to be very valuable in numerous industrial applications.

2.1 Problem Background

Optical methods have shown great promise for contact-free deformation measurement using principles of diffraction, interference and polarization. Laser light is widely used due to its unique properties [42,43]. Compared to conventional electric strain gauge [44,45] they offer many attractive advantages. Being non-contact, they have liberty in terms of measurement region and instrument utilization. Additionally, they can possibly provide a strain map, which is not possible with single measurement strain gauges. For precision deformation measurements, interferometry has been widely used, though it entails time-consuming fringe analysis and numerical differentiation for strain calculation. Diffraction techniques directly provide derivatives of displacement using a straightforward approach and thus have better potential in strain analysis.

2.1.1 Existing Systems

In 1956 Bell [28] first proposed a diffraction grating-based strain gauge. Since then, many different developments and variations have been proposed and many of them are now widely used in the industry, as reviewed by Moulder and Cardenas-Garcia and Sevenhuijsen et al [29,30]. In these techniques researchers used various grating types and imaging devices or discrete position-sensitive devices (PSDs) for sensing [26,27,31,32]. For example, Sevenhuijsen et al. [30] used a numerical grating spectrum method to measure the local strain directly. Ma and Kurita [31] used two plasma-coupled device linear image sensors to measure the location of the two diffracted spots before and after deformation. Among these, the work of Asundi and Zhao [26,41] utilizing the approach of combining high-frequency grating with PSDs, offers many advantages over the conventional electrical resistance strain gauge, specifically the adjustable gauge (beam) size and multi-point measurement, while maintaining the advantages of high sensitivity and accuracy.

A major problem is that all these works deal with sensing strain at a single point like a strain gauge. Many applications in the industry warrant the measurement of strain distribution rather than sensing strain at a single point only. These may include strain variations present at a machine component under stress, a large beam used in a building structure or even a small component used in MEMS. Diffraction strain sensors and electrical strain gauges cannot fulfill this need unless placed in an array, which is read out sequentially. Some researchers have tried with somewhat different methods involving fiber optics, but have reported observation at only 2-3 points [33].

On the other hand, there are whole-field optical strain measurement techniques, such as electronic speckle-pattern interferometry (ESPI) and Moire Interferometry, which have been widely applied in the industry [34-37]. In ESPI interference fringes are produced by the images from defusely-reflected laser light, while in Moire Interferometry fringe pattern is produced by two opposite and symmetric beams incident on the sample with grating. However, these approaches are not without their own limitations. Specifically, ESPI suffers from its low spatial resolution and relatively poor fringe visibility, and thus is mostly used for qualitative observations [34]. Moire Interferometry technique on the other hand, is not that

restrictive, but obviously needs lengthy fringe processing algorithms to yield the final output. Also, whenever there is fringe processing involved, problem of low value strain determination comes up due to the fringes being too sparse to give fine resolution measurements [38]. Additionally, with such system there is problem of decrease in fringe contrast with increasing fringe frequency. It may also be mentioned that along with its useful strain sensitivity, the technique is very much sensitive to rigid body rotations too [34].

2.2 Proposed Solution & Comparison

2.2.1 Overview

A technique for whole-field strain mapping using the sampled diffracted wavefronts is presented. This research is expected to open up a new avenue and provide a versatile tool for the industrial and structural applications, as a 2-D map of strain on the component body may provide much clearer picture to the analysis team. To our knowledge, such multipoint optical strain measurement feature has never been reported in earlier works.

A Multipoint Diffraction Strain and Tilt Sensor has been developed using a multichannel imaging position-sensitive detector, with the novel added feature of whole field strain determination. This unique feature has been implemented by simultaneous tracking of sampled wavefront diffracted from the component under test. In this sensor a high-frequency diffraction grating is bonded on the specimen, which is illuminated by two symmetric collimated laser beams. The first orders of diffracted beams impinge on a CCD camera, via a microlens array. The deviation of the individual spots generated by both the beams is directly proportional to the normal strain and a component of the shear strain.

2.2.2 Comparison with Others

Being a whole-field approach, this technique can be compared with other whole-field optical strain measurement techniques like Moire Interferometry and ESPI as given [34-37].

1. The obvious advantage of this multipoint diffraction method compared to others is its direct approach. The strain is calculated without the need of any fringe processing and numerical differentiation needed for interferometry [9,10]. Image subtraction for speckle techniques is also not needed here. This makes processing time needed for the final strain map calculation much shorter and near-real-time. We found that the time taken for the production of strain and tilt maps consisting of >1300 points will be <5 seconds.

2. At the same time it can produce map with good spatial resolution compared to other methods and specifically to speckle technique. This resolution is only bounded by the separation of the micro-lenses on the array, i.e. distance between the individually-shifting micro-spots, which is <150 microns in our case. This resolution is also not hampered at the lower strain values where farther apart fringes may degrade such resolution for fringe processing methods.

3. The system results show good combination of sensitivity and accuracy considering other whole-field approaches and specifically compared to speckle method where measurement quality is largely hampered by the poorer fringe visibility.

4. Being a simpler approach, the total computing and storage resources needed for this method are going to be lesser.

2.3 Operating Principle

The Multipoint Diffraction Strain and Tilt Sensor is developed using a high-frequency diffraction grating along with a micro-lens array and CCD based multichannel imaging PSD. A reflective diffraction grating is bonded to the surface of the specimen and follows the deformation of the underlying specimen. The grating is illuminated by two symmetric monochromatic laser beams at a prescribed angle such that the first order diffracted beams emerge normal to the specimen surface. The micro-lens array samples each of this incident

beams and focuses them as spots onto the CCD. When the specimen is deformed, tilted or rotated, the diffracted wavefronts emerging from the specimen are distorted and hence the spots shift accordingly. The symmetric beam incident from other direction gives a similar array of spot patterns. Strains at each spot location, which corresponds to a small area of the specimen, can then be readily deduced from the shift of the spots as described below. Without loss of generality, spot shifts along one direction are used in this derivation.

Figure 2.1 illustrates the principle of multipoint strain measurement using non-collimated divergent laser beams. The diffracted wavefronts emerging from the grating are sampled into wavelets by the multi-lens array and focused onto the CCD. Each wavelet represents the diffraction from a small area of the sample surface. When the grating is deformed, the position of the diffracted wavelets on the CCD would shift accordingly as shown in figure 2.2. Coming figure shows the simulated spot pattern for a 4x4 array of micro-lenses for one of the beams when the specimen is unstrained, undergoes uniform strain and non-uniform strain. The shift of the spots is proportional to the sample strain. In this particular example, the shift of the spot is along one direction. However, in general the shift would be in two directions but the principle would be unaffected as the horizontal and vertical shifts are independent of each other.

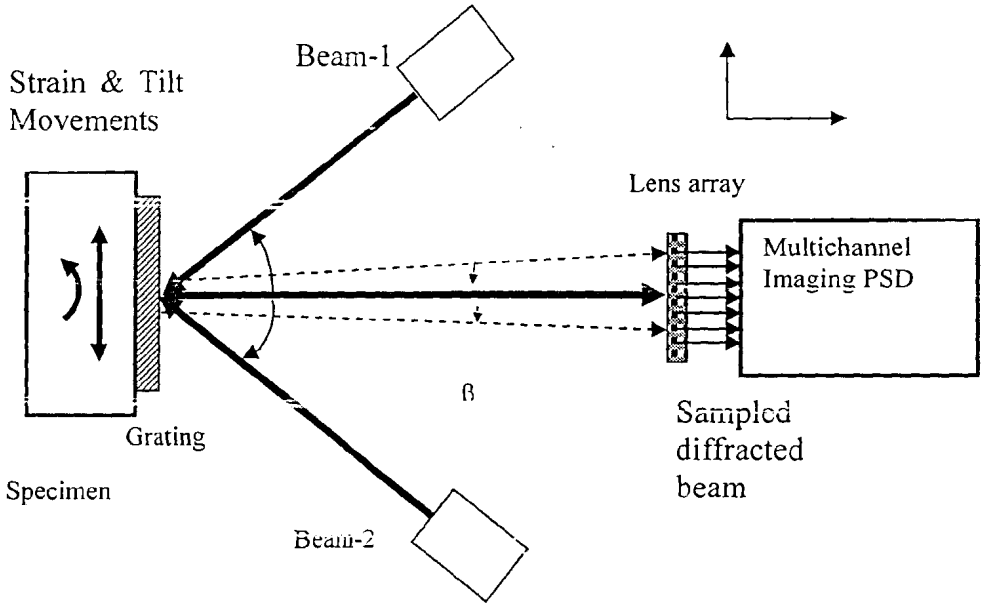

Figure 2.1. Operating principle of diffraction strain & tilt sensing

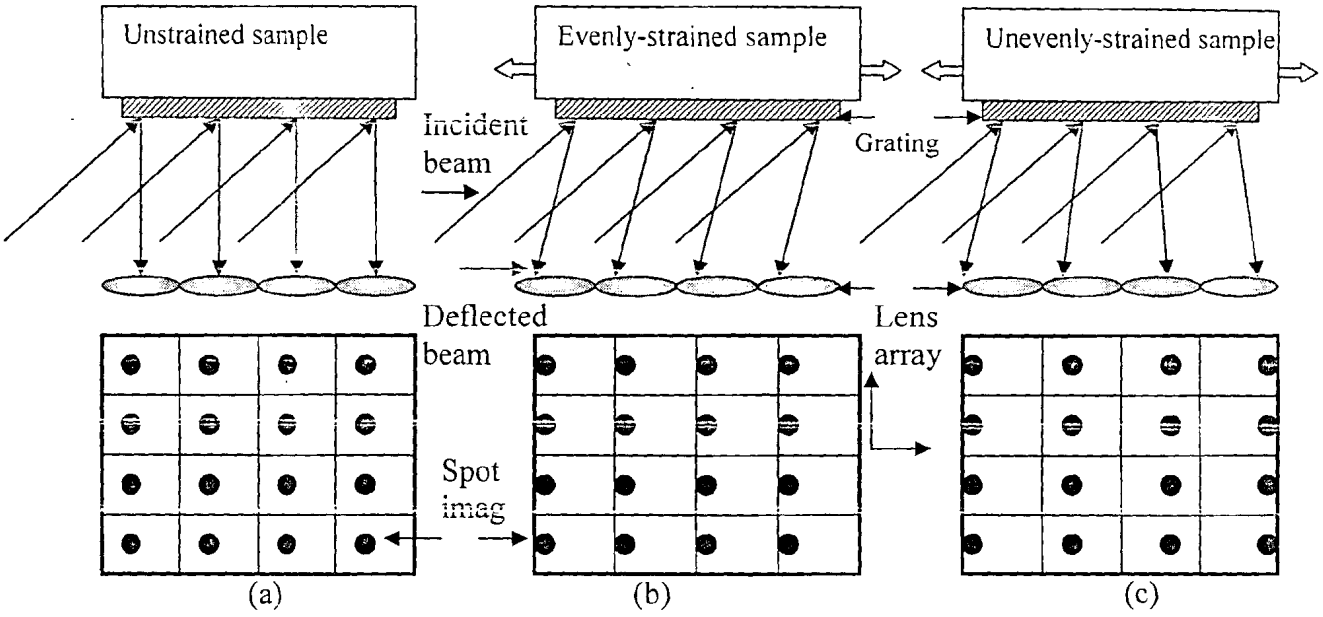

Figure 2.2. Position of individual micro-spots with (a) no strain, (b) uniform strain and (c) non-uniform strain in the sample

2.4 Basic System Theory

Starting from the well-known diffraction equation [39] and differentiating it we get

$$P(\sin\alpha + \sin\beta) = m\lambda\,, \tag{2-1}$$

$$P\cos\alpha d\alpha + dP\sin\alpha + P\cos\beta d\beta + dP\sin\beta = 0\,. \tag{2-2}$$

where α and β are the angles of illumination and diffraction, P is the pitch of the grating whose principle direction is the x-axis, m is the diffraction order (± 1) and λ is the wavelength of light.

The illumination angle is chosen such that the diffracted beam emerges normal to the grating or $\beta = 0$. Also during the experiment, the illumination angle remains unchanged or $d\alpha = 0$. Thus:

$$d\beta = -\frac{d\bar{P}}{P}\sin\alpha = -\frac{du}{dx}\sin\alpha = -\varepsilon_x \sin\alpha . \tag{2-3}$$

Here ε_x is derivative of the displacement component along the grating principle direction (du/dx), i.e. the normal component of the strain in the x-direction. The change in diffracted angle $d\beta$ can be calculated using the spot shift on the sensor surface as

$$\Delta x_1 = f d\beta = -\varepsilon_x f \sin\alpha , \tag{2-4}$$

At the same time, we may consider that if the sample undergoes some out-of-plane horizontal tilt in xz-plane, this produces the shift in the individual light spots which is understandably in the same direction. For this case if strain is not present or $dP = 0$, and angle of incidence changes as much as the tilt of the sample or $d\alpha = \Delta\theta_x$, from the earlier differential of the diffraction equation we may get

$$d\beta = -\Delta\theta_x \cos\alpha \tag{2-5}$$

Here the measured shift of the beam on the sensor is due both to the tilt of the grating and to the resulting diffraction angle change, which gives

$$d\beta = \Delta\theta_x - \Delta x_1 / f . \tag{2-6}$$

Thus the change in diffraction angle when the specimen is subject to strain, ε_x and out-of plane tilt, $\Delta\varphi$ can be deduced. Important point to consider here is that due to divergent nature of the non-collimated beams used, an extra factor K_f will be inserted. Hence the corresponding shift, Δx, of a typical spot on CCD plane can be related to the strain and tilt as

$$K_f \Delta x_1 / f = -\varepsilon_x f \sin\alpha + \Delta\phi(1+\cos\alpha), \tag{2-7}$$

$$K_f \Delta x_2 / f = +\varepsilon_x f \sin\alpha + \Delta\phi(1+\cos\alpha), \tag{2-8}$$

where f is focal length of each micro-lens, α is the angle of incidence and K_f is a multiplication factor which is 1 if the two beams are collimated and the subscripts 1 and 2 refer to the two incident beams. Solving these two equations gives

$$\varepsilon_x = K_f \frac{\Delta x_2 - \Delta x_1}{2f\sin\alpha}, \tag{2-9}$$

$$\Delta\phi = K_f \frac{\Delta x_2 + \Delta x_1}{2f(1+\cos\alpha)}. \tag{2-10}$$

The two incident beams thus enable us to separately compute the strains and the rigid body tilts of the specimen. Y-axis strain can similarly be calculated.

2.5 System Construction

The basic MDSS system setup is a compact, simple and versatile. The current system uses a 1/2" CCD camera with a 44 x 33 micro-lens array. Each micro-lens has a diameter of 144 μm and a focal length of 8.190 mm. The specimen grating is a 1200 lines/mm reflective diffraction grating. The specimen can be tilted using a precision rotation stage. Also the specimen has a strain gauge attached to the back side. A 685 nm laser diode is coupled into two optical fibers and provides the two symmetric incident beams. The spot image is digitized and processed using custom-developed software written in MATLAB® according to earlier equations.

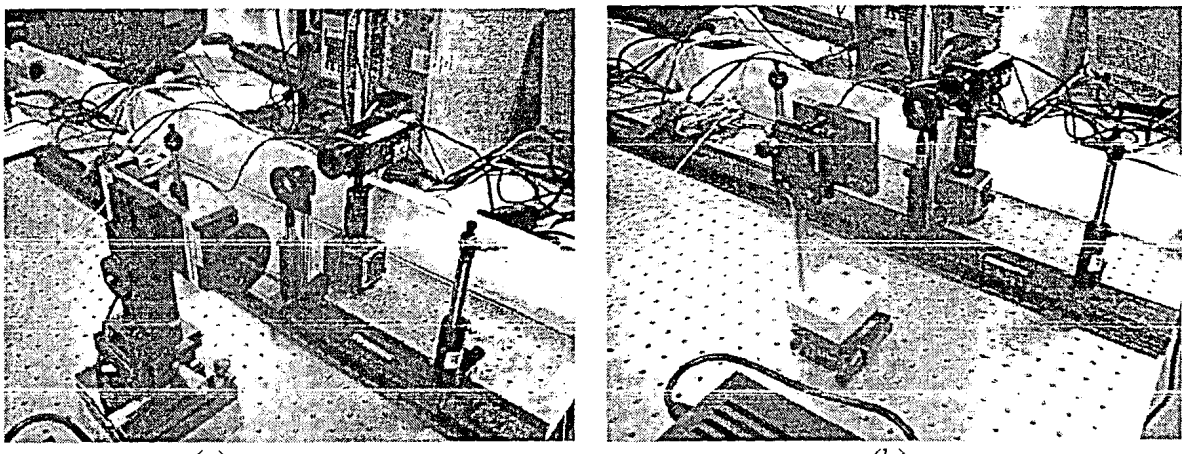

(a) (b)

Figure 2.3. MDSS based on laser diode divergent beam setup for (a) strain and (b) tilt measurements

2.6 Basic Setup Output

2.6.1 Data Processing

The process for strain measurement proceeds as follows. Record and determine centroid of the spot images for the unstrained sample for both beams (shown in Fig. 2.4(a) for one of the beams). Deform (strain and/or out-of-plane tilt) the specimen and then record the deformed spot patterns for the two beams as shown in Fig. 2.4(b). Centroid detection is critical to this routine and as seen in Fig. 2.4(c), the spot images are not perfectly circular due to imperfections in the optics and gratings, which makes it more difficult.

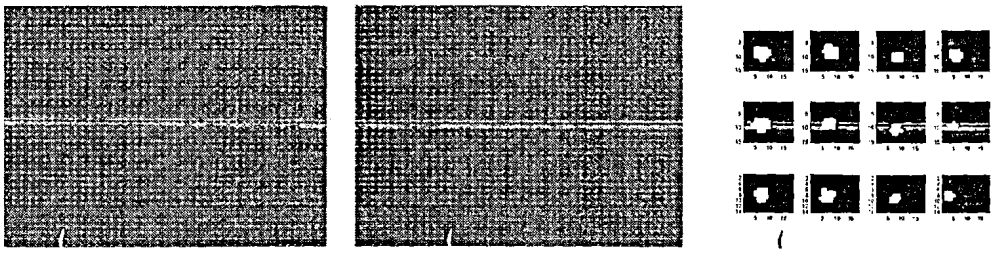

Figure 2.4. (a) Reference and (b) strained spot images, and (c) enlarged sample sub-image of spots

2.6.2 Strain and Tilt Maps

The strain and tilt can then be deduced from the shifts as presented earlier, and are shown in Fig 2.5. Normal and shear strain components can also be individually calculated as per strain equations and are shown in Fig 2.6.

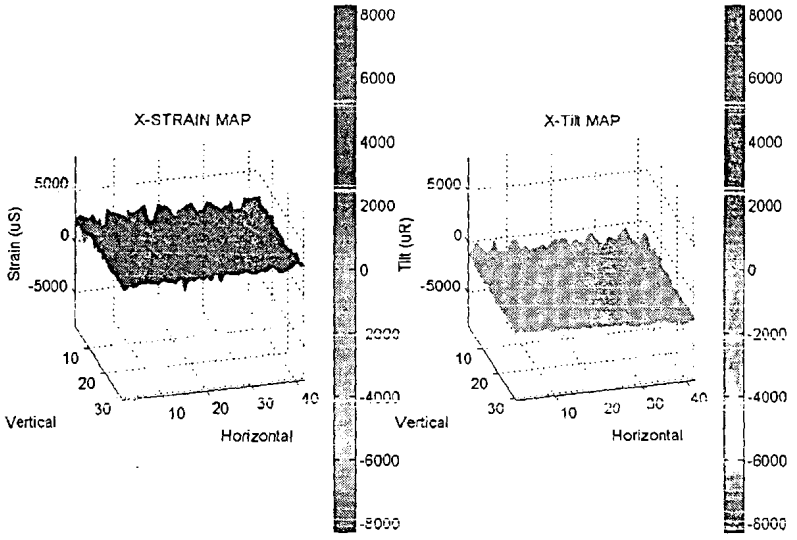

Figure 2.5. (a) Strain and (b) tilt distribution for a specimen subject to uniform strain with some inevitable tilt

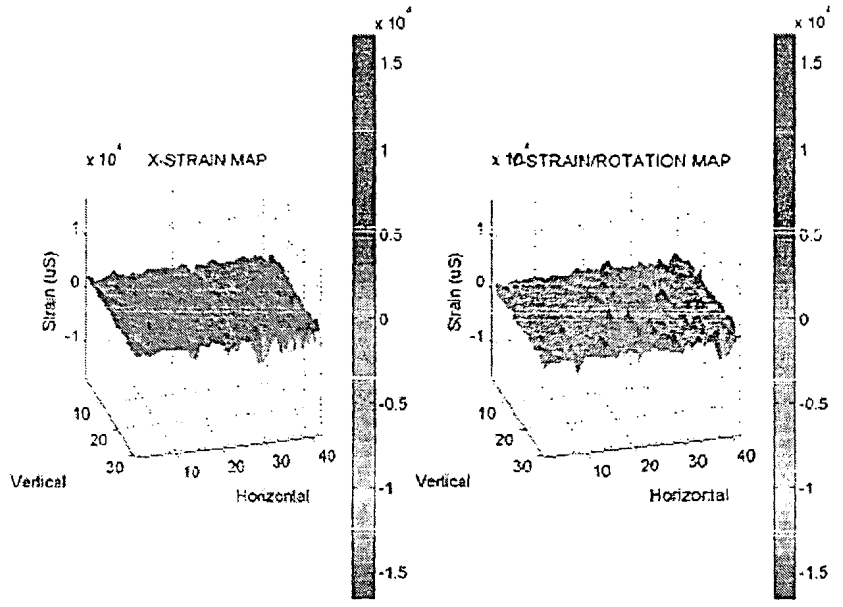

Figure 2.6. (a) Normal and (b) shear strain distribution for a specimen subject to uniform strain

2.6.3 Multi-step Curves

Figure 2.7 shows the comparison of applied strain and tilt with the measured strain and tilt for increasing deformation of the specimen.

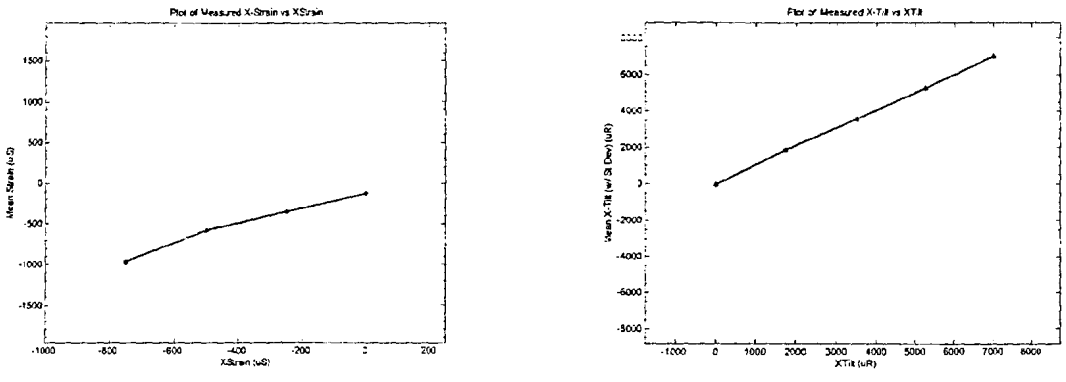

(a) (b)

Figure 2.7. (a) Applied v/s measured strain (b) Applied v/s measured tilt

2.7 Basic System Characterization

Earlier figure shows the comparison of applied strain and tilt with the measured strain and tilt for increasing deformation of the specimen. The plot shows good correlation and linearity for the measured and applied values, thus verifying the MDSS system. Some characteristics of the MDSS system can be gleaned from these results. The sensitivity to strain/tilt is governed by the centroid detection algorithm, and for a 6 pixel square micro-spot, the sensitivity is 20 uS for strain and 10 uR for tilt. The accuracy was experimentally established as the standard deviation between multiply-recorded data, and was found to be about 10 uS for the mean strain measurements. The range for maximum strain and tilt, assuming that the spots remain within the same micro-lens, is governed by the maximum allowable shift of the individual spots. Based on Eq. 2, and considering that each sub-window has a size of 18x14 pixels, the maximum measurement range is 19 mS for strain and 9 mR for tilt along x-axis. Experimentally slightly smaller values were obtained due to the irregular spot shape. Based on the above experimental data the specifications of the MDSS system are given in Table 1.

Table 2.1. Major Specifications of MDSS

Range	Measurement Linearity	Accuracy	Measurement Sensitivity	2-D Variability	Spatial Resolution
19 mε/ 9 mR	1% of FSD	10 με/ 5 μR	20 με /10 μR	10 με/ 5 μR	144 μm

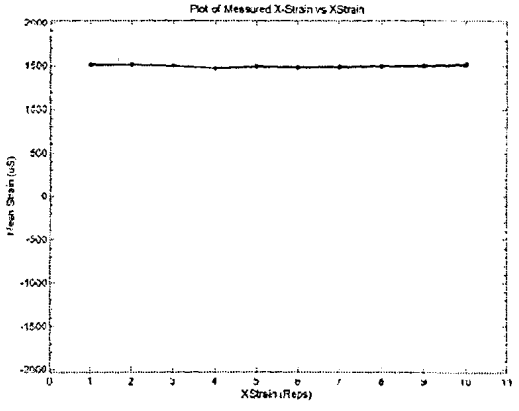

Figure 2.8. Accuracy calculation with multiple readings

2.8 Conclusions

A basic-setup MDSS system has been developed and characterized with a novel technique of simultaneous strain and tilt measurement at a large number of points. The current system is based on a simpler uncollimated laser beam setup. However, using a standard moiré Interferometric system with the current MDSS, both strain and deformation patterns can be obtained in near real time without the need for fringe processing. The system characteristics are quite impressive and can be further improved with proper choice of incident laser, micro-lens array, and algorithm. Furthermore, the system is also capable of measuring rotation and shear strain. Indeed, it is possible to measure all three strain components as well as rotation and tilt making this a truly versatile whole-field strain sensing system. The system offers many promising features including a useful combination of compactness, data collection speed and results accuracy. Diverse applications of the technique in microelectronics, micromechanics and other areas are expected.

2.8.1 Related Publications

1. S. Iqbal and A. Asundi, *Characterization of Multipoint Diffraction Strain Sensor (MISS)*, Key Engineering Materials Vol 326-328 (2006), pp 87-90.
2. S. Iqbal and A. Asundi, *Simultaneous Micro Measurements of Strain and Tilt using Multichannel PSD.* Asia-Pacific Conference on Transducers & Micro-Nano Technology, Singapore, 2006

Chapter # 3

Optical Metrology System-2:

Multipoint Diffraction Strain & Tilt Sensor Based on Moire Interferometer

3. Optical Metrology System – 2 Multipoint Diffraction Strain and Tilt Sensor Based on Moire Interferometer

A Multipoint Diffraction Strain Sensor has been developed using a moiré interferometer and multichannel imaging PSD, with the novel feature of whole field strain determination. This unique feature has been implemented by simultaneous tracking of sampled wavefront diffracted from the component under test. In this sensor a high-frequency diffraction grating is bonded on the specimen, which is illuminated by two symmetric collimated laser beams, as in a typical moiré interferometer. The first orders of diffracted beams impinge on a CCD camera, via a microlens array. The lens array serves a dual purpose - to sample the diffracted wavefront and to focus the wavefront to a number of spots on the CCD. The deviation of the individual spots generated by both of the beams is directly proportional to the normal strain and a component of the shear strain. Simultaneous strain measurement at more than a thousand points can be readily obtained and is demonstrated. This novel technique is expected to be very valuable in numerous industrial metrology applications encompassing different areas where whole-field strain map is desirable.

3.1 Operating Principle

Moiré Interferometry is normally used for optical measurement of mechanical deformation through fringe analysis. In this technique, two beams of monochromatic, coherent and collimated light symmetrically illuminate a specimen grating such that the first order diffracted beams emerge normal to the surface of grating. Interference of these two diffracted beams generates an interference pattern, which can be analyzed to obtain the specimen deformation. By recording the displacement components in two perpendicular

directions, the three in-plan strain components can be obtained through numerical differentiation [38].

Figure 3.1 illustrates the principle of multipoint strain measurement using a set-up similar to that for moiré interferometry. The diffracted wavefronts emerging from the grating are sampled into wavelets by the multi-lens array and focused onto the CCD. Each wavelet represents the diffraction from a small area of the sample surface. When the grating is strained, deformed or tilted, the position of the diffracted wavelets on the CCD would shift accordingly as shown in figure 3.2. The shift of the spots is shown to be directly proportional to the derivative of the deformation. In this particular example, the shift of the spot is along one direction. However, in general the shift would be in two directions but the principle would be unaffected as the horizontal and vertical shifts are independent of each other.

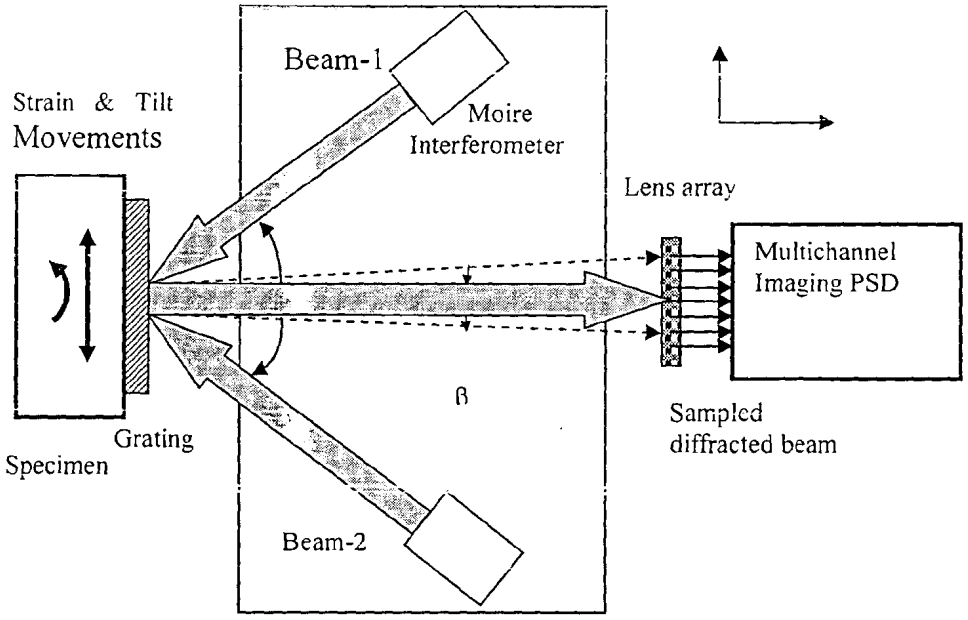

Figure 3.1. Operating principle of MDSS based on Moire Interferometer.

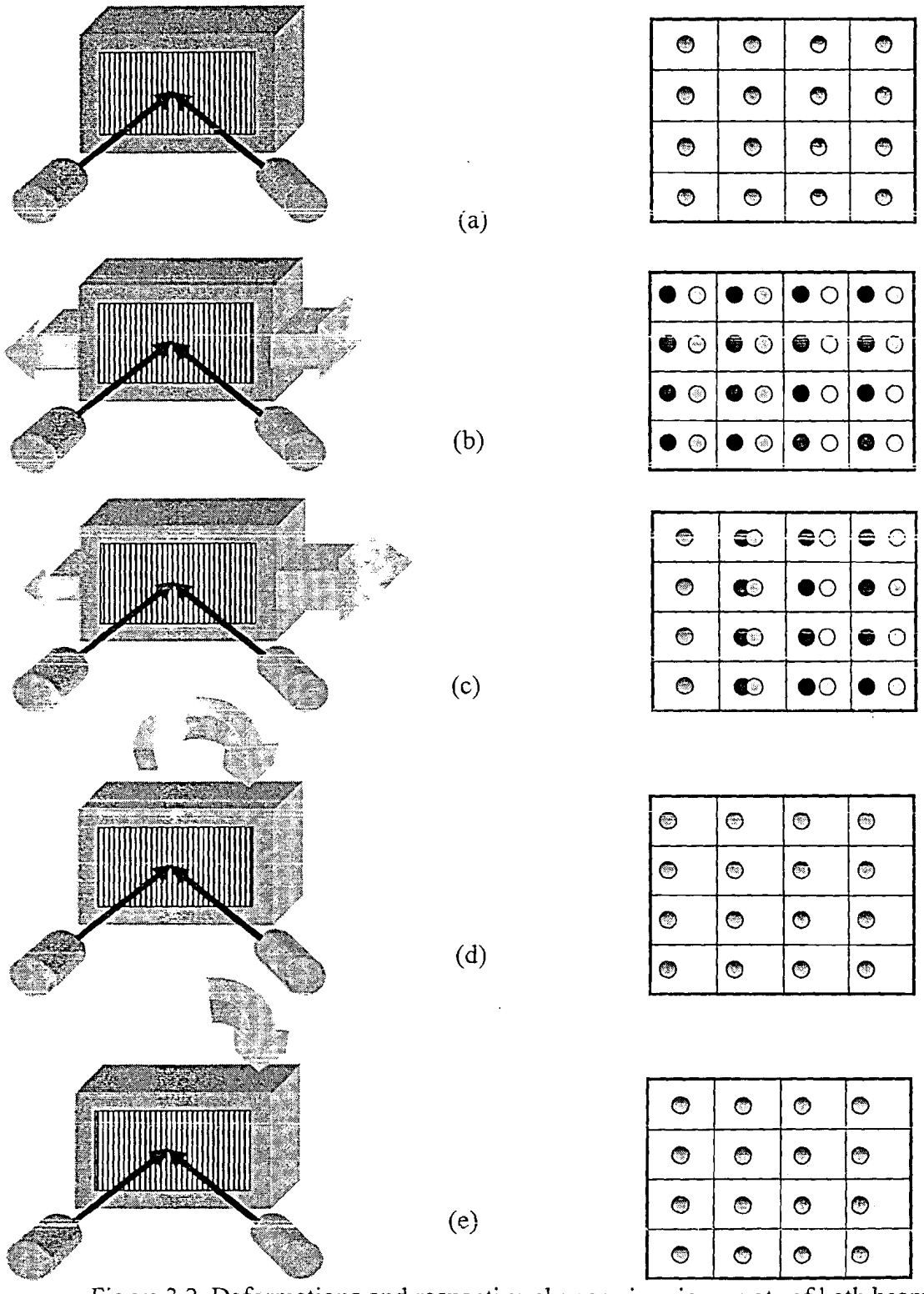

Figure 3.2. Deformations and respective changes in micro-spots of both beams (a) Unstrained sample with both spots coinciding in middle (b) Uniform strain with spots moving sideways (c) Non-uniform or heterogeneous strain (d) Uniform tilt with spots moving in tandem (e) Non-uniform tilt or warping

3.2 System Theory

Starting from the well-known diffraction equation [39] and differentiating it we get

$$P(\sin\alpha + \sin\beta) = m\lambda\,, \tag{3-1}$$

$$P\cos\alpha d\alpha + dP\sin\alpha + P\cos\beta d\beta + dP\sin\beta = 0\,. \tag{3-2}$$

where α and β are the angles of illumination and diffraction, P is the pitch of the grating whose principle direction is the x-axis, m is the diffraction order (± 1) and λ is the wavelength of light.

3.2.1 Normal Strain

The illumination angle is chosen such that the diffracted beam emerges normal to the grating or $\beta = 0$. Also during the experiment, the illumination angle remains unchanged or $d\alpha = 0$. Thus:

$$d\beta = -\frac{dP}{P}\sin\alpha = -\frac{du}{dx}\sin\alpha = -\varepsilon_x \sin\alpha\,. \tag{3-3}$$

ε_x is derivative of the displacement component along the grating principle direction (du/dx), i.e. the normal component of the strain in the x-direction. The change in diffracted angle $d\beta$ can be calculated using the spot shift on the sensor surface as

$$\Delta x_1 = f d\beta = -\varepsilon_x f \sin\alpha\,, \tag{3-4}$$

where f is the focal length of lens. The symmetrical beam incident from the opposite direction will cause an equal but opposite shift of the wavelet spot. Thus

$$\Delta x_2 = \varepsilon_x f \sin\alpha \,. \tag{3-5}$$

Combining the two equations we get

$$\varepsilon_x = \frac{du}{dx} = \frac{(\Delta x_2 - \Delta x_1)}{2f\sin\alpha} = \frac{(\Delta x_2 - \Delta x_1)P}{2f\lambda} \,. \tag{3-6}$$

The use of two beams in this manner eliminates measurement errors due to out-of-plane tilt of the specimen. Very similar expression can be derived for the y-axis strain component calculations, if the principle direction of the grating is in the y-direction and the illumination beams are in the y-z plane, then

$$\varepsilon_y = \frac{dv}{dy} = \frac{(\Delta y_2 - \Delta y_1)}{2f\sin\alpha} = \frac{(\Delta y_2 - \Delta y_1)P}{2f\lambda} \,. \tag{3-7}$$

3.2.2 Shear or Rotation

If, on the other hand, sample experiences shear strain or a rotation [38], then this will be recorded as the orthogonal movements of the spot array, i.e. for the grating lines parallel to the y-axis, spots would shift in the y-direction. As the rotation or shear is given by the orthogonal movement of the spots, it may be detected simultaneously with the normal strain [39,40]. Thus if the sample is rotated within the plane by an angle φ, its orthogonal diffraction angle is given as

$$\sin\beta_y = \sin\alpha\sin\phi \,. \tag{3-8}$$

Differentiating this and equating to spot movement as before, and noting that the diffracted beam is initially normal to the grating plane at zero rotation, we get:

$$d\beta_y = \sin\alpha d\phi = \Delta y_1 / f \,. \tag{3-9}$$

Thus for the two beams with grating principal axis along x-direction, we get

$$\Delta\phi = \frac{\Delta y_2 - \Delta y_1}{2f\sin\alpha} = \frac{du}{dy}, \tag{3-10}$$

and similarly for the grating with the principle direction along the y-direction

$$\Delta\phi = \frac{\Delta x_2 - \Delta x_1}{2f\sin\alpha} = \frac{dv}{dx}. \tag{3-11}$$

Hence all three components of in-plane strain can be deduced from this technique.

3.2.3 Horizontal & Vertical Tilts

At the same time, we may consider that if the sample undergoes some out-of-plane horizontal tilt in xz-plane, this produces the shift in the individual light spots which is understandably in the same direction. For this case if strain is not present or $dP = 0$, and angle of incidence changes as much as the tilt of the sample or $d\alpha = \Delta\theta_x$, from the earlier differential of the diffraction equation we may get

$$d\beta = -\Delta\theta_x \cos\alpha. \tag{3-12}$$

But the measured shift of the beam on the sensor is due both to the tilt of the grating and to the resulting diffraction angle change, which gives

$$d\beta = \Delta\theta_x - \Delta x_1 / f. \tag{3-13}$$

Thus as before forming expression for both of the beam shifts and adding them we get the tilt to be as

$$\Delta\theta_x = \frac{\Delta x_1 + \Delta x_2}{2f(1+\cos\alpha)}. \tag{3-14}$$

Similar expression can be formed for the vertical tilt in the yz-plane

$$\Delta\theta_y = \frac{\Delta y_1 + \Delta y_2}{2f(1+\cos\alpha)}. \tag{3-15}$$

The two incident beams thus enable us to separately compute all the strain components as well as the out-of-plane rigid body tilt at each point of the specimen.

3.3 System Construction

3.3.1 Moire Interferometer Setup

The setup for Multipoint Diffraction Strain Sensor has been developed to be compact, relatively simple and versatile at the same time, in view of its projected use in precision machine or microelectronics industry. The system is utilizing a lens-array made up of 44x33 lenslets and a 1/2" diagonal CCD detector camera with an aperture of 6.4mm x 4.8mm. The diameter of each lenslet is 144 μm and focal length of each is 8.190 mm. A polarizing attenuator controls the light intensity incident on the camera surface. A cross grating of 1200 lines/mm was bonded on the sample surface as the target. The specimen could be rotated as well as deformed in its plane. A commercial Moiré Interferometer as shown in figure 3.3 and figure 3.4 was used as it simplifies alignment and also allows for additional verification of strains from the moiré interferometric fringes, which could also be recorded. Indeed, while the multipoint diffraction strain sensor can be used on its own, it is also a convenient add-on to the commercial moiré interferometers.

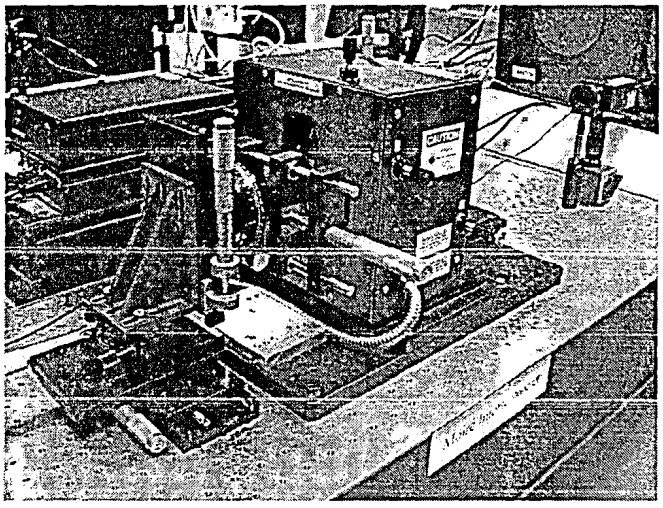

Figure 3.3. MDSS adapted to a commercial moiré interferometer with Sample loading machine

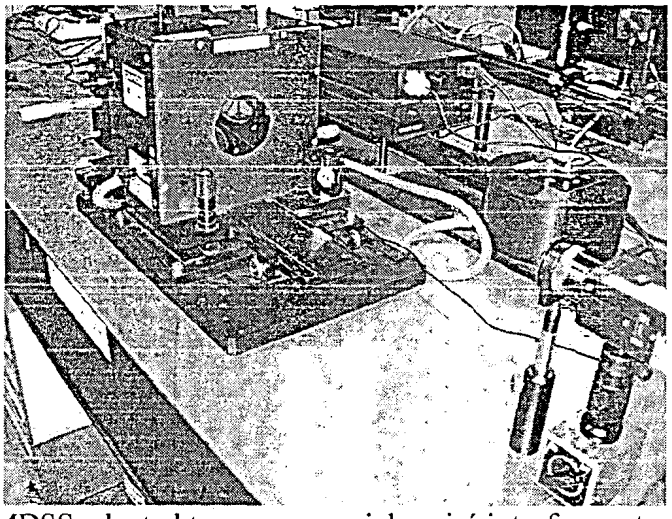

Figure 3.4. MDSS adapted to a commercial moiré interferometer with Sensor and Attenuator

3.3.2 Measurement Verification

The strain measurement is checked against the strain value calculated via fringe analysis. Thus, the average x-axis fringe spacing in the reference image and in the strained image are determined as shown in figure 3.5. Then the relative strain is calculated from difference in fringe spacing Δs and virtual grating frequency f_v as $\varepsilon_x = 1/f_v \Delta s$. For the MDSS, the normal in-plane strains are calculated using equations given earlier for u- and v-fields and for shear or

rotation. The spot centroids for each beam before and after loading is determined using a sub-pixel centroid detection algorithm and the entire calculation is programmed in MATLAB® which in addition permits other checks on the calculations to be performed as well. Each beamlet window is of about 18x14 pixel size. Illuminated pixels of light spot are determined by comparing light level of each pixel with a specific threshold and thus the sub-pixel centroid position from the illuminated pixels is computed.

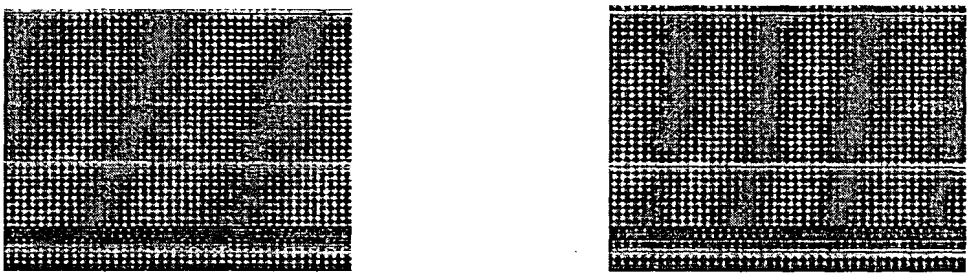

(a) (b)

Figure 3.5. Fringe pattern of (a) reference and (b) strained images for comparative strain calculation.

3.4 Moire Interferometer Setup Output

3.4.1 Data Processing

The operation of Multipoint Diffraction Strain Sensor starts by the input of reference images taken alternately by switching on the right and left interferometer beams, and recording the beams diffracted from the un-strained specimen. The centroids of the individual spots are computed from these images and stored by the system software as the reference positions. Afterwards the sample is strained and two images of the beam diffracted from the strained sample using the right and left beams are processed as before. The system computes the individual shift of each spot in the images both from the right and left beams; and thus computes the strain averaged over each sampled area. In addition, any shear (orthogonal) strain or in-plane rotation of the specimen is also calculated and displayed in the

form of a distribution map. Typical spot images along with a combined image (red for before and green for after) and an enlarged view of a few sub-images are shown in figure 3.6.

The data processing operation of the system is fairly fast and the strain map is produced almost instantly, i.e. within few seconds. Simultaneously, detailed statistics of the strain distribution are also displayed, like mean and standard deviation, etc. As an image from each of the right and left beam is needed at a certain strain condition, straining of the sample may be done in steps, while stopping and allowing for beam-switching and imaging operation. For the quicker computation process, the system also has the provision of feeding multi-step stored data of the strained images at a time and a multi-step mean strain curve is also produced, as shown later.

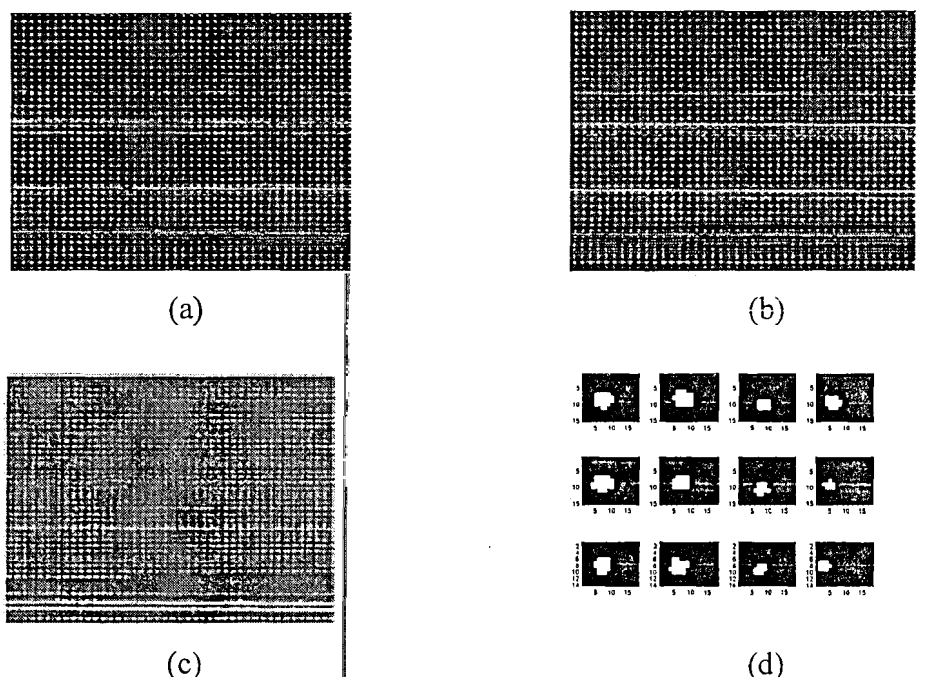

Figure 3.6. (a) Reference and (b) strained images along with (c) combined image and (d) sampled spot images.

3.4.2 Strain & Rotation Maps

The tests were mostly performed on a circular disk sample of hard plastic having about 2.5'' of diameter, with grating rigidly bonded on its surface. For the case of in-plane strain,

the resulting strain map of sampled area is shown in figure 3.7. Since the area is small and can be seen from the fringe patterns in earlier figure, the strain is fairly uniform. Although the rotation/shear strain component in this case is small, the shear strain/rotation map picks up these changes which are not apparent from the fringe pattern. Figure 3.8 and figure 3.9 show the cases of non-uniform strain by looking at the edge part of the sample or by poking a wedge on the right edge of the disk.

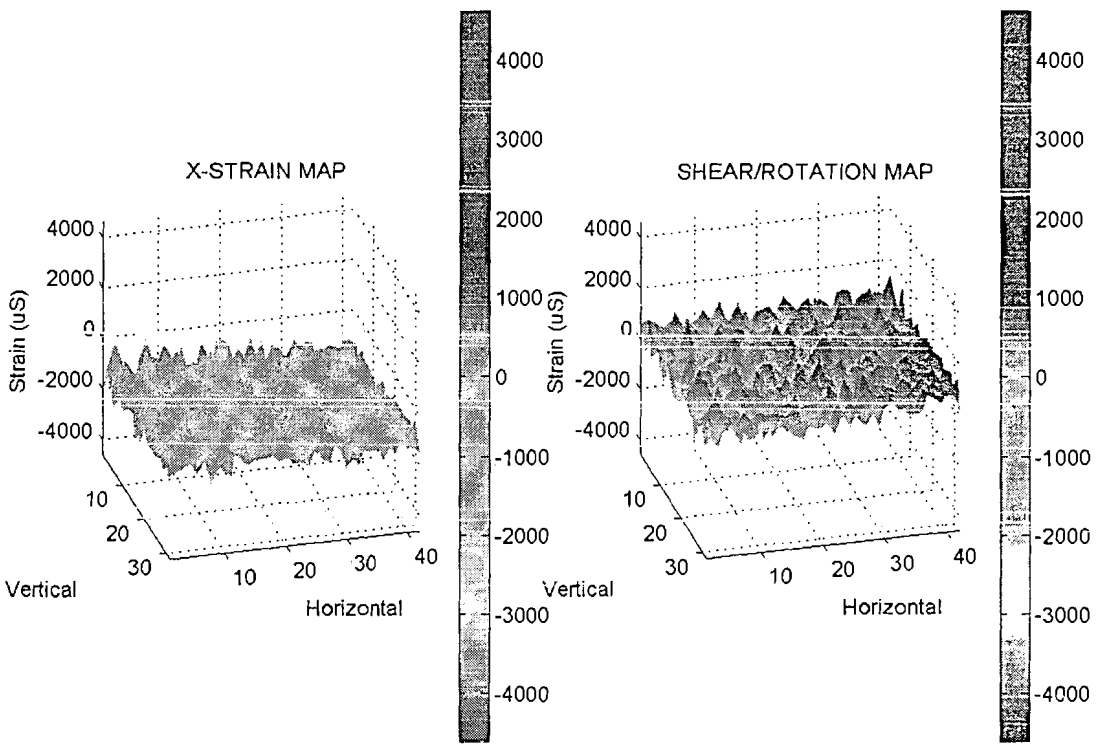

Figure 3.7 2-D Strain Map for uniform x-strain (with some shear component).

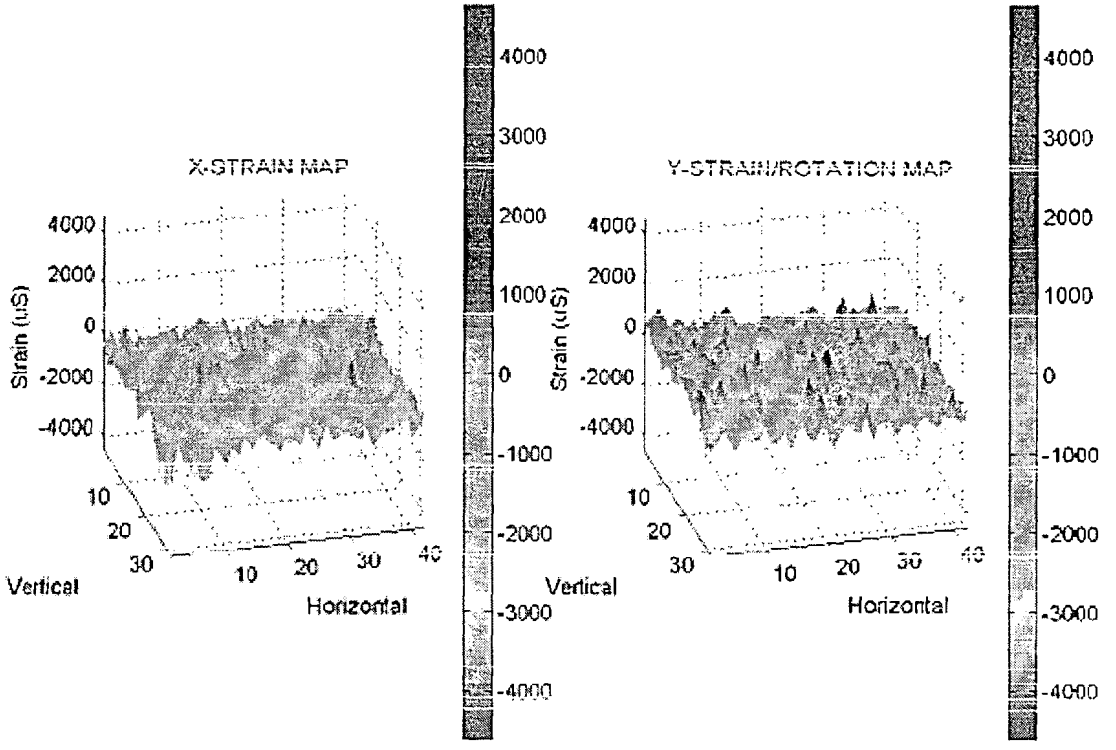

Figure 3.8. 2-D Strain Map for non-uniform strain (Map of the area near the left edge of the sample, with the left edge values being more negative)

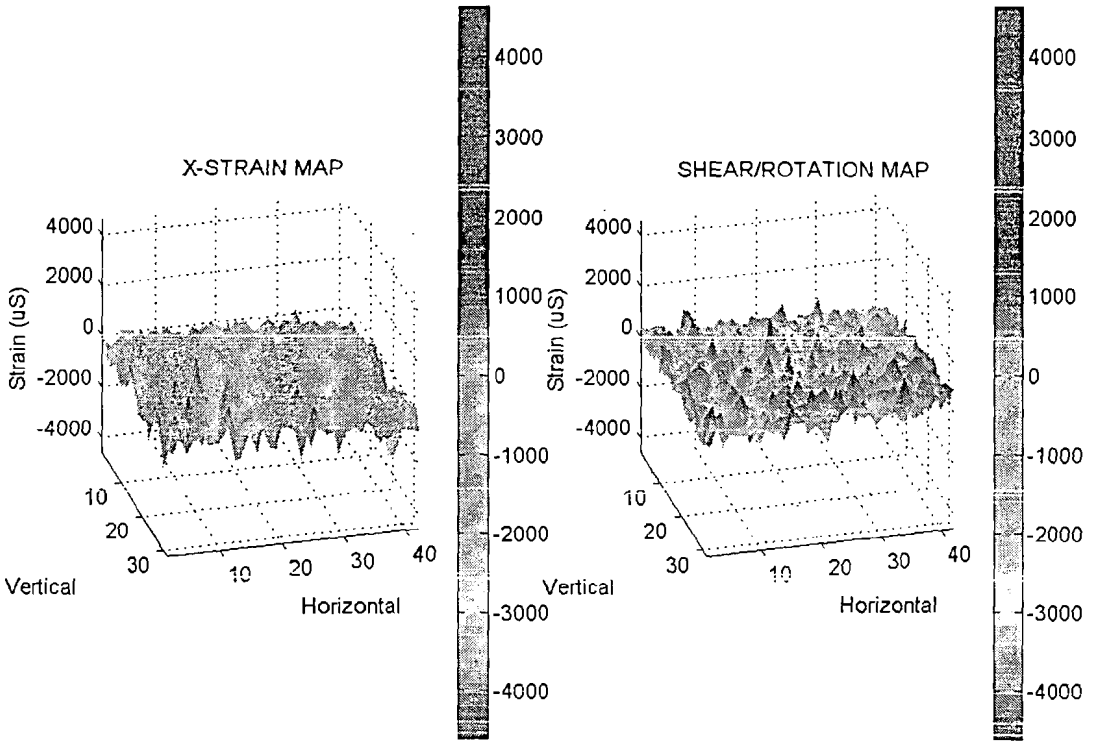

Figure 3.9. 2-D Strain Map for non-uniform strain (Poking from right side makes the right edge strain values in the map to be more negative, with a visible ditch in the middle of edge.)

3.4.3 Rotation and Tilt Maps

Figure 3.10 shows the results for the case of pure rotation. In this case, the normal strain component is zero as is to be expected and the shear component shows uniform rotation over the entire sampled area. In these maps, strain (or rotation) is given as gray-scale (color-coded) along vertical axis, with the units of *uS* (micro-strain or $\mu\varepsilon$) or *uR* (micro-radians). Figure 3.11 is simultaneously showing x-strain and x-tilt of the component.

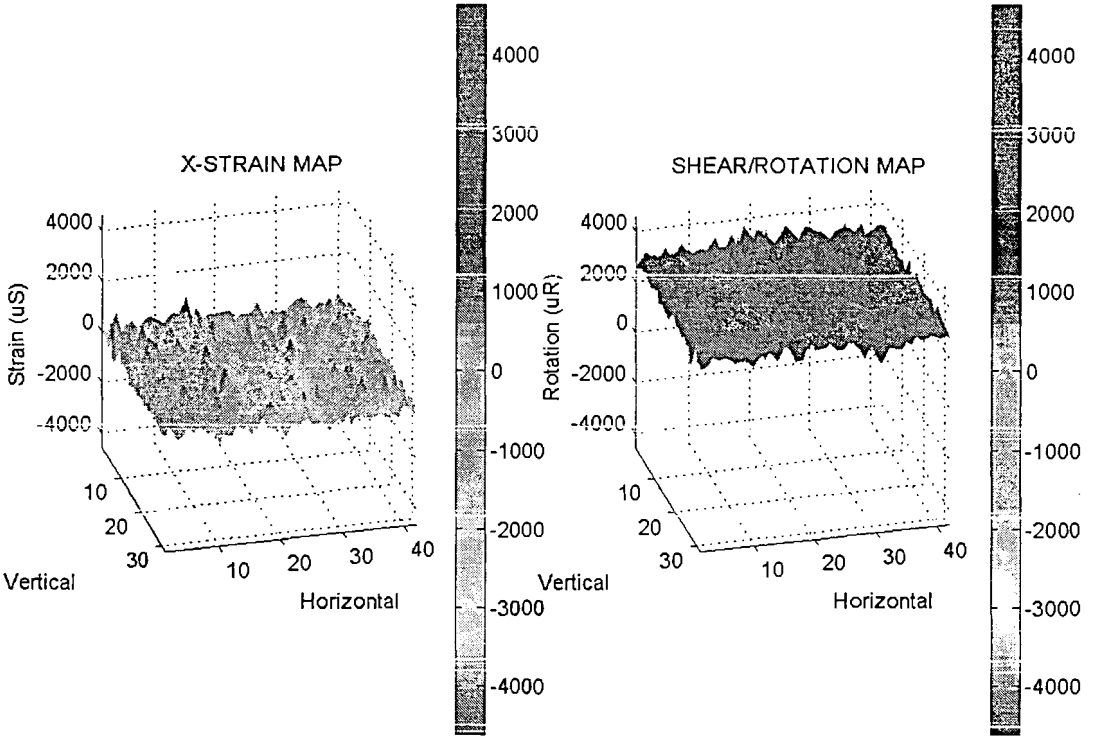

Figure 3.10. Strain and rotation maps for pure rotation applied.

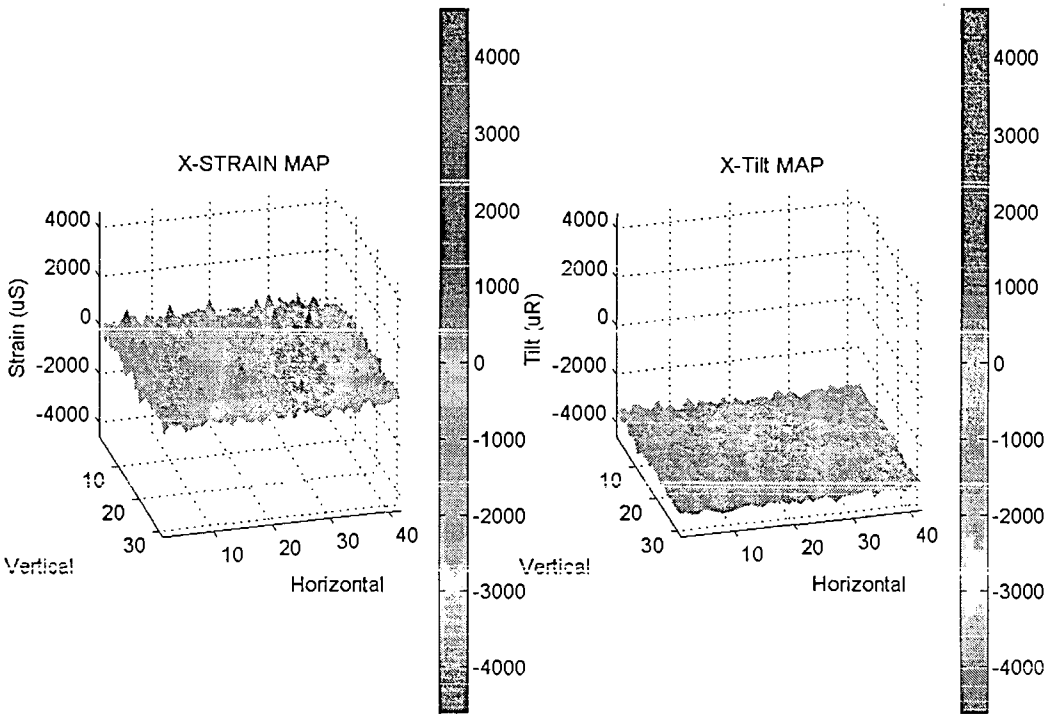

Figure 3.11. (a) Strain and (b) tilt distribution for a specimen subjected to uniform tilt

3.4.4 Multi-step Curves

To compare the results with the moiré interferometric pattern, the average strain from all the spots was determined and compared with the average strain calculated from the fringe spacing in moiré interferometry at different loads and rotations. Figure 3.12 shows the mean normal strain and shear strain comparisons for the disk under compression. Good correlation (within few percent) is found between the calculated and experimental values. Similarly for the case of rotation, the rotation measured using MDSS is compared with the rotation values applied. Once again the correlation is excellent as seen in figure 3.13. This figure contains rotations measured from both the gratings with first part corresponding to a grating with the x-direction as the principle direction and second part is for the grating with principle direction as the y-direction. Next figure 3.14 shows the results for tilt applied to the sample.

For the first part, it is normal x-tilt, while for second part it is y-tilt as v-field is used from interferometer instead of the normal u-field.

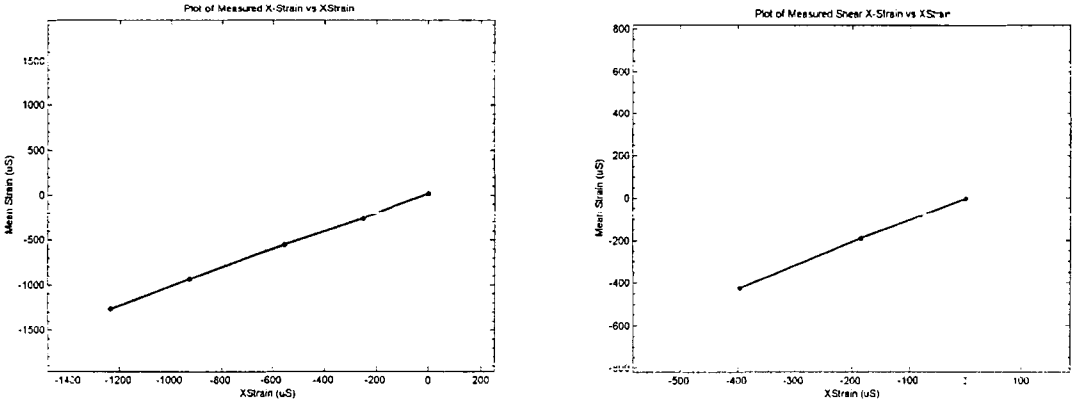

(a) (b)

Figure 3.12. Mean (a) normal x-strain and (b) shear strain for increasing applied load – comparison of measurement with MDSS (vertical) and with moiré interferometric fringe method (horizontal).

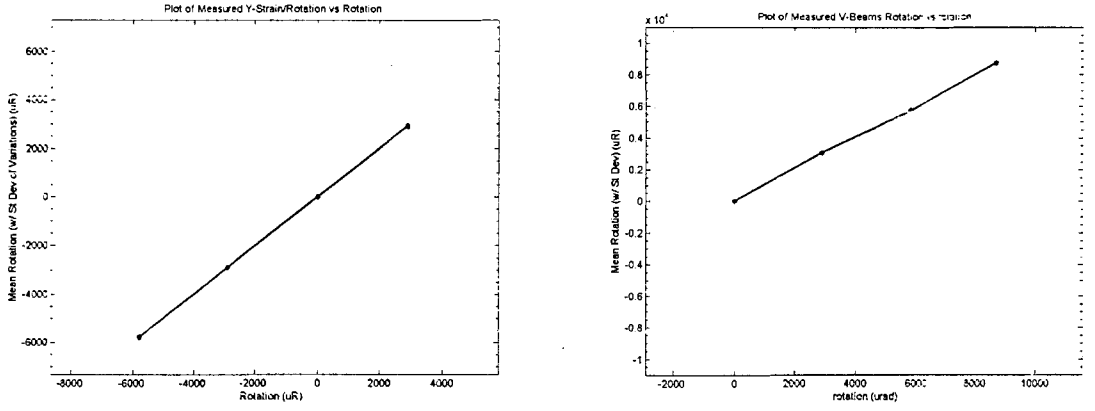

(a) (b)

Figure 3.13. Comparison of applied rotation (horizontal) with that measured using MDSS (vertical) with grating principle direction as (a) x- direction (b) y- direction.

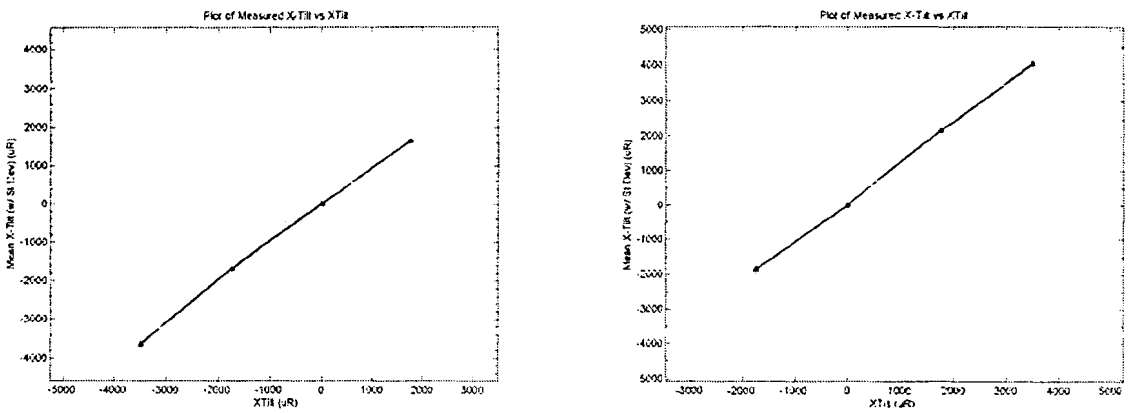

(a) (b)

Figure 3.14. Comparison of applied tilt (horizontal) with that measured using MDSS (vertical) for (a) x-tilt (b) y-tilt (v-field applied)

3.5 Design Decisions

Design of this new system passed through different stages and involved design trade-offs at these stages. Following are some of the important decisions taken en-route for performance improvement.

3.5.1 Use of Moire Interferometer

The principle of multi-channel diffraction measurement can be implemented with different laser beams having different beam properties. In the beginning of our experimentation, a pair of collimated but narrow beams from fiber laser source was used for this purpose. The obtained images of the diffracted beam are shown in figure 3.15. The obvious problem seen was that the beam could not illuminate whole screen at a time, and also that the illuminated part of the lens-array changed with the shift of the beam, thus making the reliable strain calculation very difficult. Next beam type tried was the un-collimated divergent beam from the same source, which would easily fill more than whole of the screen. The images were very uniform with discrete micro-spots, but as it soon became

obvious that the divergent incident beam would give a divergent diffracted beam. And such diverging wavefront would deviate the results from the values calculated from the theory developed, i.e. an error factor K would be needed as $\varepsilon_x = K_f\ \varepsilon_{x(un\text{-}collimated)}$. Moire Interferometer beams on the other hand are correctly-incidnet, collimated and enlarged for the needed whole-field imaging, and thus produce results being theoretically valid too.

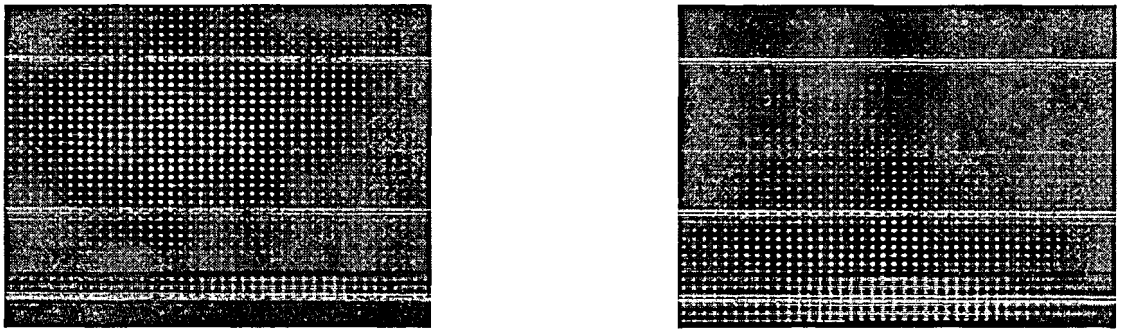

(a) (b)

Figure 3.15. Effects of spot movement on collimated narrow beam

3.5.2 Use of Two Beams for Strain Calculation

It may be mentioned that the strain in the specimen can also be calculated using a single beam diffraction, which is given by the initial equations. As pointed out earlier about errors in such measurements [27,31], the major source of error in strain calculation through diffraction is the out-of-plane tilt of the specimen surface, which also gives rise to similar spot shifts as strain. But as covered in our theoretical treatment earlier, use of two symmetrical opposite beams from Moire Interferometer produces two different spot shifts calculated from both beams. Now the tilt can easily be purged out being related to the sum of the shifts or $(\Delta x_2+\Delta x_1)$, while the strain may more cleanly be calculated being related to the difference of the shifts or $(\Delta x_2-\Delta x_1)$.

3.5.3 Image Light Thresholding for Spot Determination

The output of CCD-based camera is 8-bit gray-scale image, thus showing different levels of illumination at different pixels of lighted spot. The spot centroid was first calculated from this image and the shift of the spots was determined by comparing the information in two images. It was soon found out that the spot-shift calculation from such gray-scale image was not correct mainly owing to the inherently present light in the background pixels, e.g. the tilt of 4 pixels was measured as that of about 2 pixels. Thus as an alternate, the images were then processed by comparison of each pixel to a suitable threshold value determined by the average amount of light present in the pixels of the picture, and then were converted to binary image containing 1s for light and 0s for dark areas. This would give correct results of shift and strain calculation for different light conditions and specimens used.

Next problem came with the irregular images taken from imperfect or 'dirty' gratings bonded to the specimens, showing larger variation of light or presence of darker spots within the same image. For this purpose, the thresholding algorithm had to be modified again, as the threshold now was kept according to the average amount of light in the close-by region or in the specific sub-window being processed, instead of relating it to the cumulative average light of the image. This approach worked for most diffracted beams of varying light intensity. But it was also found that correctness of shift calculation was slightly hampered as per the variation in the certroid calculation for each sub-window. Examples of different images are given in figure 3.16.

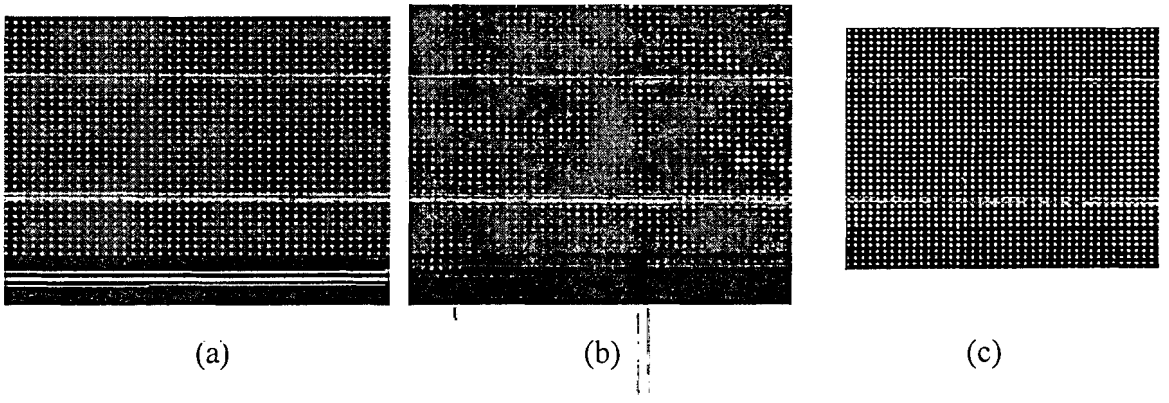

(a) (b) (c)

Figure 3.16. (a) Regular image from camera, (b) Irregular image from camera, (c) Normal image after thresholding

3.5.4 Technique for Strain Calculation Comparison

An important design and analysis issue was choosing the technique to which the strain calculation from MDSS can be reliably compared for result correctness verification. At first the samples were used with a normal strain gauge bonded on its back. It was soon found out that in compressive or negative strain applications, the measured values were non-linear and somewhat unrelated to MDSS calculations. The difference came firstly due to the fact that strain gauge is a single-element sensor whose position on the specimen may well be different from the mean position measured on the grating. And the other bigger and obvious reason of the difference is the bending effect in the specimen under compressive loads, which makes the front and back strains entirely different from each other.

Other possibility tried was the strain calculation from the mechanical movement of the loading tool sides, as a fraction of the length of the specimen. Such calculation was of course more crude and hampered by many factors including variable strain distribution, bending effects and the tolerances in the mechanical movement of the loading machine. Compared to these, fringe analysis of the Moire Interferometric patterns is the whole-field approach like ours. Its suitability for use also came from the fact that it is optical method like ours and also uses the same bonded grating for strain calculations, which makes this comparison much more meaningful and trustworthy.

3.6 System Characterization

3.6.1 Linearity or Data Correctness

Table 1 shows the comparison of applied and measured values of strain and tilt, for the uniform but gradually varying values. The applied strain values are determined by Moire Interferometric fringe processing method. The comparison shows good correlation and

linearity between the measured and applied values, thus verifying the measurement capability of this technique. Considering the maximum measurement range for this system, which is being determined later, the measurement linearity of the system comes to be within 1% of FSD for strain measurements and within 2% of FSD for the tilt measurements. One reason of larger error margin in tilt calculations is probably due to the applied values read on the screw-type mechanical gauge of the rotational stage, having larger margin of human error as compared to the fringe processing method used for the determination of applied strain.

Table 3.1. Comparison of applied and measured values of x-strain and x-tilt

Sr No	X-Strain (με)		X-Tilt (μrad)	
	Applied	Measured	Applied	Measured
1.	-1234	-1264	-3500	-3641
2.	-926	-931	-1750	-1680
3.	-555	-547	0	5
4.	-252	-254	1750	1654
5.	0	17		

3.6.2 Sensitivity

The system sensitivity to strain or tilt changes is largely governed by the imaging resolution and centroid detection algorithm for the generated micro-spot, so that the minimum shift in spot can be discerned. Considering a medium-sized spot covering the area of 6x6 pixels (which is closer to our experimentation as shown in figure 3.17), and that the minimum movement of the spot can be that of the shift in one pixel only, the minimum sensed spot shift comes to be 0.22 micron. This corresponds to the strain sensitivity of 18 με and tilt sensitivity of 8 μrad.

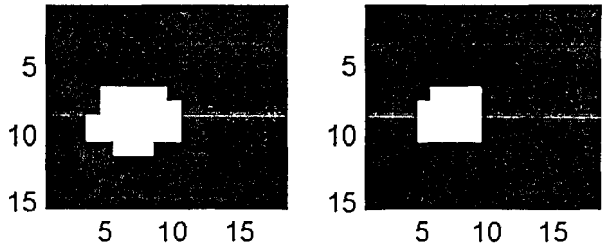

Figure 3.17. Enlarged subwindows showing micro-spots shape and size in pixels

3.6.3 Accuracy

The accuracy of the system was experimentally established as the standard deviation present in the list of multiply-recorded data, as shown in figure 3.18. It may also be noted that such data deviation differs while considering the strain present at a single point or while considering the mean strain of whole the map. It was found that the accuracy of mean strain calculation is about 3 με and that of the mean tilt calculation is about 1.5 μrad. The tighter value of tilt accuracy may well be due to more stable application of tilt to the specimen. On the other hand, accuracy for an individual point was found to be at much looser value of about 50 με. This may largely be attributed to the imaging resolution of the camera used, which comes to be significant due to the finite pixel size.

3.6.4 Range

The range for maximum strain and tilt, assuming that the spots remain within the same micro-lens area, is governed by the maximum allowable shift of the individual micro-spots as shown in figure 3.18. Based on the equations for the single-axis strain and tilt calculation derived earlier, and considering the usable size of each sub-window being 18x14 pixels minus the size of the spot, the measurement range can be calculated. Starting from the no-strain condition of both spots coinciding, the maximum spot separation obtained within a sub-window can be about 100 micron, which puts the strain measurement range at 8 mε. Similarly assuming the spots traversing whole of window during the tilt-measurements, the maximum tilt change to be measured is 7.5 mrad. These ranges are of course dependent on the pre-hand alignment of the system, and without the proper alignment the spots may go

out-of-range even with small movements. Experimentally somewhat smaller value of 5-6 mrad was achieved for the tilt measurement as shown in Fig 8, probably due to the larger measurement steps and irregularities in the spot shape.

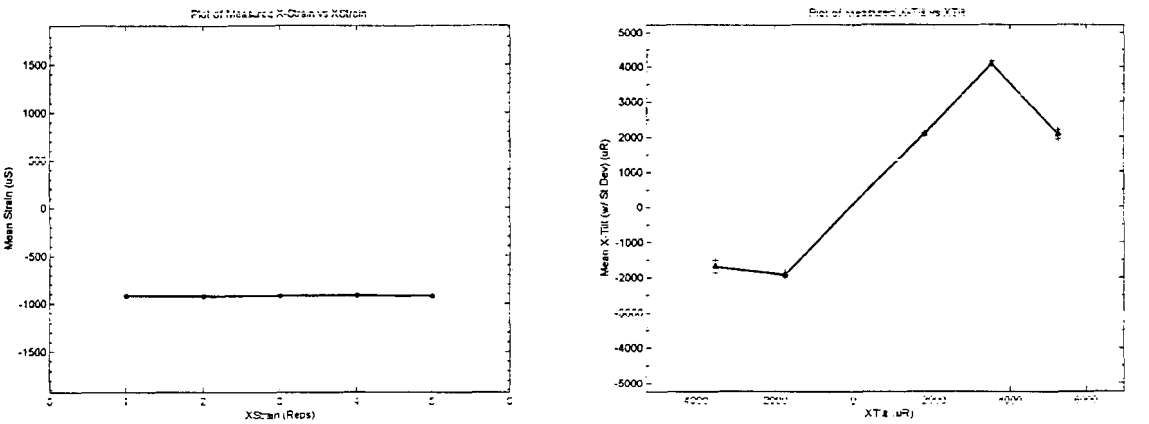

(a) (b)

Figure 3.18. (a) Multiple readings at the same strain for accuracy determination. (b) Tilt range given as linear region of the curve

3.6.5 Spatial Resolution

Spatial resolution of the system depends on the separation present between the individual micro-spots on the CCD surface. For our system having a lens-array of 44x33 lenses, and the CCD size of 6.4x4.8, this resolution value is about 145 micron, which is largely coinciding with the individual lens dia of 144 micron. Figure 3.19 shows an example of strain map for the given CCD size, while narrow peaks of irreguiar strain are evident indicating the high spatial resolution of the system.

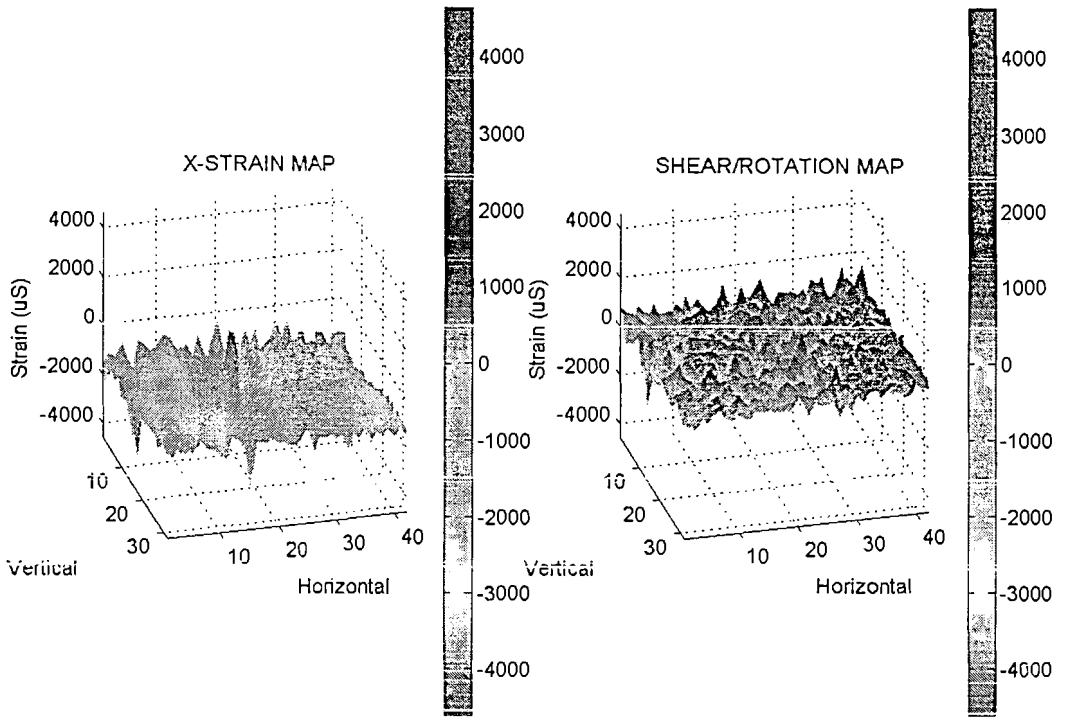

Figure 3.19. Strain map showing narrow strain peaks

3.7 Conclusions

A new system Multipoint Diffraction Strain and Tilt Sensor has been developed based on Moire Interferometer and Multichannel PSD, with a novel technique for simultaneous optical strain and tilt measurement at a large array of points. The system uses simultaneous position tracking of smaller beams diffracted differently from the various points of the component under test. Using this setup, whole-field strain and tilt distribution patterns over the component body can be obtained in near real time, without the need for fringe processing. Furthermore, the system also has capability of measuring rotation and shear strain. To sum up, it is possible to measure all three strain components as well as rotation and both tilts, making this a truly versatile whole-field strain sensing system. The system offers a promising combination of features compared to other whole-field methods, including data collection

speed, results accuracy and compactness; with its prime strength being in direct and near-real-time calculation of whole-field strain with a fine spatial resolution. The system characteristics can be further improved using finer imaging resolution and smarter processing algorithm. All these make this technique very attractive for precision applications in mechanics and micro-mechanics.

3.7.1 Related Publications

1. S. Iqbal and A. Asundi, *Multipoint Diffraction Strain Sensor: Theory and Results*, Measurement Science and Technology 17 (2006), pp 2306-2312.
2. S. Iqbal and A. Asundi, *Characterization of Multipoint Strain and Tilt Sensor based on Moire Interferometer and Multi-channel Imaging Position-sensitive Detector*, Review of Scientific Instruments 77 (2006), 113110.
3. S. Iqbal, S. Mhaisalkar and A. Asundi, *Multipoint Diffraction Strain Sensor: an add-on to Moiré Interferometer*, SPIE Optics & Photonics, San Diego, USA, 2006.

Chapter # 4

Optical Metrology Components: PSDs

Impact of Stray Illumination Noise on Response of Position-Sensitive Devices

4. Optical Metrology Components: PSDs

Impact of Stray Illumination Noise on Response of Position-Sensitive Devices

This chapter comprises a unique analysis of position-sensitive detectors used in noisy industrial environment, where several other light sources also coexist and thus produce unpredicted effects on PSD output. Many researchers of normal photo-sensors have analyzed their performance in presence of these stray noises, while this problem has many times been outlined in context of PSDs too. Nonetheless, detailed performance analysis of PSDs with stray optical noises is very much needed. For this purpose, we first describe and model these stray noises with respect to the operation of PSDs and then analyze the response of these detectors in the presence of these spurious signals. The experimental results are presented, which were obtained using PSDs with signal beams and noise sources. The experimental data is compared with the results from the proposed mathematical model and it is observed that the measured performance is within a fraction of a percent of the calculated one. The analysis of systematic errors encountered during data collection is also presented.

4.1 Problem Background

In the industry, telecommunication and other sectors, many applications require accurate measurement of displacement of objects through non-contact methods. Semiconductor position-sensitive detectors (PSDs) offer very good solutions for such applications and since their inception in late fifties, these devices have become a major tool for lateral position measurement. Two types of such devices are commonly used for position-sensing applications. The segmented PSDs or four-quadrant detectors are used for high precision and low signal-level applications where range of movement is relatively smaller or the alignment

is the objective. On the other hand, the continuous PSDs or the lateral-effect photodiodes are used for wider displacement measurement with high linearity, good resolution and fast response [51,52,60,61].

Applications of PSDs are even more diverse and widespread in the industry, including alignment, displacement sensing and as a part of other analysis instrumentation. In such environment, the system laser source is co-existing with different nearby light sources, coherent or otherwise, along with their reflections and back-scatters from various nearby surfaces. Some of the systems may involve scanning or rotating laser beams too, which may have enough energy to effect the PSD measurements in the form of periodic pulses.

Such random illumination noises may take the form of different sources types, e.g. directional, point or extended; and may fall on the detector surface in different shapes or spatial distributions. They may produce unwanted outputs while mixing with the real signal, which is coming direct from the source or via the reflector onto the detector surface. These noise sources have been mentioned or described by some of the earlier authors [51,54,62,66]. Nonetheless it is felt that a detailed operational analysis in view of PSDs is still required.

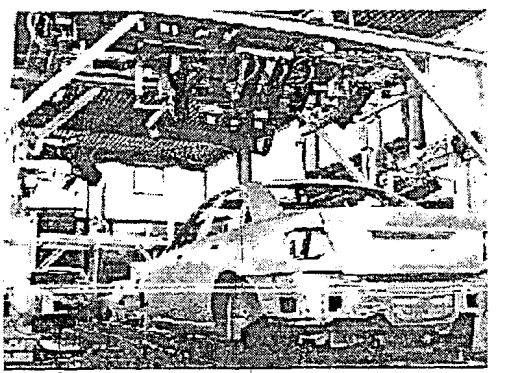

Figure 4.1. Simultaneous use of multiple closely-placed laser beams in industry (courtesy Steinbichler Optotechnic)

It may also be mentioned that for more critical measurement applications, modulation of light source is used synchronized with receiver, to avoid the effects of background light. But on the other hand, such systems become unfeasible in many standard applications due to the

practical reasons such as needed compatibility with simpler light sources, reduced technical complexity and lower system cost. Thus whole lot of industrial position measurement systems are still produced and utilized with un-modulated continuous light sources [11,12], directly effected by other illuminations. Also important is the fact that, as given by Makynen and others, even the modulated light reflected-beam sensors do suffer from stray illuminations problem in the form of unwanted reflections from close-by objects [51]. He has outlined this problem along with an effort for a solution. Thus the position response analysis presented here does also apply to these sensor types while considering the effects of such stray reflections.

4.1.1 Lateral-Effect PSDs

PSDs based on lateral-effect have a continuous construction in terms of their light-sensing area, which characterizes them from the other segmented position-sensitive detectors. Thus their construction is in the form of a single continuous photodiode, as shown in Figure 4.2. As light falls on a specific portion of LEP, the generated current carriers are divided between the extended edge electrodes on each side. This division is in proportion to the encountered respective conductance, or in inverse proportion to the relative distances of the current paths between the illuminated region and the respective electrode [60].

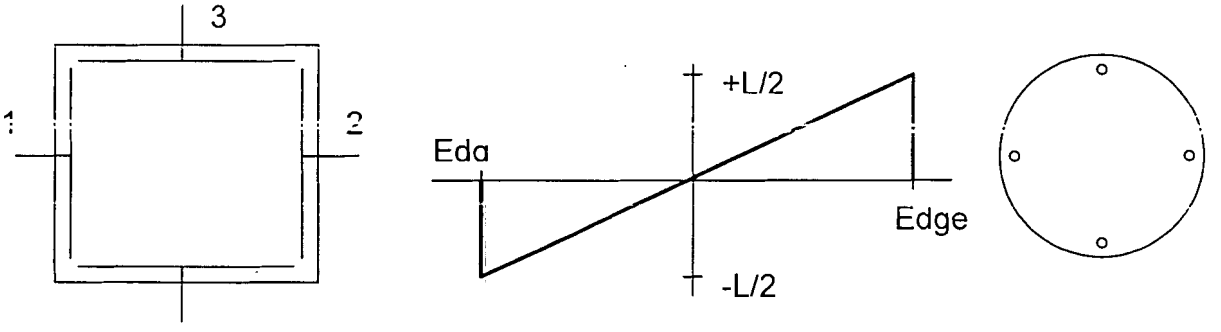

Figure. 4.2. Geometrical shape, transfer curve and pin-out of Lateral effect PSD

The important features of these lateral-effect devices include position measurement of the incident light spot for the larger dynamic range or upto the edges of the devices.

Additionally, the transfer characteristic for the light spot position measurement has very good linearity for the entire range [51]. This gives them an edge over the segmented photodetectors for many of the applications where continuous position measurement is needed. Another useful feature is that the position is measured for the centroid of the incident light beam or even divided spots. This makes them largely indifferent to the spot size and shape [63,64]. The position of the light spot is calculated from the terminal currents such that the output limits are normalized to -1 and +1 at the sensor edges. The x-axis position measured from the center of the detector in terms of the horizontal electrode currents is given in the following equation for the general duo-lateral and tetra-lateral lateral-effect PSDs [53,58]. Similar formula will be used for the y-axis position calculation in dual-axis PSD.

$$P_x = \frac{L}{2}\left(\frac{i_2 - i_1}{i_2 + i_1}\right) \tag{4-1}$$

4.1.2 Position Uncertainty of Lateral Effect PSDs

Position uncertainty of a PSD can be defined as the minimum displacement that can be resolved by a position sensor in a given electro-optical system. This is an important property of the sensing system as it more or less characterizes the quality of the sensing response of the system for smaller signals or displacements. Presence of noise heavily hampers this parameter; thus its major dependence can be described as on signal-to-noise ratio present during the system operation. This parameter may not be confused with correctness or linearity of the detector. These properties are intrinsic to the type of detector and are independent of signal-to-noise ratio.

To estimate the uncertainty of lateral-effect PSD, there are internal factors and external factors. The major spot position uncertainty due to the internal factors can be expressed in terms of speckle noise and thermal noise [54]. According to Beraldin et al, in the system what limits the performance or contribute to spot-postion uncertainty of PSDs is the presence of non-signal spurious lights, which cannot be isolated from the actual light spot position information and are inevitably interpreted as a valid signal by the PSD [54].

4.2 Noise Beams and Illuminations

The disturbing lights and illuminations may be coming from different types of sources and may be taking different spatial distribution and characteristics. Considering the sources of illuminations, the major sources have been described by Beraldin et al to be ambient illumination, direct sunlight and other laser sources [54]. These sources have been described to be the limiting factors for the performance or the fluctuation-free accuracy obtained from the operation of lateral-effect PSDs [54]. Now we categorize these sources according to their characteristics and the spatial distribution of their light on the PSD surface, and also analyze them one by one from the point of view of the normal operation of PSDs with these disturbances.

Probably the most obvious source of external noise in an optical system is background radiation. A detector will anyway be facing the black-body radiation from the background which happens to be at a specific temperature during the operation or measurement, even if specific sources are not present to emit the interfering or disturbing radiation. According to Plank's Law, this minimum background radiation illuminating any detector, or PSD to be specific, will be given as in the following equation, while other descriptions and equations are also used [62,65]. Unless their intensity is high, their usual effect may be smaller and similar to other diffused illuminations to be described hereafter.

$$\left\langle P_{opt} \right\rangle_{BG} = \int_{\Delta\nu} \frac{1}{4} I(\nu) d\nu A_{\text{det}} \frac{d\Omega}{4\pi} \tag{4-2}$$

4.2.1 Noise Beams

Probably the major source of disturbance for our analysis can be that from other directional laser beams falling on the surface of a lateral-effect PSD simultaneously, as shown in Figure 4.3. Similarly, other directional light beams and non-laser lights, which fall on the detector surface in a shape approximating a beam, may also be included in this category. Similar effect will also be produced by the illuminations, which are not directional in nature but are converted to a spot by the receiver optics. The most obvious example may

be that of parallel rays coming from a distant source and converted to a spot by the positive lens used in front of the PSD.

For the normal direct-beam or reflected-beam position sensor based on a Lateral-effect PSD, the output current produced on the PSD terminals by the main or actual incident beam is a function of certain parameters as $i_j = i_j (I_s, x_s, y_s)$ for j=1-4. In this equation I_s is the intensity of the actual beam incident on PSD's surface and x_s, y_s represent the position of the centroid of the beam on PSD's surface. Similarly, if the noise beam is falling on the surface, the output current component due to this beam may be given as $i_j' = i_j' (I_n, x_n, y_n)$ for j=1-4. Here I_n is the intensity and x_n, y_n represent the position of the centroid of the noise beam on the PSD's surface. Thus, the measured current on a terminal may be following.

$$i_{j(measured)} = i_j(I_s, x_s, y_s) + i_j'(I_n, x_n, y_n) \qquad \text{for j=1-4} \qquad (4\text{-}3)$$

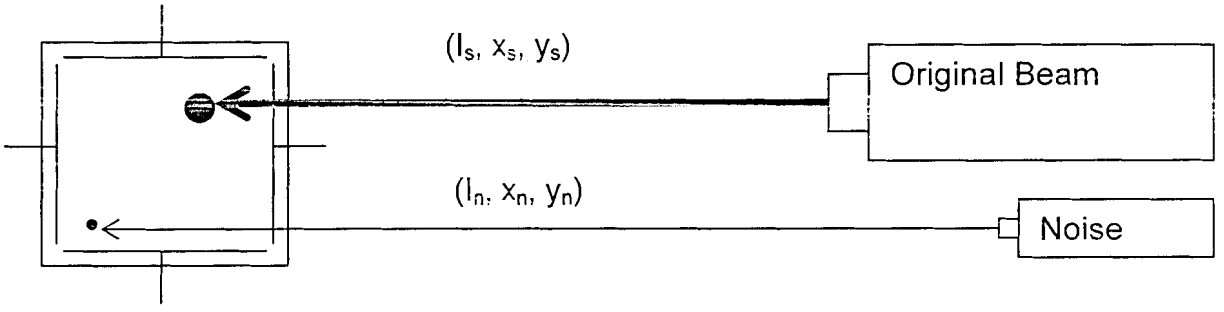

Figure 4.3. Noise beam disturbing the original beam on PSD surface

4.2.2 Noise Illuminations

The next important type of interfering illumination to be considered is the one, which is not beam-like or is not narrow enough and falls on whole of the PSD's surface area. These include the point sources whose light is falling direct on the PSD or the extended sources, diffuse reflections and background illuminations, which do not form a limited spot even after passing through the receiver optics. Ambient light is the most obvious example of this

category. Simplifying their effect on the PSD and assuming their uniformity for now, they may be approximated by a wide "spot" covering the whole of PSD area and having the centroid in the middle or the center of PSD, as shown in Figure 4.4. Thus similar to earlier representation, terminal currents are $i_j' = i_j'(I_{ill}, 0, 0)$ for j=1-4. Now I_{ill} is the intensity and 0, 0 indicate the middle position of the centroid of the interfering illumination on the PSD's surface. The measured current on a terminal may be given as following.

$$i_{j(measured)} = i_j(I_s, x_s, y_s) + i_j'(I_{ill}, 0, 0) \qquad \text{for j=1-4} \qquad (4\text{-}4)$$

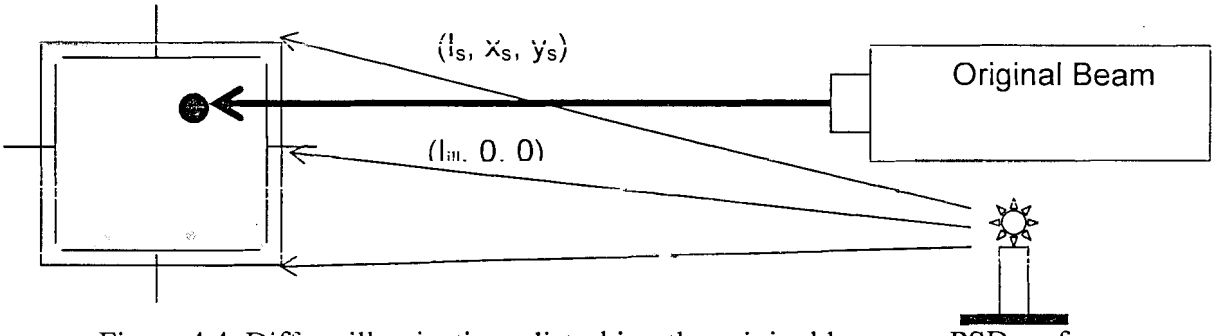

Figure 4.4. Diffuse illuminations disturbing the original beam on PSD surface

A specific category may be that of the pulsating lights or the scanning laser beams falling on the surface of PSD in the form of a pulse train. Although they may also be falling on a specific area of the detector, more common among them are going to be those approximating the diffuse illuminations covering almost entire area. This is to be expected as there is much more chance of backscatter interfering on the PSD surface instead of direct scanning light, and they are expected to take the form of diffuse illumination. The output current in this case is function of one more parameter as $i_j' = i_j'(I_{ill}, 0, 0, DC)$ for j=1-4. Here DC represents the net duty cycle of the interfering pulses impinging on the surface of PSD.

$$i_{j(measured)} = i_j(I_s, x_s, y_s) + i_j'(I_{ill}, 0, 0, DC) \qquad \text{for j=1-4} \qquad (4\text{-}5)$$

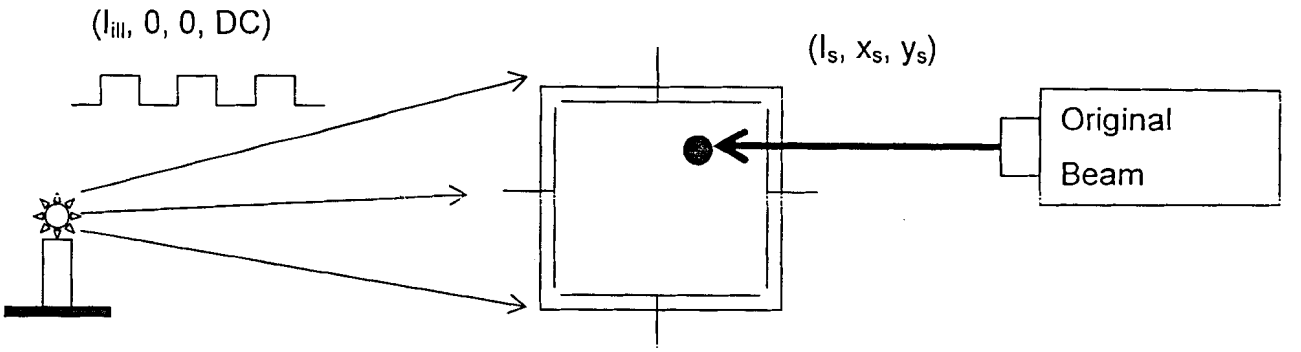

Figure 4.5. Reduced effect due to pulsating light duty cycle disturbing original beam

4.3 PSDs Performance with Optical Noise

For the normal single-beam operation, PSD gives the centroid position of the incident signal beam calculated by the individual currents as given before [51]:

$$P_{Signal} = \frac{L}{2}\left(\frac{i_2 - i_1}{i_2 + i_1}\right) \tag{4-6}$$

Suppose that instead of the 'signal beam', there is a 'noise beam' falling on the surface of PSD and generating its own currents on the output terminals. The position of the noise beam can be calculated by the similar formula as [58]:

$$P_{Noise} = \frac{L}{2}\left(\frac{i_2' - i_1'}{i_2' + i_1'}\right) \tag{4-7}$$

For the single-beam operation, calculation of the beam position is carried out in the similar manner for both of the cases. Now what will be the behaviour of the device when both the beams are incident on the surface of the PSD at the same time? According to Kawasaki & Goto, the output of PSD in this case, calculated using the terminal currents, should be equal to the intensity-weighted mean of both the light positions [63]. Thus the final position and the error from the signal position may be given as:

$$P_{Measured} = \frac{I_{Signal}}{I_{Signal} + I_{Noise}} P_{Signal} + \frac{I_{Noise}}{I_{Signal} + I_{Noise}} P_{Noise} \tag{4-8}$$

$$P_{Measured} = P_{Signal} + \frac{I_{Noise}}{I_{Signal} + I_{Noise}} \left(P_{Noise} - P_{Signal}\right) = P_{Signal} + \delta P \tag{4-9}$$

$$\delta P = K_{Intensity} dP = K_{Intensity} \left(P_{Noise} - P_{Signal}\right) \tag{4-10}$$

Thus the shift in measured position due to the presence of interfering beam depends on the mutual distance between both the sources and on the fraction of the noise intensity within the total intensity falling on PSD. This is the case when a second noise beam, which is directional in nature, is interfering with the original signal beam on the PSD. What may happen in the case where a broad illumination from a point source or an extended source is covering whole of the surface and is interfering with the original signal beam? As discussed earlier, its centeroid may be taken to be at the center of the PSD. Here the change in the final position brought by the illumination is as:

$$\delta P = K_{Intensity} dP = K_{Intensity} \left(- P_{Signal}\right) \tag{4-11}$$

Last case is about the specific category of the pulsating lights or the scanning laser beams falling on the surface of PSD in the form of a pulse train, while illuminating the PSD area as a whole. In this case the intensity of the interfering noise is actually modified in terms of the duty cycle fraction, but as the intensity of the noise is taken to be much smaller, i.e. $I_n << I_s$; thus the whole of the intensity multiple may be modified to include the DC fraction.

$$\delta P = K_{Intensity(Duty-Cycle)} dP = \frac{DC \times I_{Noise}}{I_{Signal} + DC \times I_{Noise}} dP \cong K_{Intensity} K_{Duty-cycle} \left(- P_{Signal}\right) \tag{4-12}$$

4.4 Max Uncertainty Error with Optical Noise

In order to calculate the uncertainty error introduced by the addition of noise, we consider the noise sources co-existing with the signal source, and also consider signal-to-noise ratio as:

$$\frac{S}{N} = \frac{I_{Signal}}{I_{Noise}} \tag{4-13}$$

The error introduced in this case is the difference in the measured position and the position given ideally by the signal only. This error is going to be minimum or zero if both the noise beam and the signal beam are coinciding and it is going to have the maximum value once both are maximum apart at the opposite edges of the PSD detection area. Thus, in case S/N >> 1, the maximum uncertainty error in presence of a noise beam will be as per the calculations in previous section, and comes to be:

$$\delta P_{Measured} = P_{Measured} - P_{Signal} = \frac{1}{S/N + 1}\left(P_{Noise} - P_{Signal}\right) \tag{4-14}$$

$$\delta P = \frac{1}{S/N + 1}\left(P_{Noise} - P_{Signal}\right)\Big|_{\max} = \frac{L}{S/N + 1} \cong \frac{L}{S/N} \tag{4-15}$$

Thus the maximum error introduced due to the presence of interfering beam is equal to the ratio between the length of detection area and the signal-to-noise ratio present on PSD. This is the case when a second noise beam, which is directional in nature, is interfering with the original signal beam on the PSD. What may happen in the case where a broad illumination from a point source or an extended source is covering whole the surface and is interfering with the original signal beam? In this case, its centeroid may be taken to be at the center of the PSD. Again for S/N >> 1, the maximum error in the final position brought by the illumination is as:

$$\delta P = \frac{1}{S/N + 1}\left(- P_{Signal}\right)\Big|_{\max} = \frac{L}{2(S/N + 1)} \cong \frac{L}{2\,S/N} \tag{4-16}$$

Last case is about the specific category of the pulsating lights or the scanning laser beams falling on the surface of PSD in the form of a pulse train, while illuminating the PSD area as a whole. In this case the intensity of the interfering noise is actually modified in terms of the duty cycle fraction, but as the intensity of the noise is taken to be much smaller, i.e. $I_n << I_s$; thus the whole of the intensity multiple may be modified to include the DC fraction.

$$\delta P = \frac{1}{S/_{N\times DC}+1}\left(-P_{Signal}\right)\Big|_{max} \cong \frac{1}{S/_{N}+1}\times DC\left(-P_{Signal}\right)\Big|_{max} = \frac{DC\times L}{2\left(S/_{N}+1\right)} \cong \frac{DC\times L}{2\,S/_{N}} \qquad (4\text{-}17)$$

4.5 Experimental Setup

Experimental setup for evaluating the effects of noises on the position measurements included a lateral effect PSD-based position measurement system, which was illuminated by a prime laser beam along with a noise beam or noise light source. Two laser sources used were Suwtech diode-pumped green lasers emitting at 532nm, which is produced by doubling the frequency of Nd:YVO_4 crystal output. One laser was DPGL-2100 giving upto 100 mW output with modulation control, and other was DPGL-3001F giving about 1 mW output. The beams of these lasers are CW, TEM_{00} with beam diameter < 1.0 mm and beam divergence < 1.0 mrad.

The position-sensitive detector used was Melles Griot 9mm x 9mm dual-axis lateral-effect silicon detector. This has 8 mm calibrated diameter and position resolution of ±1 μm. The detector was used in conjunction with Melles Griot microcomputer-based SpotOn optical beam position and power measurement system, model 13PSL002-PCI. The system provides software control, software linearization, selective data logging and data acquisition rate of 20 Hz. One laser head was moved by placing on PI translational movement IntelliStage C531.5i, featuring computer-control, 306 mm range and 0.1 μm linear resolution. Whole apparatus was placed on Newport 'RP Reliance' Sealed Hole Table Top, which was mounted on Newport isolation supports. The construction of the test apparatus is shown in Figure 4.6.

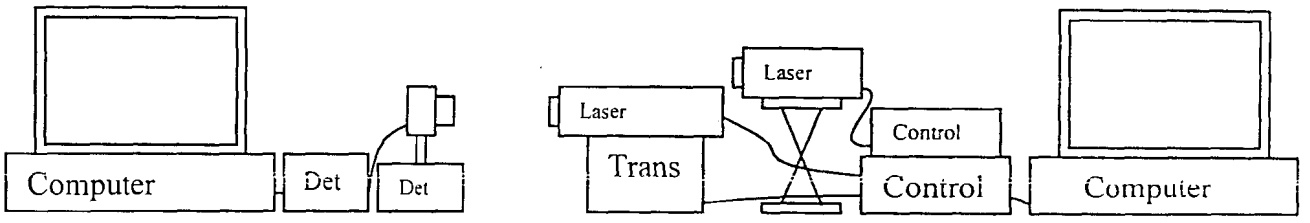

Figure 4.6. Experimental setup with computers, lasers and position detection system

4.5.1 Data Stability Measures

It was noticed that certain factors hampered the stability and repeatability of the digitized data very much, so care was taken about them to avoid any error in the readings. Ambient temperature was maintained at 20-25°C as the drift in both directions was apparently effecting the data stability. The incident intensity on the detector was used close to 1-1.5 mW, as much lower intensities were giving more jittery readings and higher intensities were risking detector saturation. Control of ambient light was practiced in order to avoid any systematic error in the data and bare minimum was used. As per laser usage practice, some warm-up time was given for the lasers and equipment temperature to stabilize, as more shaky data was noticed otherwise.

4.6 Experimental Results

This part describes the experimentation performed on the given concept. The experimental results, obtained with the use of PSDs in presence of spurious sources, are presented graphically. The obtained experimental data is also compared with the expected values from the mathematical model and the comparative results are given.

4.6.1 Noise Beams

As per noise categories described in earlier sections, the first type of noise considered is that of the interfering directional beams which fall on the detector surface and form a limited light spot. To evaluate their effect, a signal beam was projected on the PSD surface approximately at its center. The interfering beam source was placed on the translational stage and was scanned across the PSD surface calibrated area in x-direction. The measurements of net position were taken by casting it at different positions on PSD surface with the intervals of 1 mm. Two sets of data were collected with the noise beam intensity being approx 10% of the signal beam intensity in the first set and being approx 5% of the signal intensity in the second set. Both the sets of position data were compared with the calculated outcomes after the beam disturbance as per theory developed earlier. Data points were plotted with calculated position on one axis and the experimental position on other axis, and were shown along with the straight line of ideal comparative values in Figures 4.7 and 4.8.

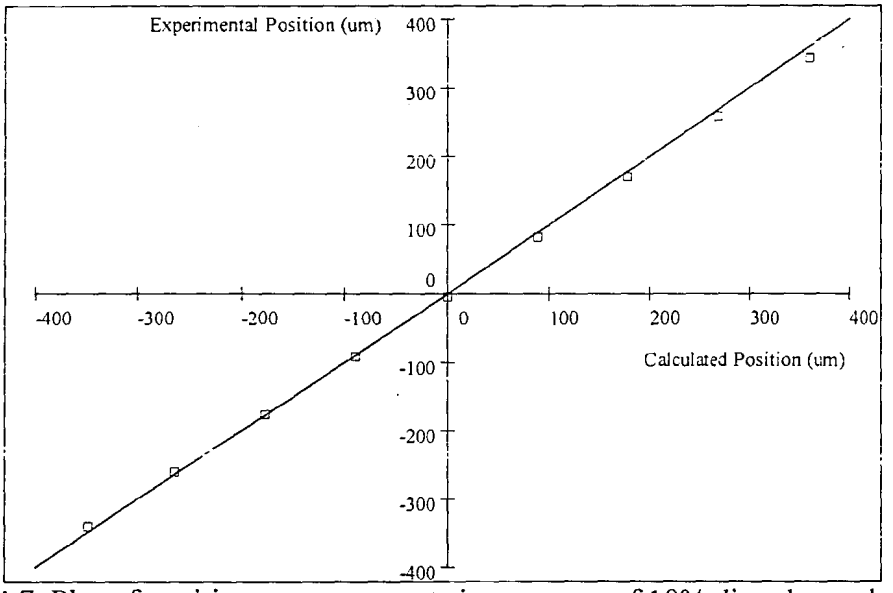

Figure 4.7. Plot of position measurements in presence of 10% disturbance beam

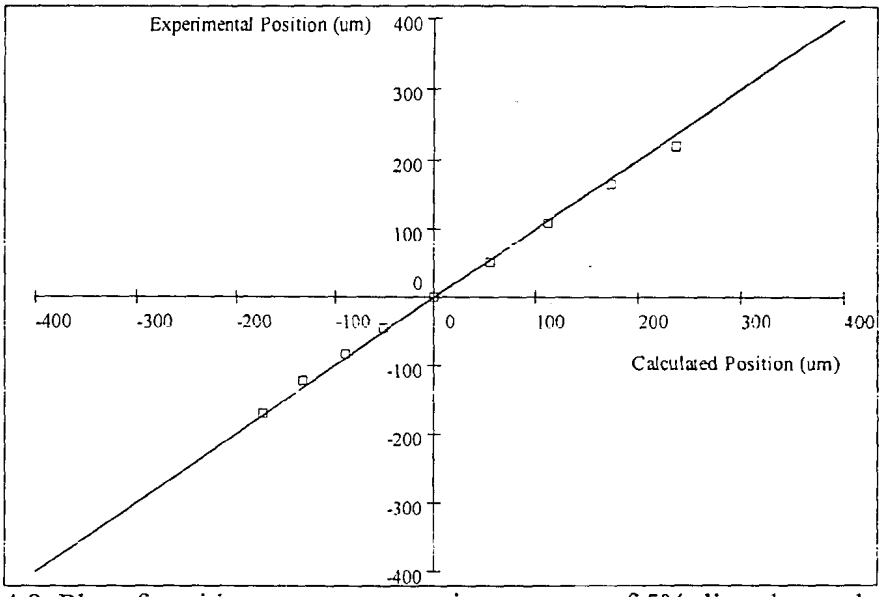

Figure 4.8. Plot of position measurements in presence of 5% disturbance beam

As seen in the plotted curves, both the sets of calculated and experimental data coincide well with each other. The maximum difference in both the data sets is about 20 μm while the maximum scale of reading is 8000 μm (-4000 μm to +4000 μm). This puts the maximum error encountered in both the experiments of 10% and 5% noise at about 0.25% of full-scale reading. The percentage experimental error has been plotted for both in Figures 4.9 and 4.10.

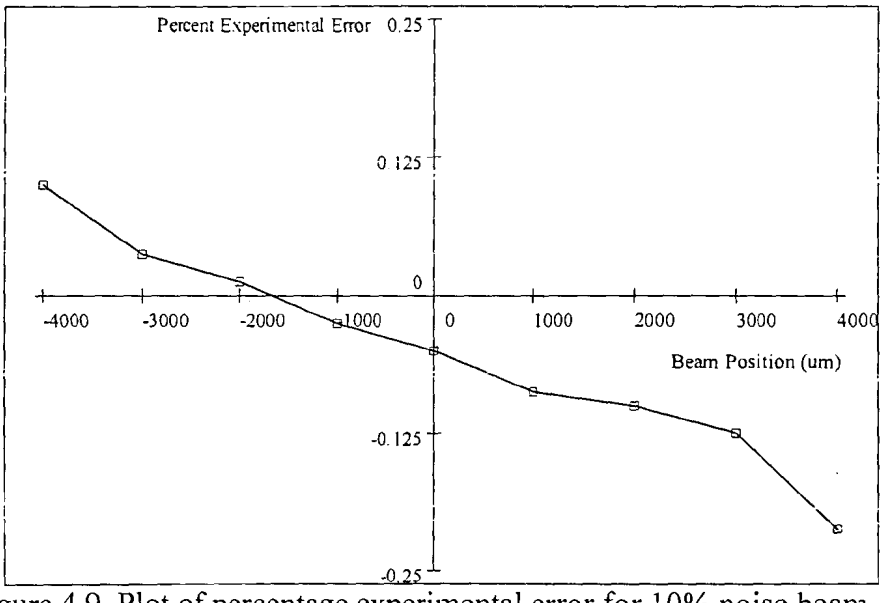

Figure 4.9. Plot of percentage experimental error for 10% noise beam

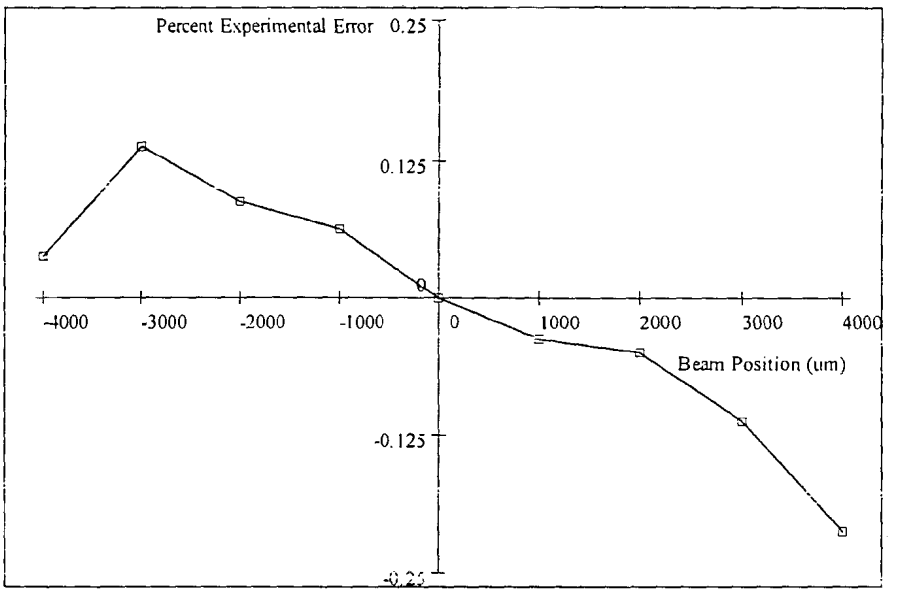

Figure 4.10. Plot of percentage experimental error for 5% noise beam

4.6.2 Noise Illuminations

The second type of optical noise mentioned earlier is that caused by the stray illuminations, which are not forming a spot on the surface and they are rather covering the entire area of PSD. This type of disturbing illumination was produced for experimentation by simultaneous effect of multiple room lights, while their total intensity falling on PSD was almost symmetrical about the center of PSD, specifically in x-direction, which is the axis of interest at the moment. The signal beam was projected at the ends of the calibrated area of PSD, i.e. at –4.0 mm and +4.0 mm. The measurements were taken with the illumination intensity being about 5% and 10% of the signal intensity. The effect of illumination on the position measurement from PSD was noted and compared with the calculated outcome differently for both the intensity percentages in Figure 4.11 (squares for 10% & circles for 5%).

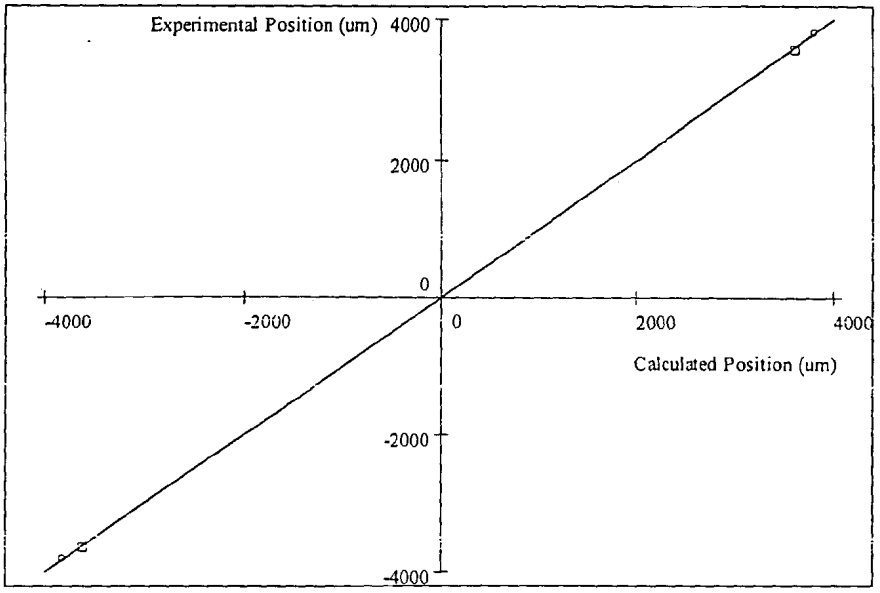

Figure 4.11. Plot of position measurement in presence of disturbing illumination

As seen in the plot, the calculated and experimental data coincide well with each other. The maximum difference in these data points is about 30 μm in the maximum scale of 8000 μm. This puts the maximum error encountered in this experiment at about 0.375% of full scale reading.

To simulate the pulsating or scanning lasers, the interfering beam was modulated at 1.0 kHz with 50% duty cycle. It was projected on the center of the PSD detection area to simulate the falling pulsating reflections or rotating lights. The signal beam was projected at the ends of the calibrated area of PSD. The measurements were taken with the unmodulated interfering intensity being about 5% and 10% of the signal intensity. The effect of interfering pulses on the position measurement from PSD was noted and compared with the calculated outcome differently for both the intensity percentages in Figure 4.12 (squares for 10% & circles for 5%).

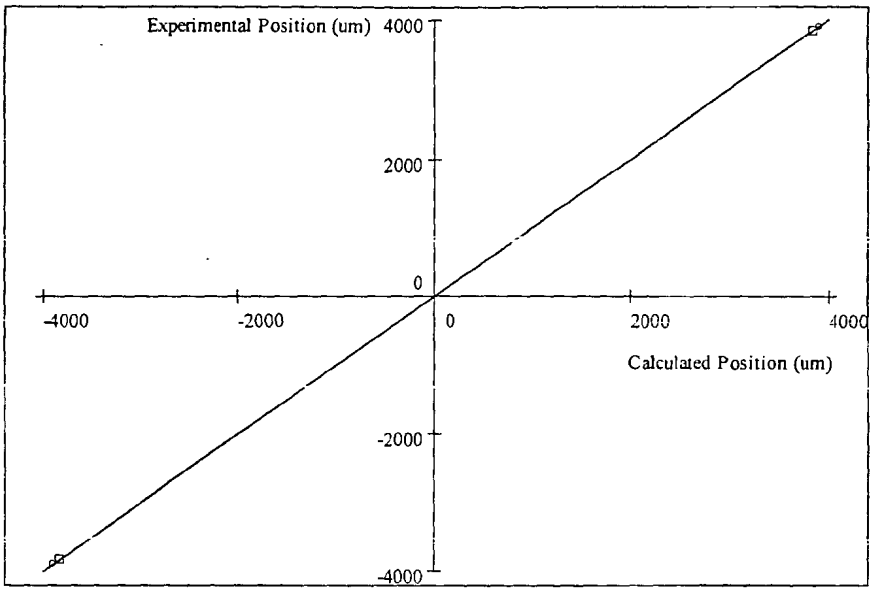

Figure 4.12. Plot of position measurement in presence of disturbing pulsed illumination

As observed in the plot, the calculated and experimental data coincide well with each other. The maximum difference in these data points is 20 μm in the maximum scale of 8000 μm. This puts the maximum error encountered in this experiment at about 0.25% of full scale reading. . The percentage experimental error has been plotted in Figures 4.12 and 4.13 for both data sets.

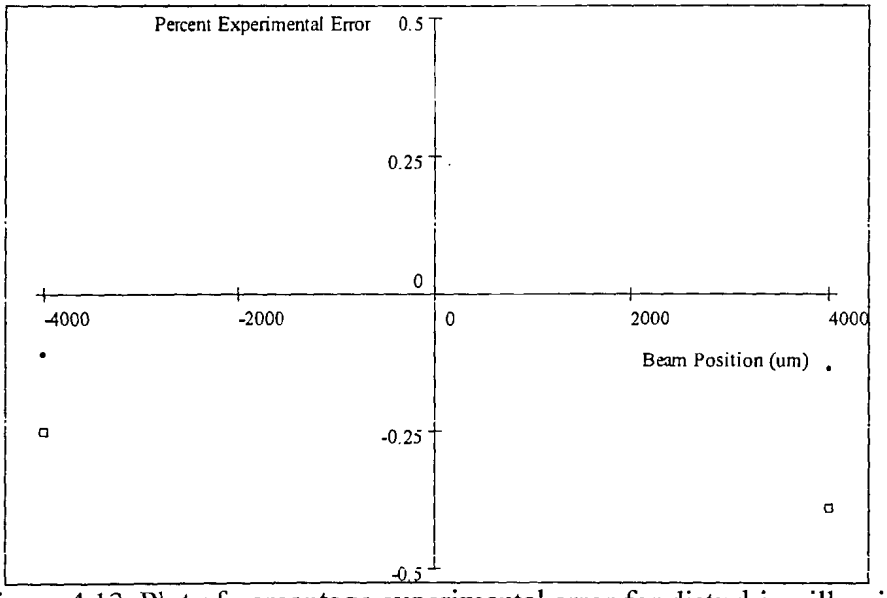

Figure 4.13. Plot of percentage experimental error for disturbing illumination

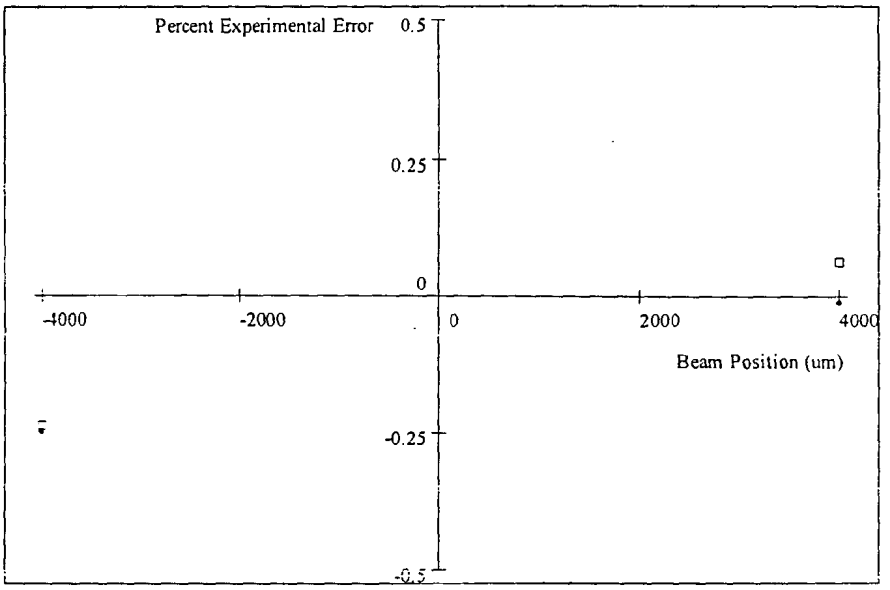

Figure 4.14. Plot of percentage experimental error for disturbing pulsed illumination

4.7 Systematic Errors

Brief analysis of systematic errors encountered in the experimental data obtained is being presented in this section. First systematic error in the obtained data is obvious while looking at the curves of data presented first. As we see, the data for the positive beam positions has a negative discrepancy from the calculated outcome and that for the negative beam positions has a positive discrepancy from the calculated outcome. We can say that for both the data the discrepancy is toward the center of the PSD. This is mainly due to the ambient light, which is taken centered at the PSD middle. Although the ambient light was reduced in the beginning to be less than 1.0 μW, this is still about 0.1% of the total intensity of approx 1.0 mW, or about 1.0% of the noise beam intensity in 10% noise experiment. According to the same superposition law, for the noise beam to be at the end, this amounts to a shift of about 40.0 μm in the noise beam, or amounts to a shift of about 4.0 μm (0.05% of FSR) in the net position output. This is of course coupled with other systematic errors and measurement errors. The error in the broad illumination noise experiments is probably not readily distinguishable in this category, due to the reasons described later.

Next major systematic error is introduced by the physical construction of the detector head. Although we have assumed that the broad illuminations effect is modeled to be centered at the middle of PSD, which should be the case even if the illuminations are coming from an angle to the normal. But in reality this is not the case due to the reflections from the glossy body of the detector assembly around the detection area becoming a shift in the illumination centroid, if the light is falling at an angle to the normal. This situation is shown in the figure for different incident angles. To investigate the effect of this shift, incident light centroid data was obtained for different incident angles of illuminations. The obtained curve is shown in Figure 4.16.

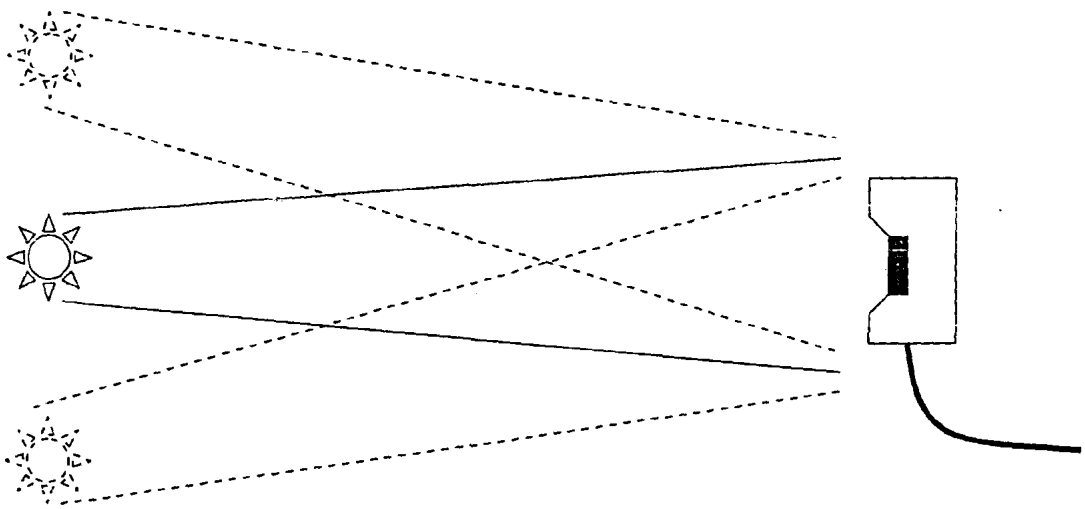

Figure 4.15. Effect of illumination incident angle on the PSD output

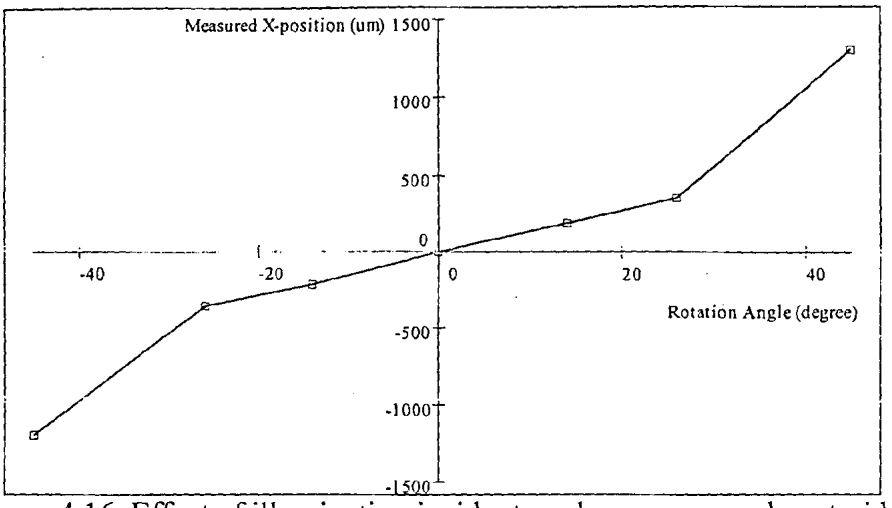

Figure 4.16. Effect of illumination incident angle on measured centroid

As observed from the plot, when we rotate PSD on its axis in front of the illumination source, the reflections from the front part of body shift the illumination centroid to that side of PSD and same happens in opposite direction of rotation. It may be noticed that the steeper increase in the centroid shift at the larger angles is due to the closer part of the body shadowing on a part of the PSD surface thus sharply shifting the centroid. It may be noted that a little negative (one-sided) bias found in the broad illumination noise experiments may well be due to this factor.

Another systematic error parameter investigated was that of y-axis displacement affecting the x-axis measurements from the PSD. For this purpose, x-axis position of the beam on PSD was maintained fixed, while it was scanned in y-axis direction from one end of the calibrated area to the other end. It was noticed that there was no explainable effect on the x-axis measurement with different y-axis displacements in this case. An overshoot in the measured value discrepancy is probably due to getting too close to the end of the calibrated area, where some non-linearity is expected. The results are shown in Figure 4.17.

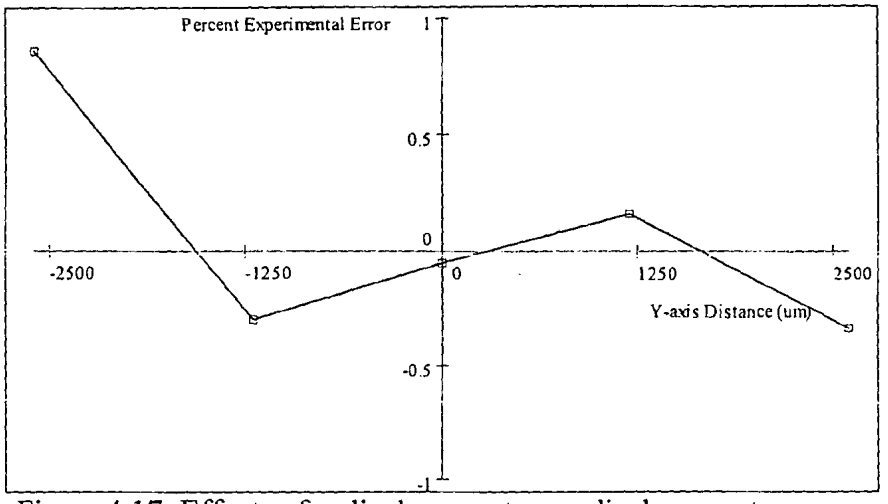

Figure 4.17. Effects of y-displacement on x-displacement measurement

4.8 Conclusions

Theory and analysis of stray beams and optical noises disturbing the position response of lateral-effect position-sensitive devices were presented in this chapter. It is found that the error introduced in the position measurement in presence of an interfering beam, or 'δP', is proportional to the distance between the centroids of both the beams and to the fraction of the noise intensity in the total. In case of a uniform or broad illumination, the same analysis applies while the centroid of the interfering illumination should be taken at the center of the PSD area. In case of scanning or pulsating lights, the produced effect should be decreased in proportion with the beam duty cycle. These results have been verified experimentally and the obtained data is within a fraction of a percent of the predicted calculations. There are other factors like the angle of illuminations which matter too. The study is expected to be very useful for the accurate & precise use of PSD-based sensors in the industries like production lines, workshops and others.

4.8.1 Related Publications

1. S. Iqbal, M. M. S. Gualini and K. Rashid, *Impact of Stray Illumination Noise on the Position Response of Position-Sensitive Devices*, Journal of Applied Sciences Vol 6-3 (2006), pp 682-687.
2. S. Iqbal, M. M. S. Gualini and K. Rashid, *Stray noises and illuminations disturbing the performance of position-sensitive devices*, SPIE Optics & Photonics, SanDiego, USA, 2005, Proceedings-5867, Paper-5.

Chapter # 5

Optical Metrology Components: Lasers

Tandem Beams Technique for Laser Welding of Galvanized Steel Sheets

5. Optical Metrology Components: Laser Beams Tandem Beams Technique for Laser Welding of Galvanized Steel Sheets

Laser welding of galvanized steel sheets in lap configuration is the challenging problem being investigated for more than two decades, originating due to the difference in the melting points of steel and zinc. Earlier solutions are either insufficient or too cumbersome to be realized in practice. Here a novel dual beams method to lap weld the galvanized steel sheets is being discussed, modeled and analyzed. This involves a pre-cursor beam and a higher-power actual beam, which are used in tandem while generated independently or otherwise split from the same source. The first beam cuts a slot, thus making an exit path for the zinc vapors, while the second beam welds as required. The paper also presents and discusses some experiments performed in laboratory using this method, along with the metallurgical analysis results from laboratory showing total absence of Zinc in the weld area.

5.1 Problem Introduction and Background

Zinc-coated steel sheets welding in lap configuration poses perhaps one of the most controversial problems. Solutions proposed in the last 27 years have not yet found an easy-to-apply realization to replace conventional spot welding which has its own shortcomings [76-82]. Advantages offered by laser welding [78,91,92] still justify quest for an efficient method. The ideal solution should firstly solve the technological problem of the residual Zinc vapors trapped in the weld joint [79,80] due to the lower boiling point of the Zinc (906°C) with respect to the melting point of Steel (1530°C). The solution should also be practical and economical enough to be installed on the production lines.

For laser welding of zinc-coated sheets in lap configuration, many techniques have been proposed to tackle the problem [76-82]. These techniques have tried from the multitude of facets to approach and solve this problem. Unfortunately due to the practicalities on the production line shop floors, few have been implemented in the real world industries. The most obvious of the methods proposed was perhaps the "prior removal of zinc coating". This method can obviously bring good results [78], but is cumbersome to implement. Also as a simpler solution, it has been tried to weld with "pulsed laser" and the results have been observed [79]. It has been noted that the weld quality is somewhat improved.

Hybrid laser beams have been used in the shape of "twin beam" or "hybrid beam" [83]. This method is of course more expensive but at the same time the system has shown impressive results. Probably a more well-known technique in this area is that of adding shims or "forced gap" between the sheets when welding in lap configuration. This method delivers very impressive results [76], but needs time-taking pre-arrangements.

The proposed method is of course an extension of the hybrid beam method involving a precursor beam. But the improvement may well be in the working principal of this method that a forced exit path is created for the zinc vapours, which is quite independent of the job geometry and many other parameters. This feature is non-existent in many of the proposed solutions.

5.2 Proposed Solution

We propose that the front beam of the tandem system shall cut a slot with a minimal kerf, while the second beam shall seam-weld, joining the two sides of the kerf, while the residual zinc evaporates through the slot ahead of it. We propose two similar hybrid solutions, one combining Nd:YAG and CO_2 lasers in tandem, the first for cutting, and the second for welding. Alternatively two beams of the same CO_2 laser source may also be used in tandem by the method, which is basically an integration of the "gap-method" proposed several years ago and the dual beam system introduced few years back [77,80,84,85,88,90].

The solution we propose is described in Figure 5.1 (top view) and Figure 5.2 (side view). A precursor laser beam cuts a slot of a few centimeters of length and a certain width in front of the keyhole. The slot will have two functions; the first is to remove the zinc coating, while the gas used in the cutting process will blow away the zinc vaporized in the cut, effectively eliminating it. We know that zinc coat removal produces the best welding results, but in our case the method is not cumbersome as in the methods previously proposed in literature. The second function of the slot is to provide a way out to the excess zinc vapors left after the cutting process. In fact the keyhole and the surrounding molten pool may exceed the dimensions of the laser beam cut width, thus involving some area where the zinc coating is still present. In this case, the slot will exhaust the zinc vapors before the rapid cooling down of the molten pool. An Nd:YAG laser beam may generate cuts with excellent kerf and surface quality, but CO_2 laser can also be used. Distance between the cutting and welding spots can be adjusted conveniently and accordingly to the 3D geometry of the component to be welded. Proper gas shielding and fumes removal can be handled quite easily.

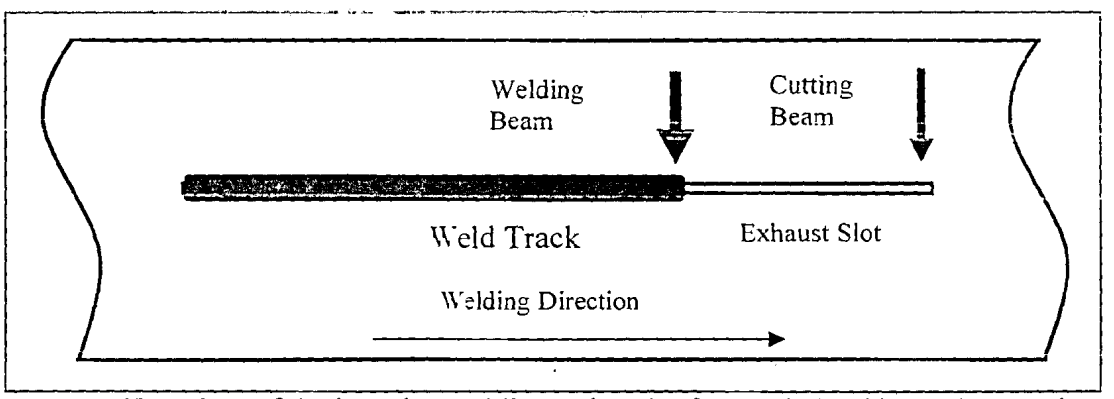

Figure 5.1. Top view of the laser lap welding using the forward slot (through both sheets)

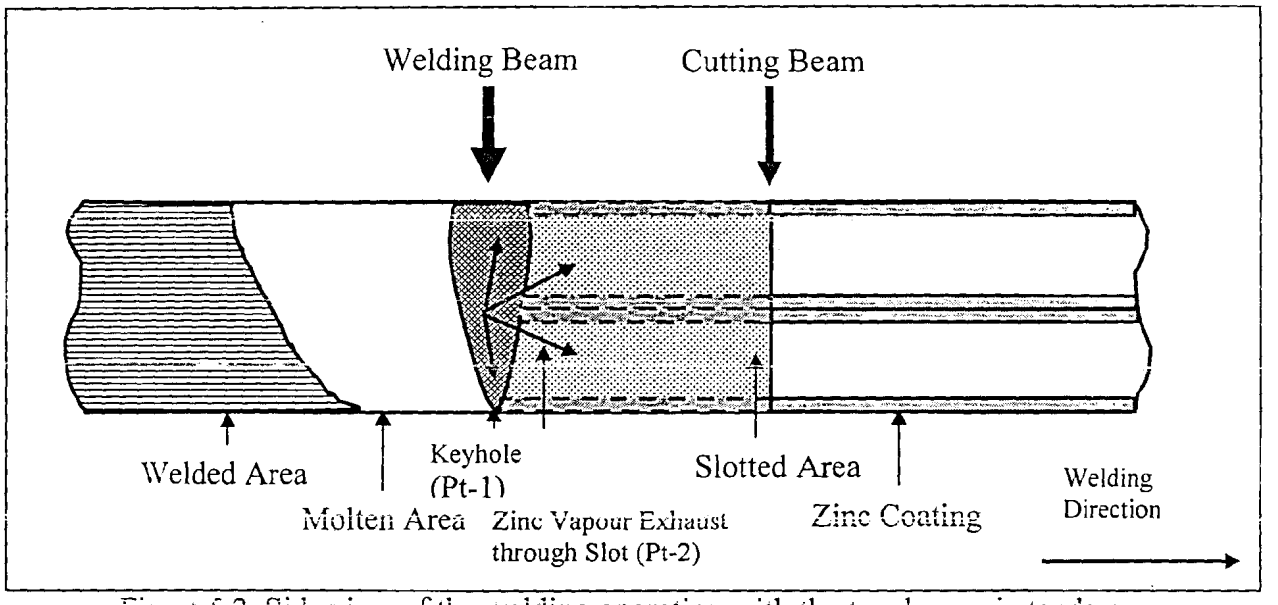

Figure 5.2. Side view of the welding operation with the two beams in tandem

The given figures show the simple view of the scheme of using the beams in tandem with the basic functions required by each of the laser, in order to give an idea of the degree of complexity of the hybrid laser welding/cutting nozzle. The CO_2 and/or Nd:YAG laser beams are sent to the work piece separately and the distance between the two can be pre-set or can otherwise be adjusted continuously by an adaptive CNC system to maximize the weld quality. The complete system may also include other modules like servomotors for the adjustment, nozzle assembly for beam delivery and the fiber optic cable supplying the laser beam to the nozzle.

5.2.1 Technical Discussion

The validity of the method has never been challenged [89], but has only been questioned once [86], fearing the high costs of utilizing two different laser sources or a higher power CO_2 laser source. The solution of combining an Nd:YAG laser to cut and a CO_2 laser to weld may be less appealing because of being more expensive. Thus, we also compare this solution with the alternative method of using an HPDL [83] along with others. The study shows the work conducted on this concept at the laboratories of Convergent-Prima in Collegno (Turin),

Italy. After recalling the theoretical model adopted, we present the experimental results and discuss our guideline for the future work.

The results obtained utilizing only the standard equipment, and not the dedicated optics or custom assemblies, definitely confirm the principle and also largely fit the behavior predicted by preliminary theoretical model. We expect that the method proposed originally by us offers a better compromise to be implemented on production line than any other method proposed until today. In our opinion the alternate method of delaying the solidification of the keyhole suffers the problem of strict control of the procedure parameters. The time window to enable the perfect solidification of the keyhole without residual Zinc is quite narrow, and is not easily controllable as the cutting of a slot, which depends more on design parameters, rather than material specifications. In fact the tolerances in the chemical composition of galvanized sheets may influence its thermal properties, resulting in a lesser quality of the weld, along with other factors like the difficulty to control the heat effects. Controlling the kerf width is quite an acquired procedure after more than 30 years of laser material processing. The kerf width is quite easily measurable utilizing any optical method available today, while measuring heat may prove more expensive and lesser accurate. We should also consider that welds on a flat material are quite easy to obtain, but the reality of a 3D application is quite challenging to be met.

As already explained, the proposed solution combines the advantages of the gap method and coating removal, which are more cumbersome and expensive than the method proposed here. Main advantages of the proposed method are those that are obtained by gap techniques, but without gap between the sheets. The proposed method is not cumbersome, a good alignment between beam and kerf and <0.1mm kerf width appears to be the only critical parameters. Secondly, the proposed method is not constrained by the actual geometry of the components to be joined. Looking at the approach, we expect the method to be relatively economical since it does not require any extra fixture and additional man-hours for pre-processing, which are quite expensive. Apparent disadvantage of the method proposed is the higher investment and the running cost of the equipment due to the use of two lasers.

5.3 Theoretical Analysis

5.3.1 Mathematical Model

Here we recall and enhance the previously reported theory [83,84,85]. In order to develop a simple but effective mathematical model we have considered the work done on the gap method [76]. The approximations introduced enable us to obtain some quantitative measures. We refer to Figure 5.3 and Figure 5.4 in order to derive some theoretical understanding and write the model in view of the given conditions. The model of references is based on the considerations that the Ferro static head on top of the weld pool generates a pressure that stops the zinc vapors from getting into the keyhole (pt-1), which are being exhausted by the cut slot providing an artificial gap (pt-2).

$$\Delta P_{12} = \rho_{Fe} g_e t_p a \tag{5-1}$$

Here 'ρ_{Fe}' is the density in kg/m^3, 'a' is the wave factor normalized to 1, 'g_e' is acceleration due to gravity in m/s^2 and 't_p' is the thickness of the steel plate. The Ferro static pressure generates a velocity of the zinc vapors at the ejection point. The exhaust velocity 'v_2' of the zinc vapors is calculated using Bernoulli's theorem as:

$$\frac{P_1}{\rho_v} = \frac{P_2}{\rho_v} + \frac{v_2^{\,2}}{2} \tag{5-2a}$$

$$v_2 = \sqrt{\frac{2\Delta P_{12}}{\rho_v}} \tag{5-2b}$$

Here ρ_v is the zinc vapor density, which can be calculated using Clausius-Clapeyron equation to be 21.87 kg/m^3 [85].

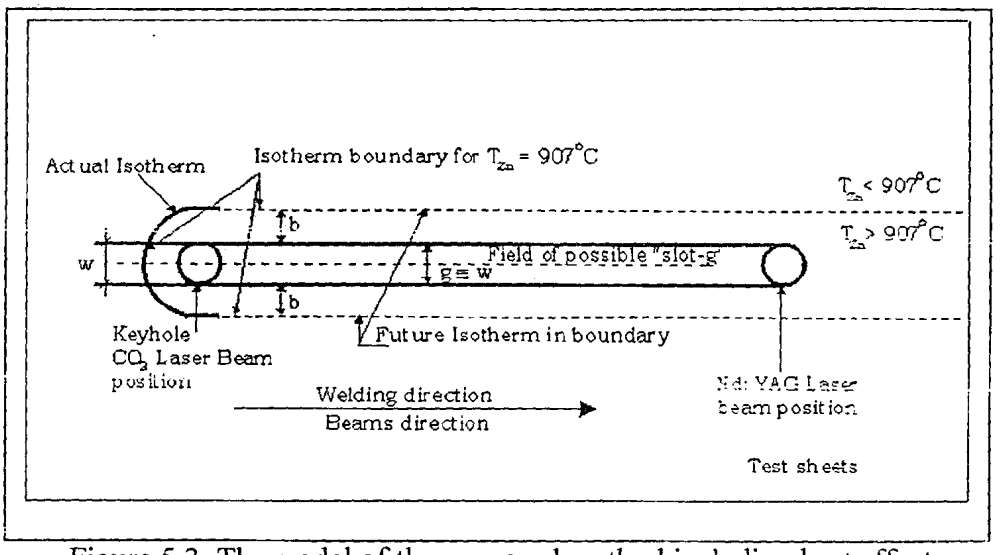

Figure 5.3. The model of the proposed method including heat effects

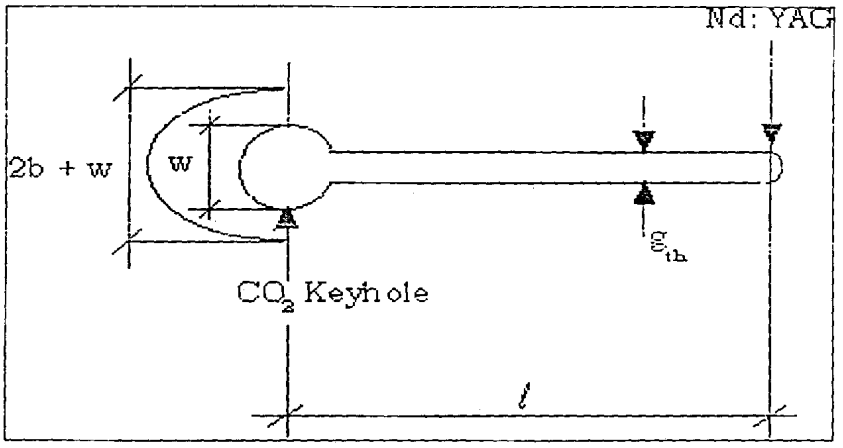

Figure 5.4. The cut and weld model showing slot and keyhole sizes

The next equations express the volume of the gases generated by the welding action and the volumes of gases that can be exhausted through the gap. It may be noted that the slot is cut by the advanced beam and the keyhole follows it at some distance. Thus, there is going to be a slot present on the sheet, even in the to-be-molten area where keyhole is being formed, having zinc on both sides of the slot. Thus the zinc would be vaporized first. The assumption is that the width of the gap is much larger than the thickness of the galvanization layer on the sheet, i.e. $g >> t_{zn}$:

$$Vol_{gen} = \frac{2t_{Zn}V\rho_s((w-g)+2b)}{\rho_v} \tag{5-3}$$

$$Vol_{exh} = 4v_2 t_{Zn} w \tag{5-4}$$

where 'b' is the width of zinc boiling isotherm out of the welding beam (HAZ), 't_{Zn}' is the thickness of the zinc layer, 'V' is the welding speed, 'ρ_s' is the solid zinc density (7140 kg/m^3), 'w' is the keyhole width and 'g' is the width of the slot. Equating both of these, we get to the needed minimum value of slot width as:

$$g = \frac{V\rho_s(w+2b)-2w\rho_v v_2}{V\rho_s} \tag{5-5}$$

while the unknown quantity 'v2' can be substituted by the earlier results of Bernoulli's theorem as:

$$g = \frac{V\rho_s(w+2b)-2w\sqrt{2\rho_v\rho_{Fe}g_e t_p}}{V\rho_s} \tag{5-6}$$

Here we are interested in finding the optimal value of slot width 'g' whose minimum value is given by this equation with the condition that all the zinc vapours will be exhausted by the slot and nothing will go inside the melt pool. The given minimum width can be decreased further if partial zinc vapour exhaust is allowed through the molten metal, i.e. some porosity is tolerable. The upper limit to this slot is posed practically by the situation that 'g' should be substantially lower than 'w' in order to allow for a proper strong weld in the presence of kerf. The value of 'g' in SI system is given as:

$$g = \frac{7140V(w+2b)-2w\sqrt{3373491t_p}}{7140V} \tag{5-7}$$

5.3.2 Simulation Results

The variation in minimum needed gap width against the changes in welding speed are plotted in Figure 5.5 for some representative values as w = 0.5mm, b = 0.1mm and t_p = 1mm. Note that the minimum gap values for very low speeds are less constrained and are largely governed by the same condition of g >> t_{zn}.

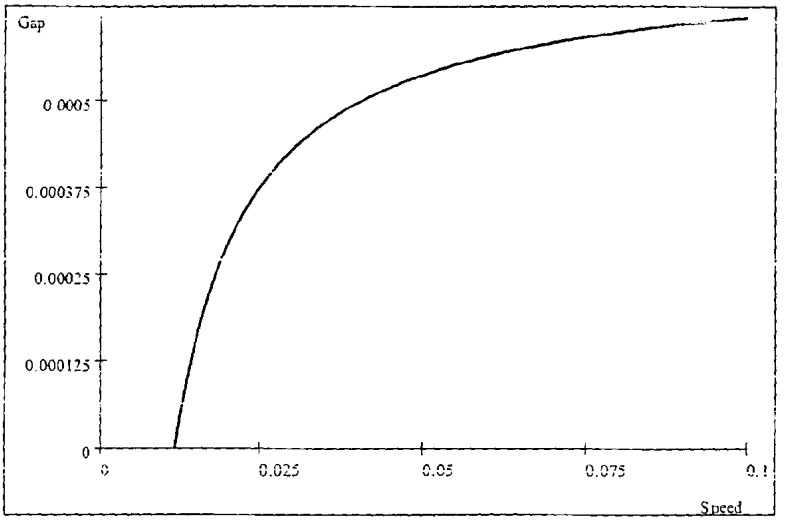

Figure 5.5. Slot width plotted against the welding speed

We are only interested in solutions with the condition w > g, which are basically given by the speed values on the left side of the above plot. The right part of the graph is for higher speed welding where the values computed for 'g' by this model become unrealizable for the given condition.

We can also analyze that how the minimum gap requirements change with the changing values of welding beam width 'w' and with the variations of steel plate thickness as shown in Figure 5.6 and Figure 5.7. In the first curve, welding beam width is varied between 0.4 - 0.6 mm, and in the second curve steel plate thickness is changed in the range of 1.0 – 1.4 mm with the darker color showing the increasing values of both the parameters.

It may be inferred that for the variations in welding beam width, there seems to be a point close to the maximum realizable gap width where the gap values are common for the

different beam widths. For the variations in the steel plate thickness, it is clear that for same target welding speed, the increased thickness of the steel plate requires lesser value of the gap width. This may look surprising at the beginning, but can be understood better considering that a larger steel plate thickness is not going to affect the amount of zinc evaporating but will give more value of ferro static head, thus forcing the zinc vapors to exhaust through the narrower gap. Thus the higher thicknesses are not a problem in this approach, until the values become prohibitive due to the higher laser welding power needs. The surface graph showing the values of the gap obtained with different welding speeds and beam widths is given in Figure 5.8.

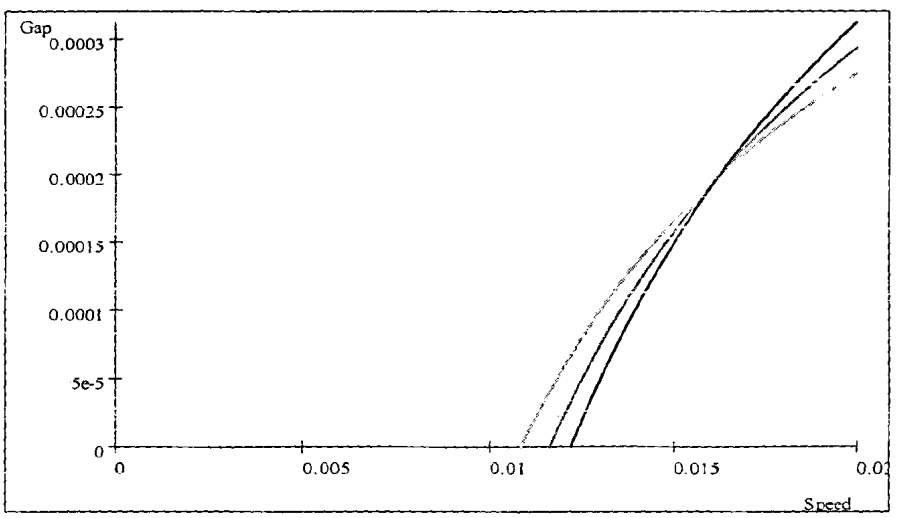

Figure 5.6. Changes in the minimum gap width with change in beam width

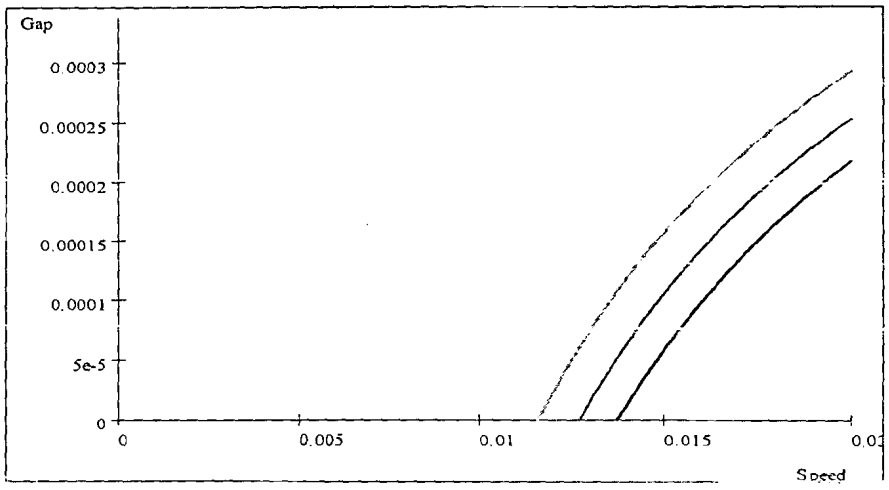

Figure 5.7. Changes in minimum gap width with changes in steel plate thickness

As the surface graph indicates, the realizable value of cut-slot width is again obtained with the lower values of welding speed, which is the back part of the graph. At the same time the variation of slot width with the welding beam diameter is pretty straight at higher speeds, and is clearly unrealizable in the front-right part of the graph. This is the situation when the speed is too high and wider welding beam is producing more zinc vapours demanding wider but unrealizable slot width. Thus the results of the model analysis are also fairly understandable by logic and intuition.

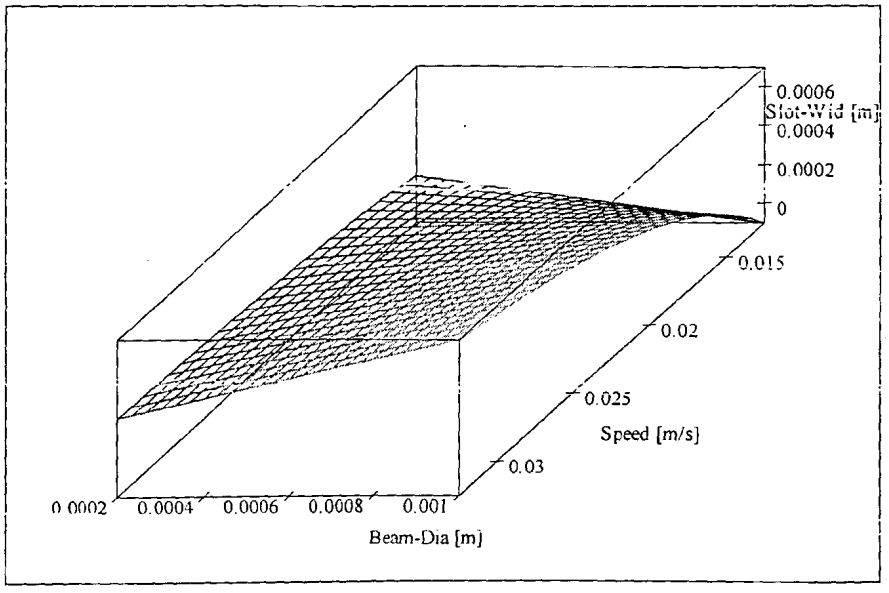

Figure 5.8. Slot width shown in surface graphics against welding speed and beam diameter

A point to ponder is probably the span of the surface graph in the rear part where the gap requirement is increasing with the decreasing beam dia. This can also be understood remembering that the smaller beam dia is also coupled with smaller exit orifice and causes problem as the heat-effected zone width 'b' is taken to be a constant present in all the cases.

5.4 Experimental results

5.4.1 Experimental Setup

The team working on this research project got some experiments conducted with this novel technique in Turin, Italy. First a test was conducted with a PRC3000 laser with M^2=3.28 and a "raw beam diameter" on the lens of about 24mm ($1/e^2$) at about 9m from the laser source (the system used is a RAPIDO (Convergent Prima). The focused beam is 0.234mm, while the Rayleigh's distance is 1.24mm. The "far field" divergence of the focused beam is 0.0945 rad (12/127). The minimal cutting kerf obtained on the double thickness of the galvanized sheets (1.6mm) is 0.15mm, even at full cutting speed. The cutting kerf is about 36% smaller than the cutting beam spot due to the mode structure of the beam. The power density @ 2500W is 5.8 $x10^{10}$ W/m^2. The focal point has been positioned on the top surface. The obtained cutting kerf is quite large (> 0.1mm) thus leading to a "weaker" weld. In fact even shifting the focal point to 3mm below the top surface means that the laser beam diameter for welding is 0.6mm, (eq to 0.88 $x10^{10}$ W/m^2), rendering it largely useless because the central part of the beam (maximum intensity), is all lost through the kerf. Without defocusing, the entire beam would be lost through the kerf. Cutting and welding have been performed with only one gas N_2, in order to save time.

Under the above conditions, it was noticed that the weld obtained is smooth and does not show "bubbles" on its surface. In the absence of proper tooling we have offset of 0.2mm across the weld path, on the right side, with the beam at 1.5 mm out of focal point. The beam size and its power intensity are such that a good keyhole only takes place if the beam

diameter covers both the kerf edges in the weld. The result was quite encouraging: we obtained an acceptable quality weld without significant defects on the surface. Obviously the weld is under-dross; in other words the upper surface is concave in the bottom direction, rather than being convex as desired. This is due to the poor contribution of material owing to a 0.15mm cutting kerf. Incidentally this is in harmony with the findings derived from the above theoretical model. From our findings it is quite evident that the kerf should be smaller. At the same time we know that the kerf cannot be made so small that it may restrict the welding speed too much.

Next the test was repeated with a Convergent Prima System 2D PLATINO with a DC25 Rofin Laser and a 5" lens. Contrary to the 3D RAPIDO, the PLATINO is a more versatile machine because it enables to move the focal point of the laser beam utilizing the CNC so that the stand-off of the tip to the galvanized sheet and the position of the laser beam relative to the material are quite independent. In both the cases of RAPIDO and PLATINO, the tip of 2mm was used for cutting and that of 3-4mm was used for welding. The kerf width obtained with the PLATINO is about 0.1mm, not lesser as desired, because the raw beam diameter on the lens is smaller (22mm) in this case of Rofin DC25, and this partially cancels the benefit of the better M^2 of the DC25. The weld speed observed was 3300 mm/min at a power of 2500W of the source.

We can also utilize a laser welding beam of elliptical cross section, by proper optical beam shaping. Figures 5.9 and 5.10 show an alternative solution to beam shaping, which is basically to use a lens with a double convex shape so that the laser beam can be doubled and the two parallel beams are focused on the same plane. In this way we will generate a double keyhole without loosing energy at the middle of the kerf. Having started with a wider kerf offers the study of the "worst case" so that by reducing the kerf width one can monitor the improvements.

5.4.2 Welding Results

Figure 5.11 shows a sheet with different welds. It can be noticed that the center part of welds 1, 2, 3, 4, 5, 9, 11 shows quite interesting results where the kerf width is ~0.15mm. Figure 5.12 shows welds 7 and 8, which are not in perfect condition due to the deformation originated by positioning of the beam on the top surface of the galvanized sheets. In this case we would speak of "Akhter/Steen effect" because the deformation somehow combines the "vertical gap" with our solution. Figure 5.13 shows the hardness profile across the welds 7 and 8. The polished sample of Figure 5.12, in etched condition was subjected to stereo metallurgical microscopy to investigate the structural characteristics of the welded as well as of the base material. Figure 5.14 shows a x400 magnification of the base material while Figure 5.15 shows a micrograph of the weld 7 region from top view and Figure 5.16 shows its cross section (x50 magnification). Figure 5.17 is micrograph of the cross section of weld 7, with an open cavity on the top. Figure 5.18 is a micrograph of weld 7 cross section structure (x400 magnification). The welds were subjected to SEM EDS analysis in order to investigate the residual Zinc contents in the welded region. Results obtained from the analysis verified the absence of Zinc contents in the weld region. Further investigations with various parameter changes are underway.

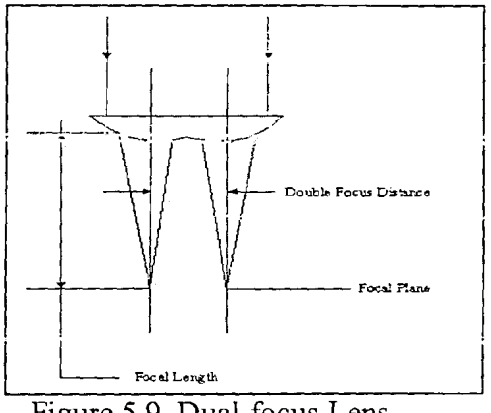

Figure 5.9. Dual-focus Lens

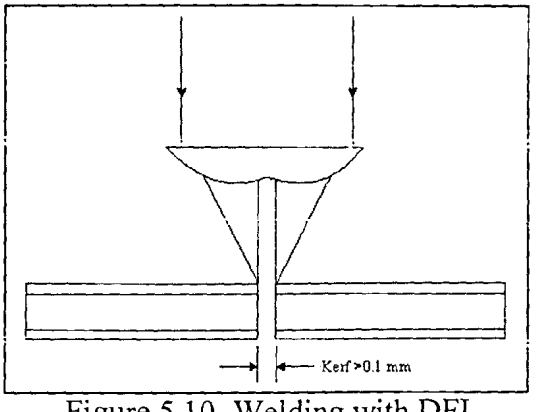

Figure 5.10. Welding with DFL

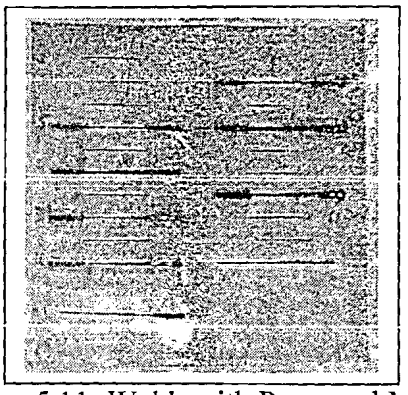

Figure 5.11. Welds with Proposed Method

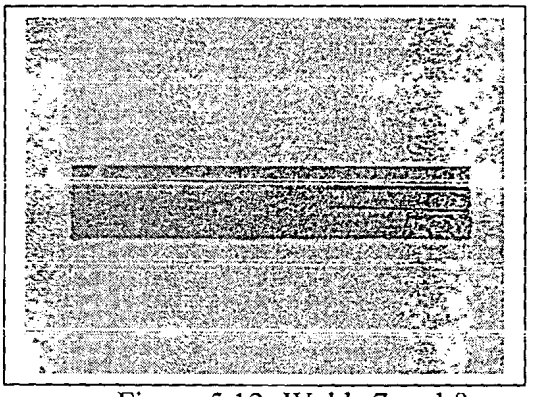

Figure 5.12. Welds 7 and 8

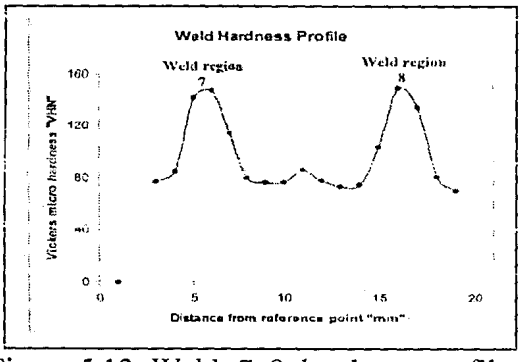

Figure 5.13. Welds 7, 8, hardness profile

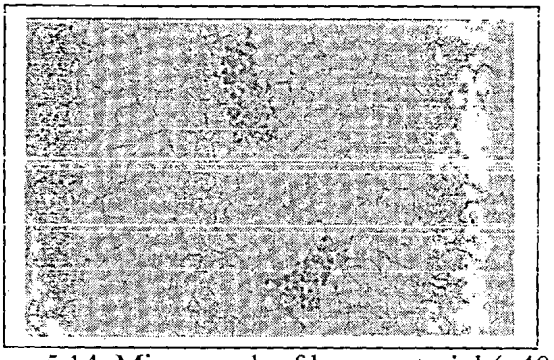

Figure 5.14. Micrograph of base material (x400)

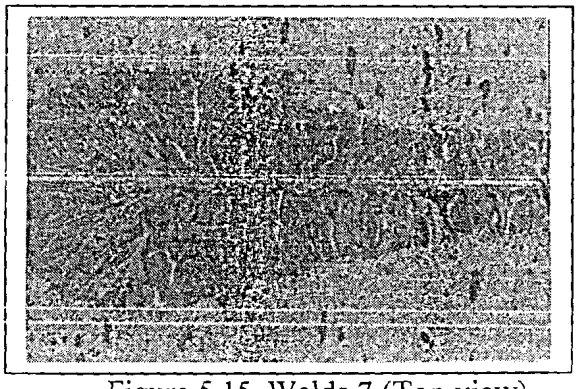

Figure 5.15. Welds 7 (Top view)

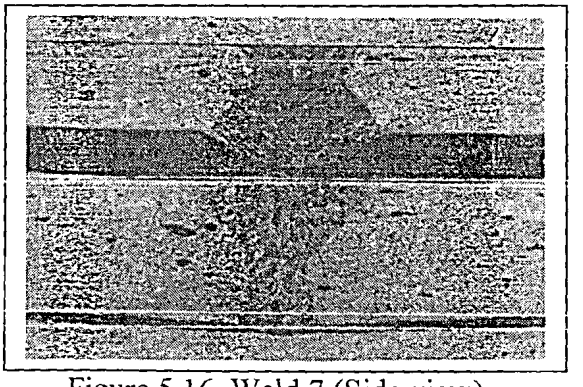

Figure 5.16. Weld 7 (Side view)

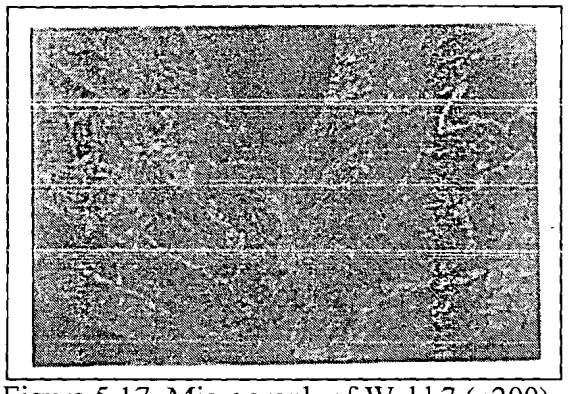

Figure 5.17. Micrograph of Weld 7 (x200)

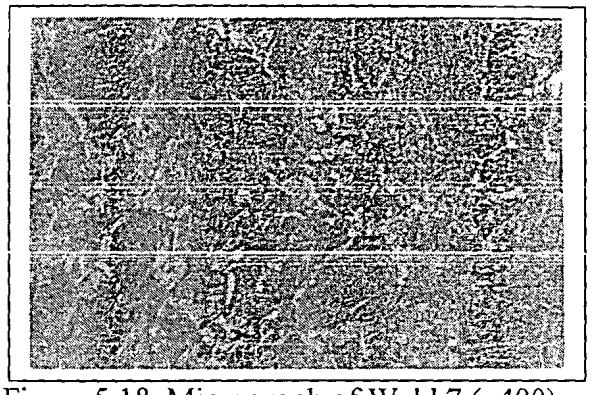

Figure 5.18. Micrograph of Weld 7 (x400)

5.5 Comparison with Other Techniques

In the past years, many techniques have been proposed to tackle the problem of laser welding of the galvanized steel in lap configuration (76-82,87]. These techniques have been proposed from a multitude of angles to approach and solve this problem. Unfortunately due to the practicalities on the production line shop floors, not many are common in the real world industries. Here a brief summary of the general analysis of our system in comparison with some of the well-known methods is given.

The most obvious of the methods proposed was perhaps the "prior removal of zinc coating". This method can yield good results, but is cumbersome to implement on the floor and is thus not practical. As another simpler solution, it has been tried to do welding with "pulsed laser" and the results have been observed. It has been noted that the weld quality is improved but still the improvement is not up to the mark and that the method ends up to be too restrictive for the involved process parameters [78,79].

Hybrid laser beams have been used in the shape of "twin beam" or "hybrid beam" [83]. This method is of course more expensive with the use of either two sources or a splitting from the higher power source is used. At the same time the system has shown impressive

results while the improvement varying with different configurations. One limitation may well be its applications with different types of geometry and shape contours of the processed job. Another may well be the difference in the material properties with the involved changes in the cooling time for the keyhole. Our proposed method is of course an extension of the hybrid beam method involving a precursor beam. The improvement may well be in the working principal of this method that a forced exit path is created for the zinc vapours, which is quite independent of the job geometry and many other parameters. This feature is non-existent in many of the proposed solutions.

Probably a more well-known technique in this area is that of adding shims or "forced gap" between the sheets when welding in lap configuration. This method delivers very impressive results with the absence of porosity in the welds [76]. But it does need time-taking pre-arrangements and becomes cumbersome on the floors due to the throughput requirements and practicalities [78].

As a comparison with this more discussed technique, the value of 'g' from our model as given earlier is compared with this gap model giving the value of minimum gap as:

$$g = \frac{16.1 V t_{zn}}{\sqrt{t_p}} \tag{5-8}$$

For the purpose of analytical comparison considering the needed gap only, which is slot gap in our case and plates gap in their case, and disregarding other parameters and practicalities mentioned above, the values of minimum or allowable gaps for both of these models are compared. This comparison is now made with the varying values of involved parameters like welding velocity etc. Our gap value is shown in solid line and the sheet gap as dashed line in Figures 5.19, 5.20 and 5.21.

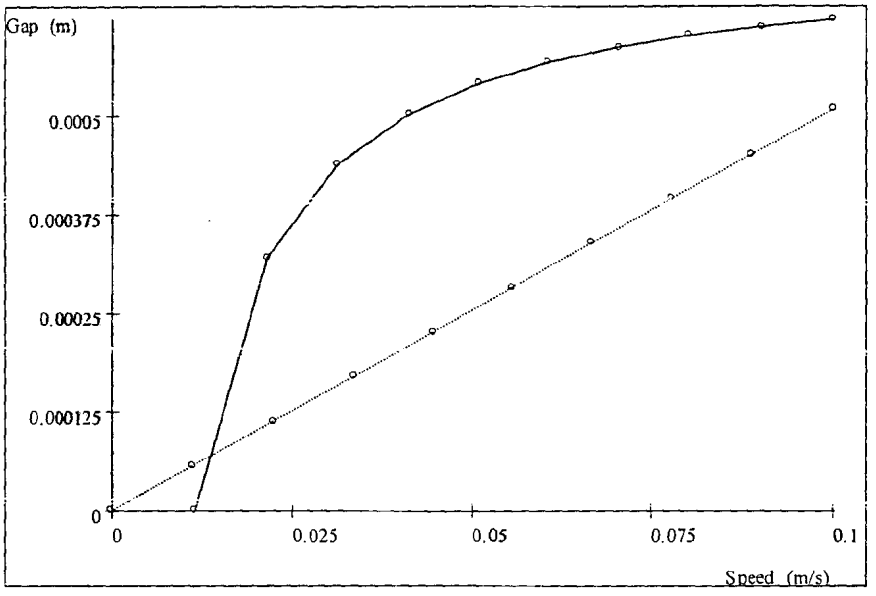

Figure 5.19. Minimum slot width plotted against welding speed for both models

Lower gap requirement between the plates in the sheet-gap model for the higher speeds is understood if it is kept in mind that exhaust in this case in multi-directional while in our case it has to go up or down into the cut slot. But in higher plate-thickness case our lower gap requirement seems to be coming from the fact that part of the zinc coating has been taken care by the cutting beam, which is non-existent in the other technique. Additionally, the sheet gap seems quite unaffected by the variation of beam diameter as the bigger beam also gives bigger beam circumference for exhaust too.

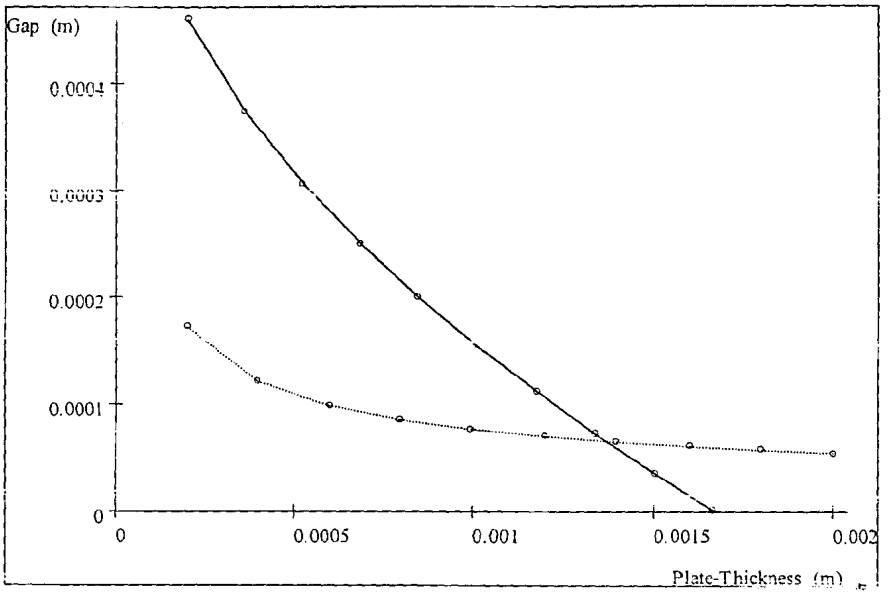

Figure 5.20. Minimum slot width plotted against thickness of plate for both models

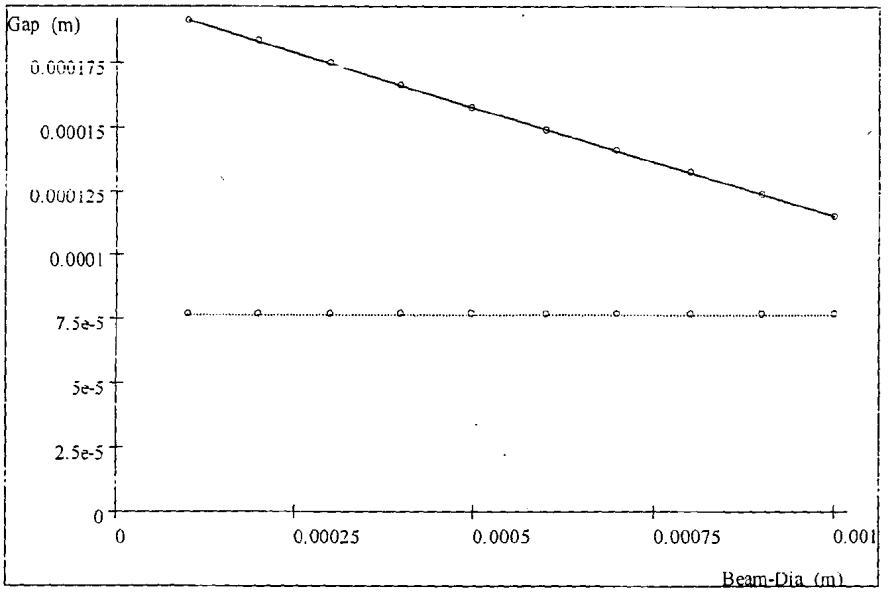

Figure 5.21. Minimum slot width plotted against beam diameter for both models

The major strength of our method comes in the ease and straightforwardness of the process and in decrease of the time required for the complete welding process and thus in the net saving of resources and capital, which can be demonstrated by the following straight forward relations:

$$\text{Time (dual beam method)} = \text{time}_{\text{clamping}} + \text{time}_{\text{welding}} \quad (5\text{-}9)$$

$$\text{Time (sheet gap method)} = \text{time}_{\text{shim-placement}} + \text{time}_{\text{clamping}} + \text{time}_{\text{welding}} \quad (5\text{-}10)$$

Therefore the proposed solution making the manufacturers independent of the zinc coatings and he may proceed as in case of normal welding while needing lesser time. Thus for all possible jobs and geometries, it may be concluded that

$$\text{Time (dual beam method)} < \text{Time (sheet gap methods)} \quad (5\text{-}11)$$

5.6 Conclusions

In this chapter a novel tandem-beams method for lap welding of galvanized steel sheets has been presented and analyzed In the theoretical part, the model of the method has been developed and simulated. In the experimental part we have utilized a basic setup and worked with actual specimens. Practical results have been obtained and the material analysis has been performed. In spite of the limitations, we have found that the cut slot favors the dispersion of Zinc vapor, and total absence of zinc content has been verified in some of laboratory results. It is concluded that the principle stands demonstrated. Further work on this technique may yield more refinements in the future. Following may be the conclusions.

1. Use of a precursor cutting beam ahead of the actual welding beam offers a promising practical solution for the welding of galvanized steel sheets in lap configuration.
2. The solution is expected to be easier for implementation on the production lines as it should not need any pre-processing or pre-arranging with additional components.
3. The solution may get rid of all the zinc vapour porosity at the lower speeds and partial of the porosity at the higher speeds.
4. The experimental results are very promising showing total absence of zinc in the welds.

5. Selection of proper source, beam alignment (between weld and cut) and proper sheet clamping are important for this method in order to avoid misalignment between weld and the kerf.
6. For even better results, a shaping optic for the welding beam may be incorporated so that its cross section is elliptical or, alternatively, a dual focus lens system may be used.

5.6.1 Related Publications

1. S. Iqbal, M. M. S. Gualini, and F. Grassi, *Laser Welding of Zinc-Coated Steel with Tandem Beams: Analysis and Comparison*, Journal of Material Processing Technology 184 (2007) pp 12-18.
2. M. M. S. Gualini, S. Iqbal and F. Grassi, *Modified dual-beam method for welding galvanized steel sheets in lap configuration*, Journal of Laser Applications Vol 18-3 (2006), pp185-191.

Chapter # 6

Summary

6. Summary

6.1 Contents in Brief

This thesis presents and analyzes laser-based optical metrology systems using position-sensitive detectors. For this purpose, a new diffraction strain measurement technique is developed, analyzed and characterized. Some research work on optical metrology components is also included, dealing with position-sensitive detectors and laser-beams.

Chapter-1 gives an introduction to optical metrology and position-sensitive detectors. In optical metrology, different properties of light or electro-magnetic waves are utilized one way or other including interference, diffraction, speckle and polarization. The properties of lasers make them very attractive for a number of metrology applications including interferometry. Semiconductor position-sensitive detectors (PSDs) offer very good solutions for position measurement applications and have become a major tool for such applications. These detectors can be of different types, which are suitable for different applications. Along with other measurement applications of optical systems, strain measurement is very important one. A number of optical techniques are routinely used for this and among these diffraction methods provide strain information directly and possess several other advantages.

In Chapter-2 a Multipoint Diffraction Strain Sensor using normal un-collimated laser beams and multichannel imaging PSD is developed and characterized with the novel feature of simultaneous strain measurement at multiple points. Unlike conventional interferometry based systems, this sensor uses principles of diffraction to measure strain at large number of points. In this sensor, a high-frequency diffraction grating is illuminated by two symmetric but divergent laser beams and the diffracted beams are sampled on a CCD camera via a micro-lens array into an array of dots. The shift of the individual dots is sensed and strains or rigid body tilt are calculated directly. This novel technique is expected to be very valuable in

numerous industrial applications. When compared with other whole-field optical strain measurement techniques like Moire Interferometry and ESPI, this technique has obvious advantages of direct approach along with a combination of good spatial resolution, sensitivity and accuracy.

In chapter-3 a new and improved system Multipoint Diffraction Strain and Tilt Sensor has been developed based on Moire Interferometer and Multichannel imaging PSD. Traditional diffraction strain sensors measure single point strain only, while the developed system has the unique feature of simultaneous optical strain and tilt measurement at a large array of points. The system uses simultaneous position tracking of smaller beamlets diffracted differently from the different points of the component under test. Using this setup, whole-field strain and tilt distribution patterns over the component body can be obtained in near real time, without the need for fringe processing. Furthermore, the system also has capability of measuring rotation and shear strain, making this a truly versatile whole-field strain sensing system. Simultaneous strain and tilt measurement at more than one thousand points is being reported. Microcomputer-based implementation of this system is described. Detailed characterization and analysis of the developed system is presented along with some important development decisions. The system offers a promising combination of features like direct and near-real-time calculation of whole-field strain along with tilt and rotation. These make this technique very much promising for precision applications in mechanics and micro-mechanics.

Chapter-4 presents work on position-sensitive detectors (PSDs) analyzing their usage in noisy industrial environment, where several other light sources also coexist. These random illuminations produce unpredicted effects on PSD output. Here we first describe these stray noises with respect to the operation of PSDs. Then we study and model how the presence of the spurious sources modifies the response of these detectors. The experimental results obtained while using PSDs with signal beams and noise sources are presented. The experimental data is compared with the results from the proposed mathematical model and it is seen that measured performance is within a fraction of a percent of the calculated one. The

analysis of systematic errors encountered during data collection is also presented. The work is expected to be very useful while designing the industrial applications of PSDs.

Chapter-5 presents work on laser beams application and analyzes their use in material processing. Laser welding of galvanized steel sheets in lap configuration is the challenging problem addressed in this work. For this purpose, dual laser beams method to lap weld galvanized steel sheets is being discussed, modeled and analyzed, involving a pre-cursor beam and a higher-power welding beam. The first beam cuts a slot, thus making an exit path for the zinc vapours, while the second beam performs the needed welding. The work also presents some experiments performed on the shop floor using this method and the results obtained from the experiments, along with the metallurgical analysis results from laboratory showing successful absence of Zinc in the weld area.

6.2 Research Contributions

6.2.1 Novel Whole-field Technique for PSD-based Diffraction Strain & Tilt Sensor

A novel whole-field strain measurement technique is developed and implemented as Multipoint Diffraction Strain and Tilt Sensor using Moire Interferometer and Multichannel PSD. All the different variations of diffraction strain sensors as developed by different researchers up to date measure single point strain only, while the whole-field strain measurement techniques like Moire Interferometry and ESPI have their own shortcomings like lengthy fringe processing and image subtraction algorithms. On the other hand, the developed system has the unique feature of direct and near-real-time diffraction-based strain and tilt measurement at a large array of points on the sample surface. The system uses simultaneous position tracking of smaller beamlets diffracted differently from different regions of the component surface under test. Using this setup, whole-field strain and tilt distribution patterns over the component body can be obtained in near real time, without the need for fringe processing. Furthermore, the system also has capability of measuring rotation and shear strain, making it a truly versatile whole-field strain sensing system. Simultaneous

strain and tilt measurement at more than one thousand points is being reported. Complete microcomputer-based implementation of this system is described. Detailed characterization and analysis of the developed system is presented along with some important development decisions.

The obvious advantage of this multipoint diffraction method compared to others is its direct and near-real-time approach. The strain is calculated without the need of any fringe processing and numerical differentiation needed for interferometry. Image subtraction for speckle techniques is also not needed here. At the same time it can produce map with good spatial resolution compared to other methods and specifically to speckle technique. This resolution is only bounded by the separation of the micro-lenses on the array and is also not hampered at the lower strain values where farther apart fringes may degrade such resolution for fringe processing methods. The system results show good combination of sensitivity and accuracy considering other whole-field approaches and specifically compared to speckle method where measurement quality is largely hampered by the poorer fringe visibility. Being a simpler approach, the total computing and storage resources needed for this method are going to be lesser.

All these features make this technique suitable for precision applications in mechanics and micro-mechanics, while offering a considerable saving in time and equipment cost. Simultaneous strain measurement at more than a thousand points can be readily obtained and is demonstrated. This research is expected to open up a new avenue and provide a versatile tool for the industrial and structural applications, as a near-real-time 2-D map of strain on the component body may provide much clearer picture to the analysis team.

6.2.2 Analysis of Position-Sensitive Devices Response with Stray Illumination Noise

Applications of PSDs are diverse and widespread in the industry, including alignment, displacement sensing and as a part of other analysis instrumentation. In such environment, the system laser source co-exists with different nearby light sources, coherent or otherwise, along with their reflections and back-scatters from various nearby surfaces. Some of the

systems may involve scanning or rotating laser beams too, which may have enough energy to effect the PSD measurements in the form of periodic pulses.

A unique analysis of position-sensitive detectors while used in noisy industrial environment is presented, where several other light sources also coexist and produce unpredicted effects on PSD output. Many researchers of other normal photo-sensors have analyzed their performance in presence of these stray noises, while this problem has many times been outlined in context of PSDs too. Nonetheless, detailed performance analysis of PSDs with stray optical noises is very much needed. For this purpose, we first describe and model these stray noises with respect to the operation of PSDs and then analyze the response of these detectors in the presence of these spurious signals. The experimental results are presented, which were obtained using PSDs with signal beams and noise sources. The experimental data is compared with the results from the proposed mathematical model and it is observed that the measured performance is within a fraction of a percent of the calculated one. The analysis of systematic errors encountered during data collection is also presented. The study is expected to be very useful for the accurate & precise use of PSD-based sensors in the industrial units like production lines, workshops and others.

6.2.3 New Tandem Beams Technique for Laser Welding of Galvanized Steel Sheets

Laser welding of galvanized steel sheets in lap configuration is the challenging problem being investigated for more than two decades, originating due to the difference in the melting points of steel and zinc. Earlier solutions are either insufficient or too cumbersome to be realized in practice. For this purpose, a new tandem-beams technique is being discussed, modeled and analyzed, involving a pre-cursor beam and a higher-power welding beam. The first beam cuts a slot, thus making an exit path for the zinc vapours, while the second beam performs the needed welding. The work also presents some experiments performed on the shop floor using this method and the results obtained from the experiments, along with the metallurgical analysis results from laboratory showing successful absence of Zinc in the weld area. At the same time, this technique is expected to be very useful in workshop implementation and welding throughput.

6.3 Further Questions

The developed system Multipoint Diffraction Strain and Tilt Sensor opens up a new avenue for further developments in the area of diffraction-based whole-field analysis, which can be brought to the point of industrial implementations with the attractive and unprecedented features. Specifically important are the further experimentation with imaging sensors with different array dimensions, lenslet sizes and pixels sizes. This is going to experimentally establish the dependence of different strain sensor parameters on the imaging sensor characteristics. Also we may come to know what may be the parameter limits of the technique under consideration. Better algorithms for the spot centroid detection should be tried and the results to be compared with actual values. Detailed comparative study of this system with other whole-field techniques with diverse variety of samples can also be conducted.

In case of PSD performance with optical noises, similar analysis can be conducted with other types of PSDs too. A 2-dimentional analysis with a variety of noise sources and their orientations can be made with lateral-effect PSD as well as with others.

For tandem-beam laser welding technique, the approach is due to be tested with different test pieces and their complex geometrical shapes. The needed size of the cutting slot kerf is to be experimentally established at diverse values of speed and plate thickness. The collected results can be compared with other approaches suggested so far.

References

References

1. Photonics Spectra, *The Photonics Dictionary,* 39th Edition, 1993
2. CORD, *Lasers and Electro-Optics Tutorial, www.cord.org, 2001*
3. RP-Photonics, *Encyclopedia of Laser Physics and Technology, www.rp-photonics.com, 2006*
4. Gasvik K., *Optical Metrology,* John Wiley & Sons, 2002.
5. Ready J. F., *Industrial Applications of Lasers,* Academic Press, 1997
6. Hecht J., *The Laser Guidebook, McGraw Hill Inc. USA, 1992*
7. Donati S., *Electro-optical Instrumentation: Sensing and Measuring with Lasers, Prentice Hall, 2004.*
8. Charschan S. S., *Lasers in Industry,* Van Nostrand Reinhold Co, New York, 1972
9. Luxon J. T. and Parker D. E., *Industrial Lasers and Their Applications, Prentice Hall, New Jersey, USA, 1985.*
10. Silva Girao P. M. B., *An overview and a contribution to the optical measurement of linear displacement,* IEEE Sen. J. Vol 1-4, p. 322-331, 2001
11. On-Track Photonics, *OT-301 versatile position sensing amplifier*, Product data sheet
12. Melles Griot, *SpotOn optical beam position and power measurement system*, Product manual, 2002
13. Noorlag D. J. W. and Middelhoeck S., *Two-dimensional position-sensitive photodetector with high linearity made with standard IC-technology,* Sol. Stat. & Elec. Dev., Vol. 3(3), p. 57-82, 1979.
14. On-Track Photonics, *PSD Vs CCD, Application note*
15. Gottwald R., *Kern Space: An automated non-contact 3-D measuring system for industrial applications,* Proc. of 7th International Conference on Robot Vision and Sensory Controls Zurich, Switzerland, p. 3-12, 1988.
16. SiTek Electro Optics, *PSD user's manual – Position sensing detectors,* Sweden, 1996

17. Bose C. B. and Amir I., *Design of fiducials for accurate registration using machine vision,* IEE Trans. on Patt. Ana. and Mach. Int. Vol 12(12), p. 1196-1200, 1990.

18. Schaefer P. et al, *Accuracy of position detection using a position-sensitive detector,* IEEE Trans. Inst. Meas. Vol 47-4, p. 914-919, 1998.

19. Narayanan C. et al, *Noise analysis for position-sensitive detectors,* IEEE Trans. Inst. Meas. Vol 46-5, 1137-1144, 1997.

20. Wang W. and Busch-Vishniac I. J., *The linearity and sensitivity of lateral effect postion sensitive devices – an improved geometry,* IEEE Trans. Elec. Devices Vol 36-11, p. 2475-2480, 1989.

21. Fink D. and Christiansen D., *Electronics Engineers Handbook,* McGraw Hill.

22. – 25. Void

26. Asundi A. and Zhao B., *Optical strain sensor using position-sensitive detector and diffraction grating: error analysis,* Opt. Eng. Vol. 39-6, p. 1655-1651, 2000.

27. Zhao B. et al., *Optical strain sensor using median density grating foil: Rivaling the electric strain gauge,* Rev. Sci. Inst. Vol. 72-2, p. 1554-1558, 2001.

28. Bell J. F., *Determination of dynamic plastic strain through the use of diffraction gratings,* J. Appl. Phys. Vol. 27, p. 1109–1113, 1956.

29. Moulder J. C. and Cardenas-Garcia J. F., *Two-dimensional strain analysis using a video optical diffractometer,* Exp. Tech. Vol. 17, p. 11–16, 1993.

30. Sevenhuijsen P. J. et al: *Current trends in obtaining deformation data from grids,* Exp. Tech., p. 22–26, 1993.

31. Ma Y. and Kurita M., *Strain measurement using high-frequency diffraction grating,* JSME Int. J. A Vol. 36-3, p. 309–313, 1993.

32. Kozlowska A., *Fiber optic grating interferometer for in-plane displacement measurement,* Interferometry '94: Interferometric Fiber Sensing, E. Udd and R. P. Tatam, Eds., Proc. SPIE Vol. 2341, p. 124–131, 1994.

33. Chiang Y. J. et al, *Multipoint temperature-independent fiber-Bragg-grating strain-sensing system employing an optical-power-detection scheme,* Appl. Opt. Vol. 41, p. 1661-1667, 2002.

34. Cordero R. R. et al, *Whole-Field Analysis of Uniaxial Tensile Tests by Moiré Interferometry,* Opt Laser Eng, Vol. 43, pp. 919-936, 2005.

35. Nicoletto G., *On the visualization of heterogeneous plastic strains by Moiré interferometry,* Opt Laser Eng, Vol. 37, pp. 433-442, 2002.

36. Vial-Edwards C. et al, 2001 *Electronic Speckle Pattern Interferometry analysis of tensile tests of semihard copper sheets*, Exp Mech, Vol. 41, pp. 58-62, 2001.

37. Labbé F. et al, *Monitoring the plastic deformation progression of a specimen undergoing tensile deformation by moiré interferometry*, Meas Sci Technol, Vol. 16, pp. 1469-1476, 2005.

38. Post D., Han B. and Ifju P., *High sensitivity Moiré: experimental analysis for mechanics and materials*, Springer-Verlag, New York, 1994.

39. Palmer C. A. and Loewen E. G., *Diffraction Grating Handbook*, Thermo RGL, New York, 2000.

40. Harvey J. E. and Vernold, C. L., *Description of diffraction grating behavior in direction cosine space,* Appl. Opt. Vol. 37, p. 8158-8160, 1998

41. Asundi A. and Zhao B., *Optical grating diffraction method: From strain microscope to strain gauge,* Supp. to OPN Opt. & Phot. News Vol 10-11, p. 7167-7169, 1999

42. Siegman A. E., *An introduction to lasers and masers,* McGraw Hill Book Co., New York, USA, 1971.

43. Svelto O., *Principles of Lasers,* Plenum Press, New York, USA, 1982.

44. Helfrick A. D. and Cooper W. D., *Modern electronic instrumentation and measurement techniques,* Prentice Hall, USA, 1990.

45. Graf R. F., *Modern dictionary of electronics,* Radio Shack 1978.

46. – 50. Void

51. Makynen A., *Position-sensitive devices and sensor systems for optical tracking and displacement sensing applications*, Doctoral Dissertation, University of Oulu, Finland, 2000

52. Makynen A. et al., *Digital optical position-sensitive detector*, IEEE Inst. And Meas. Tech Conf., Como, Italy, pp. 2358-2360, 2004

53. Woltring J., *Single- and dual-axis lateral photodetectors of rectangular shape*, IEEE Trans. Electron Devices, vol ED-22, pp 581-586, 1975

54. Beraldin J.-A., Blais F. et al, *Optimized position sensors for flying-spot active triangulation system*, Proceedings of Fourth Inter. Conf. on 3-D Digital Imaging and Modeling, Banff, Canada, NRC47083, pp 334-341, 2003.

55. Bennett S. J. and Gates J. W. C., *The design of detector arrays for laser alignment systems*, J. Phys. E: Sci. Inst. Vol. 3, pp 65-68, 1970.

56. Toyoda M. et al, *Measurement of the characteristics of a quadrant avalanche photo-diode application to a laser tracking system*, Opt. Engg. Vol 41(01), pp 145-149, 2002.

57. Wallmark J. T., *A new semiconductor photocell using lateral photoeffect*, Proc. of the IRE – 45, p. 474-483, 1957.

58. UDT Instruments, *Non-contact position sensing using optical detectors*, Application note

59. UDT Sensors, *Non-contact optical position sensing using silicon photodetectors*, Application note 13, 1982

60. Makynen A. et al., *Positioning resolution of the position-sensitive detectors, in high background illumination*, IEEE Trans. Instrum. Meas., vol 45, pp 324-326, Feb 1996

61. Makynen A., Kostamovaara J., *Accuracy of lateral displacement sensing in atmospheric turbulence using a retroreflector and a position-sensitive detector*, Opt. Eng. 36(11), pp. 3119–3126, 1997.

62. Verdeyen J. T., *Laser Electronics*, Prentice Hall International, 1981

63. Kawasaki A. and Goto M., *On the position response of a position-sensitive detector (PSD) irradiated with multiple light beams*, Sensors and Actuators, vol A21-A23, pp 534-537, 1990

64. Qian D. et al., *A method for measurement of multiple light spot positions on one position-sensitive detectors (PSD)*, IEEE Trans. Instrum. Meas., vol 42, pp 14-18, Feb 1993

65. Hobbs P. C. D, *Building electro-optical systems, making it all work*, John Wiley & Sons Inc, 2000

66. Breault Research Organization, *Stray Light Analysis Tutorial*, Short Course, 2006.

67. Beraldin, J. A., *Active 3D sensing*, Sco. Norm. Sup. Pisa, Canada, 2000.

68. – 75. Void

76. Akhter R., Steen W. M. and Watkins K. G., *Welding Zinc-Coated Steel with a laser and the Properties of the Weldment*, J. Laser Appl., Vol. 3, No. 2, pp. 9-20, 1991.

77. Akhter R., Steen W. M. and Cruciani D., *Laser Welding of Zinc Coated Steel*, Proceedings of 6th International Conference on Lasers in Manufacturing (LIM6), Birmingham, U.K., pp. 93-104, 1989.

78. Naeem M. and Stolarczyk J., *High Power Nd:YAG Welding of Automotive Materials*, Proceedings of ICALEO2000, Dearborn, USA, pp. A20-A27, 2000.

79. Kielwasser M. et al, *Physical Process During Pulsed Laser and CW-CO_2 Laser Welding of Zinc Coated Steel*, Proceedings of ICALEO2000, Dearborn, USA, pp. A10-A19, 2000.

80. Deney P. and Xie J., *The Welding of Galvanized Steel*, Proceedings of ICALEO2000, Dearborn, USA, pp..A1-A9, 2000.

81. Goebel G. et al, *Laser Welding with Long Focal Length Optics*, Proceedings of ICALEO2000, Dearborn, USA, pp. A28-A37, 2000.

82. Dasgupta A., Mazumder J. and Bembenek M., *Alloying Based Laser Welding of Galvanized Steel*, Proceedings of ICALEO2000, Dearborn, USA, pp. A38-A45, 2000.

83. Bonss S., Brenner B. and Beyer E., *Innovations in laser hybrid technology*, Ind. Laser Sol., Jan2000, pp. 29-33, 2000.

84. Gualini M. M. S., *Laser Welding of Zinc Coated Steel Sheets: An Old Problem with a Possible Solution*, Proceedings of ICALEO2001, Jacksonville, USA, pp. 492, 2001.

85. Akhter R. and Gualini M. M. S., *Matehmatical Modeling of the Laser Spot Welding of Zinc Coated Steel in Lap Configuration*, Proceedings of ICALEO1998, San Diego, USA, pp. 207-216, 1998.

86. Poprawe R., *Personal Communications*, Fraunhofer Institute for Laser Technology.

87. Delle Piane A. D. et al, *Method of Laser Welding Sheet Metal Protected by Low-Vaporizing-Temperature Materials*, U.S. Patent 4682002, 1987.

88. Iqbal S., Gualini M. M. S. and Grassi F., *Laser welding of galvanized steel: analytical study in view of dual-beam solution,* ISAM2005, Islamabad, Pakistan, 2005.

89. Petring D., *Personal communication,* PICALO2006, Melbourne, Australia, 2006.

90. Gualini M. M. S. et al, *New considerations and experimental results on laser lap welding of zinc-coated steel sheets,* Proceedings of PICALO2006, Melbourne, Australia, 2006.

91. Ready J. F. and Farson D. F., *LIA handbook of laser material processing,* Laser Institute of America, 2001.

92. Steen W. M., *Laser Material Processing,* Springer-Verlag, 1991.

Appendix A

Lab Instrumentation

Appendix A: Lab Instrumentation

Compact Monochrome CCD Camera Reinforced for Mechanical Shock Tolerance

2600 SERIES — High Performance RS-170 or CCIR 1/2" On-Chip Microlens Sensor

The Cohu 2600 Series CCD camera has been designed specifically to withstand the extensive mechanical shock and vibration that is typically found when using oversized lenses, or in machine vision applications. It will serve equally well in surveillance applications under the same conditions, such as transit vehicles or high ambient noise locations.

The front casting of the 2600 Series directly supports the lens. The camera body therefore absorbs all mechanical load of the lens and mounting apparatus. This direct and rigid structural path between the camera body and load allows for more flexible installation options and increased reliability.

In a package measuring only 1.5" (H) x 3.75" (D) x 2" (W), you get 580 horizontal line resolution, microlens sensor technology for dramatic sensitivity and dynamic range.

The electrical features of the 2600 Series give it versatility, reliability, and value.

The camera features a 1/2"-format on-chip microlens sensor, which improves sensitivity and dynamic range, while reducing dark current, lag, and blooming. For video applications prone to streaking problems, a 1000:1 overload capability allows incidental light overloads up to 10 times that of other cameras. An electronic shutter allows the camera to track rapidly moving subjects.

RS-170 and CCIR models are available, and both have 20 dB of AGC for high sensitivity in low light level applications.

Electronic iris provides eight f-stops of automatic light control. This electronic shutter provides control from 1/60 to 1/15,000 second. This is of particular importance when the images are fast-moving or the camera is mounted on a vibrating source.

From board-level design to its cast aluminum enclosure, you can expect the highest performance, durability, and value from the Cohu 2600 Series CCD camera.

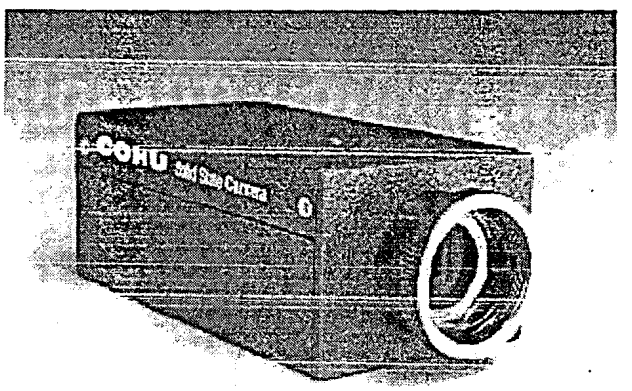

The 2600 Series CCD camera has been specially engineered for machine vision and robotic applications to endure repetitive shock and vibration. Standard model is painted black, and custom colors are available.

APPLICATIONS

- Image Processing
- Machine Vision
- Test and Measurement
- Laboratory
- Robotic Mechanisms
- Transportation Systems
- Surveillance
- Access Control

FEATURES AND BENEFITS

- Extra Rigid -for super-stable optical path, larger lenses
- High Performance -for clear images and positive identification
- 1/2" On-chip-microlens Interline Transfer Imager dramatically improves dynamic range and sensitivity and virtually eliminates overload streaking
- High Sensitivity permits operation over a broad range of light levels
- High Signal-to-Noise Ratio for clear, noise-free video
- "C" or "CS" Lens Mount expands your choice of lenses
- 1000:1 Overload Capability permits incidental light overloads up to ten times that of other CCD cameras
- Two-Year Warranty
- Made in U.S.A. - direct factory support

Designed and manufactured in the U.S.A.

COHU

Cohu, Inc. / Electronics Division

2600 Series Monochrome CCD Cameras

ORDERING INFORMATION

26X	2 -	X	X	0	X/	XXXX
Format	Power	Sync Option	Optical Filter	Unassigned	Options	Lenses
2 1/2" RS-170	2 12 VDC	1 Crystal	0 None		0 None	Consult factory
5 1/2" CCIR		2 Genlock	1 IR		3 Elec. Iris (RS-170)	
					4 DC Iris	
					5 Elec. Iris (CCIR)	

SPECIFICATIONS

Pick up Device
½" Interline transfer, enhanced sensitivity with microlens sensor
Resolution
RS-170: 580 HTVL
CCIR: 560 HTVL
Picture Elements
RS-170: 768 (H) x 494 (V)
CCIR: 752 (H) x 582 (V)
Synchronization
Internal: Crystal
External: H&V, async reset, optional external genlock
Electronic Shutter
1/60 to 1/10,000 switch selectable
Signal-to-Noise
55dB (gain 0, gamma 1)
38dB (gain 20 dB, gamma 1)

Gamma
.45 to 1.0 continually variable
AGC
20 dB range, auto or manual control
Integration
2-16 fields
Auto Lens Output
Reference video or DC drive
Lens Voltage
11 VDC
Sensitivity
Full Spectrum IR Filter
Full video, no AGC:
.005 fc (.05 lux) .25 fc (2.5 lux)
80% video, AGC on:
.005 fc (.05 lux) .018 fc (.18Lux)
30% video, AGC on:
.002 fc (.02 lux) .01 fc (.1 lux)

Input Power Requirement
12 VDC, 3.6 W
115 VAC, 50/60 Hz
Lens Mount
C/CS
Ambient Temperature Limits
-4° F (20° C) to 140°F (60° C)
Relative Humidity
to 95% non-condensing
Shock
30 g's, 11mS duration, 3 axes
Mounts
¼-20 female, top and bottom, with accessory mounting base (included)
Weight
<8oz (230 g) without lens

DIMENSIONS

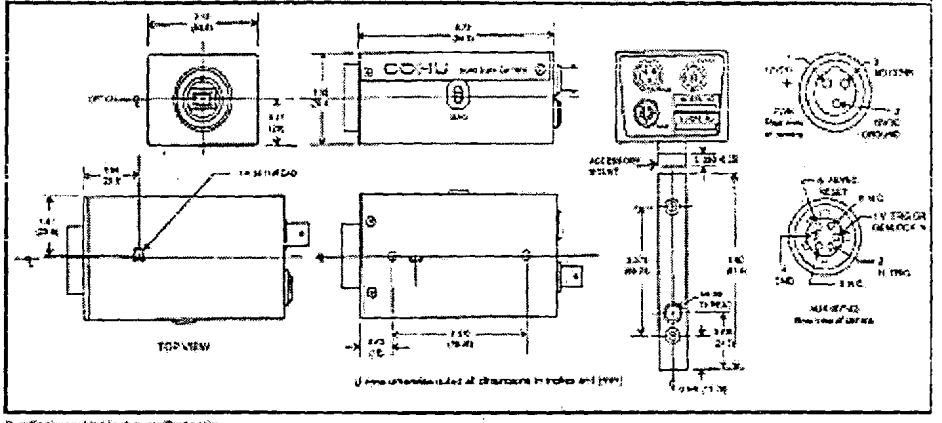

Cohu, Inc./Electronics Division
P.O. Box 85623 San Diego, CA 92186
Phone: 858/277-6700 • Fax: 858/277-0221 • Internet: www.cohu-cameras.com

ADVANCED VIDEO TECHNOLOGY
Made in the U.S.A.

COHU
Cohu, Inc. / Electronics Division

WaveFront SCIENCES

Complete Light Analysis System™

The CLAS™ - 2D is a turn-key optical analysis system providing a complete hardware/software solution to quantitative beam analysis of pulsed or cw lasers and complete optical systems. Replacing interferometers, beam analyzers and beam quality meters, the CLAS™ - 2D provides a cost effective, multi-use instrument for laboratory, quality control and process monitoring applications.

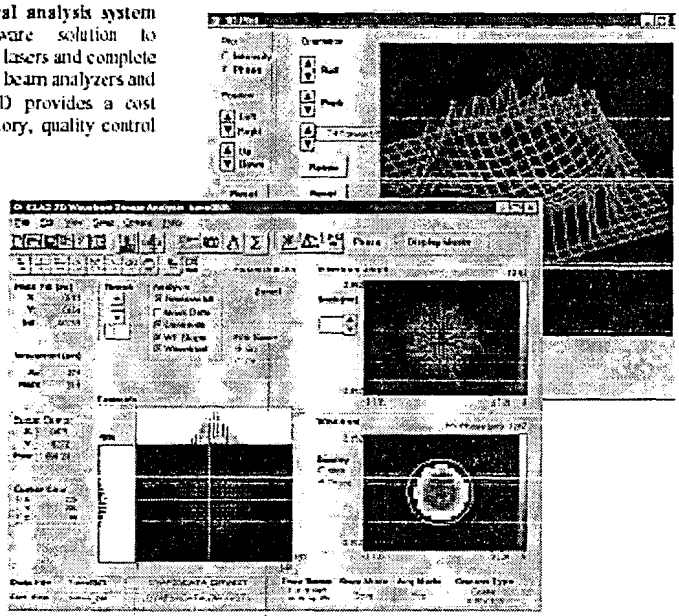

The ultimate in beam analysis, the CLAS™-2D combines the best features of a beam analyzer with those of an interferometer to provide a measurement of the intensity and phase distribution of the beam. In addition to the spatial irradiance and phase profiles, the beam analysis module includes M^2 and Gaussian beam parameters, near- and far-field propagation, MTF, RMS wavefront, Strehl ratio and many other parameters. Laser alignment, process and quality control, optics testing, and dynamic wavefront acquisition and analysis are now available in this simple to use, easy to setup system.

Several live screens support instrument setup and optical path alignment. Analysis modes provide rapid adjustment and collimation of an optical beam. It is now possible to align lasers using quantitative feedback for pointing and positioning.

The complete optical train can be measured by using an appropriate source. Optical flats, spheres, aspheres, cylinders and exotic optics can often be measured without expensive test plates or null correctors. Seidel and Zernike aberration coefficients are calculated directly from the data. Raw image, wavefront, irradiance, wavefront gradient, fringes, MTF and 3D plot displays are available.

The CLAS™ - 2D is so insensitive to vibration that an optical table is not required. Most measurements can be made on an ordinary lab bench. In addition, CLAS™ - 2D works well with a broad band source.

The Windows based user environment makes data acquisition and analysis a snap. Interactive windows display intensity and phase in 3-D while analysis features provide M^2 analysis, propagation, MTF, aberration coefficients and monomial or Zernike modes. **All with instant display of the data.**

Production testing of lasers, optical components and optical systems is supported with additional software. Acceptance test data logging and report generation may be configured for each

Instant Phase™ and More!!!!

- Simultaneous measurement of phase and intensity
- High speed, single frame data acquisition
- Large dynamic range (30-1102 tilt)
- Extremely high sensitivity (λ/150)
- Multi-frame acquisition for dynamic analysis
- No reference beams required
- No phase unwrapping required
- Compact, rugged design
- Insensitive to vibration
- Custom configurations for demanding metrology requirements

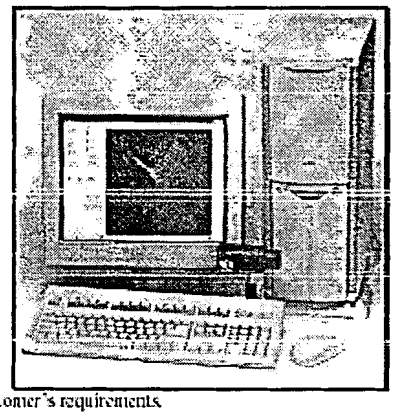

customer's requirements.

System Specifications
The CLAS™-2D system is a complete, turn-key optical analysis system. The user simply unpacks the system, connects five connectors and the system is up and running. All hardware and software components necessary to immediately begin beam analysis are included in the base system cost.

Wavefront Sensor
Based upon a high speed CCD sensor camera built exclusively for WaveFront Sciences, this sensor includes a custom micro-optic lens array with a bandwidth of 300 - 1100 nm.

Control System
The CLAS™-2D provides a complete control system with all the necessary components to perform beam analysis as well as general purpose scientific computing. Computer technology is changing rapidly. At WaveFront Sciences we want our customers to be provided with the most current technology consistent with reliability and reasonable cost. Please call for the system configuration currently shipping with the baseline system.

Analysis and Control Software
The CLAS™-2D comes complete with custom control and optical analysis software. A user-friendly graphical interface provides the CLAS™-2D with menu driven controls for calibration, data acquisition, data display and analysis. This software is installed, calibrated and tested when it arrives at your lab. Optical parameters available through the standard analysis package include:

- irradiance and phase distribution
- tilt, focus, astigmatism, coma, spherical and higher order aberrations (Zernike and monomial representations)
- beam width, position, shape, amplitude distribution
- beam waist (width and location) and divergence
- beam quality (M^2 and Strehl ratio)
- near- and far- field propagation analysis and MTF

Display Modes:
User selectable screens are used to display acquired and analyzed data. These views include:

Intensity distribution (2D and 3D)	Intensity Level
Wavefront contour (2D and 3D)	Real Time Alignment
Wavefront slope vector plot	Beam Parameters
Raw image	Versatile Data Analysis
Reference file create	Fringe Display

Analysis: Zernike/Monomial fits and coefficients, can display tilt, focus or marked term subtracted images

Additional Features:
Multi-frame acquisition and analysis for time series studies
Averaging (BOXCAR, Exponential, and running)
Data masking, xy slices, user control of Zernike circle
Multi-format export capability (Zemax, Matlab and ASCII)
Production environment interface available
Report printing

Physical Specifications:
Weight and size: 9.4 oz., 4.375" x 2.0" x 1.75"
Power: 2.5 Watts (excluding control computer)

Sensor Options:

Diameter	Focal Length	Array Size	Sens.*	Dyn. Range*
252 µm	25mm	25 x 19	λ/150	30 λ
198 µm	15.5 mm	31 x 24	λ/100	40 λ
144 µm	8mm	44 x 33	λ/50	50 λ
108 µm	4.6 mm	58 x 44	λ/30	70 λ
72 µm	2mm	88 x 66	λ/10	120 λ

* Minimum measurable wavefront w/Zernike reconstructor
* waves of tilt @ 632nm

Exposure: 1/60 - 1/10,000 second (asynchronous pulsed available)

Specs are nominal performance of standard system. Higher performance upgrades are available with different cameras. Please see the CLAS-2D Sensor Options Summary for complete information on available sensors and performance specifications.

Specifications subject to change without notice. WFSI, CLAS, Instant Phase and Complete Light Analysis System are trademarks of WaveFront Sciences, Inc.

U.S. Patent 5,936,726. Other patents pending.

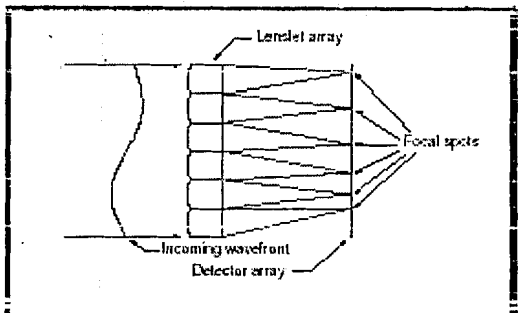

The CLAS™-2D uses a micro-optic lenslet array to dissect a light beam into multiple focal spots. The positions of these focal spots are used to measure the optical wavefront.

PEMI II

2nd Generation
Portable
Engineering
Moiré
Interferometer

Photo Mechanics

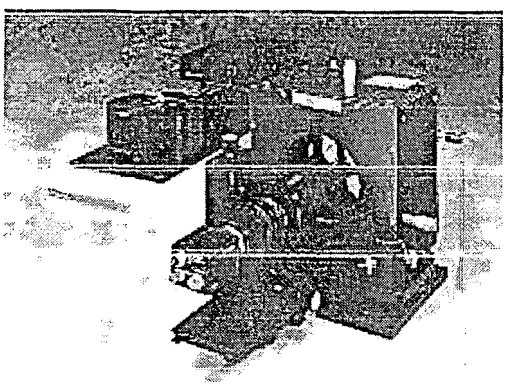

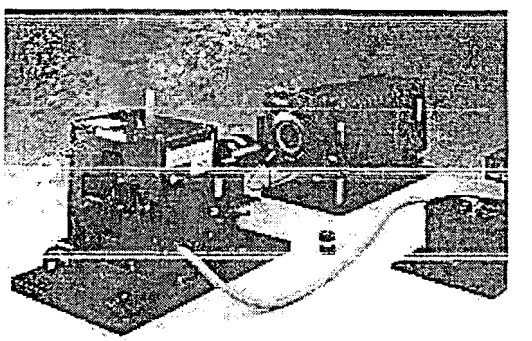

MACRO AND MICRO QUANTITATIVE DEFORMATION ANALYZER

Spot-On™ Lateral-Effect Detector Systems

Spot-On™ PCI/PCMCIA Lateral-Effect Detector Systems

Dual-axis lateral-effect detectors are ideal for measuring alignment and large beam deflections. Unlike quadrant detectors, they can measure the position of the beam anywhere within the surface of the detector. Dual sensors and custom housings are available. Please contact Melles Griot application engineers for more information.

Spot-On™ PCI/PCMCIA
Lateral-Effect Detector Systems

	PRODUCT NUMBER
PCMCIA version	13 PSL 004
PCI version	13 PSL 005

Note: Fiber not included.

SPECIFICATIONS: Spot-On™ PCI/PCMCIA
LATERAL-EFFECT DETECTOR SYSTEMS

Detector Type: Dual-axis lateral effect
Detector Size:
13 PSL 004: 10 × 10 mm
13 PSL 005: 10 × 10 mm
Measurement Range:
8-mm diameter circle centered on the detector center
Position Resolution: ± 1 µm
Position Accuracy: ± 50 µm over the calibrated area
Calibrated Spectral Range:
Position: 350–1050 nm
Power: 400–1000 nm
Power Range: 10 µW to 10 mW
Power Accuracy:
± 5% for a 1-mW Gaussian beam, 4 mm in diameter (no ND filter)
Plug-in Card Configuration: PCI or PCMCIA
System Requirements:
800-MHz Pentium 3 or higher running Windows® 98, Me, NT (except for PCMCIA version), 2000, or XP
16-MByte RAM
20-MByte hard drive space
2-MByte 16-bit color VGA card
Weight: Sensor head and cable 175 g; card, 100 g

Windows® is a registered trademark of Microsoft Corporation.

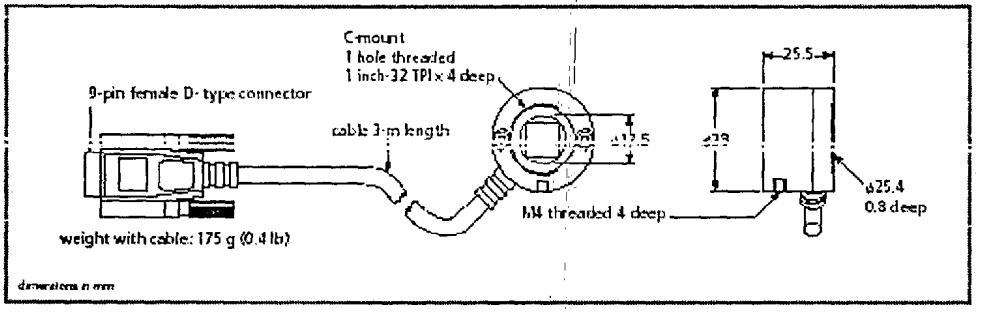

13 PSL-series lateral-effect detector system

Appendix B

Output Data

Appendix B: Output Data

Data Files for Multi-step Curves by MDSS

```
Each Data Record=[Applied-value,
                  Mean-strain-x, Mean-strain-y,
                  StDev-strain-x, StDev-strain-y,
                  Mean-tilt-x, Mean-tilt-y,
                  StDev-tilt-x, StDev-tilt-y]


-1.2340000e+003 -1.2644671e+003 -4.3102480e+002  4.1413388e+002
3.9321890e+002  4.4777397e+002  1.1018694e+003  4.6275599e+002
1.8214973e+002
 -9.2600000e+002 -9.3118881e+002 -2.4093607e+002  3.8247138e+002
3.7205530e+002  8.6934141e+001  8.5377885e+002  3.5172826e+002
1.7155373e+002
 -5.5500000e+002 -5.4753985e+002 -3.4445082e+001  3.4725633e+002
3.5211003e+002 -1.0432366e+002  3.3734775e+002  2.3679390e+002
1.5749931e+002
 -2.5200000e+002 -2.5443681e+002 -5.8670922e+001  2.8747364e+002
3.0512724e+002 -7.4918879e+001  5.5879154e+001  1.6412170e+002
1.3781899e+002
  0.0000000e+000  1.7326794e+001 -5.1013798e+000  9.4278840e+001
9.5059733e+001  4.2771859e+000  1.3948619e+000  4.2673390e+001
4.3569167e+001
```

```
-3.9700000e+002 -4.2370386e+002  2.9691654e+002  2.9702776e+002
2.8366733e+002 -1.8364211e+003 -1.3936061e+003  3.8624344e+002
1.6096319e+002
 -1.8500000e+002 -1.9085325e+002  1.0215405e+002  2.8374939e+002
2.7058716e+002  1.6474859e+002  8.5247006e+001  1.8628446e+002
1.3526753e+002
  0.0000000e+000 -4.0211314e+000 -2.5886015e-002  1.1131352e+002
1.0438135e+002 -1.6197402e+000 -9.7512309e-002  4.7802252e+001
4.7302681e+001
```

```
-5.8000000e+003  7.8825933e+001 -5.7823139e+003  3.9698839e+001
6.9419185e+001 -1.1774112e+001 -4.5420624e+001  2.0501445e+001
2.6408012e+001
 -2.9000000e+003  4.1445769e+001 -2.9088145e+003  3.6814274e+001
5.2056939e+001 -7.2621429e+000 -3.3990546e+001  1.9357660e+001
2.6446129e+001
  0.0000000e+000  1.8248201e+000  2.8500403e+000  1.6440537e+001
1.8871223e+001 -2.9793241e+000  1.4365731e+000  7.7363352e+000
9.1404416e+000
  2.9000000e+003 -3.1553840e+001  2.8990697e+003  3.4491181e+001
8.6625435e+001  5.1109574e+000 -5.4906384e+000  1.8729608e+001
3.8402524e+001
```

```
0.0000000e+000  5.1047994e-002  2.2221899e+000  1.6414248e+001
1.5629388e+001  2.7408508e+000 -5.6779913e-001  6.7223418e+000
6.6331311e+000
  2.9000000e+003  3.0908509e+003  1.3317299e+002  6.0559251e+001
5.7248515e+001  2.9754582e+001 -4.1482501e+001  2.5244561e+001
2.2631789e+001
  5.8000000e+003  5.7180516e+003  2.4764081e+002  6.0310568e+001
5.8256181e+001  4.0358857e+001 -7.0263260e+001  2.8231301e+001
2.6267807e+001
  8.7000000e+003  8.7337294e+003  3.7217584e+002  9.3468040e+001
5.9079579e+001  7.0035598e+001 -1.0984666e+002  5.4489246e+001
2.2826177e+001
```

```
-3.5000000e+003 -1.0031072e+002 -1.9055499e+001  4.1285028e+001
2.9601426e+001 -3.6412666e+003 -3.4753045e+001  2.0395450e+001
2.2834656e+001
 -1.7500000e+003 -5.4944001e+001 -4.9950550e+000  3.6999363e+001
-3.4794491e+001 -1.6800345e+003 -1.7602376e+001  2.3395828e+001
2.1426806e+001
  0.0000000e+000 -1.2574894e+001  3.7885600e+000  2.5380386e+001
2.6024933e+001  5.1692722e+000  7.1022673e-001  9.7061620e+000
8.9643431e+000
  1.7500000e+003  4.3641952e+001  8.3724604e+000  4.6564960e+001
3.8423471e+001  1.6543081e+003  1.8570026e+001  2.4516146e+001
1.8604845e+001
```

```
-1.7500000e+003 -7.5961791e+001  3.2319939e+000  5.3358801e+001
3.5600274e+001 -1.8747104e+003 -1.0938267e+001  2.8568137e+001
2.0776718e+001
  0.0000000e+000  3.7068079e-001 -3.6898883e+000  1.7466338e+001
1.9430502e+001 -4.8016575e+000  6.8075374e-001  6.1370356e+000
8.9421259e+000
  1.7500000e+003  8.1476553e+001 -1.0238848e+001  4.2550072e+001
3.7814599e+001  2.1603021e+003  2.8945863e+001  1.9939891e+001
2.2131739e+001
  3.5000000e+003  1.6310057e+002 -7.8392384e-001  1.1179500e+002
3.2413000e+001  4.0335660e+003  3.6790994e+001  5.4240675e+001
1.9873971e+001
```

Appendix C

Source Code

Appendix C: Source Code

Source Code for MDSS

```
%%%%%%%%%%%%%%%%%%%%%%%%%%%%%%%%%%%%%%%%%%%%%%%%%%%%%%%%%%%%%%%%%%%%%%%%%%%%%%%%%
%
% M file for multiple centroid strain calculation of repeated images
%
%%%%%%%%%%%%%%%%%%%%%%%%%%%%%%%%%%%%%%%%%%%%%%%%%%%%%%%%%%%%%%%%%%%%%%%%%%%%%%%%%

function mimstrain(var, unit, count, comment)

MINYMAX = 500;
global RES;
RES = [];

disp('****************************************************')
disp('***    Dual Beam Multiple Point Strain Sensor    ***')
disp('****************************************************')
disp(' ')

auto = '1';
if nargin >= 3
    cnt = str2num(count);
    str1 = sprintf('%s-Rref.bmp', var);
    str3 = sprintf('%s-Lref.bmp', var);
    str = sprintf('Press any char for ref %s, %s alignment ... ', str1, str3);
    kin = input(str, 's');
       while ~isempty(kin)
        input('Press Enter for right file check ... ');
        mcpos(str1, auto);
        set(gcf, 'Visible', 'On');
        input('Press Enter for left file check ... ');
        mcpos(str3, auto);
        set(gcf, 'Visible', 'On');
        kin = input('Enter any char for alignment, none to proceed ... ', 's');
       end
       disp(' ')

    for i = 1 : cnt;
        str2 = sprintf('%s-R%d.bmp', var, i);
        str4 = sprintf('%s-L%d.bmp', var, i);
        str = sprintf('Enter shift val for calc with %s, %s ... ', str2, str4);
        disp(' ');
       vin = input(str);
        RES = [RES; 0 0 0 0 0 0 0 0 0];
        RES(i, 1) = vin;
        mcstrain(auto, str1, str2, str3, str4);
    end
    input('Press Enter for plot generation ... ');
else
       kin = input('Enter any char for alignment, none to proceed ... ', 's');
       while ~isempty(kin)
        input('Press Enter for Ref-R.bmp check ... ');
        mcpos('Ref-R.bmp', auto);
        set(gcf, 'Visible', 'On');
        input('Press Enter for Ref-L.bmp check ... ');
        mcpos('Ref-L.bmp', auto);
        set(gcf, 'Visible', 'On');
```

```
        kin = input('Enter any char for alignment, none to proceed ... ', 's');
        end
        disp(' ')

        cnt = 0;
        vin = input('Enter shift val or a num for strain calc, none to end ... ');
        while ~isempty(vin)
        RES = [RES; 0 0 0 0 0 0 0 0 0];
        cnt = cnt + 1;
        RES(cnt, 1) = vin;
        input('Press Enter for calc with Str-R.bmp, Str-L.bmp ... ');
        mcstrain(auto);
        set(gcf, 'Visible', 'On');
        vin = input('Enter shift val or a num for strain calc, none to end ... ');
        end
end

if nargin ~= 0 && ~isempty(RES)
    RES = sortrows(RES);
    xdiff = abs(RES(1,1)) / 2;
    if size(RES,1) > 1
        xdiff = min(RES(2,1)-RES(1,1), RES(size(RES,1),1)-RES(size(RES,1)-1,1));
    end
    if nargin >= 4
        com = sprintf('  -  (%s)', comment);
    else
        com = '';
    end
    xstr = sprintf('%s (%s)%s', var, unit, com);

    figure;
    plot(RES(:,1), RES(:,7),'-k^', 'LineWidth',2, ...
         'MarkerEdgeColor','k', 'MarkerFaceColor','k', 'MarkerSize',4);
    ymax = max(max(RES(:,7))+mean(RES(:,9)), abs(min(RES(:,7))-mean(RES(:,9))));
    ymax = max(1.25 * ymax, MINYMAX);
    axis([RES(1,1)-xdiff, RES(size(RES,1),1)+xdiff, -1*ymax, ymax]);
    xlabel(xstr);
    ylabel('Mean Y-Tilt (w/ St Dev) (uR)');
    str = sprintf('Plot of Measured Y-Tilt vs %s', var);
    title(str);
    set(gca, 'YMinorTick', 'on');
    hold on
    for i = 1 : size(RES,1),
        indvec = [RES(i,1) RES(i,1)];
        sdvec = [RES(i,7)-RES(i,9) RES(i,7)+RES(i,9)];
        plot(indvec, sdvec, ':k+');
    end
    set(gcf, 'position', get(gcf, 'position') + [-200 -200 -100 -100]);
    str = sprintf('%s-YTilt', var);
    hgsave(str);

    figure;
    plot(RES(:,1), RES(:,3),'-kd', 'LineWidth',2, ...
         'MarkerEdgeColor','k', 'MarkerFaceColor','k', 'MarkerSize',4);
    ymax = max(max(RES(:,3))+mean(RES(:,5)), abs(min(RES(:,3))-mean(RES(:,5))));
    ymax = max(1.25 * ymax, MINYMAX);
    axis([RES(1,1)-xdiff, RES(size(RES,1),1)+xdiff, -1*ymax, ymax]);
    xlabel(xstr);
    ylabel('Mean Rotation (w/ St Dev of Variations) (uR)');
    str = sprintf('Plot of Measured Y-Strain/Rotation vs %s', var);
%    ylabel('Mean Y-Strain (w/ St Dev of Variations) (uR)');
%    str = sprintf('Plot of Measured Shear Strain vs %s', var);
    title(str);
    set(gca, 'YMinorTick', 'on');
    hold on
    for i = 1 : size(RES,1),
        indvec = [RES(i,1) RES(i,1)];
        sdvec = [RES(i,3)-RES(i,5) RES(i,3)+RES(i,5)];
        plot(indvec, sdvec, ':k+');
    end
    set(gcf, 'position', get(gcf, 'position') + [-200 100 -100 -100]);
```

```
    str = sprintf('%s-Rot', var);
    hgsave(str);

    figure;
    plot(RES(:,1), RES(:,6),'-k^', 'LineWidth',2, ...
         'MarkerEdgeColor','k', 'MarkerFaceColor','k', 'MarkerSize',4);
    ymax = max(max(RES(:,6))+mean(RES(:,8)), abs(min(RES(:,6))-mean(RES(:,8))));
    ymax = max(1.25 * ymax, MINYMAX);
    axis([RES(1,1)-xdiff, RES(size(RES,1),1)+xdiff, -1*ymax, ymax]);
    xlabel(xstr);
    ylabel('Mean X-Tilt (w/ St Dev) (uR)');
    str = sprintf('Plot of Measured X-Tilt vs %s', var);
    title(str);
    set(gca, 'YMinorTick', 'on');
    hold on
    for i = 1 : size(RES,1),
        indvec = [RES(i,1) RES(i,1)];
        sdvec = [RES(i,6)-RES(i,8) RES(i,6)+RES(i,8)];
        plot(indvec, sdvec, ':k+');
    end
    set(gcf, 'position', get(gcf, 'position') + [100 -200 -100 -100]);
    str = sprintf('%s-XTilt', var);
    hgsave(str);

    figure;
    plot(RES(:,1), RES(:,2),'-ko', 'LineWidth',2,
         'MarkerEdgeColor','k', 'MarkerFaceColor','k', 'MarkerSize',4);
    ymax = max(max(RES(:,2))+mean(RES(:,4)), abs(min(RES(:,2))-mean(RES(:,4))));
    ymax = max(1.25 * ymax, MINYMAX);
    axis([RES(1,1)-xdiff, RES(size(RES,1),1)+xdiff, -1*ymax, ymax]);
    xlabel(xstr);
    ylabel('Mean Strain (uS)');
%    ylabel('Mean Strain (w/ St Dev) (uS)');
%    ylabel('Mean Strain (w/ St Dev of Variations) (uS)');
    str = sprintf('Plot of Measured X-Strain vs %s', var);
%    ylabel('Mean Y-Strain (w/ St Dev of Variations) (uR)');
%    str = sprintf('Plot of Measured V-Beams Strain vs %s', var);
    title(str);
    set(gca, 'YMinorTick', 'on');
    hold on
    for i = 1 : size(RES,1),
        indvec = [RES(i,1) RES(i,1)];
        sdvec = [RES(i,2)-RES(i,4) RES(i,2)+RES(i,4)];
%        plot(indvec, sdvec, ':k+');
    end
    set(gcf, 'position', get(gcf, 'position') + [100 100 -100 -100]);
    str = sprintf('%s-XStr', var);
    hgsave(str);

    str = sprintf('%s.dat', var);
    save(str, 'RES', '-ASCII');
end

clear global RES;
disp(' ')
disp('Goodbye');
disp(' ')
```

```
%%%%%%%%%%%%%%%%%%%%%%%%%%%%%%%%%%%%%%%%%%%%%%%%%%%%%%%%%%%%%%%%%%%%%%%%%%%%%%%%
%
% M file for multiple centroid strain calculation using centroid function
%
%%%%%%%%%%%%%%%%%%%%%%%%%%%%%%%%%%%%%%%%%%%%%%%%%%%%%%%%%%%%%%%%%%%%%%%%%%%%%%%%

function mcstrain(auto,right1,right2,left1,left2, ...
        segx,segy,flen,pxlen,pylen,inang,thsd,show,adjt)

XCORMLT = 1.0;
YCORMLT = 1.0;
SIGNMLT = -1.0;
%XCORMLT = 1.2;
%YCORMLT = 1.85;
%SIGNMLT = 1.0;
global RES;

if nargin == 0 || (nargin ~= 0 && auto ~= '1')
    auto = 0;
end

if auto ~= '1' && nargin < 5
    right1 = input('Name of Right reference image file? ', 's');
    right2 = input('Name of Right strained image file (same size)? ', 's');
    left1 = input('Name of Left reference image file? ', 's');
    left2 = input('Name of Left strained image file (same size)? ', 's');
end
if (auto == '1' && nargin < 5) || isempty(right1)
    right1 = 'Ref-R.bmp';
end
if (auto == '1' && nargin < 5) || isempty(right2)
    right2 = 'Str-R.bmp';
end
if (auto == '1' && nargin < 5) || isempty(left1)
    left1 = 'Ref-L.bmp';
end
if (auto == '1' && nargin < 5) || isempty(left2)
    left2 = 'Str-L.bmp';
end
%disp(' ')

if auto ~= '1' && nargin < 14
    segx = input('Number of horizontal image segments? ');
    segy = input('Number of vertical image segments? ');
    flen = input('Focal length of lens array? ');
    pxlen = input('X-direction size of a pixel? ');
    pylen = input('Y-direction size of a pixel? ');
    inang = input('incidnet beam angle (alpha) ? ');
    thsd = input('Threshold for background elimination? ', 's');
    show = input('Show images and calculations? ', 's');
    adjt = input('Ignore the bottom rows of image? ', 's');
end

if auto == '1' || isempty(segx)
%    segx = 42.427;
    segx = 42.78;
%    segx = 43.15;
%    segx = 42.6;
end
if auto == '1' || isempty(segy)
%    segy = 38.528;
    segy = 39.22;
end
if auto == '1' || isempty(flen)
    flen = 8190;
end
if auto == '1' || isempty(pxlen)
    pxlen = 8.4;
end
if auto == '1' || isempty(pylen)
    pylen = 9.8;
```

```
end
if auto == '1' || isempty(inang)
%    inang = 0.96;
    inang = 0.86;
end
if auto == '1' || isempty(thsd)
    thsd = '1';
end
if auto == '1' || isempty(show)
    show = 'y';
end
if auto == '1' || isempty(adjt)
    adjt = 'y';
end
disp(' ')

if thsd == '1' || thsd == 'g'
    mthval1 = 0;
    mthval2 = 0;
    pic2 = imread(right1);
    finf = imfinfo(right1);
    bpp = finf.BitDepth;
    thval1 = (2^bpp)/2;
    if thsd == 'g'
        thval1 = (thval1 + mean(mean(double(pic2)))) / 2;
        mthval1 = thval1;
        pic = pic2 > thval1;
    else
        pic = pic2;
    end

    pic2 = imread(right2);
    finf = imfinfo(right2);
    bpp = finf.BitDepth;
    thval2 = (2^bpp)/2;
    if thsd == 'g'
        thval2 = (thval2 + mean(mean(double(pic2)))) / 2;
        mthval2 = thval2;
        pic1 = pic2 > thval2;
    else
        pic1 = pic2;
    end
else
    pic = imread(right1);
    pic1 = imread(right2);
end

[maxy, maxx] = size(pic);
subx = maxx/segx;
suby = maxy/segy;
xmlt = pxlen;
ymlt = pylen;
fdiv = 2 * flen;
if adjt == 'y' || adjt =='Y'
    segy = segy - 7;
end
segx1 = fix(segx);
segy1 = fix(segy);

if show == 'y' || show == 'Y'
       str = sprintf('Rt image files = %s, %s', right1, right2);
       disp(str)
       str = sprintf('Lt image files = %s, %s', left1, left2);
       disp(str)
       str = sprintf('Image size =     %6.2f x %6.2f', maxx, maxy);
       disp(str)
       str = sprintf('No of segments = %6.2f x %6.2f, Seg size = %6.2f x %6.2f', segx, segy,
subx, suby);
       disp(str)
       str = sprintf('X/Y multiples =  %6.2f x %6.2f, Flen div = %d', xmlt, ymlt, fdiv);
       disp(str)
```

```
        str = sprintf('Alpha =  %6.2f, Sin(a) = %6.2f, Cos(a) = %6.2f', inang, sin(inang),
cos(inang));
        disp(str)
end

lthval = 0;
shftx = zeros(segy1, segx1);
shfty = zeros(segy1, segx1);
blnk1 = 0;
blnk2 = 0;
for i = 0:segy1-1
    for j = 0:segx1-1
        i1 = i+1;
        j1 = j+1;
        if thsd == 'l'
            subpic2 = pic(round(i*suby+1):round(i1*suby), round(j*subx+1):round(j1*subx));
%            lthval = mean(mean(double(subpic2)));
            lthval = (thval1 + 3*mean(mean(double(subpic2)))) / 4;
%            lthval = 3*max(max(double(subpic2)))/4;
            mthval1 = mthval1 + lthval;
            subpic = subpic2 > lthval;
        else
            subpic = pic(round(i*suby+1):round(i1*suby), round(j*subx+1):round(j1*subx));
        end
        [cenx, ceny, bk] = centroid(subpic);
        if bk == 1
            blnk1 = blnk1 + 1;
        end

        if thsd == 'l'
            subpic2 = pic1(round(i*suby+1):round(i1*suby), round(j*subx+1):round(j1*subx));
%            lthval = mean(mean(double(subpic2)));
            lthval = (thval2 + 3*mean(mean(double(subpic2)))) / 4;
%            lthval = 3*max(max(double(subpic2)))/4;
            mthval2 = mthval2 + lthval;
            subpic1 = subpic2 > lthval;
        else
            subpic1 = pic1(round(i*suby+1):round(i1*suby), round(j*subx+1):round(j1*subx));
        end
        [cenx1, ceny1, bk1] = centroid(subpic1);
        if bk1 == 1
            blnk2 = blnk2 + 1;
        end
        if thsd == 'l' || (bk == 1 && bk1 == 1)
            shftx(i1,j1) = xmlt * (cenx1-cenx);
            shfty(i1,j1) = ymlt * (ceny1-ceny);
        end
        if i == 0 && j ==0
            subplot(3,4,3), subimage(subpic)
            subplot(3,4,4), subimage(subpic1)
        end
        if i == fix(segy1/2) && j == fix(segx1/2)
            subplot(3,4,7), subimage(subpic)
            subplot(3,4,8), subimage(subpic1)
        end
    end
end

if show == 'y' || show == 'Y'
%    subplot(2,4,3), subimage(pic)
%    subplot(2,4,7), subimage(pic1)
%    subplot(2,4,4), subimage(subpic)
%    subplot(2,4,8), subimage(subpic1)
    subplot(3,4,11), subimage(subpic)
    subplot(3,4,12), subimage(subpic1)
end

if thsd == 'l' || thsd == 'g'
    mthval3 = 0;
    mthval4 = 0;
    pic2 = imread(left1);
```

```
    finf = imfinfo(left1);
    bpp = finf.BitDepth;
    thval3 = (2^bpp)/2;
    if thsd == 'g'
        thval3 = (thval3 + mean(mean(double(pic2)))) / 2;
        mthval3 = thval3;
        pic = pic2 > thval3;
    else
        pic = pic2;
    end

    pic2 = imread(left2);
    finf = imfinfo(left2);
    bpp = finf.BitDepth;
    thval4 = (2^bpp)/2;
    if thsd == 'g'
        thval4 = (thval4 + mean(mean(double(pic2)))) / 2;
        mthval4 = thval4;
        pic1 = pic2 > thval4;
    else
        pic1 = pic2;
    end
else
    pic = imread(left1);
    pic1 = imread(left2);
end

shftx1 = zeros(segy1, segx1);
shfty1 = zeros(segy1, segx1);
strnx = zeros(segy1, segx1);
strny = zeros(segy1, segx1);
tiltx = zeros(segy1, segx1);
tilty = zeros(segy1, segx1);
blnk3 = 0;
blnk4 = 0;
skip = segx1 * segy1;
for i = 0:segy1-1
    for j = 0:segx1-1
        i1 = i+1;
        j1 = j+1;
        if thsd == 'l'
            subpic2 = pic(round(i*suby+1):round(i1*suby), round(j*subx+1):round(j1*subx));
%            lthval = mean(mean(double(subpic2)));
            lthval = (thval3 + 3*mean(mean(double(subpic2)))) / 4;
%            lthval = 3*max(max(double(subpic2)))/4;
            mthval3 = mthval3 + lthval;
            subpic = subpic2 > lthval;
        else
            subpic = pic(round(i*suby+1):round(i1*suby), round(j*subx+1):round(j1*subx));
        end
        [cenx, ceny, bk] = centroid(subpic);
        if bk == 1
            blnk3 = blnk3 + 1;
        end

        if thsd == 'l'
            subpic2 = pic1(round(i*suby+1):round(i1*suby), round(j*subx+1):round(j1*subx));
%            lthval = mean(mean(double(subpic2)));
            lthval = (thval4 + 3*mean(mean(double(subpic2)))) / 4;
%            lthval = 3*max(max(double(subpic2)))/4;
            mthval4 = mthval4 + lthval;
            subpic1 = subpic2 > lthval;
        else
            subpic1 = pic1(round(i*suby+1):round(i1*suby), round(j*subx+1):round(j1*subx));
        end
        [cenx1, ceny1, bk1] = centroid(subpic1);
        if bk1 == 1
            blnk4 = blnk4 + 1;
        end
        if thsd ~= 'l' || (bk ~= 1 && bk1 ~= 1)
            shftx1(i1,j1) = xmlt * (cenx1-cenx);
```

```
            shfty1(i1,j1) = ymlt * (ceny1-ceny);
            if thsd ~= 'l' || (shftx(i1,j1) ~= 0 && shfty(i1,j1) ~= 0)
                strnx(i1,j1) = SIGNMLT * 1000000 * XCORMLT * (shftx1(i1,j1)-shftx(i1,j1)) /
fdiv / sin(inang);
                strny(i1,j1) = SIGNMLT * 1000000 * YCORMLT * (shfty1(i1,j1)-shfty(i1,j1)) /
fdiv / sin(inang);
                tiltx(i1,j1) = 1000000 * XCORMLT * (shftx1(i1,j1)+shftx(i1,j1)) / fdiv /
(1+cos(inang));
                tilty(i1,j1) = 1000000 * YCORMLT * (shfty1(i1,j1)+shfty(i1,j1)) / fdiv /
(1+cos(inang));
                skip = skip - 1;
            end
        end
        if i == 0 && j ==0
            subplot(3,4,1), subimage(subpic)
            subplot(3,4,2), subimage(subpic1)
        end
        if i == fix(segy1/2) && j == fix(segx1/2)
            subplot(3,4,5), subimage(subpic)
            subplot(3,4,6), subimage(subpic1)
%            s = size(RES,1);
%            RES(s,10) = strnx(i1,j1);
        end
    end
end

if show == 'y' || show == 'Y'
%    subplot(2,4,2), subimage(pic)
%    subplot(2,4,6), subimage(pic1)
%    subplot(2,4,1), subimage(subpic)
%    subplot(2,4,5), subimage(subpic1)
    subplot(3,4,9), subimage(subpic)
    subplot(3,4,10), subimage(subpic1)
    set(gcf, 'position', get(gcf, 'position') + [-100 -200 200 50])
    figure
end

if thsd == 'l' || thsd == 'g'
    if thsd == 'l'
        mthval1 = mthval1 / (segx1 * segy1);
        mthval2 = mthval2 / (segx1 * segy1);
        mthval3 = mthval3 / (segx1 * segy1);
        mthval4 = mthval4 / (segx1 * segy1);
    end
    if show == 'y' || show == 'Y'
        str = sprintf('Rt images blanks = %d, %d, Thresholds = %6.2f, %6.2f', blnk1, blnk2,
mthval1, mthval2);
        disp(str)
        str = sprintf('Lt images blanks = %d, %d, Thresholds = %6.2f, %6.2f', blnk3, blnk4,
mthval3, mthval4);
        disp(str)
        str = sprintf('Total skips = %d out of %d\n', skip, segx1 * segy1);
        disp(str)
    end
end

if thsd ~= 'l'
        mx = mean(mean(shftx));
        my = mean(mean(shfty));
        sx = std(std(shftx));
        sy = std(std(shfty));
        mx1 = mean(mean(shftx1));
        my1 = mean(mean(shfty1));
        sx1 = std(std(shftx1));
        sy1 = std(std(shfty1));
        meanx = mean(mean(strnx));
        meany = mean(mean(strny));
        stdx = std(std(strnx));
        stdy = std(std(strny));
        tmx = mean(mean(tiltx));
        tmy = mean(mean(tilty));
```

```
        tsx = std(std(tiltx));
        tsy = std(std(tilty));
else
        mx = nzmean(shftx);
        my = nzmean(shfty);
        sx = nzstd(shftx);
        sy = nzstd(shfty);
        mx1 = nzmean(shftx1);
        my1 = nzmean(shfty1);
        sx1 = nzstd(shftx1);
        sy1 = nzstd(shfty1);
        meanx = nzmean(strnx);
        meany = nzmean(strny);
        stdx = nzstd(strnx);
        stdy = nzstd(strny);
        tmx = nzmean(tiltx);
        tmy = nzmean(tilty);
        tsx = nzstd(tiltx);
        tsy = nzstd(tilty);
end

mcdx = (max(sum(strnx)) - min(sum(strnx))) / segy1;
mrdx = (max(sum(strnx,2)) - min(sum(strnx,2))) / segx1;
mcdy = (max(sum(strny)) - min(sum(strny))) / segy1;
mrdy = (max(sum(strny,2)) - min(sum(strny,2))) / segx1;
hsegy1 = ceil(segy1 / 2);
hsegx1 = ceil(segx1 / 2);
actx = mean(mean(strnx(:,segx1-hsegx1-1:segx1))) - mean(mean(strnx(:,1:hsegx1)));
artx = mean(mean(strnx(segy1-hsegy1+1:segy1,:),2)) - mean(mean(strnx(1:hsegy1,:),2));
acty = mean(mean(strny(:,segx1-hsegx1-1:segx1))) - mean(mean(strny(:,1:hsegx1)));
arty = mean(mean(strny(segy1-hsegy1+1:segy1,:),2)) - mean(mean(strny(1:hsegy1,:),2));

%str = sprintf('%d %d %d, %d %d %d', segx1, segx1-hsegx1+1, hsegx1, segy1, segy1-hsegy1+1,
hsegy1);
%disp(str)
str = sprintf('Mean x-strain = %8.2f uS,  St dev of x-strain = %8.2f uS', meanx, stdx);
disp(str)
str = sprintf('Mean y-strain = %8.2f uS,  St dev of y-strain = %8.2f uS', meany, stdy);
disp(str)

if show == 'y' || show == 'Y'
        disp(' ')
    str = sprintf('Max x-str h-ripple = %8.2f uS,  Max x-str v-ripple = %8.2f uS', mcdx,
mrdx);
        disp(str)
        str = sprintf('Max y-str h-ripple = %8.2f uS,  Max y-str v-ripple = %8.2f uS', mcdy,
mrdy);
        disp(str)
        str = sprintf('Appr x-str h-tilt =  %8.2f uS,  Appr x-str v-tilt =  %8.2f uS', actx,
artx);
        disp(str)
        str = sprintf('Appr y-str h-tilt =  %8.2f uS,  Appr y-str v-tilt =  %8.2f uS', acty,
arty);
        disp(str)
        disp(' ')
    str = sprintf('Mean x-tilt =     %7.2f uR,  St dev = %7.2f uR', tmx, tsx);
    disp(str)
    str = sprintf('Mean y-tilt =     %7.2f uR,  St dev = %7.2f uR', tmy, tsy);
    disp(str)
    str = sprintf('Mean Rt x-shift = %7.2f um,  St dev = %7.2f um', mx, sx);
    disp(str)
    str = sprintf('Mean Rt y-shift = %7.2f um,  St dev = %7.2f um', my, sy);
    disp(str)
    str = sprintf('Mean Lt x-shift = %7.2f um,  St dev = %7.2f um', mx1, sx1);
    disp(str)
    str = sprintf('Mean Lt y-shift = %7.2f um,  St dev = %7.2f um\n', my1, sy1);
    disp(str)
else
    if thsd == 'l' || thsd == 'g'
        str = sprintf('Max xy ripple = %7.2f,%7.2f uS, blank = %d, skip = %d', mcdx, mrdy,
blnk1+blnk2+blnk3+blnk4, skip);
```

```
    else
        str = sprintf('Max xy ripple = %7.2f,%7.2f uS, No thresholding\n', mcdx, mrdy);
    end
    disp(str)
    str = sprintf('Mean Rt shift = %7.2f,%7.2f um,  Lt shift = %7.2f,%7.2f um\n', mx, my,
- mx1, my1);
    disp(str)
end

if ~isempty(RES)
    i = size(RES,1);
    RES(i,2) = meanx;
    RES(i,3) = meany;
    RES(i,4) = stdx;
    RES(i,5) = stdy;
    RES(i,6) = tmx;
    RES(i,7) = tmy;
    RES(i,8) = tsx;
    RES(i,9) = tsy;
end

%subxy = max(subx, suby);
%zmax = ceil(subxy / 2);
%zmin = floor(-1 * subxy / 2);
%zmax = pxlen * subx * 1000000 / fdiv;
%zmin = -1 * pxlen * subx * 1000000 / fdiv;
maxxy = max(XCORMLT*xmlt*subx, YCORMLT*ymlt*suby);
%zmax = maxxy * 1000000 / fdiv;
%zmin = -1 * maxxy * 1000000 / fdiv;
zmax = maxxy * 1000000 / fdiv / 2;
zmin = -1 * maxxy * 1000000 / fdiv / 2;
subplot(1,2,1), surf(strnx,'edgecolor','none')
colormap hsv
%light
%camlight headlight, lighting phong
shading interp
axis ij
%axis equal
axis square
axis([1,segx1,1,segy1,zmin,zmax,zmin,zmax])
view(-15,25)
xlabel('Horizontal')
ylabel('Vertical')
zlabel('Strain (uS)')
title('X-STRAIN MAP')
colorbar

subplot(1,2,2), surf(strny,'edgecolor','none')
%subplot(1,2,2), surf(tiltx,'edgecolor','none')
colormap hsv
%light
%camlight headlight, lighting phong
shading interp
axis ij
%axis equal
axis square
axis([1,segx1,1,segy1,zmin,zmax,zmin,zmax])
view(-15,25)
xlabel('Horizontal')
ylabel('Vertical')
zlabel('Strain (uS)')
title('Y-STRAIN/ROTATION MAP')
%zlabel('Tilt (uR)')
%title('X-Tilt MAP')
colorbar

%set(gcf, 'position', [1 31 1280 918])
% cenx
% ceny
% pic1 = logical(pic);
% imshow(pic,[]); pixval on
```

```
% image(pic)
```

```
%%%%%%%%%%%%%%%%%%%%%%%%%%%%%%%%%%%%%%%%%%%%%%%%%%%%%%%%%%%%%%%%%%%%%%%%%%%%%%%%
%
% M file for centroid calculation
%
%%%%%%%%%%%%%%%%%%%%%%%%%%%%%%%%%%%%%%%%%%%%%%%%%%%%%%%%%%%%%%%%%%%%%%%%%%%%%%%%
% Function for centroid of a segment
function [meanx,meany,blnk] = centroid(pic)
[x,y,z] = size(pic);
if(z==1)
    ;
else
    pic = rgb2gray(pic);
end

im = pic;
[rows,cols] = size(im);
x = ones(rows,1)*[1:cols];
y = [1:rows]'*ones(1,cols);

area = sum(sum(im));
if area ~= 0
    meanx = sum(sum(double(im).*x))/area;
    meany = sum(sum(double(im).*y))/area;
    blnk = 0;
else
    meanx = cols/2;
    meany = rows/2;
    blnk = 1;
end



function mean = nzmean(a)
m = 0;
b = 0;
for i=1:size(a,1),
    for j=1:size(a,2),
        if a(i,j) ~= 0
            m = m + a(i,j);
        else
            b = b + 1;
        end
    end
end
mean = m / (size(a,1)*size(a,2) - b);



function std = nzstd(a)
s = 0;
b = 0;
al = a - nzmean(a);
for i=1:size(a,1),
    for j=1:size(a,2),
        if a(i,j) ~= 0
            s = s + al(i,j)*al(i,j);
        else
            b = b + 1;
        end
    end
end
std = sqrt(s / (size(a,1)*size(a,2) - b));
```

Appendix D

Research Publications

Key Engineering Materials Vols. 326-328 (2006) pp. 87-90
online at http://www.scientific.net

Characterization of Multipoint Diffraction Strain Sensor (MISS)

S. Iqbal[1, a], A. Asundi[2,b]

[1]Faculty of Applied Sciences, International I University, H-10, Islamabad, Pakistan

[2]School of Mechanical & Aeronautical Engineering, Nanyang Technological University, Singapore

[a]squresh7@yahoo.com, [b]anand.asundi@pmail.ntu.edu.sg

Keywords: strain sensor, diffraction grating, multi-lens array, laser beam, tilt measurement, CCD, spot centroid.

Abstract. A Multipoint Diffraction Strain Sensor (MISS) with the novel feature of simultaneous strain measurement at multiple points is characterized. Unlike conventional interferometry based systems, this patented sensor uses principles of diffraction to directly measure strain at large number of points. In this sensor, a high-frequency diffraction grating is illuminated by two symmetric laser beams and the diffracted beams are sampled on a CCD camera via a micro-lens array into an array of dots. The shift of the individual dots is sensed and strains or rigid body tilt are calculated directly. This novel technique is expected to be very valuable in numerous industrial applications.

Introduction

Optical methods are widely applied for the strain measurement in material and components. Interference has been widely used as a method for precision deformation measurement. However, there is a need to analyse a fringe pattern before useful information such as strains can be obtained. Diffraction based methods provide a means to directly measure strain measurement without the need for time-consuming fringe analysis and interpretation. Bell [1] first proposed diffraction grating-based strain gauge and since then many different innovations have been proposed [2,3]. Asundi et al [4,5] first proposed the use of a high-frequency diffraction grating along with a Position Sensing Detector (PSD) to provide a novel alternative to the conventional electrical resistance strain gauges with the same characteristics and direct read-out of strain components. All the above strain sensors including the electrical resistance strain gauge, are point-wise measuring systems. Now, a new patented [6] system has been developed which extends the earlier point diffraction strain sensors to a Multipoint Diffraction Strain Sensor (MISS). In this paper, the characteristics and specifications of MISS are explored. To our knowledge, such multipoint optical strain measurement feature has never been reported in earlier works.

Theory

The Multipoint Diffraction Strain Sensor (MISS) using a high-frequency diffraction grating along with a micro-lens array based CCD detector. A reflective diffraction grating is bonded to the surface of the specimen and follows the deformation of the underlying specimen. The grating is illuminated by two symmetric monochromatic laser beams at a prescribed angle such that the first order diffracted beams emerge normal to the specimen surface. The micro-lens array samples each of this incident beams and focuses them as spots onto the CCD. When the specimen is deformed, tilted or rotated, the diffracted wavefronts emerging from the specimen are distorted and hence the spots shift accordingly. Figure 1 shows the simulated spot pattern for a 4x4 array of micro-lenses for one of the beams when the specimen is unstrained, undergoes uniform strain and non-uniform strain. The symmetric beam incident from other direction gives a similar array of spot patterns. Strains at each spot location which corresponds to a small area of the specimen can then be readily deduced from the shift of the spots as described below. Without loss of generality, spots shifts along one direction are used in this derivation.

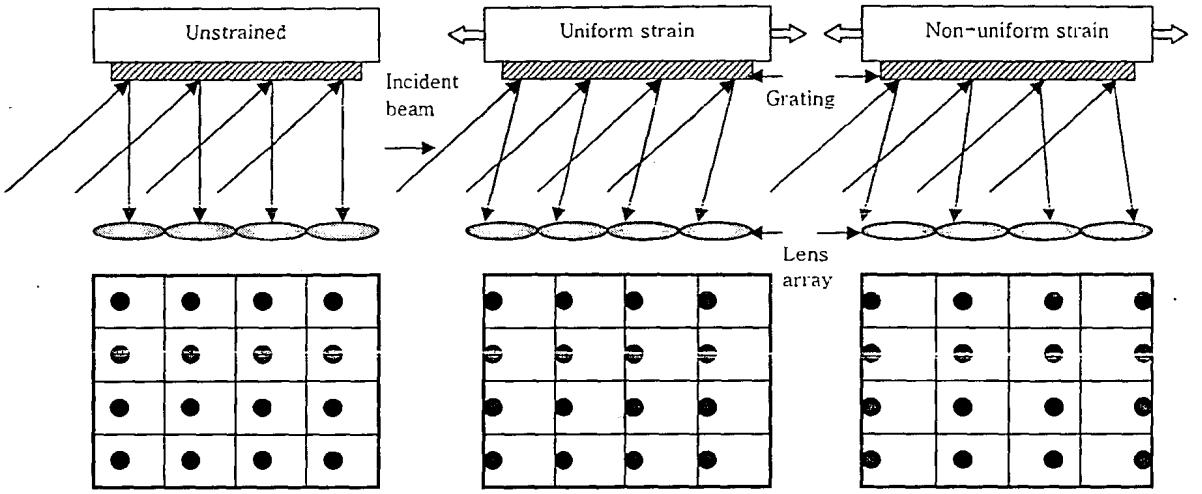

Fig. 1: Multipoint Diffraction Sensor principle

Starting from the well-known diffraction equation, the change in diffraction angle when the specimen is subject to strain, ε_x and out-of plane tilt, $\Delta\varphi$ can be deduced. Hence the corresponding shift, Δx, of a typical spot on the CCD plane can be related to the strain and tilt as

$$K_f \Delta x_1 / f = -\varepsilon_x f \sin\alpha + \Delta\phi(1+\cos\alpha),$$
$$K_f \Delta x_2 / f = +\varepsilon_x f \sin\alpha + \Delta\phi(1+\cos\alpha), \quad (1)$$

where f is focal length of each micro-lens, α is the angle of incidence and K_f is a multiplication factor which is 1 if the two beams are collimated and the subscripts 1 and 2 refer to the two incident beams. Solving these two equations gives

$$\varepsilon_x = K_f \frac{\Delta x_2 - \Delta x_1}{2f\sin\alpha},$$
$$\Delta\phi = K_f \frac{\Delta x_2 + \Delta x_1}{2f(1+\cos\alpha)}. \quad (2)$$

The two incident beams thus enable us to separately compute the strains and the rigid body tilts of the specimen.

System Construction

The MISS system is a compact, simple and versatile. The current system uses a 1/2" CCD camera with a 44 x 33 micro-lens array. Each micro-lens has a diameter of 144 μm and a focal length of 8.190 mm. The specimen grating is a 1200 lines/mm reflective diffraction grating. The specimen can be tilted using a precision rotation stage. Also the specimen has a strain gauge attached to the back side. A 685 nm laser diode is coupled into two optical fibers and provides the two symmetric incident beams. The spot image is digitized and processed using custom-developed software written in MATLAB® according to Eq. 2.

Results and System Performance

The process for strain measurement proceeds as follows. Record and determine centroid of the spot images for the unstrained sample (shown in Fig. 2(a) for one of the beams). Deform (strain and/or out-of-plane tilt) the specimen and record the deformed spot patterns for the two beams as shown in Fig. 2(b). Centroid detection is critical to this routine and as can be observed in Fig. 2(c), the spot images are not perfectly circular due to imperfections in the optics and gratings. The strain and tilt can then be deduced from the shifts according to Eq. 2, and are shown in Fig. 3.

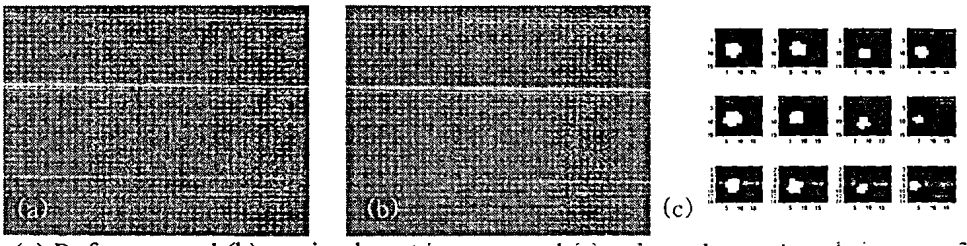

Fig. 2: (a) Reference and (b) strained spot images, and (c) enlarged sample sub-image of spots

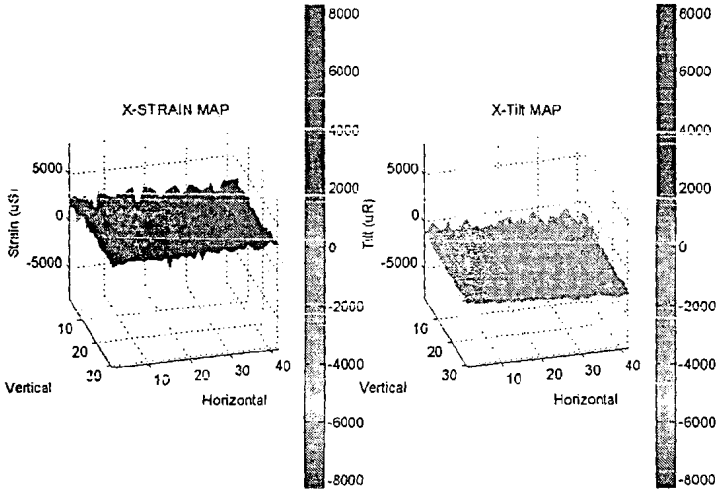

Fig. 3: (a) Strain and (b) tilt distribution for a specimen subject to uniform strain

Figure 4 shows the comparison of applied strain and tilt with the measured strain and tilt for increasing deformation of the specimen. The plot shows good correlation and linearity for the measured and applied values, thus verifying the MISS system. Some characteristics of the MISS system can be gleaned from these results. The sensitivity to strain/tilt is governed by the centroid detection algorithm, and for a 6 pixel square micro-spot, the sensitivity is 20 uε for strain and 10 uR for tilt. The accuracy was experimentally established as the standard deviation between multiply-recorded data, and was found to be about 10 uε for the mean strain measurements. The range for maximum strain and tilt, assuming that the spots remain within the same micro-lens, is governed by the maximum allowable shift of the individual spots. Based on Eq. 2, and considering that each sub-window has a size of 18x14 pixels, the maximum measurement range is 19 mε for strain and 9 mR for tilt along x-axis. Experimentally slightly smaller values were obtained due to the irregular spot shape. Based on the above experimental data the specifications of the MISS system are as given in Table 1.

INSTITUTE OF PHYSICS PUBLISHING MEASUREMENT SCIENCE AND TECHNOLOGY
Meas. Sci. Technol. 17 (2006) 2306–2312 doi:10.1088/0957-0233/17/8/036

Multipoint diffraction strain sensor: theory and results

S Iqbal[1] and A Asundi[2]

[1] Faculty of Applied Sciences, International I University, Sector H-10, Islamabad, Pakistan
[2] School of Mechanical and Aerospace Engineering, Nanyang Technological University, Singapore

E-mail: squresh7@yahoo.com and anand.asundi@pmail.ntu.edu.sg

Received 6 March 2006, in final form 22 April 2006
Published 20 July 2006
Online at stacks.iop.org/MST/17/2306

Abstract
A multipoint diffraction strain sensor has been developed using a moiré interferometer with the novel added feature of whole-field strain determination. This unique feature has been implemented by simultaneous tracking of sampled wavefront diffracted from the component under test. In this sensor a high-frequency diffraction grating is bonded on the specimen, which is illuminated by two symmetric collimated laser beams, as in a typical moiré interferometer. The first orders of diffracted beams impinge on a CCD camera, via a microlens array. The lens array serves a dual purpose—to sample the diffracted wavefront and to focus the wavefront to a number of spots on the CCD. The deviation of the individual spots generated by both the beams is directly proportional to the normal strain and a component of the shear strain. Simultaneous strain measurement at more than a thousand points can be readily obtained and is demonstrated in this paper. This novel technique is expected to be very valuable in numerous industrial metrology applications.

Keywords: strain sensor, diffraction grating, multi-lens array, laser beam, tilt measurement, CCD, spot centroid

(Some figures in this article are in colour only in the electronic version)

1. Introduction

Optical methods have shown great promise for contact-free deformation measurement using principles of diffraction, interference and polarization. For precision deformation measurements, interferometry has been widely used, though it entails time-consuming fringe analysis and numerical differentiation for strain calculation. Diffraction techniques directly provide derivatives of displacement using a straightforward approach and thus have better potential in strain analysis.

In 1956 Bell [1] first proposed a diffraction grating-based strain gauge. Since then, many different developments and variations have been proposed and many of them are now widely used in the industry, as reviewed by Moulder and Cardenas-Garcia [2] and Sevenhuijsen *et al* [3]. In these techniques researchers used various grating types and used imaging devices or position-sensitive devices (PSDs) for sensing [4–7]. Among these, the work of Asundi and Zhao [6] utilizing the approach of combining high-frequency grating with PSDs, offers many advantages over the conventional electrical resistance strain gauge, specifically the adjustable gauge (beam) size and multi-point measurement, while maintaining the advantages of high sensitivity and accuracy.

All these works deal with sensing strain at a single point like a strain gauge. Many applications in the industry warrant the measurement of strain distribution rather than sensing strain at a single point only. These may include strain variations present at a machine component under stress, a large beam used in a building structure or even a small component used in MEMS. Diffraction strain sensors and electrical strain gauges cannot fulfil this need unless placed in an array which is read out sequentially.

This paper presents a novel patented [8] technique for whole-field strain mapping using the sampled diffracted

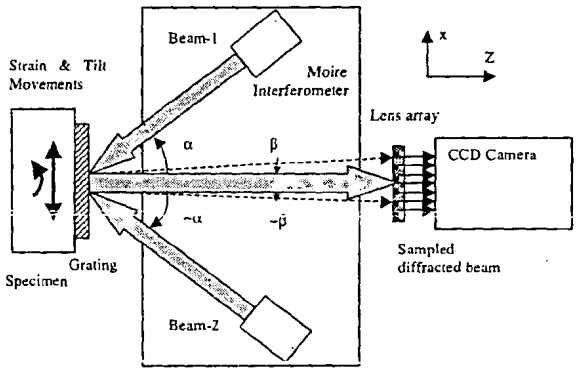

Figure 1. Operating principle of MDSS based on a moiré interferometer.

wavefronts. This research is expected to open up a new avenue and provide a versatile tool for industrial and structural applications, as a 2D map of strain on the component body may provide a much clearer picture to the analysis team.

Being a whole-field approach, this technique may also be compared with other whole-field strain measurement techniques such as moiré interferometry and ESPI. The obvious advantage of this technique compared to these is its direct approach. The strain is calculated without the need of any fringe processing and numerical differentiation needed for interferometry [9, 10]. Image subtraction for speckle techniques is also not needed here, which makes processing time much shorter and near real time. Also the total setup and the needed resources are going to be less. At the same time it can produce a map with good spatial resolution, which is only bounded by the separation of the micro-lenses on the array, i.e. distance between the individually shifting micro-spots. A clearer comparison of the technique is to be drawn as we go further with this work.

2. Theory

Moiré interferometry is normally used for optical measurement of mechanical deformation through fringe analysis. In this technique, two beams of monochromatic, coherent and collimated light symmetrically illuminate a specimen grating such that the first-order diffracted beams emerge normal to the surface of the grating. Interference of these two diffracted beams generates an interference pattern, which can be analysed to obtain the specimen deformation [11]. By recording the displacement components in two perpendicular directions, the three in-plane strain components can be obtained through numerical differentiation.

Figure 1 illustrates the principle of multipoint strain measurement using a setup similar to that for moiré interferometry. The diffracted wavefronts emerging from the grating are sampled into wavelets by the multi-lens array and focused onto the CCD. Each wavelet represents the diffraction from a small area of the sample surface. When the grating is deformed, the position of the diffracted wavelets on the CCD would shift accordingly as shown in figure 2. The shift of the spots is shown to be directly proportional to the derivative of the deformation. In this particular example, the shift of the spot is along one direction. However, in general the shift would be in two directions but the principle would be unaffected as the horizontal and vertical shifts are independent of each other.

Starting from the well-known diffraction equation [12] and differentiating it we get

$$P(\sin\alpha + \sin\beta) = m\lambda, \tag{1}$$

$$P\cos\alpha\,\mathrm{d}\alpha + \mathrm{d}P\sin\alpha + P\cos\beta\,\mathrm{d}\beta + \mathrm{d}P\sin\beta = 0, \tag{2}$$

where α, β are the angles of illumination and diffraction, P is the pitch of the grating whose principal direction is the x-axis (figure 1), m is the diffraction order (± 1) and λ is the wavelength of light.

The illumination angle is chosen such that the diffracted beam is normal to the grating or $\beta = 0$. Also during the experiment, the illumination angle remains unchanged or $\mathrm{d}\alpha = 0$. Thus

$$\mathrm{d}\beta = -\frac{\mathrm{d}P}{P}\sin\alpha = -\frac{\mathrm{d}u}{\mathrm{d}x}\sin\alpha = -\varepsilon_x \sin\alpha. \tag{3}$$

Here ε_x is the derivative of the displacement component along the grating principle direction ($\mathrm{d}u/\mathrm{d}x$), i.e. the normal component of the strain in the x-direction. The change in

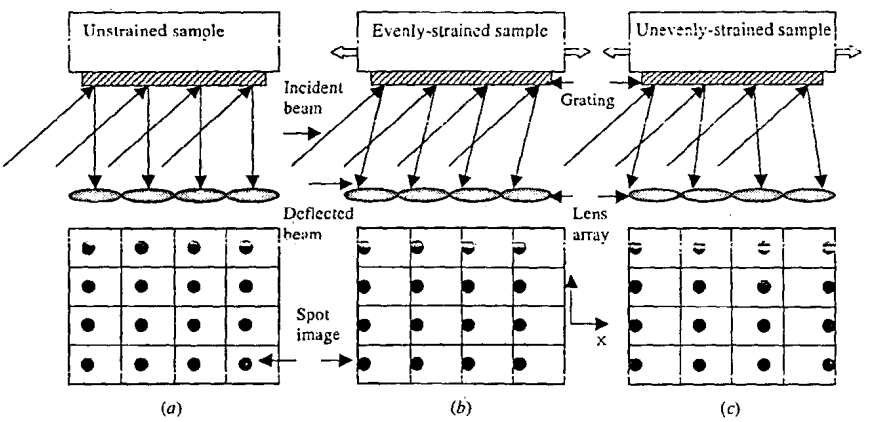

Figure 2. Position of individual micro-spots with (*a*) no strain, (*b*) uniform strain and (*c*) non-uniform strain in the sample.

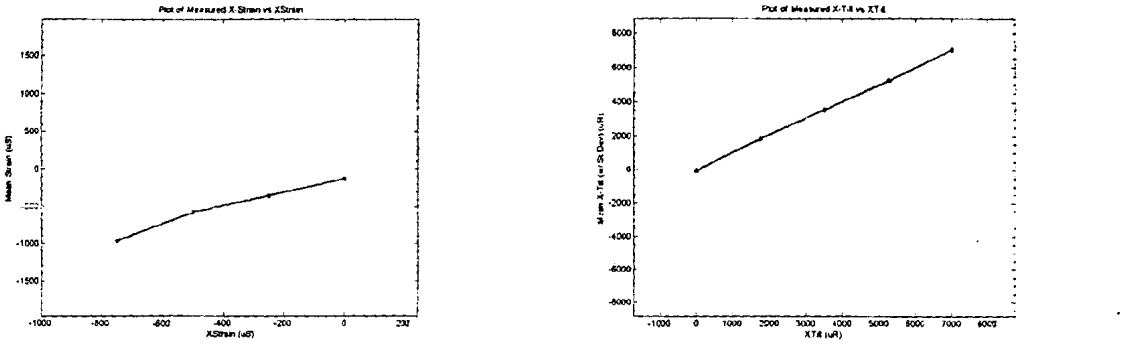

(a) (b)

Fig. 4: (a) Applied v/s measured strain (b) Applied v/s measured tilt

Table 1: Major Specifications of MDSS

Range	Measurement Linearity	Accuracy	Measurement Sensitivity	2-D Variability	Spatial Resolution
19 mε/ 9 mR	1% of FSD	10 με/ 5 μR	20 με /10 μR	10 με/ 5 μR	144 μm

Conclusions

A MISS system has been developed and characterized with a novel technique of simultaneous strain and tilt measurement at a large number of points. The current system is based on a simpler uncollimated laser beam setup. However, using a standard moiré Interferometric system with the current MISS, both strain and deformation patterns can be obtained in near real time without the need for fringe processing. The system characteristics are quite impressive and can be further improved with proper choice of incident laser, micro-lens array, and algorithm. Furthermore, the system is also capable of measuring rotation and shear strain. Indeed, it is possible to measure all three strain components as well as rotation and tilt making this a truly versatile whole-field strain sensing system. The system offers many promising features including a useful combination of compactness, data collection speed and results accuracy. Diverse applications of the technique in microelectronics, micromechanics and other areas are expected.

References

[1] J. F. Bell: *Determination of dynamic plastic strain through the use of diffraction gratings*, J. Appl. Phys. Vol. 27 (1956), p. 1109–1113.

[2] J. C. Moulder and J. F. Cardenas-Garcia: *Two-dimensional strain analysis using a video optical diffractometer*, Exp. Tech. Vol. 17 (1993), p. 11–16.

[3] P. J. Sevenhuijsen, J. S. Sirkis, and F. Bremand: *Current trends in obtaining deformation data from grids*, Exp. Tech. (1993), p. 22–26.

[4] A. Asundi and B. Zhao: *Optical strain sensor using position-sensitive detector and diffraction grating: error analysis*, Opt. Eng. Vol. 39-6 (2000), p. 1655-1651.

[5] B. Zhao, H. Xie and A. Asundi: *Optical strain sensor using median density grating foil: Rivaling the electric strain gauge*, Rev. Sci. Inst. Vol. 72-2 (2001), p. 1554-1558.

[6] A. Asundi, S. Mhaisalkar and A. Priyadarshi, *Moiré Interferometric Strain Sensor*, US Patent Application, PAT/026/05/05/US - Moire Interferometric Strain Sensor (2005).

diffracted angle $d\beta$ can be calculated using the spot shift on the sensor surface as

$$\Delta x_1 = f\,d\beta = -\varepsilon_x f \sin\alpha, \tag{4}$$

where f is the focal length of the lens. The symmetrical beam incident from the equal but opposite direction will cause an equal but opposite shift of the wavelet spot. Thus

$$\Delta x_1 = -\varepsilon_x f \sin\alpha. \tag{5a}$$

$$\Delta x_2 = \varepsilon_x f \sin\alpha. \tag{5b}$$

Combining the two equations we get

$$\varepsilon_x = \frac{du}{dx} = \frac{\Delta x_2 - \Delta x_1}{2f\sin\alpha} = \frac{(\Delta x_2 - \Delta x_1)P}{2f\lambda}. \tag{6}$$

The use of two beams in this manner eliminates measurement errors due to out-of-plane tilt of the specimen. A very similar expression can be derived for the y-axis strain component calculations. If the principal direction of the grating is the y-direction and the illumination beams are in the y–z plane, then

$$\varepsilon_y = \frac{dv}{dy} = \frac{\Delta y_2 - \Delta y_1}{2f\sin\alpha} = \frac{(\Delta y_2 - \Delta y_1)P}{2f\lambda}. \tag{7}$$

If, on the other hand, the sample experiences shear strain or a rotation [11, 12], then this will be recorded as orthogonal movements of the spot array, i.e. for the grating lines parallel to the y-axis, the spots would shift in the y-direction (figure 2). As the rotation or shear is given by the orthogonal movement of the spots, it may be detected simultaneously with the normal strain. Thus if the sample is rotated within the plane by an angle ϕ, its orthogonal diffraction angle is [12] given by

$$\sin\beta_y = \sin\alpha\sin\phi. \tag{8}$$

Differentiating this and equating to spot movement as before, and noting that the diffracted beam is initially normal to the grating plane at zero rotation, we get

$$d\beta_y = \sin\alpha\,d\phi = \Delta y_1/f. \tag{9}$$

Thus for the two beams with the grating principal axis along the x-direction, we get

$$\Delta\phi = \frac{\Delta y_2 - \Delta y_1}{2f\sin\alpha} = \frac{du}{dy}, \tag{10a}$$

and similarly for the grating with the principal direction along the y-direction,

$$\Delta\phi = \frac{\Delta x_2 - \Delta x_1}{2f\sin\alpha} = \frac{dv}{dx}. \tag{10b}$$

Hence all three components of in-plane strain can be deduced.

3. System construction

The setup for the multipoint diffraction strain sensor has been developed to be compact, relatively simple and versatile at the same time, in view of its projected use in precision machine or microelectronics industry. The system utilizes a lens array made up of 44 × 33 lenslets and a 1/2″ diagonal CCD detector camera with an aperture of 6.4 mm × 4.8 mm. The diameter of each lenslet is 144 μm and the focal length of each is 8.190 mm. A polarizing attenuator controls the light intensity incident on the camera surface. A cross grating of 1200 lines mm^{-1} was bonded on the sample surface as the target. The specimen could be rotated as well as deformed in its plane. A commercial moiré interferometer as shown in figure 3 was used as it simplifies alignment and also allows for additional verification of strains from the moiré interferometric fringes, which could also be recorded. Indeed, while the multipoint diffraction strain sensor can be used on its own, it is also a convenient add-on to commercial moiré interferometers.

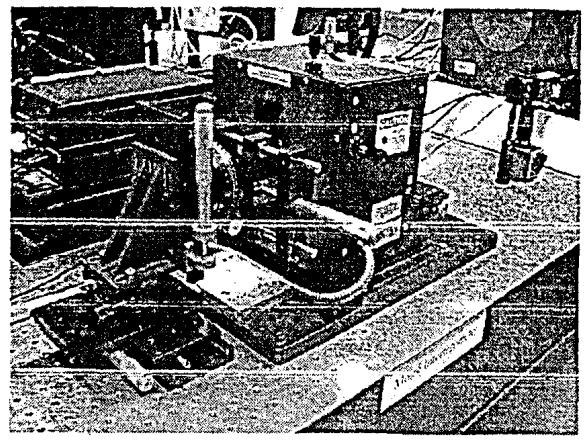

Figure 3. MDSS adapted to a commercial moiré interferometer.

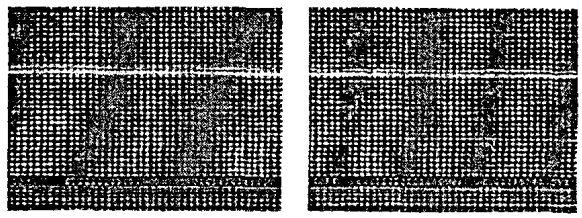

(*a*) (*b*)

Figure 4. Fringe pattern of (*a*) reference and (*b*) strained images for comparative strain calculation.

The strain measurement is checked against the strain value calculated via fringe analysis. Thus, the average x-axis fringe spacing in the reference image and in the strained image are determined as shown in figure 4. Then the relative strain is calculated from the difference in fringe spacing Δs and virtual grating frequency f_v as $\varepsilon_x = 1/f_v\Delta s$. For the MDSS, the normal in-plane strains are calculated using equations (6) and (7) for u- and v-fields respectively, while equation (10) is used for shear or rotation. The spot centroids for each beam before and after loading are determined using a sub-pixel centroid detection algorithm and the entire calculation is programmed in MATLAB® which in addition permits other checks on the calculations to be performed as well. Each beamlet window is of about 18 × 14 pixel size. Illuminated pixels of light spot are determined by comparing the light level of each pixel with a specific threshold and thus the sub-pixel centroid position from the illuminated pixels is computed.

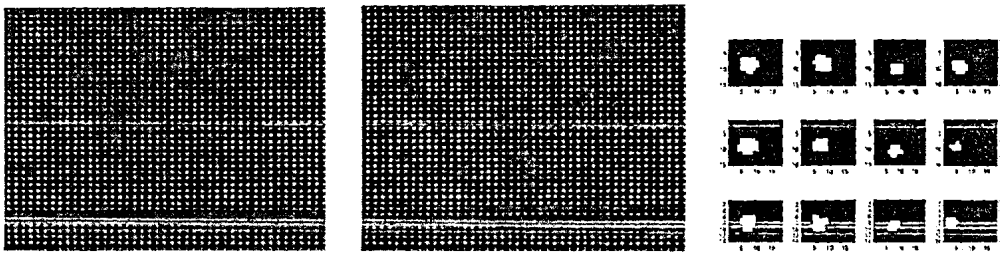

(*a*) (*b*) (*c*)

Figure 5. (*a*) Reference and (*b*) strained images along with (*c*) sampled spot images.

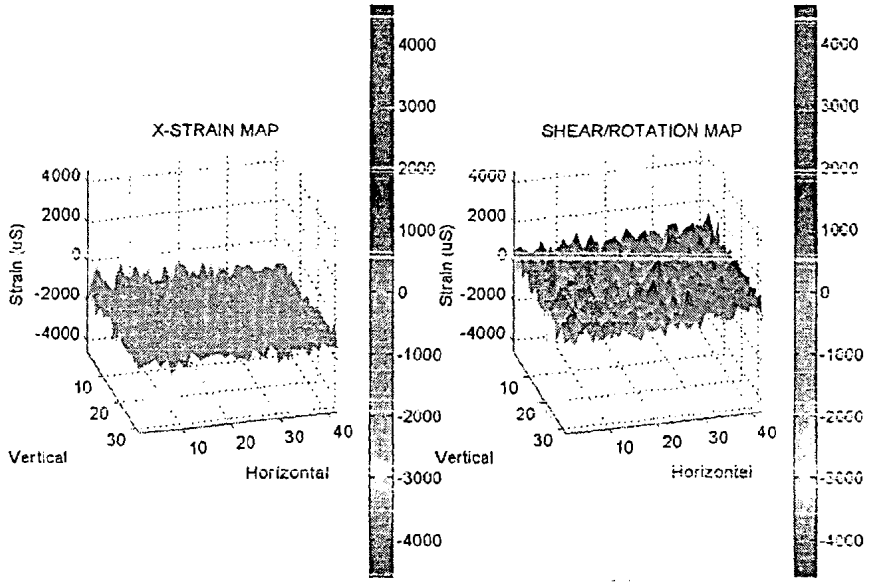

Figure 6. 2D strain map for uniform *x*-strain (with some shear component).

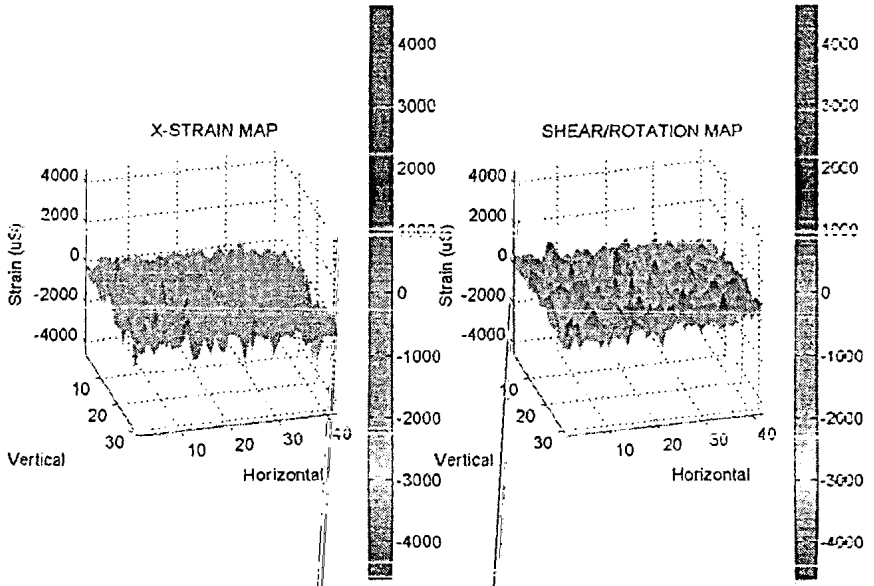

Figure 7. 2D strain map for non-uniform strain (poking from the right-hand side makes the right edge strain values in the map more negative, with a visible ditch in the middle of the edge.)

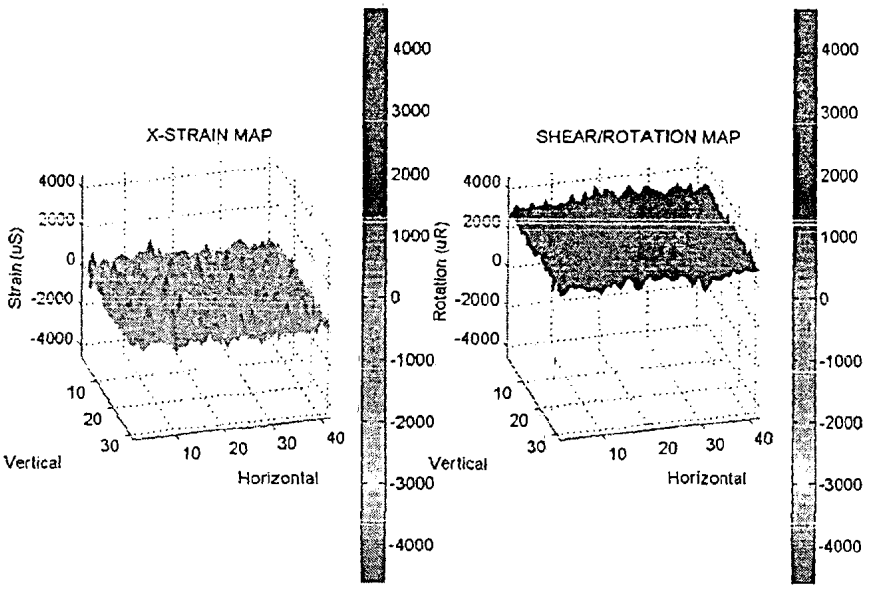

Figure 8. Strain and rotation maps for pure rotation applied.

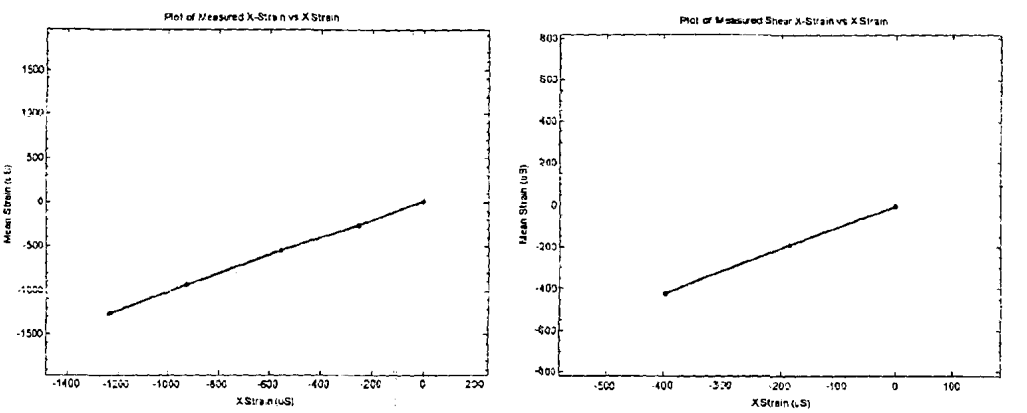

(a) (b)

Figure 9. Mean (*a*) normal *x*-strain and (*b*) shear strain for increasing applied load—comparison of measurement with MDSS (vertical) and with the moiré interferometric fringe method (horizontal).

4. System output

The operation of the multipoint diffraction strain sensor starts by the input of reference images taken alternately by switching on the right and left interferometer beams, and recording the beams diffracted from the unstrained specimen. The centroids of the individual spots are computed from these images and stored by the system software as the reference positions. Afterwards the sample is strained and two images of the beam diffracted from the strained sample using the right and left beams are processed as before. The system computes the individual shift of each spot in the images both from the right and left beams and thus computes the strain averaged over each sampled area. In addition, any shear (orthogonal) strain or in-plane rotation of the specimen is also calculated and displayed in the form of a distribution map. Typical spot images along with an enlarged view of a few subimages are shown in figure 5.

The data processing operation of the system is fairly fast and the strain map is produced almost instantly, i.e. within a few seconds. Simultaneously, detailed statistics of the strain distribution are also displayed, such as mean, standard deviation, etc. As an image from each of the right and left beams is needed under a certain strain condition, straining of the sample may be done in steps, while stopping and allowing for beam switching and imaging operations. For a quicker computation process, the system also has the provision of feeding multi-step stored data of the strained images at a time and a multi-step mean strain curve is also produced, as shown later.

The tests were mostly performed on a circular disc sample of hard plastic about 2.5″ of diameter, with a grating rigidly bonded on its surface. For the case of in-plane strain, the resulting strain map of sampled area is shown in figure 6. Since the area is small and as can be seen from the

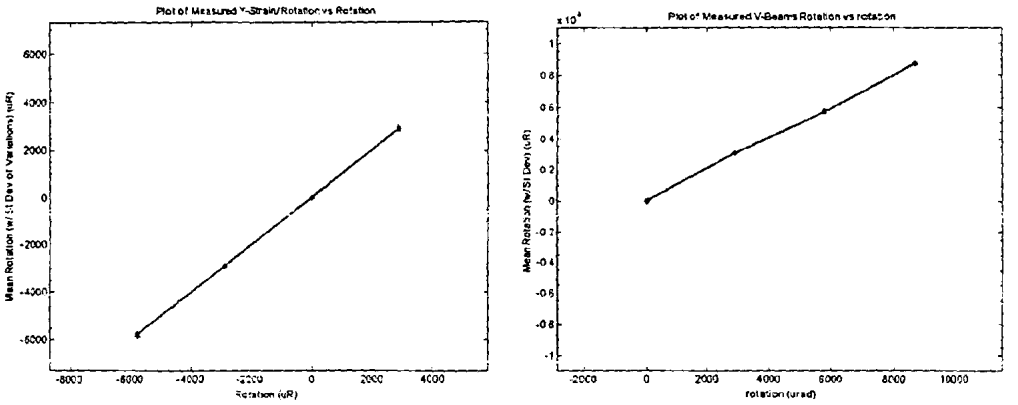

(*a*) (*b*)

Figure 10. Comparison of applied rotation (horizontal) with that measured using MDSS (vertical) with the grating principal direction as (*a*) *x*-direction and (*b*) *y*-direction.

fringe patterns in figure 4, the strain is fairly uniform. Also, although the rotation/shear strain component in this case is small, the shear strain/rotation map picks up these changes which are not apparent from the fringe pattern. Figure 7 shows the case of non-uniform strain by poking a wedge on the right edge of the disc. Figure 8 shows the results for the case of pure rotation. In this case, the normal strain component is zero as is to be expected and the shear component shows uniform rotation over the entire sampled area. In these maps, strain (or rotation) is given as grey-scale (colour-coded) along the vertical axis, with the units of μS (micro-strain or $\mu\varepsilon$) or μR (micro-radians).

To compare the results with the moiré interferometric pattern, the average strain from all the spots was determined and compared with the average strain calculated from the fringe spacing in moiré interferometry at different loads and rotations. Figure 9 shows the mean normal strain and shear strain comparisons for the disc under compression. Good correlation (within a few per cent) is found between the calculated and experimental values. Similarly for the case of rotation, the rotation measured using MDSS is compared with the rotation values applied. Once again the correlation is excellent as seen in figure 10. This figure contains rotations measured from both the gratings with figure 10(*a*) corresponding to a grating with the *x*-direction as the principal direction and figure 10(*b*) shows the grating with the *y*-direction as the principal direction.

5. Conclusions

A new multipoint diffraction strain sensor has been developed with the novel feature of simultaneous strain measurement at a large array of points. The system is based on the simultaneous position tracking of diffracted wavelets of the distorted wave, emerging from the component under test. With the use of a commercial moiré interferometer system, both strain and deformation distribution patterns can be obtained in near real time without the need for fringe processing. Furthermore, the system is also capable of measuring rotation and shear strain. Indeed, it is possible to measure all three strain components as well as rotation, *x*-tilt and *y*-tilt making this a truly versatile whole-field strain/tilt sensing system. The system offers many promising features including a useful combination of compactness, data collection speed and accuracy of results. This novel technique is expected to be very valuable in numerous industrial metrology applications in micromechanics, microelectronics and other areas.

Acknowledgments

The authors are deeply indebted to School of Mechanical and Aerospace Engineering, Nanyang Technological University for provision of necessary facilities for this work. We are also grateful to the staff and students of the Photonics and Microsciences Lab, and specifically to Mr Vijay Raj Singh. Support from Mr Subodh Mhaisalkar is also gratefully acknowledged. This work was supported by Pakistan Higher Education Commission scholarship.

References

[1] Bell J F 1956 Determination of dynamic plastic strain through the use of diffraction gratings *J. Appl. Phys.* **27** 1109–13

[2] Moulder J C and Cardenas-Garcia J F 1993 Two-dimensional strain analysis using a video optical diffractometer *Exp. Tech.* **17** 11–6

[3] Sevenhuijsen P J, Sirkis J S and Bremand F 1993 Current trends in obtaining deformation data from grids *Exp. Tech.* **17** 22–6

[4] Ma Y and Kurita M 1993 Strain measurement using high-frequency diffraction grating *JSME Int. J.* A **36** 309–13

[5] Kozlowska A 1994 Fiber optic grating interferometer for in-plane displacement measurement *Interferometry '94: Interferometric Fiber Sensing: Proc. SPIE* vol 2341 ed E Udd and R P Tatam pp 124–31

[6] Asundi A and Zhao B 2000 Optical strain sensor using position-sensitive detector and diffraction grating: error analysis *Opt. Eng.* **39** 1645–51

[7] Zhao B, Xie H and Asundi A 2001 Optical strain sensor using median density grating foil: rivaling the electric strain gauge *Rev. Sci. Instrum.* **72** 1554–8

[8] Asundi A, Mhaisalkar S and Priyadarshi A 2005 Moiré interferometric strain sensor, Ref: PAT/026/05/05/US (patent applied)

[9] Cordero R R, François M, Lira I and Vial-Edwards C 2005 Whole-field analysis of uniaxial tensile tests by moiré interferometry *Opt. Lasers Eng.* 43 919–36
[10] Nicoletto G 2002 On the visualization of heterogeneous plastic strains by moiré interferometry *Opt. Lasers Eng.* 37 433–42
[11] Post D, Han B and Ifju P 1994 *High Sensitivity Moiré: Experimental Analysis for Mechanics and Materials* (New York: Springer)
[12] Palmer C A and Loewen E G 2000 *Diffraction Grating Handbook* (New York: Thermo RGL)

Characterization of multipoint diffraction strain and tilt sensor based on moiré interferometer and multichannel imaging position-sensitive detector

Salman Iqbal and Anand Asundi
School of Mechanical and Aerospace Engineering, 50 Nanyang Avenue, Singapore 639798

(Received 6 August 2006; accepted 2 October 2006; published online 29 November 2006)

A multipoint diffraction strain and tilt sensor using a multichannel imaging position-sensitive detector has been developed and characterized, with the novel feature of simultaneous measurement of strain and tilt at a large array of points. Unlike conventional interferometry based systems, this new whole-field measurement system uses principles of diffraction to directly measure strain at the desired points. The system utilizes a moiré interferometer for the generation of two coherent and symmetric beams, which illuminate a high-frequency diffraction grating, bonded on the surface of the sample under test. The core of the system is a charge coupled device camera fitted with an array of microlenses, which samples the diffracted beam into an array of beamlets. The camera with lens array, which is being used as array-type multichannel position-sensitive detectors, senses the shift of the individual microspots. The deviation is then processed and the normal and shear strains are calculated at that spot along with rigid-body tilt. The combined results are graphically shown to the user as two-dimensional strain and tilt maps. Simultaneous strain measurement at more than 1300 points has been successfully obtained with the spatial resolution of better than 150 μm. This novel technique has many useful features compared to other whole-field optical strain measurement techniques and is expected to be very valuable in experimental mechanics of microsystems and devices. © *2006 American Institute of Physics.* [DOI: 10.1063/1.2372732]

I. INTRODUCTION

For contactless measurement of displacement, rotation, and strain, optical methods are widely applied. The instruments for strain measurement use the principles of diffraction, interference, or polarization. For precision deformation measurement, interferometry has been widely used, though it entails time-consuming fringe analysis. Diffraction is a relatively straight forward technique for direct strain measurement. Another important advantage is that, in addition to strain, rigid-body tilts and rotations can also be determined separately which is not easily done with interferometers. Bell[1] first proposed a diffraction grating-based strain gauge in 1956. Since then, many different developments and variations have been proposed as reviewed by Moulder and Cardenas-Garcia[2] and Sevenhuijsen *et al.*[3] In these techniques researchers used diverse setups with- low and high-frequency gratings and position-sensitive devices (PSDs) or charge coupled device (CCD) detectors.[4–7]

In all the earlier works, strain is determined at a single point like a strain gauge. Many applications in industry require measurement of nonuniform strain distribution rather than sensing strain at a single point only. In addition to strain, the component may undergo in-plane rotation or out-of-plane tilt under the stressing forces. These tilts should be separately sensed or at least be singled out from the measured strain. Also important is the case of warping, where a flexible component undergoes nonuniform tilt. The diffraction strain sensors, or the electrical strain gauges, cannot fulfill the need of multipoint strain sensing unless placed in an array configuration, and of course are not equipped for the multiplane tilt measurements.

Here we present a novel technique for whole-field strain and tilt mapping,[8] by sensing the movement pattern of sampled diffracted wave front. This research is expected to open up a new avenue and provide a versatile tool for the industrial and structural applications. To our knowledge, such multipoint optical strain and tilt measurement feature has never been reported in earlier works.

Being a whole-field approach, this technique can be compared with other whole-field optical strain measurement techniques such as moiré interferometry and electronic speckle pattern interferometry as follows.

(i) The obvious advantage of this multipoint diffraction method compared to others is its direct approach. The strain is calculated without the need of any fringe processing and numerical differentiation needed for interferometry.[9,10] Image subtraction for speckle techniques is also not needed here. This makes processing time needed for the final strain map calculation much shorter and near real time. We found the time taken for the production of strain and tilt maps consisting of more than 1300 points to be less than 5 s.

(ii) At the same time it can produce map with good spatial resolution compared to other methods and specifically to speckle technique. Here this resolution is only limited by the separation of the microlenses on the array, which is 150 μm in the present system.

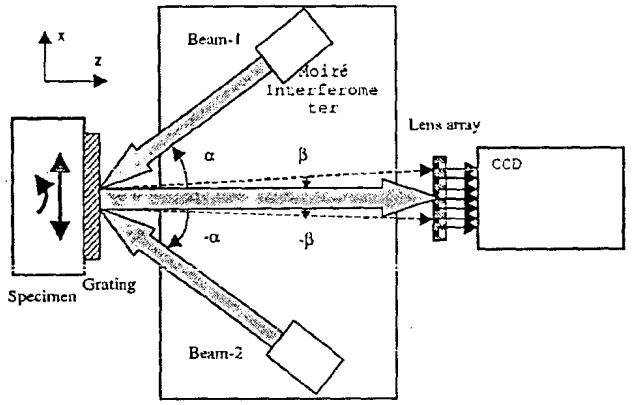

FIG. 1. Multipoint diffraction strain and tilt sensor principle.

(iii) The results show good combination of sensitivity and accuracy considering other whole-field approaches and specifically compared to speckle method where measurement quality is largely hampered by the poorer fringe visibility.

(iv) Being a simpler approach, the total computing and storage resources needed for this method are going to be smaller.

II. THEORY

In conventional moiré interferometry two symmetrical beams of monochromatic coherent light illuminate a specimen with a grating bonded on it such that the first diffraction orders emerge normal to the surface. These diffracted beams interfere to generate fringe patterns, which provide contours of displacement component in the principal direction of the grating. These fringes can be processed and numerically differentiated to give in-plane strains.[11] Due to the interference effect, rigid-body tilt is automatically canceled out. On the other hand, the proposed system samples each of the diffracted beams separately via a microlens array. The difference in diffraction angles is determined and used to compute in-plane strains as well as out-of-plane tilt.

Figure 1 illustrates the principle of multipoint strain and tilt measurement adapted to a conventional moiré interferometer. The diffracted beams are sequentially sampled by the lens array and focused onto a CCD detector. Each sampled beamlet represents the diffraction from a specific region of the specimen grating. When the grating is deformed, tilted, or rotated, the position of the diffracted beamlets shifts accordingly. The shift of these diffraction spots is directly proportional to the strain, rotation, or tilt experienced by the sample. Figure 2 shows schematically the movement of microspots sampled from the two diffracted beams, when the specimen is strained or tilted. The movement of the microspots is in opposite directions for strain but moves in the same direction for tilt.

Consider the setup in Fig. 1, where the two beams interrogate the grating with the principal direction along the x axis. Starting from the well-known diffraction equation,[12] and then taking its differential, we get

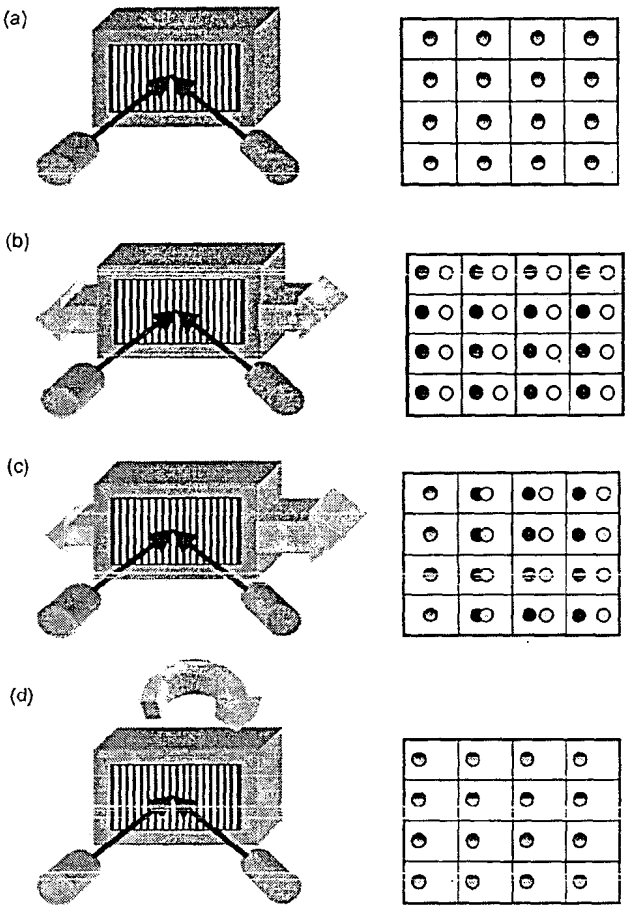

FIG. 2. Deformations and respective changes in microspots of both beams: (a) unstrained sample with both spots coinciding in the middle, (b) uniform strain with spots moving sideways, (c) nonuniform or heterogeneous strain, and (d) uniform tilt with spots moving in tandem.

$$P(\sin\alpha + \sin\beta) = m\lambda, \tag{1}$$

$$P\cos\alpha d\alpha + dP\sin\alpha + P\cos\beta d\beta + dP\sin\beta = 0, \tag{2}$$

where P is the pitch of the specimen grating, α and β are the angles of incidence and diffraction, and λ is the wavelength of the light.

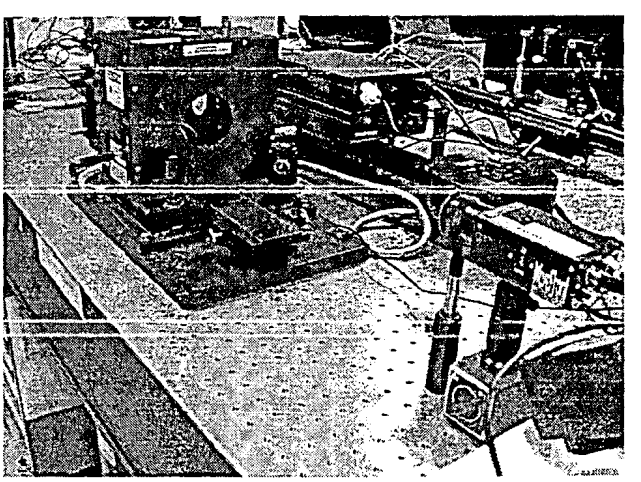

FIG. 3. (Color online) MDSS adapted to a commercial moiré interferometer.

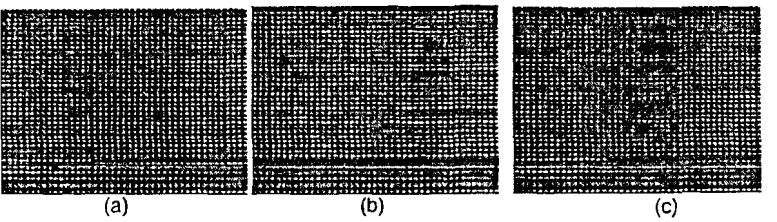

FIG. 4. (Color online) Typical spot images for one beam (a) before load and (b) after load. (c) Combined color image with red spots before deformation and green spots after deformation.

If the angle of incidence is chosen such that the diffracted beam is normal to the specimen, i.e., $\beta=0$, and also noting that the angle of incidence remains unchanged or $d\alpha=0$, Eq. (2) can be simplified to

$$d\beta = -\left(\frac{dP}{P}\right)\sin\alpha = -\varepsilon_x \sin\alpha. \tag{3}$$

Here ε_x is the component of the strain in the x direction. The change in diffracted angle $d\beta$ can be determined by calculating the spot shift on the CCD sensor. For the symmetric beam, since the angle of incidence is negative, the diffracted beam would have an equal but opposite change in angle. Hence the relative shift between the two diffracted beams,[6,7] gives the normal strain as

$$\varepsilon_x = \frac{du}{dx} = \frac{d\beta}{2\sin\alpha} = \frac{\Delta x}{2f\sin\alpha} = \frac{\Delta x^* P}{2f\lambda}, \tag{4}$$

where Δx is the relative shift between the two spots as shown in Fig. 2(b) and f is the focal length of lenses in the lens array.

Similarly, the normal strain component in the y direction is obtained by interrogating the grating whose principal direction is along the y axis,

$$\varepsilon_y = \frac{dv}{dy} = \frac{(\Delta y_2 - \Delta y_1)}{2f\sin\alpha} = \frac{(\Delta y_2 - \Delta y_1)P}{2f\lambda}. \tag{5}$$

In addition, if the sample undergoes out-of-plane tilt in the xz plane, the individual light spots would also shift but in this case in the same direction. Since in this case the grating period does not change, i.e., $dP=0$, and the change in the angle of incidence is equal to the tilt of the sample or $d\alpha = \Delta\theta_x$. Eq. (2) becomes

$$d\beta = -\Delta\theta_x \cos\alpha. \tag{6}$$

Hence the measured shift of the beam on the sensor is due to the tilt of the grating and the resulting diffraction angle change, which gives

$$d\beta = \Delta\theta_x - \frac{\Delta x_1}{f}. \tag{7}$$

Thus adding the shift of the two beams, the tilt can be derived as

$$\Delta\theta_x = \frac{\Delta x_1 + \Delta x_2}{2f(1+\cos\alpha)}. \tag{8}$$

A similar expression can be formed for the vertical tilt in the yz plane to be

$$\Delta\theta_y = \frac{\Delta y_1 + \Delta y_2}{2f(1+\cos\alpha)}. \tag{9}$$

The two incident beams thus enable us to separately compute all the strain components as well as the out-of-plane rigid-body tilt at each point of the specimen.

III. SYSTEM CONSTRUCTION AND RESULTS

The setup for a multipoint diffraction strain sensor (MDSS) is compact, simple, and versatile owing to its projected use in precision machine or microelectronics industry. The system uses a 44×33 microlens array coupled to a 6.4×4.8 mm^2 CCD detector. The diameter of each microlens is 144 μm with a focal length of 8.190 mm. The specimen is a circular disk under compressive loading onto which a reflective high-frequency 1200 lines/mm cross-line diffraction grating is bonded. The specimen placed on a precision rotational stage is diametrically strained by a mechanical loading machine. The specimen is set up in a commercial moiré interferometer, which also allows for the additional verification of strain values from the moiré interferometric fringes that could be simultaneously recorded. Figure 3 is a photograph of the system.

The operation of the MDSS starts by taking the reference images of sampled diffracted beams produced by the right and left beams incident on the unstrained specimen. The specimen is then strained or tilted and two diffracted images are recorded. The system computes the shift of each spot in the image both from the right and left beams; and thus computes the local strain present at that spot using Eq. (4) or (5). Along with this, any out-of-plane tilt of the specimen is also calculated using Eqs. (8) and (9). Typical images before and after strain for one of the beams is shown in Fig. 4.

The strain measurement by our system is checked and compared against the strain value calculated via interferometric fringe analysis. Thus, the average x-axis fringe spacing in the reference image and in the strained image are determined, as shown in Fig. 5. Then the relative strain is calculated from difference in fringe spacing Δs and virtual grating frequency f_v as $\varepsilon_x = 1/f_v\Delta s$. For the MDSS, the nor-

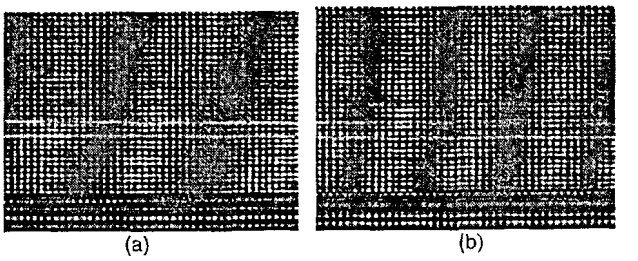

FIG. 5. Fringe pattern of (a) reference and (b) strained images for comparative strain calculation.

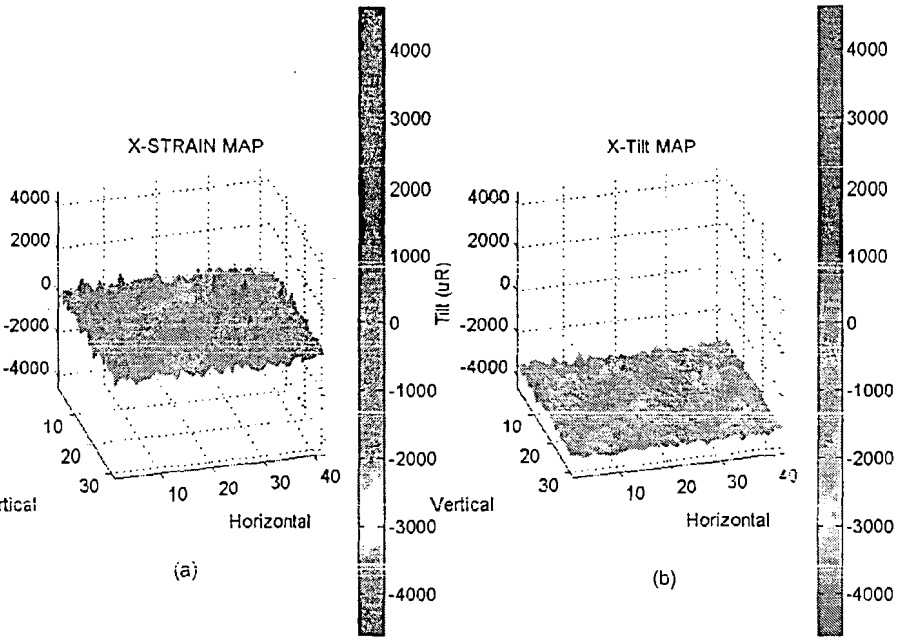

FIG. 6. (a) Strain and (b) tilt distribution for a specimen subjected to uniform tilt.

l in-plane strains and the tilt are calculated using the equations given earlier. The spot centroids for each beam before d after loading are determined using a subpixel centroid tection algorithm.

The two-dimensional maps of x strain and x tilt for applied tilt are shown in Fig. 6. For pure rigid-body tilt, there ould be no strain as is evident from the figure. The small mps in the strain plot are attributed to imperfections in the ating or optical alignment. This highlights the sensitivity of e method as the fringe patterns do not show any fringes as expected. The system also has the provision of plotting a ain curve for gradually increasing strain or tilt using the ltiple sets of strained images for each step.

SYSTEM CHARACTERIZATION

Table I shows the comparison of the average applied and easured values of strain and tilt, for specimen subject to nstant strain/tilt. The applied strain values are deduced m the moiré interferometric fringe patterns, which were nultaneously recorded while the tilt is measured using the rnier on the rotational stage. The comparison shows good rrelation and linearity between the measured and applied lues, thus verifying the measurement capability of this chnique. The measurement linearity of the system is within 1% of full-scale deflection for strain measurements and within 2% of full-scale deflection for the tilt measurements.

The system sensitivity to strain or tilt changes depends on the resolution of the CCD and the centroid detection algorithm. For a spot covering an area of 6×6 pixels (which is typical in the current experiment as shown in Fig. 7), and a smallest detectable shift of one pixel, the strain sensitivity is 18 $\mu\varepsilon$ and tilt sensitivity is 8 μrad.

With regard to the accuracy of the system, one needs to consider the accuracy of different spots over the entire CCD array to ensure that the same strains are measured at all points. This is referred to as global accuracy. On the other hand, the repeatability of measurement at a single sensing area is a measure of the system's local accuracy. The global accuracy of the system was experimentally established as the standard deviation of multiple-recorded data, as shown in Fig. 8. It was found that the global accuracy of mean strain calculation is about 3 $\mu\varepsilon$ and that of the mean tilt calculation is about 1.5 μrad. On the other hand, the local accuracy was found to be 50 $\mu\varepsilon$ which is primarily due to the pixel resolution and centroid detection algorithm.

The range for maximum strain and tilt, assuming that the spots remain within the same microlens area, is governed by the maximum allowable shift of the individual microspots. The measurement range can be calculated based on the equations for the single-axis strain and tilt calculation derived earlier, and considering the usable size of each subwindow is 18×14 pixels minus the size of the spot. Starting from the

BLE I. Comparison of average applied and measured values of x strain x tilt.

x strain ($\mu\varepsilon$)		x tilt (μ rad)	
Applied	Measured	Applied	Measured
−1234	−1264	−3500	−3641
−926	−931	−1750	−1680
−555	−547	0	5
−252	−254	1750	1654
0	17		

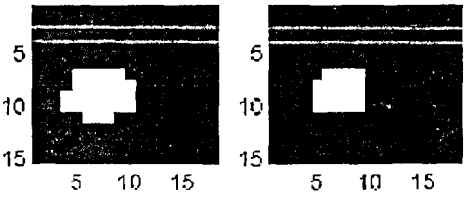

FIG. 7. Enlarged subwindows showing microspots' shape and size in pixels.

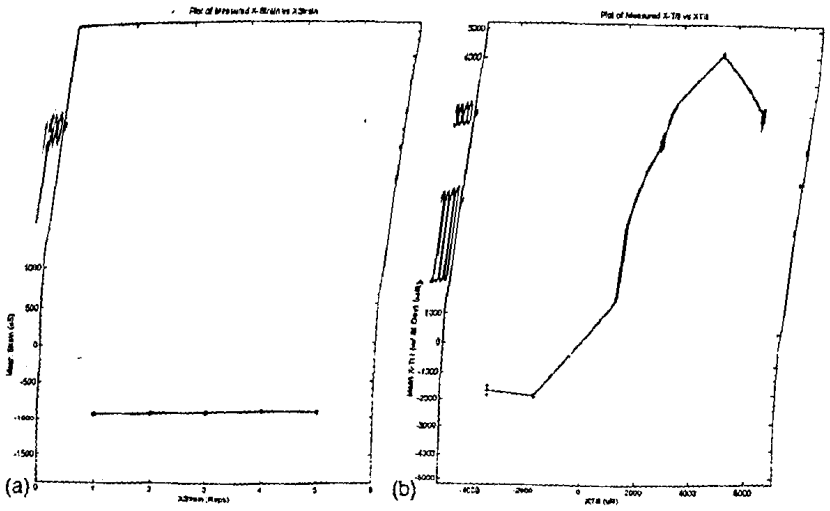

FIG. 8. (a) Multiple readings at the same strain fo accuracy determination; (b) tilt range given as a linea region of the curve.

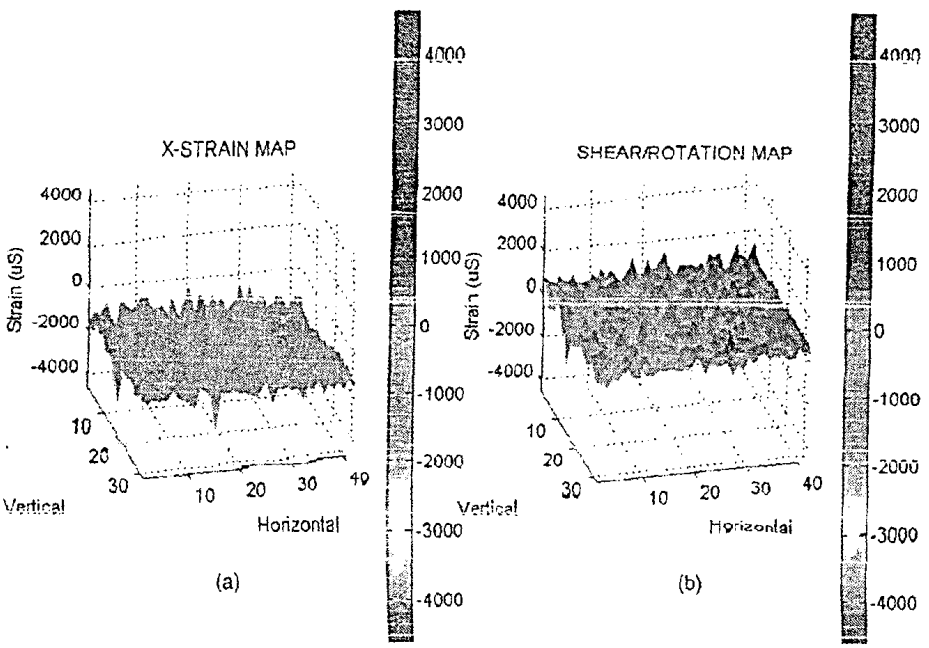

FIG. 9. (Color online) Strain map showing narrow strain peaks.

no-strain condition of coincident spots, the maximum spot separation obtained within a subwindow is about 100 μm, which puts the strain measurement range at 8 me. Similarly the maximum tilt change to be measured is 7.5 mrad. Experimentally smaller values of 5–6 mrad were achieved for the tilt measurement as shown in Fig. 8, probably due to the larger measurement steps and irregularities in the spot shape.

The spatial resolution of the system depends on the separation between the individual microspots on the CCD surface. For a 44×33 lens array and a 6.4×4.8 mm^2 CCD, this resolution is about 145 μm which coincides with the diameter of the microlens of 144 μm. Figure 9 shows an example of the strain map for the given CCD size, where peaks of irregular strain are evident indicating the high spatial resolution of the system.

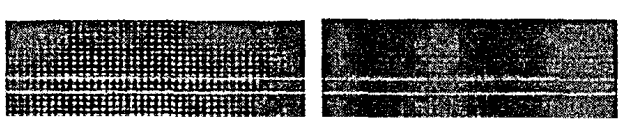

V. DESIGN DECISIONS

Design of this new system passed through different stages and involved design trade-offs at these stages. Following are some of the important decisions taken en route for performance improvement.

A. Use of moiré interferometer

The principle of multichannel diffraction measurement can be implemented with different laser beams having different beam properties. In the beginning of our experimentation, a pair of collimated but narrow beams from fiber laser source was used for this purpose. The images obtained of the diffracted beam are shown in Fig. 10. The obvious problem seen was that the beam could not illuminate the whole screen at the same time, and also that the illuminated part of the lens array changed with the shift of the beam, thus making the reliable strain calculation very difficult. The next beam type tried was the uncollimated divergent beam from the same source, which would easily fill more than the whole of the

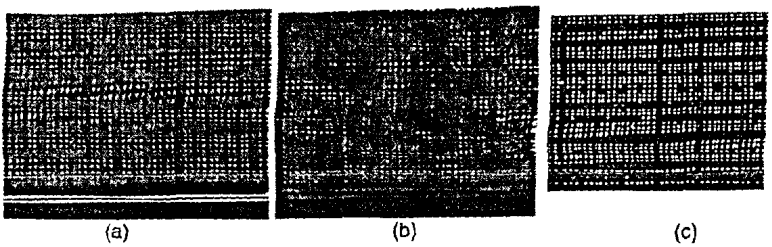

FIG. 11. (a) Regular image from camera, (b) irregular image from camera due to impared or worn-out grating, and (c) normal image after thresholding.

terferometer beams on the other hand are correctly incident, collimated, and enlarged for the whole-field imaging needed, and thus produced results that were also theoretically valid.

B. Use of two beams for strain calculation

It may be mentioned that the strain in the specimen can also be calculated using a single beam diffraction, which is given by the initial equations. As pointed out earlier about errors in such measurements,[4,7] the major source of error in strain calculation through diffraction is the out-of-plane tilt of the specimen surface, which also gives rise to similar spot shifts as strain. But as covered in our theoretical treatment earlier, the use of two symmetrical opposite beams from moiré interferometer produces two different spot shifts calculated from both beams. Now the tilt can easily be purged out being related to the sum of the shifts or $(\Delta x_2+\Delta x_1)$, while the strain may be more cleanly calculated being related to the difference of the shifts or $(\Delta x_2-\Delta x_1)$.

C. Image light thresholding for spot determination

The output of CCD-based camera is 8 bit gray-scale image, thus showing different levels of illumination at different pixels of lighted spot. The spot centroid was first calculated from this image and the shift of the spots was determined by comparing the information in two images. It was soon found out the spot-shift calculation from such gray-scale image was not correct mainly owing to the light inherently present in the background pixels, e.g., the tilt of 4 pixels was measured as that of about 2 pixels. Thus as an alternate, the images were then processed by comparison of each pixel to a suitable threshold value determined by the average amount of light present in the pixels of the picture, and then were converted to binary image containing 1*s* for light and 0*s* for dark areas. This would give correct results of shift and strain calculation for most different light conditions and specimens used.

The next problem came with the irregular images taken from imperfect or "dirty" gratings bonded to the specimens, showing larger variation of light or presence of darker spots within the same image. For this purpose, the thresholding algorithm had to be modified again, as the threshold now was kept according to the average amount of light in the close-by region or in the specific subwindow being processed, instead of relating it to the cumulative average light of the image. This approach worked for most diffracted beams of varying light intensity. But it was also found that the correctness of shift calculation was slightly hampered as per the variation in the centroid calculation for each subwindow. Examples of different images are given in Fig. 11.

VI. DISCUSSIONS

A new system multipoint diffraction strain and tilt sensor has been developed for simultaneous measurement of strain and tilt at a large array of points. A microlens array samples the diffracted beam into smaller wave fronts and provides a spot image which shifts due to deformation or rigid-body tilt of the specimen. Monitoring the individual shifts of each microspot, both the whole-field strain and tilt of the specimen can be separately deduced with good combination of accuracy and speed.

After detailed characterization, the measurement linearity of the system is found to be 1%–2% of full-scale deflection for strain and tilt measurements. The system sensitivity to strain or tilt changes is about 18 $\mu\varepsilon$ and 8 μrad, respectively. The global accuracy of mean strain calculation is about 3 $\mu\varepsilon$ and that of the mean tilt calculation is about 1.5 μrad. On the other hand, the local accuracy was found to be 50 $\mu\varepsilon$. For the lens array used, the strain measurement range is found to be 8 mε, while the tilt measurement range is 7.5 mrad. The spatial resolution of the system is 145 μm.

ACKNOWLEDGMENTS

The authors thank the School of Mechanical and Aerospace Engineering, Nanyang Technological University for the facilities for this work. The authors are also grateful to the staff and students of the Photonics and Microsciences Laboratory, and specifically to Vijay Raj Singh. Financial support from Dr. Subodh Mhaisalkar is also gratefully acknowledged. This work was supported by Pakistan Higher Education Commission scholarship.

[1] J. F. Bell, J. Appl. Phys. 27, 1109 (1956).
[2] J. C. Moulder and J. F. Cardenas-Garcia, Exp. Tech. 17, 11 (1993).
[3] P. J. Sevenhuijsen, J. S. Sirkis, and F. Bremand, Exp. Tech. 17, 22 (1993).
[4] Y. Ma and M. Kurita, JSME Int. J., Ser. A 36, 309 (1993).
[5] A. Kozlowska, Proc. SPIE 2341, 124 (1994).
[6] A. Asundi and B. Zhao, Opt. Eng. (Bellingham) 39, 1645 (2000).
[7] B. Zhao, H. Xie, and A. Asundi, Rev. Sci. Instrum. 72, 1554 (2001).
[8] A. Asundi, S. Mhaisalkar, and A. Priyadarshi, U.S. Patent NO. PAT/026/05/05/US (26 May 2005).
[9] R. R. Cordero, M. François, I. Lira, and C. Vial-Edwards, Opt. Lasers Eng. 43, 919 (2005).
[10] G. Nicoletto, Opt. Lasers Eng. 37, 433 (2002).
[11] D. Post, B. Han, and P. Ifju, *High Sensitivity Moiré: Experimental Analysis for Mechanics and Materials* (Springer, New York, 1994).
[12] C. A. Palmer and E. G. Loewen, *Diffraction Grating Handbook* (Thermo RGL, New York, 2000).

Journal of Applied Sciences 6 (3): 682-687, 2006
ISSN 1812-5654

Impact of Stray Illumination Noise on the Position Response of Position-Sensitive Devices

S. Iqbal, M.M.S. Gualini and K. Rashid
Faculty of Applied Sciences, International Islamic University, Islamabad, Pakistan

Abstract: Position-sensitive Devices (PSDs) are often used in the industrial environment, where the system light source used for position measurement is co-existing with many other light sources in the vicinity, along with their reflections and back-scatters from various surfaces. These unavoidable stray beams and illumination noises may fall on the detector surface in different spatial distributions and produce unpredicted variations in their position response. Some of the light sources may even have flying or rotating beams of sufficient energy. In this study, attempt was made to model and analyze these stray noises with respect to the operation of PSDs. Thus it was investigated how the presence of the spurious sources changes the behaviour of these detectors and how much is the position output modified quantitatively. The experimental results obtained by using PSDs and signal beams along with the spurious sources are presented. The obtained data is compared with the results from the proposed mathematical model to be within fraction of a percent of error.

Key words: Position-sensitive Detectors, background noise, lateral-effect detectors

INTRODUCTION

In the industry, telecommunication and other sectors, many applications require accurate measurement of displacement of objects through non-contact methods. Semiconductor Position-sensitive Detectors (PSDs) offer very good solutions for such applications and since their inception in late fifties, these devices have become a major tool for lateral position measurement[1]. Two types of such devices are commonly used for position-sensing applications[1,2]. The segmented PSDs or four-quadrant detectors are used for high precision and low signal-level applications where range of movement is relatively smaller or the alignment is the objective. On the other hand, the continuous PSDs or the lateral-effect photodiodes are used for wider displacement measurement with high linearity, good resolution and fast response[3].

Applications of PSDs are even more diverse and widespread in the industry, including alignment, displacement sensing and as a part of other analysis instrumentation. In such environment, the system laser source is co-existing with different nearby light sources, coherent or otherwise, along with their reflections and back-scatters from various nearby surfaces. Some of the systems may involve scanning or rotating laser beams too, which may have enough energy to effect the PSD measurements in the form of periodic pulses.

Such random illumination noises may take the form of different sources types, e.g., directional, point or extended and may fall on the detector surface in different shapes or spatial distributions. They may produce unwanted outputs while mixing with the real signal, which is coming direct from the source or via the reflector onto the detector surface. These noise sources have been mentioned or described by some of the earlier authors[1,2,4]. Nonetheless it is felt that a detailed operational analysis is still required.

It may also be mentioned that for more critical measurement applications, modulation of light source is used synchronized with receiver, to avoid the effects of background light. But on the other hand, such systems become unfeasible in many standard applications due to the practical reasons such as needed compatibility with simpler light sources, reduced technical complexity and lower system cost. Thus whole lot of industrial position measurement systems are still produced and utilized with un-modulated continuous light sources[5,6], directly effected by other illuminations. Also important is the fact that, as given by Makynen *et al.*[1], even the modulated light reflected-beam sensors do suffer from stray illuminations problem in the form of unwanted reflections from close-by objects and outlined this problem along with an effort for a solution. Thus the position response analysis presented here does also apply to these sensor types while considering the effects of such stray reflections.

PSDs basing on lateral-effect have a continuous construction in terms of their light-sensing area, which characterizes them from the other segmented position-sensitive detectors. Thus their construction is in

Corresponding Author: S. Iqbal, Faculty of Applied Sciences, International Islamic University, Islamabad, Pakistan
Tel: 051-4478031, Fax: 051-4449043

the form of a single continuous photodiode, as shown in Fig. 1. As the light falls on a specific portion of LEP, the generated current carriers are divided between the extended edge electrodes on each side. This division is in proportion to the encountered respective conductance, or in inverse proportion to the relative distances of the current paths between the illuminated region and the respective electrode[2].

The important features of these lateral-effect devices include position measurement of the incident light spot for the larger dynamic range or upto the edges of the devices. Additionally, the transfer characteristic for the light spot position measurement has very good linearity for the entire range[1]. This gives them an edge over the segmented photodetectors for many of the applications where continuous position measurement is needed. Another useful feature is that the position is measured for the centroid of the incident light beam. This makes them largely indifferent to the spot size and shape[7]. The position of the light spot is calculated from the terminal currents such that the output limits are normalized to −1 and +1 at the sensor edges. The final position along x-axis measured from the center of the detector is given by following for the general duo-lateral and tetra-lateral effect PSDs[8,9]. Similar formula will be used for the y-axis position calculation in dual-axis PSD.

$$P_x = \frac{L}{2}\left(\frac{i_2 - i_1}{i_2 + i_1}\right) \qquad (1)$$

Noise beams and illuminations: The disturbing lights and illuminations may be coming from different types of sources and may be taking different spatial distribution and characteristics. Considering the sources of illuminations, the major sources have been described by Beraldin *et al.*[10] to be ambient illumination, direct sunlight and other laser sources. These sources have been described to be the limiting factors for the performance or fluctuation-free resolution obtained from the operation of the continuous or lateral-effect PSDs[10]. In the following we categorize them according to their characteristics and the spatial distribution of their light on the PSD surface and also analyze them one by one from the point of view of the normal operation of PSDs and the disturbances caused in its output.

Probably the most obvious source of external noise in an optical system is background radiation. Any detector will anyway be facing the black-body radiation from the background which happens to be at a specific temperature during the operation or measurement, even if specific sources are not present to emit the interfering or disturbing radiation. According to Plank's Law, this minimum background radiation illuminating any detector, or PSD to be specific, will be given as following[4], while other descriptions and equations are also used[11]. Unless their intensity is high, their usual effect may be smaller and similar to other diffused illuminations to be described hereafter.

$$\left(P_{opt}\right)_{BG} = \int_{\Delta\nu}\frac{1}{4}\iota(\nu)d\nu A_{det}\frac{d\Omega}{4\pi} \qquad (2)$$

Probably the major source of disturbance for our analysis can be that from other directional laser beams falling on the surface of a lateral-effect PSD simultaneously, as shown in Fig. 2. Similarly, other directional light beams and non-laser lights, which fall on the detector surface in a shape approximating a beam, may also be included in this category[12]. Similar effect will also be produced by the illuminations, which are not directional in nature but are converted to a spot by the receiver optics. The most obvious example may be that of parallel rays coming from a distant source and converted to a spot by the positive lens used in front of the PSD.

For the normal direct-beam or reflected-beam position sensor based on a Lateral-effect PSD, the output current produced on the PSD terminals by the main or actual incident beam is function of certain parameters as $i_j = i_j(I_s, x_s, y_s)$ for j = 1-4. Here I_s is the intensity of the actual beam incident on PSD's surface and x_s, y_s give the position of the centroid of the beam on PSD's surface. Similarly, if the noise beam is falling on the surface, the output current component due to this beam may be given as $i_j' = i_j'(I_n, x_n, y_n)$ for j = 1-4. Here, I_n is the intensity and x_n, y_n give the position of the centroid of the noise beam on the PSD's surface.

The next important type of interfering illumination to be considered is the one, which is not beam-like or otherwise is not narrow enough and falls on whole of the PSD's surface area. These include the point sources whose light is falling direct on the PSD or the extended sources, diffuse reflections and background illuminations, which do not form a limited spot even after passing through the receiver optics. Ambient light is the most obvious example of this category. Simplifying their effect on the PSD, they may be approximated by a wide spot covering whole of the PSD area and having the centroid in the middle or the center of PSD, as shown in Fig. 3. Thus as earlier, $i_j' = i_j'(I_{III}, 0, 0)$ for j = 1-4. Here, I_{III} is the intensity and 0, 0 indicate the middle position of the centroid of the interfering illumination on the PSD's surface.

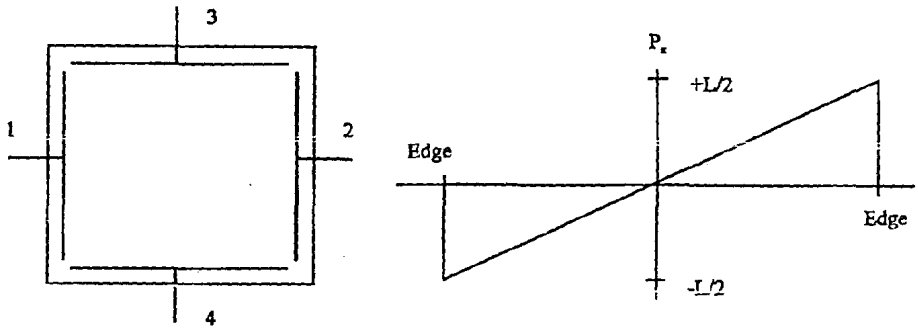

Fig. 1: Geometrical shape and transfer curve of Lateral effect PSD

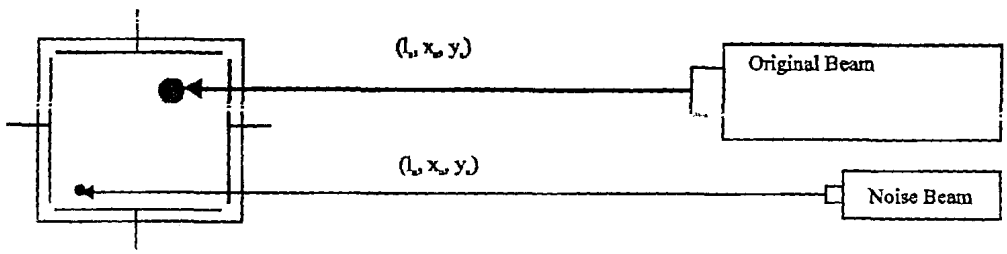

Fig. 2: Noise beam disturbing the original beam on PSD surface

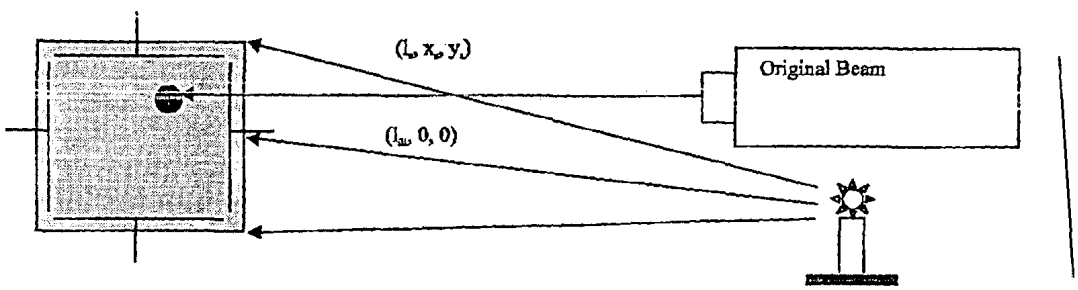

Fig. 3: Diffuse illuminations disturbing the original beam on PSD surface

A specific category may be that of the pulsating lights or the scanning laser beams falling on the surface of PSD in the form of a pulse train. Although they may also be falling on a specific area of the detector, much more common are going to be those approximating the diffuse illuminations covering almost entire area. This is to be expected as there is much more chance of backscatter interfering on the PSD surface instead of direct scanning light and they are expected to take the form of diffuse illumination. The output current in this case is function of one more parameter as $i_j' = i_j'$ (I_{ill}, 0, 0, DC) for j=1-4. Here DC represents the net duty cycle of the interfering pulses impinging on the surface of PSD.

Position response error with optical noise: For the normal single-beam operation, PSD gives the centroid position of the incident signal beam calculated by the individual currents as given before.

$$P_{Signal} = \frac{L}{2}\left(\frac{i_2 - i_1}{i_2 + i_1}\right) \quad (3)$$

Suppose that instead of the signal beam, there is a 'noise beam' falling on the surface of PSD and generating its own currents on the output terminals. The position of the noise beam can be calculated by the similar formula as following:

$$P_{Noise} = \frac{L}{2}\left(\frac{i_2' - i_1'}{i_2' + i_1'}\right) \quad (4)$$

So, for the single-beam operation, calculation of the beam position is carried out in the similar manner for both of the cases. But what will be the behaviour of the device when both the beams are incident on the surface of the PSD at the same time? According to Kawasaki and Goto[7], the output of PSD, calculated using the terminal currents, in this case should be equal to the intensity-weighted mean of both the light positions. Thus the final position and the error from the signal position may be given as following:

$$P_{Measured} = \frac{I_{Signal}}{I_{Signal} + I_{Noise}} P_{Signal} + \frac{I_{Noise}}{I_{Signal} + I_{Noise}} P_{Noise} \quad (5)$$

$$P_{Measured} = P_{Signal} + \frac{I_{Noise}}{I_{Signal} + I_{Noise}}\left(P_{Noise} - P_{Signal}\right) = P_{Signal} + \delta P \quad (6)$$

$$\delta P = K_{Intensity} dP = K_{Intensity}\left(P_{Noise} - P_{Signal}\right) \quad (7)$$

Thus the shift in measured position due to the presence of interfering beam depends on the mutual distance between both the sources and on the fraction of the noise intensity within the total intensity falling on PSD. This is the case when a second noise beam, which is directional in nature, is interfering with the original signal beam on the PSD. What may happen in the case where a broad illumination from a point source or an extended source is covering whole of the surface and is interfering with the original signal beam? As discussed earlier, its centeroid may be taken to be at the center of the PSD. Here the change in the final position brought by the illumination is as following.

$$\delta P = K_{Intensity} dP = K_{Intensity}\left(-P_{Signal}\right) \quad (8)$$

Last case is about the specific category of the pulsating lights or the scanning laser beams falling on the surface of PSD in the form of a pulse train, while illuminating the PSD area as a whole. In this case the intensity of the interfering noise is actually modified in terms of the duty cycle fraction, but as the intensity of the noise is taken to be much smaller, i.e., $I_n << I_s$; thus the whole of the intensity multiple may be modified to include the DC fraction.

$$\delta P = K_{Intensity(Duty-Cycle)} dP = \frac{DC \times I_{Noise}}{I_{Signal} + DC \times I_{Noise}} \times dP$$
$$dP \cong K_{Intensity} K_{Duty-cycle}\left(-P_{Signal}\right) \quad (9)$$

EXPERIMENTAL METHOD

Experimental setup for evaluating the effects of noises on the position measurements included a lateral effect PSD-based position measurement system, which was illuminated by a prime laser beam along with a noise beam or noise light source. Two laser sources used were Suwtech diode-pumped green lasers emitting at 0532 nm, which is produced by doubling the frequency of Nd:YVO_4 crystal output. One laser was DPGL-2100 giving upto 100 mW output with modulation control and other was DPGL-3001F giving about 1 mW output. The beams of these lasers are CW, TEM_{00} with beam diameter <1.0 mm and beam divergence <1.0 mrad.

The position-sensitive detector used was Melles Griot 9x9 mm dual-axis lateral-effect silicon detector. This has 8 mm-calibrated diameter and position resolution of ±1 μm. The detector was used in conjunction with Melles Griot microcomputer-based spot on optical beam position and power measurement system, model 13PSL002-PCI. The system provides software control, software linearization, selective data logging and data acquisition rate of 20 Hz. One laser head was moved by placing on PI translational movement IntelliStage C531.5i, featuring computer-control, 306 mm range and 0.1 μm linear resolution. Whole apparatus was placed on Newport RP Reliance Sealed Hole Table Top, which was mounted on Newport isolation supports. The construction of the test apparatus is shown in the given Fig. 4.

It was noticed that certain factors hampered the stability and repeatability of the digitized data very much, so care was taken about them to avoid any error in the

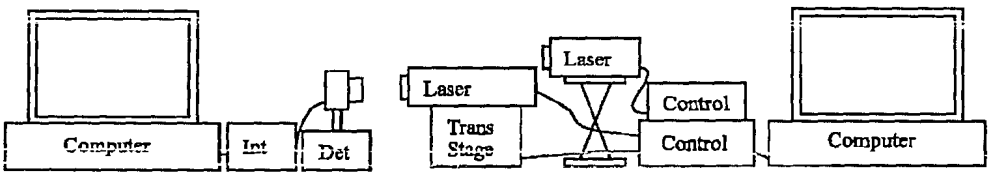

Fig. 4: Experimental setup with computers, lasers and position detection system

readings. Ambient temperature was maintained at 20-25°C as the drift in both directions was apparently effecting the data stability. The incident intensity on the detector was used close to 1-1.5 mW, as much lower intensities were giving more jittery readings and higher intensities were risking detector saturation. Control of ambient light was practiced in order to avoid any systematic error in the data and bare minimum was used. As per laser usage practice, some warm-up time was given for the lasers and equipment temperature to stabilize, as more shaky data was noticed otherwise.

RESULTS AND DISCUSSION

As per noise categories described in earlier sections, the first type of noise considered is that of the interfering directional beams which fall on the detector surface and form a limited light spot. To evaluate their effect, a signal beam was projected on the PSD surface approximately at its center. The interfering beam source was placed on the translational stage and was scanned across the PSD of net position were taken by casting it at different positions on PSD surface with the intervals of 1 mm. Two sets of data were collected with the noise beam intensity being approx 10% of the signal beam intensity in the first set and being approx 5% of the signal intensity in the second set. Both the sets of position data were compared with the calculated outcomes after the beam disturbance as per theory developed earlier. Data points were plotted with calculated position on one axis and the experimental position on other axis and were shown along with the straight line of ideal comparative values in Fig. 5 and 6.

As seen in the plotted curves, both the sets of calculated and experimental data coincide well with each other. The maximum difference in both of the data sets is about 20 μm while the maximum scale of reading is 8000 μm (-4000 to +4000 μm). This puts the maximum error encountered in both the experiments of 10 and 5% noise at about 0.25% of full-scale reading.

The second type of optical noise mentioned earlier is that caused by the stray illuminations, which are not forming a spot on the surface and they are rather covering the entire area of PSD. This type of disturbing illumination was produced for experimentation by simultaneous effect of multiple room lights, while their total intensity falling on PSD was almost symmetrical about the center of PSD, specifically in x-direction, which is the axis of interest at the moment. The signal beam was projected at the ends of the calibrated area of PSD, i.e. at – 4.0 and + 4.0 mm. The measurements were taken with the illumination intensity being about 5 and 10% of the signal intensity. The effect of illumination on the position measurement from PSD was noted and compared with the calculated

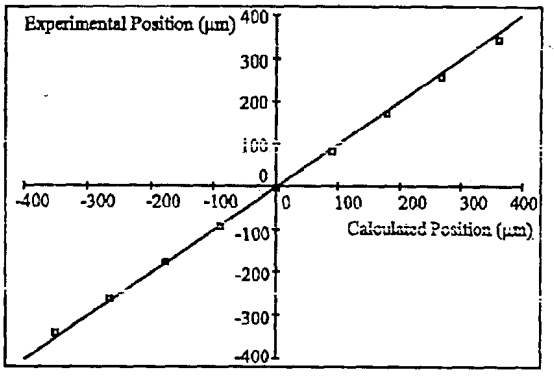

Fig. 5: Plot of position measurements in presence of 10% disturbance beam

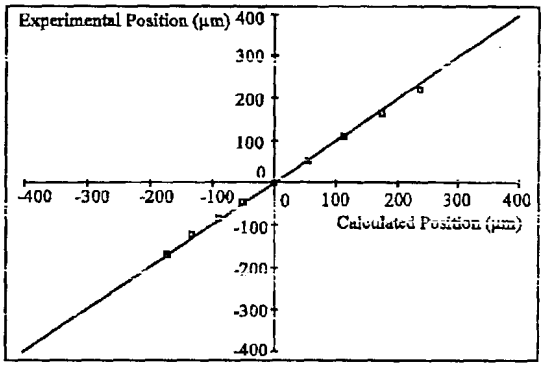

Fig. 6: Plot of position measurements in presence of 5% disturbance beam

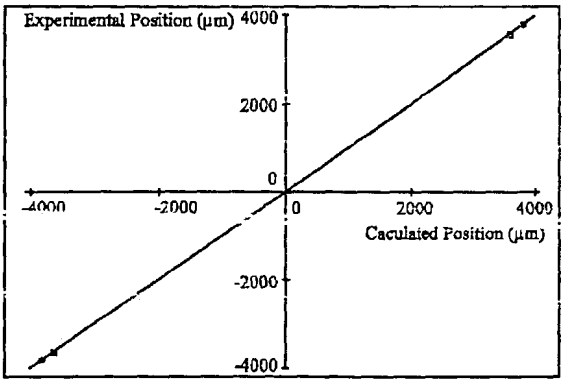

Fig. 7: Plot of position measurement in presence of disturbing illumination

outcome differently for both the intensity percentages in Fig. 7 (squares for 10%).

As seen in the plot, the calculated and experimental data coincide well with each other. The maximum difference in these data points is about 30 μm in the maximum scale of 8000 μm. This puts the maximum error

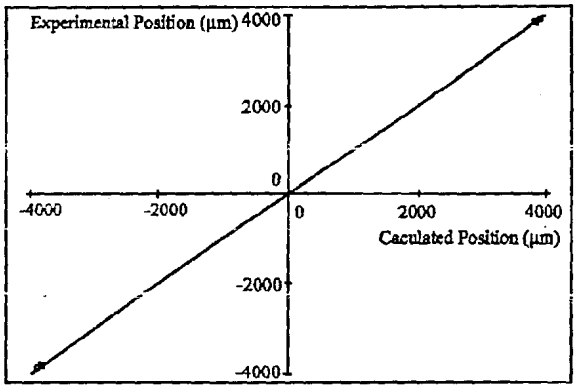

Fig. 8: Plot of position Measurment in presence of disturbing pulsed illumination

encountered in this experiment at about 0.375% of full scale reading.

To simulate the pulsating or scanning lasers, the interfering beam was modulated at 1.0 kHz with 50% duty cycle. It was projected on the center of the PSD detection area to simulate the falling pulsating reflections or rotating lights. The signal beam was projected at the ends of the calibrated area of PSD. The measurements were taken with the unmodulated interfering intensity being about 5 and 10% of the signal intensity. The effect of interfering pulses on the position measurement from PSD was noted and compared with the calculated outcome differently for both the intensity percentages in Fig. 8 (squares for 10%).

As seen in the plot, the calculated and experimental data coincide well with each other. The maximum difference in these data points is 20 μm in the maximum scale of 8000 μm. This puts the maximum error encountered in this experiment at about 0.25% of full scale reading.

CONCLUSIONS

Theory and analysis of stray beams and optical noises disturbing the position response of lateral-effect position-sensitive devices were presented in this study. It is found that the error introduced in the position measurement in the presence of an interfering beam or δP, is proportional to the distance between the centroids of both the beams and to the fraction of the noise intensity in the total. In case of a uniform or broad illumination, the same analysis applies while the centroid of the interfering illumination should be taken at the center of the PSD area. In case of scanning or pulsating lights, the produced effect should be decreased in proportion with the beam duty cycle. These results have been verified experimentally and the obtained data is within a fraction of a percent of the predicted calculations.

ACKNOWLEDGEMENTS

We are very thankful to Dr. Nasrullah, Chairman LEO Center at FUUAST, Islamabad for his useful comments. We are grateful to Dr. Khalid Rashid, Dean FAS and Dr. Sikandar Hayat Khiyal, Head CS Dept of IIU Islamabad for their help. Part of the research work was supported by the merit scholarship granted by Higher Education Commission, Pakistan. Equipment support provided by IICS and specifically by Mr. Karim Ahmad there is also gratefully acknowledged. In the end we want to mention that we are deeply indebted to our wives for their never-failing support.

REFERENCES

1. Makynen, A., 2000. Position-sensitive devices and sensor systems for optical tracking and displacement sensing applications. Ph.D Thesis, University of Oulu, Finland.
2. Makynen, A., J. Kostamovaara and R. Myllyla, 1996. Positioning resolution of the position-sensitive detectors, in high background illumination. IEEE Trans. Instrum. Meas., 45: 324-326.
3. Qian, D., W. Wang, I.J. Busch-Vishniac and A.B. Buckman, 1993. A method for measurement of multiple light spot positions on one position-sensitive detectors (PSD). IEEE Trans. Instrum. Meas., 42: 14-18.
4. Verdeyen, J.T., 1981. Laser Electronics. Printice Hall International, pp: 587-588.
5. Melles Griot. SpotOn optical beam position and power measurement system. Product Manual.
6. On-Track Photonics. OT-301 versatile position sensing amplifier. Product data sheet.
7. Kawasaki A. and M. Goto, 1990. On the position response of a position-sensitive detector (PSD) irradiated with multiple light beams. Sensors and Actuators, A21-A23: 534-537.
8. Woltring, J., 1975. Single- and dual-axis lateral photodetectors of rectangular shape. IEEE Trans. Electron Devices, ED-22: 581-586.
9. UDT Instruments. Non-contact position sensing using optical detectors. Application note.
10. Beraldin, J.A., F. Blais and M. Rioux *et al.*, 2003. Optimized position sensors for flying-spot active triangulation system. Proceedings of 4th Intl. Conf. on 3-D Digital Imaging and Modeling, Banff, Canada, NRC47083, pp: 334-341.
11. Hobbs, P.C.D. 2000. Building Electro-optical Systems, Making it All work. John Wiley and Sons Inc, pp: 51-53.
12. Iqbal, S., M.M.S. Gualini and K. Rashid, 2005. Stray noises and illuminations disturbing the performance of position-sensitive devices. SPIE Symposium on Optics and Photonics, San Diego, USA, Proceedings of SPIE 5867, Pap 05.

ELSEVIER

Journal of Materials Processing Technology 184 (2007) 12–18

Journal of Materials Processing Technology

www.elsevier.com/locate/jmatprotec

Laser welding of zinc-coated steel with tandem beams: Analysis and comparison

S. Iqbal [a,*], M.M.S. Gualini [c], F. Grassi [b]

[a] Faculty of Applied Sciences, International I University, Islamabad, Pakistan
[b] Convergent Prima Industrie, Collegno (Turin), Italy
[c] Department of Applied Physics, Federal Urdu University of Arts, Sciences & Technology, Islamabad, Pakistan

Received 7 March 2005; received in revised form 25 September 2006; accepted 13 October 2006

Abstract

A new method of using two tandem laser beams for lap welding of galvanized steel sheets is being discussed and modeled along with its comparative study. This involves a pre-cursor beam and a higher-power actual beam, generated independently or otherwise split from the same source. The first beam cuts a slot, thus making an exit path for the zinc vapours, while the second beam performs the needed welding. The paper discusses some early experimental results of the method, including the metallurgical analysis obtained in laboratory showing total absence of zinc in the weld area. A comparison of the proposed system with other techniques proposed in the recent years is also drawn along with some quantitative analysis. General analysis in industrial perspective also supports this method to be easier to implement on the production lines, along with entailing some process time saving.

Keywords: Laser welding; Precursor beam; Galvanized steel sheets; Keyhole formation

1. Introduction

Welding of zinc-coated steel sheets in lap configuration poses a challenging problem to the researchers. As given in Refs. [1–5], the solutions proposed in the last many years have not yet found an easy-to-apply realization to replace conventional spot welding and its electrodes [2]. The many advantages offered by laser welding technology still justify an ongoing quest for some efficient method. The ideal solution should firstly solve the technological problem of the residual zinc vapours trapped in the joint weld due to the lower boiling point of the zinc (907 °C) with respect to melting point of steel Fe (1530 °C). The solution should also be practical and economical enough to be installed on the production lines. For this purpose, this dual beam solution is proposed [1].

2. Pre-cursor beam solution

In this new two beam method, the front beam of the tandem system will cut a slot with a minimal kerf and the second beam will perform lap welding while also seam-welding the two sides of the kerf. The target is that the residual zinc during the welding evaporates through the slot already cut ahead of it. Two similar hybrid solutions are being proposed [1], where one is combining Nd:YAG and CO_2 lasers in tandem, the first for cutting, and the second for welding. Alternatively two beams of the same CO_2 laser source may also be used in tandem in the solution, which is virtually an advanced integration of the "gap-method" introduced several years ago [2] and the dual beam system proposed later on [3]. Here Figs. 1 and 2 show the welds carried out with this new method.

The given solution is described in Fig. 3 (top view). A laser beam cuts a slot of a few centimeters length and a certain width in front of the keyhole. The slot serves two functions; firstly removal of zinc coating and secondly elimination of the vapourized zinc that blows away by the gas used in the cutting process. Although the zinc coat removal here may produce the best welding results, but this new method is not cumbersome as the methods previously proposed in literature [3]. The second function of the slot is to provide a way-out to the zinc vapours, which are to be produced by the keyhole of the welding beam. In fact the keyhole and the surrounding molten pool may well exceed the dimensions of the cut slot width, thus involving some

* Corresponding author.
E-mail address: squresh7@yahoo.com (S. Iqbal).

0924-0136/$ – see front matter © 2006 Elsevier B.V. All rights reserved.
doi:10.1016/j.jmatprotec.2006.10.043

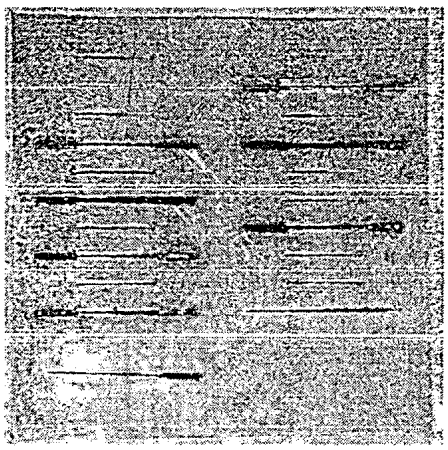

Fig. 1. Welds with the new method.

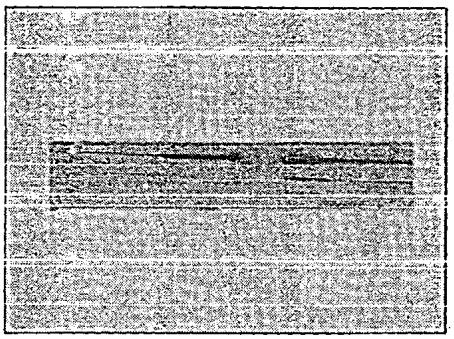

Fig. 2. Analyzed welds (7 and 8).

ea where the zinc coating is still present. In this case, the slot ll exhaust the zinc vapours before the rapid cooling down the molten pool. An Nd:YAG laser beam may generate cuts th excellent kerf and surface quality, but a CO_2 laser can also used. Distance between the cutting and welding spots can be nveniently adjusted according to the 3D geometry of the com-nent to be welded. Proper gas shielding and fumes removal n be handled quite easily too.

In Fig. 4, a basic scheme of using the two beams in tan-m with the basic functions required by each of the laser are presented, in order to give an idea of the degree of complexity of the hybrid laser welding/cutting nozzle. The CO_2 and/or Nd:YAG laser beams are sent to the work piece separately and the distance between the two can be pre-set or can otherwise be adjusted continuously by an adaptive CNC system to maximize the weld quality.

Regarding its feasibility, once a question was posed about the possible high costs of utilizing two different laser sources or one higher power CO_2 laser source. In fact this difference may not be significant considering the savings in time and human work-hours needed for some other schemes. The present paper shows the work conducted on this concept at the laboratories of Convergent-Prima in Collegno (Turin), Italy. After recalling the theoretical model and outlining the experimental results, a comparative analysis with some other schemes is also presented.

3. General discussion

The results obtained utilizing standard equipment, without any dedicated optics or custom assemblies, definitely confirm the principle suggested theoretically [1] and also consolidate the behavior predicted by the theoretical model. It is hoped that this solution offers a better compromise to be implemented on the production lines than any other method [1–12] proposed until today. For example, the alternate method of delaying the solidification of the keyhole suffers the problem of strict control of the procedural parameters. The time window to enable the perfect solidification of the keyhole without residual zinc is quite narrow, and is not as easily controllable as the cutting of a slot, which depends more on design parameters rather than the material specifications. Also that the tolerances in the chemical composition of galvanized sheets may influence its thermal properties, thus resulting in a lesser quality of the weld, along with other factors like the difficulty to control the heat effects. Controlling the kerf width is quite an acquired procedure after more than 30 years of laser material processing. The kerf width is quite easily measurable utilizing common optical methods available today, while measuring heat may prove more expensive and lesser accurate than an optical fringes methods used to measure the kerf width in real time. And it may also be noted that the welds on a flat material are quite easy to obtain, but the reality of a 3D application is quite challenging to be met.

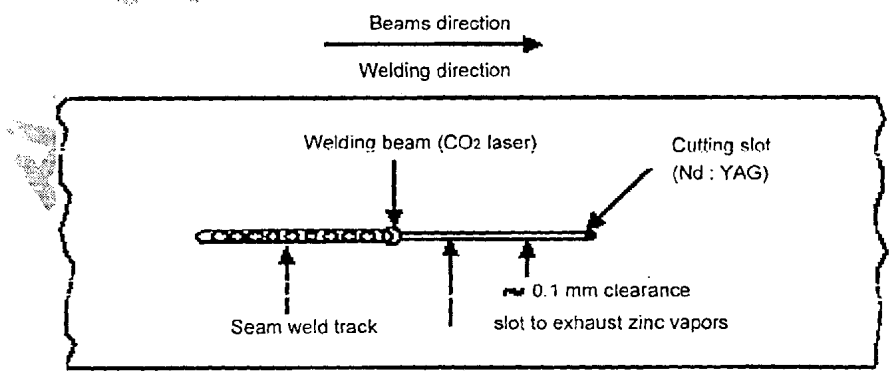

Fig. 3. Top view of the laser lap welding using the forward slot (through both sheets).

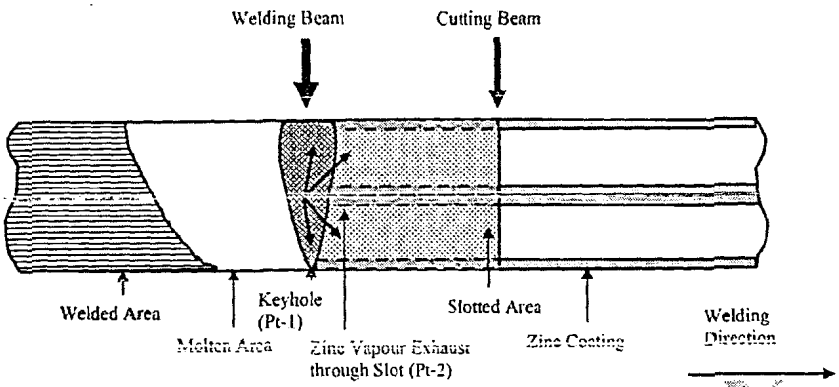

Fig. 4. Side view of the welding operation with the two beams in tandem.

The proposed solution combines the advantages of the gap ethod [2] and coating removal method [1,3,12], which are more mbersome and expensive for the production lines [13] than the ethod proposed here. Main advantages of the proposed method e those obtained by the gap techniques, while not having to roduce a gap between the sheets. The proposed method is not mbersome; a good alignment between the beam and the kerf, d ~0.1 mm kerf width appear to be the only critical require-ents. Secondly, the proposed method is not constrained by the ual geometry of the components to be joined. The proposed ethod is relatively economical since it does not require any tra fixture and additional manual work, which are quite expen-e. As outlined earlier, the possible demerit of the method oposed can be somewhat higher investment and running cost. It may be noted that in case of a slot passing through the two erlapped sheets, the Nd:YAG laser operates as per needs of s procedure. In particular the cut width can be as narrow as μm; while generally the moderate cutting speed of Nd:YAG ers is easily obtained to match the keyhole welding speeds the same thickness of metal sheet.

Mathematical model and simulation

In order to develop a simple and effective mathematical odel, one may take into consideration the earlier work on s model [1] and the work done on the gap method [9,11]. e introduced approximations help to obtain some quantita-e measures. Fig. 5, in conjunction with Fig. 4, helps to derive

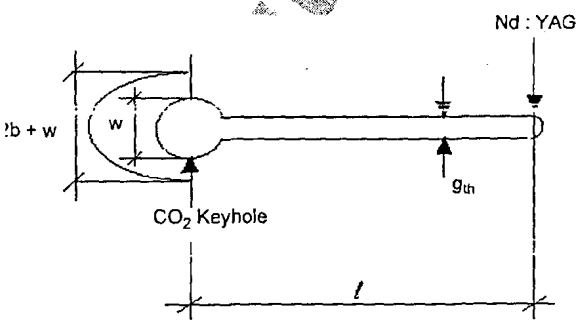

Fig. 5. The cut and weld model showing slot and keyhole sizes.

some theoretical insights from the available mathematical model [11] under the dual beam conditions. The model is based on the considerations that the Ferro static head on top of the weld pool generates a pressure that stops the zinc vapours from getting into the keynole (pt-1), which are being exhausted by the cut slot providing an artificial gap (pt-2):

$$\Delta P_{12} = \rho_{Fe} g_e t_p a \tag{1}$$

Here 'ρ_{Fe}' is the density in kg/m^3, 'a' the wave factor normalized to 1, 'g_e' acceleration due to gravity in m^2/s and 't_p' is the thickness of the steel plate. The Ferro static pressure [11] generates a velocity of the zinc vapours at the ejection point. The exhaust velocity 'v_2' of the zinc vapours is calculated using Bernoulli's theorem as

$$v_2 = \sqrt{\frac{2\Delta P_{12}}{\rho_v}} \tag{2}$$

while ρ_v is the zinc vapour density, which can be calculated using Clausius–Clapeyron equation [9], and in this case $\rho_v = 21.87\,\text{kg/m}^3$.

The following equations express the volume of the gases generated by the welding beam, and the volume of gases that can be exhausted through the gap or the slot present in the middle of the to-be-molten area having zinc on the both sides of the slot:

$$\text{Vol}_{gen} = \frac{2t_{Zn} V \rho_s ((w - g) + 2b)}{\rho_v} \tag{3}$$

$$\text{Vol}_{exh} = 4 v_2 t_{Zn} w \tag{4}$$

In these, 'b' is the width of zinc boiling isotherm, 't_{Zn}' the thickness of the zinc layer, 'V' the welding speed, 'ρ_s' the solid zinc density (7140 kg/m^3), 'w' the keyhole width and 'g' is the width of the slot. Equating both of these, the needed value of slot width is

$$g = \frac{V\rho_s(w + 2b) - 2w\rho_v v_2}{V\rho_s} \tag{5}$$

$$g = \frac{V\rho_s(w + 2b) - 2w\sqrt{2\rho_v \rho_{Fe} g_e t_p}}{V\rho_s} \tag{6}$$

Here the more useful value of slot width 'g' is whose minimum value is given by this equation, with the condition that all the

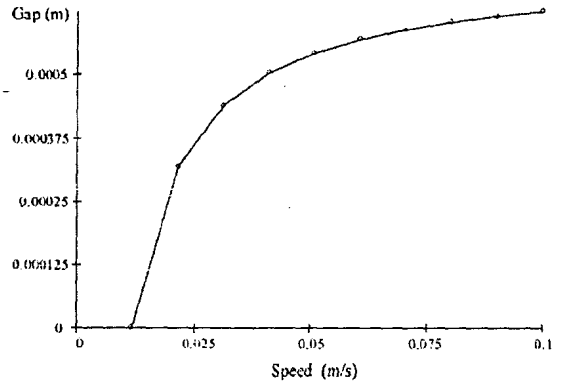

Fig. 6. Slot width plotted against the welding speed.

zinc vapours will be exhausted by the slot and nothing will go inside the melt pool. The given width can be decreased further if partial zinc vapour exhaust is allowed through the molten metal, i.e. some porosity is tolerable. The upper limit to this slot is posed practically by the situation that 'g' should be substantially lower than 'w' in order to allow for a proper strong weld in the presence of kerf. The value of 'g' in SI system is given as following:

$$g = \frac{7140V(w+2b) - 2w\sqrt{3373491t_p}}{7140V} \quad (7)$$

The variations in minimum needed gap width against the changes is welding speed are plotted here in Fig. 6 for some representative values as $w = 0.4$ mm, $b = 0.1$ mm and $t_p = 0.8$ mm. Note that the minimum gap values for very low speeds are less constrained and are largely governed by the condition that they may be realizable and that $g \gg t_{Zn}$. As given, here the useful solutions are those with the condition $w > g$ along with some margin, which are basically given by the speed values in the left part of the plot above. The right part of the surface graph is for higher speed welding where the values computed for 'g' by this model become unrealizable. Next is the requirement of minimum gap plotted against the welding beam diameter in Fig. 7 for the moderate welding speed of $V = 15$ mm/s.

A point to ponder is that the gap requirement is increasing with the decreasing beam diameter. This can also be understood

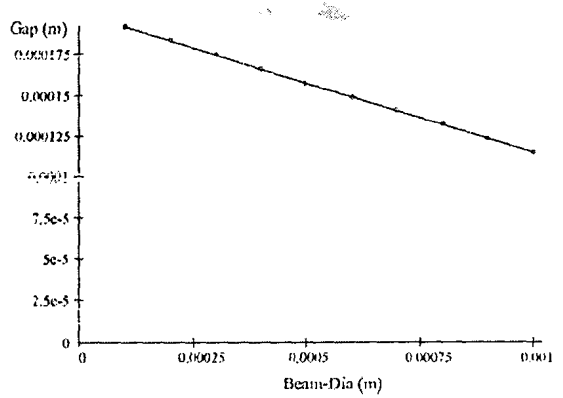

Fig. 7. Minimum slot width plotted against beam diameter.

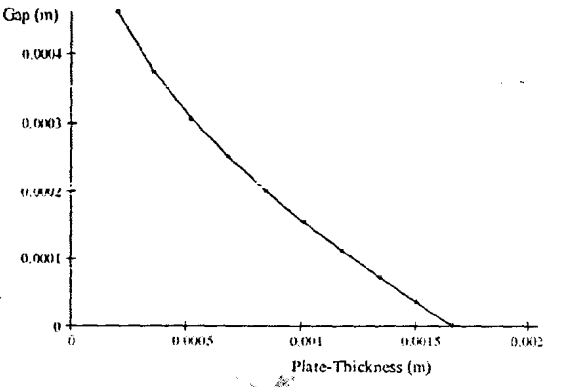

Fig. 8. Minimum slot width plotted against thickness of plate.

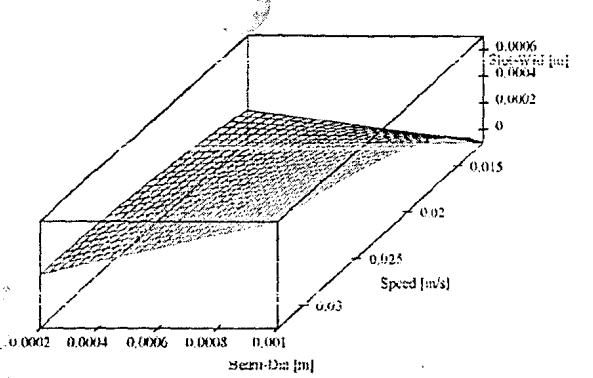

Fig. 9. Slot width shown in surface graphics against welding speed and beam diameter.

remembering that the smaller beam diameter is also coupled with smaller exit orifice and causes problem as the heat-effected zone width 'b' is taken to be a constant present in all the cases. Next is the plot of minimum gap against steel plate thickness in Fig. 8 for the same speed.

Decrease in the minimum gap requirement with the increase in the plate thickness is understandable by remembering that it is the ferro-static head which is an impeding factor for the zinc vapours to get into the melt pool. Thus for thicker plates, heavier pressure can push the vapours through the narrower slots; while the zero gap requirement is governed by the same condition of $g \gg t_{zn}$. Next is the 3D graphics of combined effect of speed and beam diameter as plotted in Fig. 9.

As the surface graph indicates, the realizable value of cut-slot width is again obtained with the lower values of welding speed, which is the rear part of the graph. At the same time the variation of slot width with the welding beam diameter is pretty straight at higher speeds, and is clearly unrealizable in the front-right part of the graph. This is the situation when the speed is too high and wider welding beam is producing more zinc vapours demanding wider but unrealizable slot width. Thus the results of the model analysis are also fairly understandable by logic and intuition.

5. Experimental results

Experiments with this method were conducted with a PRC3000 laser having $M^2 = 3.28$ and a "raw beam diameter" on the lens of about 24 mm ($1/e^2$) at about

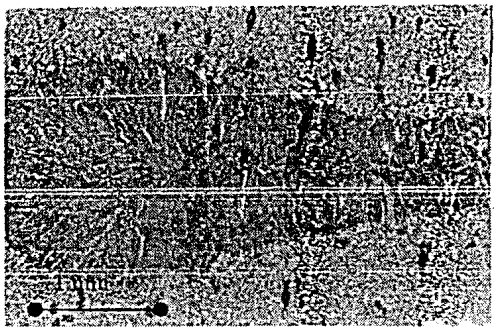

Fig. 10. Micrograph of weld 7 (top view).

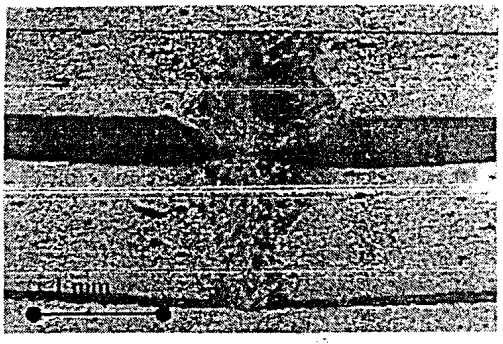

Fig. 11. Micrograph of weld 7 (50×).

from the laser source (the system used is a RAPIDO Convergent Prima). focused beam is 0.234 mm, while the Rayleigh's distance is 1.24 mm. The field" divergence of the focused beam is 0.0945 rad (12/127). The minimal ing kerf obtained on the double thickness of the galvanized sheets (1.6 mm) 15 mm, even at full cutting speed. The cutting kerf is about 36% smaller the cutting beam spot due to the mode structure of the beam. The power ity at 2500 W is 3.8×10^{10} W/m^2. The focal point has been positioned on op surface. The obtained cutting kerf is quite large (>0.1 mm) thus leading "weaker" weld, closer to a thermal weld than to a pure keyhole weld owing e poor contribution of the material at the weld spot. In fact even shifting the l point to 3 mm below the top surface means that the laser beam diameter velding is 0.6 mm, (equal to 0.88×10^{10} W/m^2), rendering it largely useless use the central part of the beam (maximum intensity), is all lost through the . Without defocusing, the entire beam would be lost through the kerf. Cutting welding have been performed with only one gas N_2, in order to save time. Under the above conditions it was noticed that the weld obtained is smooth does not show "bubbles" on its surface. In the absence of proper tooling, e is offset of 0.2 mm across the weld path, on the right side, with the beam at nm out of focal point. The beam size and its power intensity are such that a d keyhole only takes place if the beam diameter covers both the kerf edges in weld. The result was quite encouraging that an acceptable quality weld was ined without significant defects on the surface. Obviously the weld is under-s; in other words the upper surface is concave in the bottom direction, rather being convex as desired. This is due to the poor contribution of material wider cutting kerf. Incidentally this is in rough harmony with the findings ved from the above theoretical model. From these experimental findings it ite evident that the kerf should be smaller (0.05 mm or 1/3 of the previous).

The tests were repeated with a Convergent Prima System 2D PLATINO with C25 Rofin Laser and a 5" lens. Contrary to the 3D RAPIDO, the PLATINO is ore versatile machine because it enables to move the focal point of the laser n utilizing the CNC. Thus the stand-off of the tip to the galvanized sheet and position of the laser beam relative to the material are quite independent. In the cases of RAPIDO and PLATINO, the tip of 2 mm was used for cutting that of 3–4 mm for welding. The kerf width obtained with the PLATINO is t 0.1 mm, not lesser as desired, because the raw beam diameter on the lens is ller (22 mm) in this case of Rofin DC25, and this partially cancels the benefit ue better M^2 of the DC25. The weld speed observed was 3300 mm/min at a er of 2500 W of the source.

In earlier section, Fig. 1 shows a sheet with different welds. As it can be ed the center part of welds 1, 2, 3, 4, 5, 9, 11 shows quite interesting lts where the kerf width is ~0.15 mm. Fig. 2 shows welds 7 and 8 which ot in perfect condition due to the deformation originated by positioning ie beam on the top surface of the galvanized sheets. The polished sample ig. 2, in etched condition was subjected to stereo metallurgical microscopy vestigate the structural characteristics of the welded as well as of the base rial. Fig. 10 shows a micrograph of the weld 7 region from top view and 11 shows its cross section (50× magnification). The welds were subjected EM EDS analysis in order to investigate the residual zinc contents in the ded region. Results obtained from the analysis verified the absence of zinc ents in the weld region.

6. Comparison with other techniques

In the recent years, many techniques have been proposed to tackle the problem of laser welding of the galvanized steel in lap configuration [2–9]. These techniques have tried from the multitude of facets to approach and solve this problem. Unfortunately due to the practicalities on the production line shop floors, few have been implemented in the real world industries. In the following lines, brief summary of the general analysis of the proposed system when compared to some of the well-known methods is given.

The most obvious of the methods proposed was perhaps the "prior removal of zinc coating". This method can obviously yield good results [3], but is cumbersome to implement on the floor and is thus not practical. Also as a simpler solution, it has been tried to weld with "pulsed laser" and the results have been observed [4]. It has been noted that the weld quality is improved but still the improvement is not up to mark and that the method ends up to be too restrictive for the involved process parameters.

Hybrid laser beams have been used in the shape of "twin beam" or "hybrid beam" [11]. This method is of course more expensive with the use of either two sources or a splitting from the higher power source is used. But at the same time the system has shown impressive results while the improvement varying with different configurations. One limitation may well be its applications with different types of geometry and shape contours of the processed job. Another may well be the difference in the material properties with the involved changes in the cooling time for the keyhole. The proposed method is of course an extension of the hybrid beam method involving a precursor beam. But the improvement may well be in the working principal of this method that a forced exit path is created for the zinc vapours, which is quite independent of the job geometry and many other parameters. This feature is non-existent in many of the proposed solutions.

Probably a more well-known technique in this area is that of adding shims or "forced gap" between the sheets when welding in lap configuration. This method delivers very impressive results with the absence of porosity in the welds [12]. But at the same time, it needs time-taking pre-arrangements and becomes cumbersome on the floors due to the throughput requirements and practicalities [3].

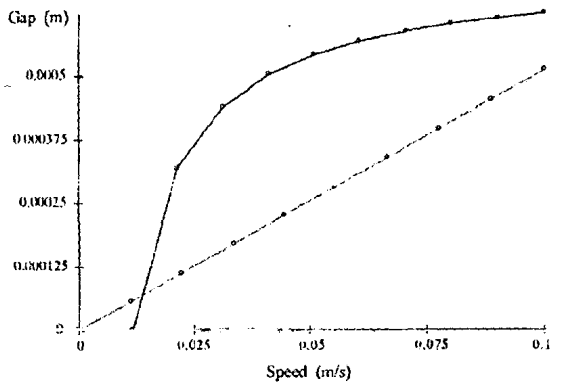

Fig. 12. Minimum slot width plotted against welding speed for both models.

As a comparison with this more discussed technique, the value of 'g' from the proposed model as given earlier is compared with this gap model [12] giving the value of minimum gap as following:

$$g = \frac{16.1 V t_{Zn}}{\sqrt{t_p}} \tag{8}$$

For the purpose of analytical comparison considering the needed gap only, which is slot gap in the proposed case and plates gap in their case, and disregarding other parameters and practicalities mentioned above, the values of minimum or allowable gaps for both of these models are compared. This comparison is now made with the varying values of involved parameters like welding velocity, etc. Here gap value if proposed system is shown in solid line and the sheet gap of other system as dashed line in Figs. 12–14.

Lower gap requirement between the plates in the sheet-gap model for the higher speeds is understood if it is kept in mind that exhaust in this case in multi-directional while in slot model case it has to go up or down into the cut slot. But in higher plate-thickness case the lower slot thickness requirement seems to be coming from the fact that part of the zinc coating has been taken care by the cutting beam which is non-existent in the other case. Additionally, the sheet gap seems quite unaffected by the variation of beam diameter as the bigger beam also gives bigger beam circumference for exhaust too.

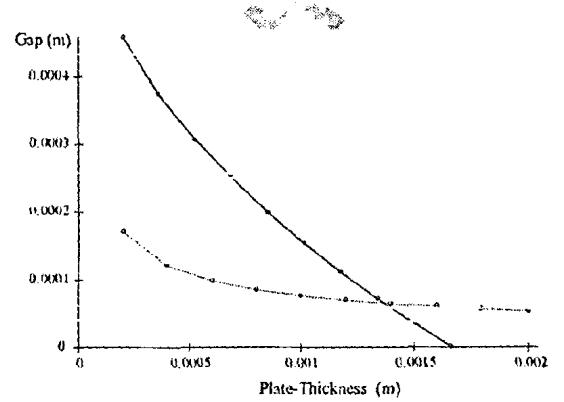

Fig. 13. Minimum slot width plotted against thickness of plate for both models.

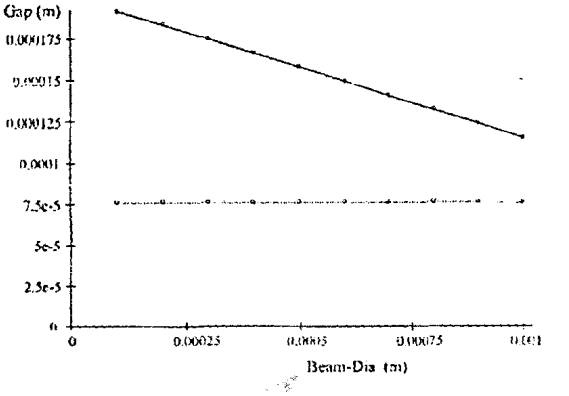

Fig. 14. Minimum slot width plotted against beam diameter for both models.

But the major strength of the proposed method comes in the ease and straightforwardness of the process and in decrease of the time required for the complete welding process and thus in the net saving of resources and capital as can be demonstrated by the following straight forward relations:

$$\text{time (dual beam method)} = \text{time}_{\text{clamping}} + \text{time}_{\text{welding}} \tag{9}$$

$$\text{time (sheet gap method)} = \text{time}_{\text{shim-placement}} + \text{time}_{\text{clamping}} + \text{time}_{\text{welding}} \tag{10}$$

Therefore, the proposed solution making the manufacturers independent of the zinc coatings and he may proceed as in case of normal welding while needing lesser time. Thus for all possible jobs and geometries, it may be concluded that

$$\text{time (dual beam method)} < \text{time (sheet gap methods)} \tag{11}$$

7. Conclusions

Tandem-beams laser welding of zinc-coated steel sheets in lap configuration has been described. For experimentation, a basic setup with standard equipment was utilized, while repeatedly using a single laser source. In spite of these limitations, it was found that the cut slot favors the dispersion of zinc vapours. The lab results have also verified the absence of zinc in the welded area. Thus the principle stands demonstrated. Following may be the conclusions.

1. Use of a cutting beam ahead of the welding beam offers a promising practical solution for the welding of the galvanized steel sheets in lap configuration.
2. The solution is easier as it does not need any pre-processing, pre-arranging with additional components or contour limitations and the welders may proceed with the jobs as per non-coated steel.
3. The solution may get rid of all the zinc vapour porosity at the lower speeds and partial of the porosity at the higher speeds.
4. The experimental results are very promising showing total absence of zinc in the welds.
5. Selection of proper source, beam alignment (between weld and cut) and proper sheet clamping are important too.

olution may end up in saving of total time needed for ng.

ledgements

uthors feel deeply indebted to Convergent-Prima for ng the tests and for providing the technical support. We rly thank Dr. Ing. G. Carbonato and Dr. Ing. A. Delle r providing useful suggestions and for helping in the tup. A specific word of thanks to Dr. Tauqir and his he metallurgy lab, for the accurate tests conducted. Part nding was provided by Higher Education Commission, and part of work was facilitated by IICS, Rawalpindi.

ces

S. Gualini, Laser welding of zinc coated steel sheets. An old problem possible solution, in: Proceedings of the ICALEO2001, Jacksonville, 2001, p. 492.
hter, W.M. Steen, D. Cruciani, Laser welding of zinc coated steel, in: edings of the Sixth International Conference on Lasers in Manufac- (LIM6), Birmingham, UK, 1989, pp. 93–104.
aeem, J. Stolarczyk, High power Nd:YAG welding of automotive ials, in: Proceedings of the ICALEO2000, Dearborn, USA, 2000, pp. A27.
[4] M. Kielwasser, R. Fabbro, R. Petring, R. Poprawe, Physical process during pulsed laser and CW–CO_2 laser welding of zinc coated steel, in: Proceedings of the ICALEO2000, Dearborn, USA, 2000, pp. A10–A19.
[5] P. Deney, J. Xie, The welding of galvanized steel, in: Proceedings of the ICALEO2000, Dearborn, USA, 2000, pp. A1–A9.
[6] G. Goebel, D. Havrilla, A. Wetzig, E. Beyer, Laser welding with long focal length optics, in: Proceedings of the ICALEO2000, Dearborn, USA, 2000, pp. A28–A37.
[7] A. Dasgupta, J. Mazumder, M. Bembenek, Alloying based laser welding of galvanized steel, in: Proceedings of the ICALEO2000, Dearborn, USA, 2000, pp. A38–A45.
[8] A.D. Delle Piane, F. Sartorio, M. Cantello, G. Ghiringhello, Method of laser welding sheet metal protected by low-vaporizing-temperature materials, US Patent 4,682,002 (1987).
[9] R. Akhter, M.M.S. Gualini, Matehmatical modeling of the laser spot welding of zinc coated steel in lap configuration, in: Proceedings of the ICALEO1998, San Diego, USA, 1998, pp. 207–216.
[10] R. Poprawe, Fraunhofer Institute for Laser Technology, personal communication.
[11] S. Bonss, B. Brenner, E. Beyer, Innovations in laser hybrid technology, Ind. Laser Sol. (2000) 29–33.
[12] R. Akhter, W.M. Steen, K.G. Watkins, Welding zinc-coated steel with a laser and the properties of the weldment, J. Laser Appl. 3 (2) (1991) 9–20.
[13] M.M.S. Gualini, Towards a solution of laser welding of zinc coated steel sheets, in: Proceedings of the ICALEO2002, Scottsdale, USA, 2002.

Modified dual-beam method for welding galvanized steel sheets in lap configuration

M. M. S. Gualini[a] and S. Iqbal
Faculty of Applied Sciences, International I University, Islamabad, Pakistan

F. Grassi
Convergent Prima Industrie, Collegno (Turin), Italy

(Received 10 January 2005; accepted for publication 19 September 2005)

The dual laser beams method to lap weld galvanized steel sheets is being discussed, modeled, and analyzed, involving a precursor beam and a higher-power actual beam used in tandem and generated independently or otherwise split from the same source (Nd:yttrium-aluminum-garnet or CO_2 laser). The first beam cuts a slot, thus making an exit path for the zinc vapors, while the second beam welds as required. The article also presents and discusses some experiments performed in laboratory using this method, along with the metallurgical analysis results from laboratory showing total absence of zinc in the weld area. © *2006 Laser Institute of America.*

Key words: laser welding, precursor beam, galvanized steel sheets, keyhole formation

I. INTRODUCTION

Zinc-coated steel sheets welding in lap configuration poses perhaps one of the most controversial problems. Solutions proposed[1–9] in the last 27 years have not yet found an easy-to-apply realization to replace spot welding and its electrodes, which have short lifetime.[2] The many advantages offered by laser welding[3] still justify a quest for very efficient methods. The ideal solution should firstly solve the technological problem of the residual zinc vapors trapped in the weld joint[4] due to the lower boiling point of the zinc (906 °C) with respect to that of steel Fe (1530 °C). The solution should also be practical and economical enough to be installed on the production lines.

II. PROPOSED SOLUTION AND SOME DISCUSSION

We first proposed that the front beam of the tandem system shall cut a slot with a minimal kerf, while the second beam shall seam-weld, joining the two sides of the kerf, while the residual zinc evaporates through the slot ahead of it. We proposed[1] two similar hybrid solutions, one combining Nd:yttrium-aluminum-garnet (YAG) and CO_2 lasers in tandem, the first for cutting, and the second for welding. Alternatively two beams of the same CO_2 laser source may also be used in tandem by the method originally proposed,[1] which is basically an integration of the "gap-method" proposed[2] several years ago and the dual beam system introduced few years back.[5]

The validity of the method proposed first theoretically, has never been challenged, but has only been questioned once,[10] fearing the high costs of utilizing two different laser sources or a higher power CO_2 laser source. The solution of combining a Nd:YAG laser to cut and a CO_2 laser to weld may be less appealing because of being more expensive. In another paper[1] we compared this solution with the alternative method of using a HPDL (Ref. 11) along with others. The present article shows the work conducted on this concept at the laboratories of Convergent-Prima in Collegno (Turin), Italy. After recalling the theoretical model adopted, we present the experimental results and discuss our guideline for the future work.

The results obtained utilizing only the standard equipment, and not the dedicated optics or custom assemblies, definitely confirm the principle, which was suggested theoretically and summarily in our previous work[1] and also largely fit the behavior predicted by preliminary theoretical model. We expect that the method proposed originally by us[1] offers a better compromise to be implemented on production line than any other method[1–12] proposed until today. In our opinion the alternate method of delaying the solidification of the keyhole suffers from the problem of strict control of the procedure parameters. The time window to enable the perfect solidification of the keyhole without residual zinc is quite narrow, and is not easily controllable as the cutting of a slot, which depends more on design parameters, rather than material specifications. In fact, the tolerances in the chemical composition of galvanized sheets may influence its thermal properties, thus resulting in a lesser quality of the weld, along with other factors like the difficulty to control the heat effects. Controlling the kerf width is quite an acquired procedure after more than 30 years of laser material processing. The kerf width is quite easily measurable utilizing any optical method available today, while measuring heat may prove more expensive and lesser accurate. We should also consider that welds on a flat material are quite easy to obtain, but the reality of a three-dimensional (3D) application is quite a challenge to be met.

III. GENERAL ANALYSIS

As already explained,[13] the proposed solution combines the advantages of the gap method[2] and coating removal,[1,5,12]

[a]Electronic mail: optica97@hotmail.com

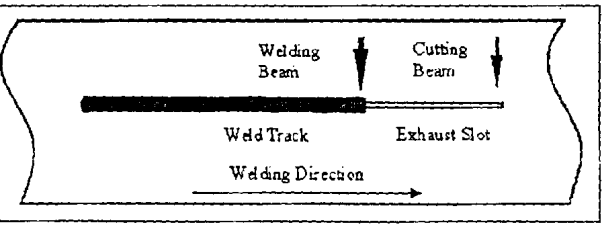

. 1. Top view of the laser lap welding using the forward slot (through h sheets).

hich are more cumbersome and expensive[13] than the thod proposed here. The main advantages of the proposed thod are those that are obtained by gap techniques, but thout a gap between the sheets. The proposed method is t cumbersome, a good alignment between the beam and rf and <0.1 mm kerf width appear to be the only critical rameters. Second, the proposed method is not constrained the actual geometry of the components to be joined. oking at the approach, we expect the method to be rela- ely economical since it does not require any extra fixture d additional man-hours for preprocessing, which are quite pensive. The apparent disadvantage of the method pro- sed is the higher investment and the running cost of the uipment due to the use of two lasers.

The solution we propose is described in Fig. 1 (top view) d Fig. 2 (side view). A precursor laser beam cuts a slot of ew centimeters of length and a certain width in front of the yhole. The slot will have two functions; the first is to re- ve the zinc coating, while the gas used in the cutting ocess will blow away the zinc vaporized in the cut, effec- ely eliminating it. We know that zinc coat removal pro- ces the best welding results, but in this case it is not cum- rsome as in the methods previously proposed in literature.[5] e second function of the slot is to provide a way out to the cess zinc vapors left after the cutting process. In fact the yhole and the surrounding molten pool may exceed the nensions of the laser beam cut width, thus involving some a where the zinc coating is still present. In this case, the t will exhaust the zinc vapors before the rapid cooling wn of the molten pool. A Nd:YAG laser beam may gener- cuts with excellent kerf and surface quality, but a CO_2 er can also be used. The distance between the cutting and lding spots can be adjusted conveniently and accordingly the 3D geometry of the component to be welded. Proper shielding and fumes removal can be handled quite easily.

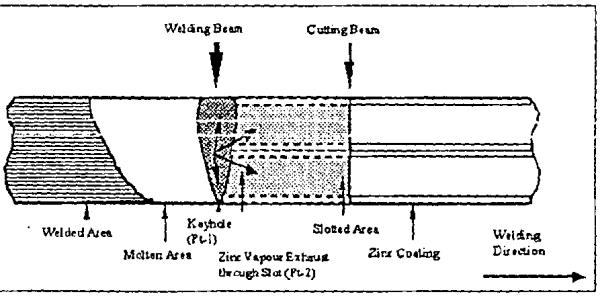

. 2. Side view of the welding operation with the two beams in tandem.

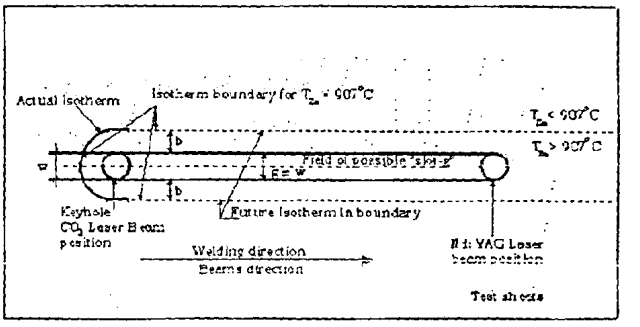

FIG. 3. The model of the proposed method including heat effects.

The figures show the simple view of the scheme of using the beams in tandem with the basic functions required by each of the laser, in order to give an idea of the degree of complexity of the hybrid laser welding/cutting nozzle. The CO_2 and/or Nd:YAG laser beams are sent to the work piece separately and the distance between the two can be preset or can otherwise be adjusted continuously by an adaptive CNC system to maximize the weld quality. It may be mentioned that the figures do not include other items like servomotors for the adjustment, the Nd:YAG nozzle assembly (100% R mirror + focusing lens system) to cut the slot or the fiber optic cable supplying the Nd:YAG laser beam to the nozzle.

IV. THEORETICAL ANALYSIS

We recall and enhance here the previously reported theory.[13] In order to develop a simple but effective mathematical model we have considered the work done by the gap method.[9,11] The approximations introduced enable us to obtain some quantitative measures. We refer to Figs. 3 and 4 in order to derive some theoretical understanding and write the model in view of the given conditions. The model of Refs. 9 and 11 is based on the considerations that the Ferro static head on top of the weld pool generates a pressure that stops the zinc vapors from getting into the keyhole (pt-1), which are being exhausted by the cut slot providing an artificial gap (pt-2),

$$\Delta P_{12} = \rho_{Fe} g_e t_p a. \tag{i}$$

Here "ρ_{Fe}" is the density in kg/m^3, "a" is the wave factor normalized to 1, "g_e" is acceleration due to gravity in m/s^2, and "t_p" is the thickness of the steel plate. The Ferro static pressure[11] generates a velocity of the zinc vapors at the ejection point. The exhaust velocity "v_2" of the zinc vapors is

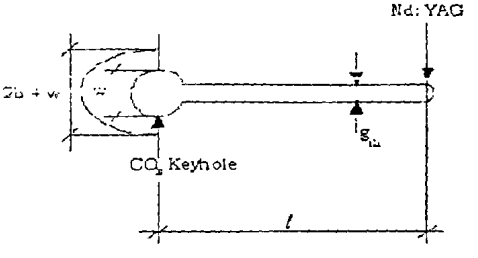

FIG. 4. The cut and weld model showing slot and keyhole sizes.

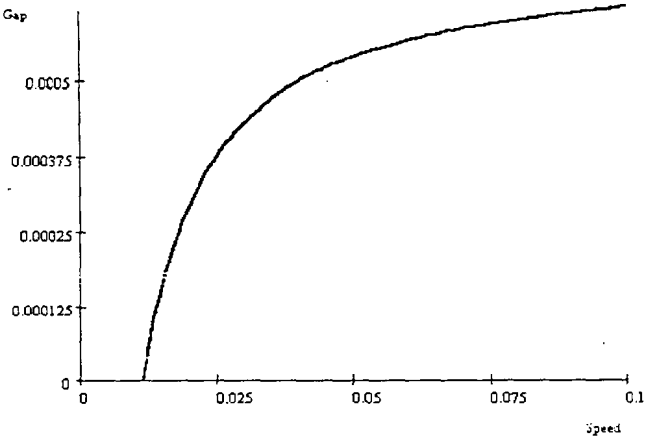

FIG. 5. Slot width plotted against the welding speed.

calculated using Bernoulli's theorem as follows:

$$\frac{P_1}{\rho_v} = \frac{P_2}{\rho_v} + \frac{v_2^2}{2}, \tag{2a}$$

$$v_2 = \sqrt{\frac{2\Delta P_{12}}{\rho_v}}, \tag{2b}$$

where ρ_v is the zinc vapor density, which can be calculated using Clausius-Clapeyron equation.[9] We calculated $\rho_v = 21.87\ \text{kg/m}^3$.

The following equations express the volume of the gases generated by the welding action and the volumes of gases that can be exhausted through the gap. It may be noted that the slot is cut by the advanced beam and the keyhole follows it at some distance. There is going to be a slot present on the sheet, even in the to-be-molten area where keyhole is being formed, having zinc on the both sides of the slot. Thus the zinc would be vaporized first. The assumption is that the width of the gap is much larger than the thickness of the galvanization layer, i.e., $g \gg t_{Zn}$,

$$\text{Vol}_{gen} = \frac{2t_{Zn}V\rho_s[(w-g)+2b]}{\rho_v}, \tag{3}$$

$$\text{Vol}_{exh} = 4v_2 t_{Zn} w. \tag{4}$$

In these, "b" is the width of zinc boiling isotherm out of the welding beam (HAZ), "t_{Zn}" is the thickness of the zinc layer, "V" is the welding speed, "ρ_s" is the solid zinc density (7140 kg/m^3), "w" is the keyhole width, and "g" is the width of the slot. Equating both of these, we get to the needed minimum value of slot width

$$g = \frac{V\rho_s(w+2b) - 2w\rho_v v_2}{V\rho_s}. \tag{5}$$

In this equation, the unknown quantity "$v2$" can be substituted by the earlier results of Bernoulli's theorem

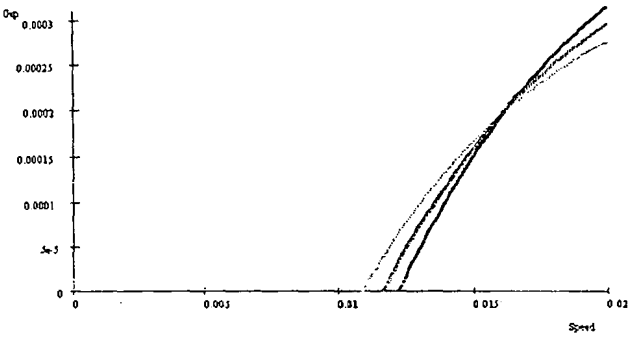

FIG. 6. Changes in the minimum gap width with change in beam width.

$$g = \frac{V\rho_s(w+2b) - 2w\sqrt{2\rho_v\rho_{Fe}g_e t_p}}{V\rho_s}. \tag{6}$$

Here we are interested in finding the optimal value of slot width g whose minimum value is given by this equation with the condition that all the zinc vapors will be exhausted by the slot and nothing will go inside the melt pool. The given minimum width can be decreased further if partial zinc vapor exhaust is allowed through the molten metal, i.e., some porosity is tolerable. The upper limit to this slot is posed practically by the situation that g should be substantially lower than w in order to allow for a proper strong weld in the presence of kerf. The value of g in Systeme International system is given as follows:

$$g = \frac{7140V(w+2b) - 2w\sqrt{3\,373\,491 t_p}}{7140V}. \tag{7}$$

The variation in minimum needed gap width against the changes is welding speed are plotted here in Fig. 5 for some representative values as $w=0.5$ mm, $b=0.1$ mm, and $t_p = 1$ mm. Note that the minimum gap values for very low speeds are less constrained and are largely governed by the same condition of $g \gg t_{Zn}$.

Here we are only interested in solutions with the condition $w > g$, which is basically given by the speed values in the left part of the plot earlier. The right part of the graph is for higher speed welding where the values computed for g by this model become unrealizable for the given condition.

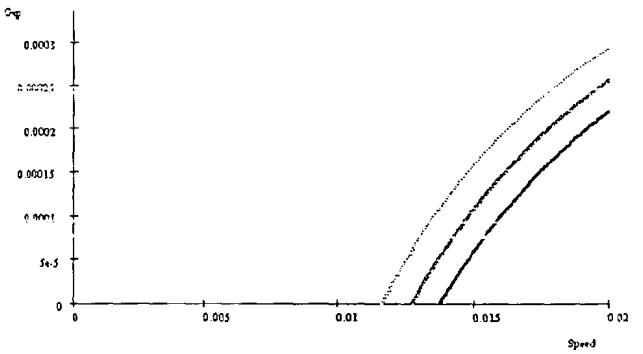

FIG. 7. Changes in minimum gap width with changes in steel plate thickness.

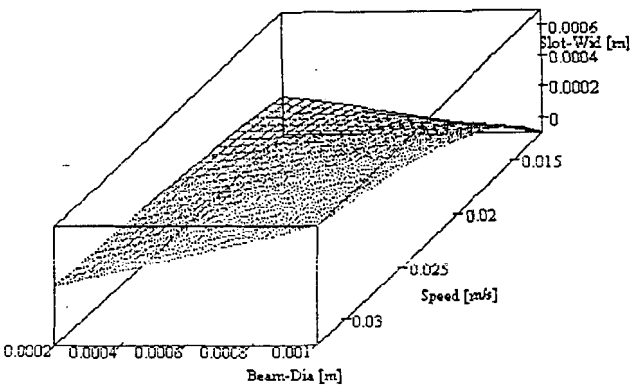

FIG. 8. Slot width shown in surface graphics against welding speed and beam diameter.

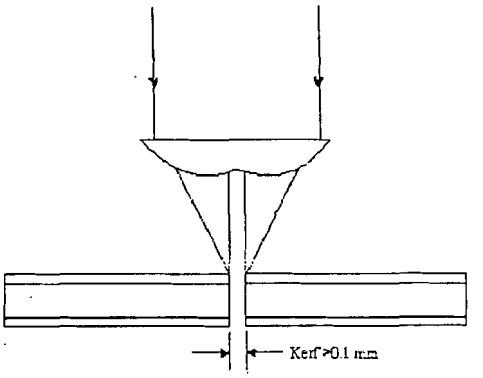

FIG. 10. Welding with a dual-focus lens.

Now we can also analyze that how the minimum gap requirements change with the changing values of welding beam width w and with the variations of steel plate thickness as shown in Figs. 6 and 7. In the first curve, the welding beam width is varied between 0.4 and 0.6 mm, and in the second curve steel plate thickness is changed in the range of 1.0–1.4 mm with the darker color showing the increasing values of both the parameters.

It may be inferred that for the variations in the welding beam width, there seems to be a point close to the maximum realizable gap width where the gap values are common for the different beam widths. For the variations in the steel plate thickness, it is clear that for the same target welding speed, the increased thickness of the steel plate requires a lesser value of the gap width. This may look surprising at the beginning, but can be understood better considering that a larger steel plate thickness is not going to effect the amount of zinc evaporating but will give more value of ferrostatic head, thus forcing the zinc vapors to exhaust through the narrower gap. Thus the higher thicknesses are not a problem in this approach, until the values become prohibitive due to the higher laser welding power needs. The surface graph showing the values of the gap obtained with different welding speeds and beam widths is given in Fig. 8.

As the surface graph indicates, the realizable value of cut-slot width is again obtained with the lower values of welding speed, which is the backpart of the graph. At the same time the variation of slot width with the welding beam diameter is pretty straight at higher speeds, and is clearly unrealizable in the front-right part of the graph. This is the situation when the speed is too high and the wider welding beam is producing more zinc vapors demanding a wider but unrealizable slot width. Thus the results of the model analysis are also fairly understandable by logic and intuition.

A point to ponder is probably the span of the surface graphics in the rear part where the gap requirement is increasing with the decreasing beam diameter. This can also be understood remembering that the smaller beam diameter is also coupled with a smaller exit orifice and causes problems as the heat-effected zone width b is taken to be a constant present in all the cases.

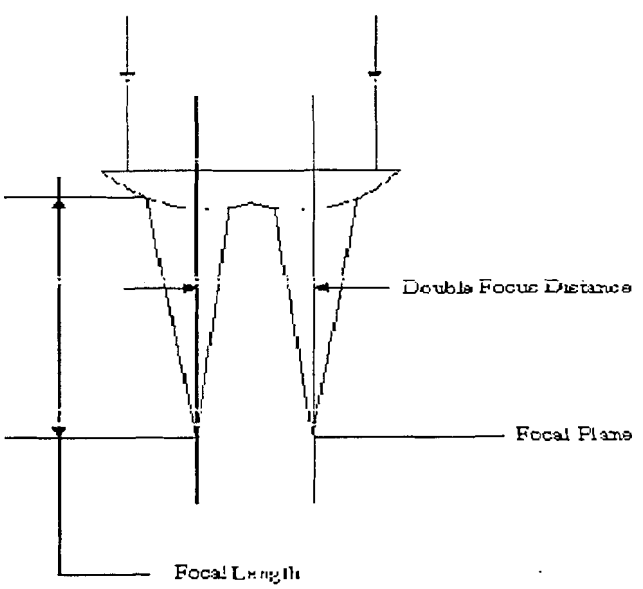

FIG. 9. Dual-focus lens.

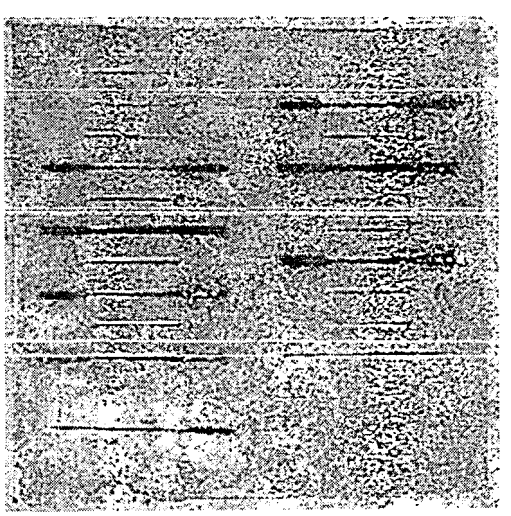

FIG. 11. Welds with proposed method.

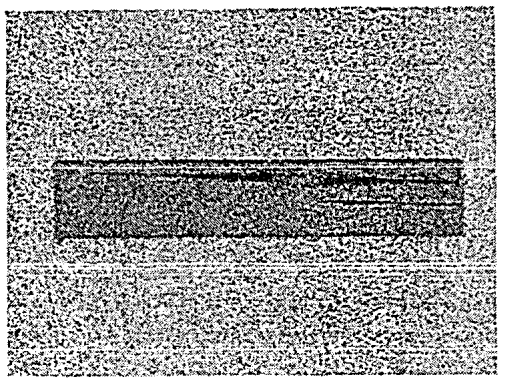

FIG. 12. Welds 7 and 8.

XPERIMENTAL RESULTS

We have conducted tests with a PRC3000 laser with a 3.28 and a "raw beam diameter" on the lens of about m ($1/e^2$) at about 9 m from the laser source [the system is a RAPIDO (Convergent Prima)]. The focused beam 234 mm, while the Rayleigh's distance is 1.24 mm. The field" divergence of the focused beam is 0.0945 rad 127). The minimal cutting kerf obtained on the double ness of the galvanized sheets (1.6 mm) is 0.15 mm, at full cutting speed. The cutting kerf is about 36% ler than the cutting beam spot due to the mode structure he beam. The power density @ 2500 W is 5.8 ^{10} W/m^2. The focal point has been positioned on the top ice. The obtained cutting kerf is quite large (>0.1 mm) leading to a "weaker" weld. In fact, even shifting the point to 3 mm below the top surface means that the beam diameter for welding is 0.6 mm (equal to 0.88 ^{10} W/m^2), rendering it largely useless because the central part of the beam (maximum intensity), is all lost through kerf. Without defocusing, the entire beam would be lost igh the kerf. Cutting and welding have been performed only one gas N_2, in order to save time.

Under the earlier conditions we have noticed that the obtained is smooth and does not show "bubbles" on its ice. In the absence of proper tooling we have offset of mm across the weld path, on the right side, with the n at 1.5 mm out of focal point. The beam size and its

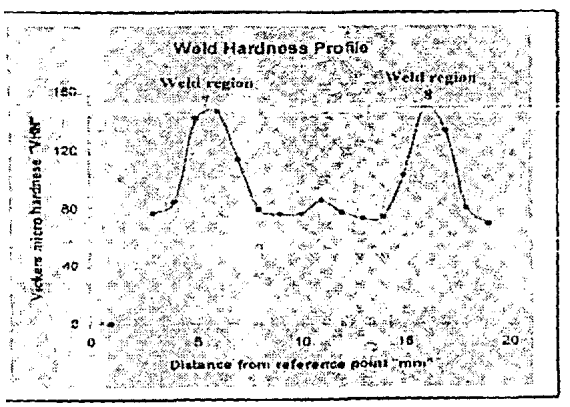

FIG. 13. Welds 7, 8, hardness profile.

FIG. 14. Micrograph of base material (×400).

power intensity are such that a good keyhole only takes place if the beam diameter covers both the kerf edges in the weld. The result was quite encouraging: we obtained an acceptable quality weld without significant defects on the surface. Obviously the weld is underdross; in other words the upper surface is concave in the bottom direction, rather than being convex as desired. This is due to the poor contribution of material owing to a 0.15 mm cutting kerf. Incidentally this is in harmony with the findings derived from the earlier theoretical model. From our findings it is quite evident that the kerf should be smaller. But at the same time we know that the kerf cannot be made too small so as to restrict the welding speed too much.

We have repeated the tests with a Convergent Prima System 2D PLATINO with a DC25 Rofin Laser and a 5 in. lens. Contrary to the 3D RAPIDO, the PLATINO is a more versatile machine because it enables to move the focal point of the laser beam utilizing the CNC so that the stand-off of the tip to the galvanized sheet and the position of the laser beam relative to the material are quite independent. In both the cases of RAPIDO and PLATINO, we used the tip of 2 mm for cutting and 3–4 mm for welding. The kerf width obtained with the PLATINO is about 0.1 mm, not lesser as desired, because the raw beam diameter on the lens is smaller (22 mm) in this case of Rofin DC25, and this partially cancels the benefit of the better M^2 of the DC25. The weld speed observed was 3300 mm/min at a power of 2500 W of the source.

In the future, we may also utilize a laser-welding beam of elliptical cross section, by proper optical beam shaping. Figures 9 and 10 show this alternative solution to beam shap-

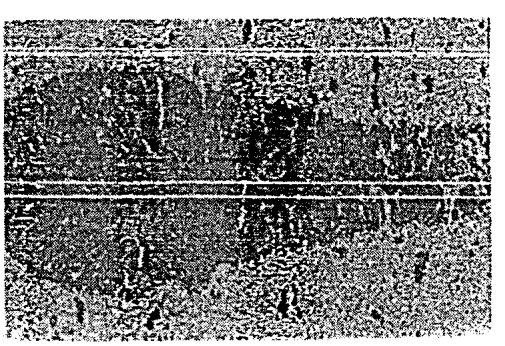

FIG. 15. Micrograph of weld 7 * top view.

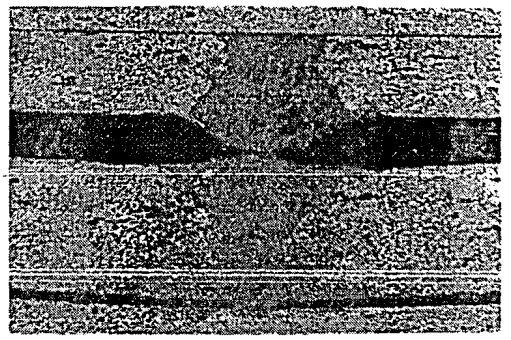

FIG. 16. Micrograph of weld 7 * side view.

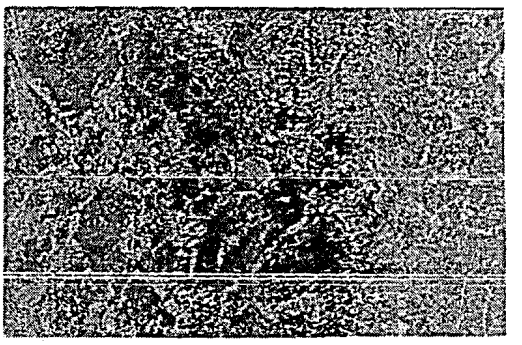

FIG. 18. Micrograph of weld 7 (×400).

ing, which is basically to use a lens with a double convex shape so that the laser beam can be doubled and the two parallel beams are losing energy at the middle of the kerf. Having started with a wider kerf offers the study of the "worst case" so that by reducing the kerf width one can monitor the improvements.

Figure 11 shows a sheet with different obtained welds. As it can be noticed the center part of welds 1, 2, 3, 4, 5, 9, and 11 show quite interesting results where the kerf width is ~0.15 mm. Figure 12 chows welds 7 and 8 which are not in perfect condition due to the deformation originated by positioning of the beam on the top surface of the galvanized sheets. In this case we could speak of a "Akhter/Steen effect" because the deformation somehow combines the "vertical gap" with our solution. Figure 13 shows the hardness profile across the welds 7 and 8. the polished samp[le of Fig. 12, in rtched condition was subjected to stereo metallurgical microscopy to investigate the structural characteristics of the welded as well as of the base material. Figure 14 shows a ×400 magnification of the base material while Fig. 15 shows a micrograph of the weld 7 region from top view and Fig. 16 shows its cross section (×50 magnification). Figure 17 is a micrograph of the cross section of weld 7, with an open cavity on the top. Figure 18 is a microfraph of weld 7 cross section structure (×400 magnification). The welds were subjected to SEM EDS (scanning electron microscopy energy dispersive electroscopy) analysis in order to investigate the residual zinc contents in the weld region. Further investigation with various parameter changes is underway.

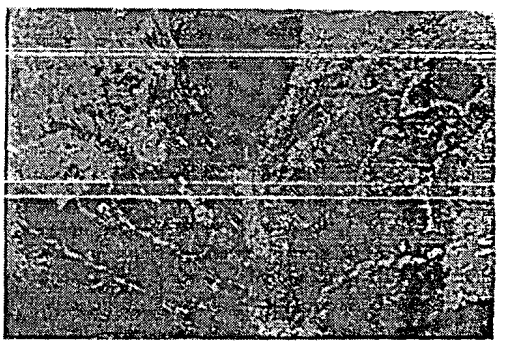

FIG. 17. Micrograph of weld 7 (×200).

VI. CONCLUSIONS

In the theoretical part we produced and analyzed the model of the modified two-beam method involving one precursor beam for cutting. In the experimental part we have utilized a very basic setup with standard equipment and the available resources. Practical results have been obtained in this representative setup and the material analysis has been performed. In spite of the limitations, we have found that the cut slot favors the dispersion of zinc vapor, and thus the principle stands demonstrated. Further experimentation is expected to be carried out in due course of time. The following may be the conclusions:

(1) Use of a precursor cutting beam ahead of the actual welding beam offers a promising practical solution for the welding of the galvanized steel sheets in lap configuration.
(2) The solution is expected to be easier for implementation on the production lines as it should not need any preprocessing or prearranging with additional components.
(3) The solution may get rid of all the zinc vapor porosity at the lower speeds and partial of the porosity at the higher speeds.
(4) The experimental results are very promising showing total absence of zinc in the welds.
(5) Selection of the proper source, beam alignment (between weld and cut), and proper sheet clamping are important for this method in order to avoid misalignment between weld and the kerf.
(6) For even better results, a shaping optic for the welding beam may be incorporated so that its cross section is elliptical or, alternatively, a dual focus lens system may be used.

ACKNOWLEDGMENTS

The authors feel deeply indebted to Convergent-Prima, Italy for conducting the tests, with particular thanks to Dr. Ing. G. Carbonato and Dr. Ing. A. Delle Piane. The authors want to thank Dr. William Steen and Dr. Rehan Akhtar for the useful feedback about the discussed approach. A specific word of thanks to Dr. Tauqeer and his team of the metallurgy lab for the precision analysis. The authors are indebted to Higher Education Commission for research grant and IICS,

Rawalpindi for facilitating this work. Finally, the authors express particular gratitude for the never-failing support of their families.

[1]M. M. S. Gualini, "Laser Welding of Zinc Coated Steel Sheets. An Old Problem with a Possible Solution," *Proceedings of ICALEO2001, Jacksonville, October 2001*, p. 492.
[2]R. Akhter, W. M. Steen, and D. Cruciani, "Laser Welding of Zinc Coated Steel," *Proceedings of the 6th International Conference on Lasers in Manufacturing (LIM6), Birminghain, UK, 1989*, pp. 93–104.
[3]M. Naeem and J. Stolarczyk, "High Power Nd:YAG Welding of Automotive Materials," *Proceedings of ICALEO2000, Dearborn, MI, October 2000* (LIA, Orlando, FL, 2000). Vol. 91, pp. A20–A27.
[4]M. Kielwasser, R. Fabbro, R. Petring, and R. Poprawe, "Pnysical Process During Pulsed Laser and CW-CO_2 Laser Welding of Zinc Coated Steel," *Proceedings of ICALEO2000, Dearborn, MI, October 2000* (LIA, Orlando, FL, 2000), Vol. 91, pp. A10–A19.
[5]P. Deney and J. Xie, "The Welding of Galvanized Steel," *Proceedings of ICALEO2000, Dearborn, MI, October 2000* (LIA, Orlando, FL, 2000), Vol. 91, pp. A1–A9.
[6]G. Goebel, D. Havrilla, A. Wetzig, and E. Beyer, "Laser Welding with Long Focal Length Optics," *Proceedings of ICALEO2000, Dearborn, October 2000* (LIA, Orlando, FL, 2000), Vol. 91, pp. A28–A37.
[7]A. Dasgupta, J. Mazumder, and M. Bembenek, "Alloying Based L Welding of Galvanized Steel," *Proceedings of ICALEO2000, Dearb MI, October 2000* (LIA, Orlando, FL, 2000), Vol. 91, pp. A38–A45.
[8]A. D. Delle Piane, F. Sartorio, M. Cantello, and G. Ghiringhello, "Met of Laser Welding Sheet Metal Protected by Low-Vaporizing-Temperat Materials," U.S. Patent No. 4682002, July 1987.
[9]R. Akhter and M. M. S. Gualini, "Mathematical Modeling of the La Spot Welding of Zinc Coated Steel in Lap Configuration," *Proceedings ICALEO1998, November 1998* (LIA), Sec. F, pp. 207–216.
[10]R. Poprawe, Fraunhofer Institute for Laser Technology (personal comm nication).
[11]S. Bonss, B. Brenner, and E. Beyer, "Innovations in Laser Hybrid Tec nology," Ind. Laser Sol., 29–33 (2001).
[12]R. Akhter, W. M. Steen, and K. G. Watkins, "Welding Zinc-Coated Ste with a Laser and the Properties of the Weldment," J. Laser Appl. 3, 9– (1991).
[13]M. M. S. Gualini, "Towards a Solution of Laser Welding of Zinc Coat Steel Sheets," *Proceedings of ICALEO2002, Scottsdale, AZ, Octob 2002*, (LIA, Orlando, FL, 2002), Vol. 94.